MRI-gebaseerde attenuatiecorrectie voor emissietomografie

MRI-Based Attenuation Correction for Emission Tomography

Vincent Keereman

Promotoren: prof. dr. S. Vandenberghe, prof. dr. C. Vanhove
Proefschrift ingediend tot het behalen van de graad van
Doctor in de Ingenieurswetenschappen: Biomedische Ingenieurstechnieken

Vakgroep Elektronica en Informatiesystemen
Voorzitter: prof. dr. ir. J. Van Campenhout
Faculteit Ingenieurswetenschappen en Architectuur
Academiejaar 2011 - 2012

UNIVERSITEIT
GENT

ISBN 978-90-8578-474-6
NUR 954
Wettelijk depot: D/2011/10.500/77

Department of Electronics and Information Systems
Faculty of Engineering and Architecture
Ghent University

UNIVERSITEIT GENT

MEDISIP
IBiTech - IBBT
Campus Heymans, Block B
De Pintelaan 185
9000 Ghent
Belgium

Promotors:
Prof. dr. Stefaan Vandenberghe
Prof. dr. Christian Vanhove

Board of examiners:
Prof. dr. ir. Rik Van de Walle, Ghent University, chairman
Prof. dr. ir. Roel Van Holen, Ghent University, secretary
Dr. Ewout Vansteenkiste, Ghent University
Prof. dr. Tony Lahoutte, Vrije Universiteit Brussel
Prof. dr. Sibylle Ziegler, Technische Universität München
Prof. dr. Tobias Schaeffter, King's College London
Prof. dr. Stefaan Vandenberghe, Ghent University
Prof. dr. Christian Vanhove, Ghent University

This work was supported by the 7th Framework Programme of the European Union through the projects HYPERimage (Grant Agreement No 201651) and SUBLIMA (Grant Agreement No 241711).

Acknowledgements

This dissertation is the result of four years of work. This work could not have been done without the direct or indirect support of so many people, each and everyone of which I'm grateful to have worked with. First of all I want to thank my promotor prof. dr. Stefaan Vandenberghe, for the initial trust and for giving me the opportunity to start working at MEDISIP in a rather special situation. Also for the endless list of ideas he supplied me with during these last four years. Finally, for maintaining such an informal and friendly atmosphere at our lab, which makes working there such a great experience. I also want to thank my co-promotor prof. dr. Christian Vanhove, for the fruitful collaboration on the experiments in Brussels. He joined our lab more recently and has been a tremendous help since then as well.

I want to express my gratitude to all of my colleagues at MEDISIP, many of whom have become very good friends over the years. We have had so much fun that it hardly ever felt like work. Specifically I want to thank Roel for the many scientific discussions, for always being ready to help and of course for the many hilarious nights out, from the kebab bars of Dresden to the rock festivals of Belgium. Also present for most of those nights was Pieter (van Mierlo), whom I also want to thank for always keeping the atmosphere in our office and for the great trip to Kyoto. Although he was working on EEG, Pieter was never afraid to chip in on some PET discussions as well. Another essential part of our office was Pieter (Mollet). Always motivated, he is a pleasure to work with. I also tremendously enjoyed our trips, be it around the American east coast or just to Aachen - at least when we were not staying in a hotel in the wrong city. Hendrik, who has been one of my best friends for many years, also joined us last year and we've had a lot of laughs since he did. Ewout, who was not always in our office, was still around enough to make plenty insightful remarks. I want to thank Bert, for our trip to Montreal and for always being so up-to-speed on everything. Karen, for always smiling and never being intimidated by the masculin majority at MEDISIP. Gregor, for sharing the music. Karel, for all the practical advice.

Victoria, for willing to share the office with such loud men. Anne-Marie and Saskia, for all the administrative support. Scharon and Benedicte, for the help in the lab, and Enrico, Kasper, Sinem, Faruk and Samuel.

I also want to thank some of my ex- (or semi-ex-) colleagues. Hans, for always having an open door for questions. Erwann, for always being so happy and helping me during my first months at MEDISIP. Prof. dr. ir. Steven Staelens, for always having an opinion. Tom, for making parties unforgettable. Els, for helping me out with my first MRI scans and for the dinners in New York. Jan, for the help with GATE, and Long, Steven, Eva, Sara, Jeroen, Tom, Yves and Ayfer.

This work would also not have been possible without the help from many people who do not work at MEDISIP. First of all Yves at the UZ Brussel as well as his former colleague Tom, for the many hours performing experiments on the 3T. Prof. dr. Yves De Deene, for having an answer to any MRI-related question. Steven, for the many research meetings and the trip to Hawaii. I also want to thank everyone in the HYPERimage and SUBLIMA collaborations.

Apart from all the people at work, I also owe a lot of gratitude to my family. First of all to my girlfriend Lynn, for always supporting me. Even during these last few very busy months, you've been great. It must be difficult from time to time to have workaholic for a boyfriend. To my parents, for giving me all the opportunities I can think of. Your continuing interest is my greatest motivation. To my brothers Stefan and Filip and to Elke and Eline, for the many great times we have spent together - and for reminding me from time to time that doing a PhD is not a real job. To my godchild Anna-Louise, for making me smile - I'm sure you will surprise us one day. To Emilie and Bonpapa, who are sadly no longer among us but who's memory inspires us everyday to make the most of life. And to the rest of the family.

I also want to thank all of my friends for their support. Especially Jeroen, for always being honest. Bart, for always having my back. Melissa, for putting up with me since high school. Pieter-Jan and Stijn, for all the fun we've had with The Jesters. Lode, for the legendary expressions. Sara, for the great talks. Also my fellow medical students, especially those who helped me out with course notes - Ina in particular. And all others which I'm not forgetting here but simply omitting due to a lack of space: thank you!

Vincent Keereman
Ghent, December 2011

"I am sure my fellow-scientists will agree with me if I say that whatever we were able to achieve in our later years had its origin in the experiences of our youth and in the hopes and wishes which were formed before and during our time as students. It seems that this situation is not restricted to science but is more generally human."

Felix Bloch, Swiss physicist. Banquet speech on the evening before receiving the Nobel Prize in Physics 1952 together with Edward Purcell for their work on NMR.

Table of Contents

List of Figures

List of Tables

List of acronyms

A

APD	Avalanche PhotoDiode

B

BOLD	Blood Oxygen Level Dependent

C

CLEAR	Constant LEvel AppeaRance
CT	X-ray Computed Tomography
CZT	Cadmium-Zinc-Telluride

D

DCE-MRI	Delayed Contrast Enhanced MRI
DMSA	DiMercaptoSuccinic Acid

F

FBP	Filtered BackProjection
FDG	FluoroDeoxyGlucose
FID	Free Inductive Decay
fMRI	functional MRI

G

GATE	GEANT Application for Tomographic Emission
GE	Gradient Echo
GEANT4	Geometry And Tracking 4

H

HMPAO	HexaMethylPropyleneAmine Oxime
HU	Hounsfield Units

L

LOR	Line Of Response
LSO	Lutetium oxyorthosylicate
LYSO	Lutetium-Yttrium oxyorthosylicate

M

MAA	Macro-Aggregated Albumin
MAG3	MercaptoAcetyltriGlycine
MC	Monte Carlo
MCAT	Mathematical Cardiac Torso phantom

MDP	Medronic acid
MIBG	MetaIodoBenzylGuanidine
ML-EM	Maximum Likelihood - Expectation Maximization
MRA	Magnetic Resonance Angiography
MRF	Markov Random Field
MRI	Magnetic Resonance Imaging
MRS	Magnetic Resonance Spectroscopy

N

NCAT	NURBS-based Cardiac Torso phantom
NMR	Nuclear Magnetic Resonance

O

OSEM	Ordered Subsets Expectation Maximization

P

PD	Proton Density
PET	Positron Emission Tomography
PMMA	Poly(Methyl MethAcrylate)
PMT	PhotoMultiplier Tube

R

RF	RadioFrequency

S

SE	Spin Echo
SENSE	SENSitivity Encoding
SiPM	Silicon PhotoMultiplier
SPECT	Single Photon Emission Computed Tomography

T

TEW	Triple Energy Window
TF	Transmitted Fraction

U

UTE	Ultrashort Echo Time

V

VOI	Volume-Of-Interest

English summary

Nederlandstalige samenvatting

English summary

The work presented in this dissertation is situated in the field of multimodal medical imaging, specifically in the combination of emission tomography with magnetic resonance imaging (MRI). Emission tomography is based on the tracer principle, in which a radioactive isotope linked to a biochemically interesting molecule is administered to the patient. By recording the radiation emitted by the isotope and using specialized reconstruction algorithms, the distribution of the tracer within the body can be derived. Two types of isotopes are used in emission tomography: positron emitters and single photon emitters, used in positron emission tomography (PET) and single photon emission computed tomography (SPECT) respectively. Currently, there is a lot of research into combining the functional information obtained with PET or SPECT with anatomical information from MRI. MRI is a medical imaging technique which is based on the acquisition of RF signals from protons and offers high resolution as well as very good soft tissue contrast.

In PET or SPECT, different image-degrading effects are present which need to be corrected for in the reconstruction algorithm. Photon attenuation is one of the major effects in both modalities. To correct for photon attenuation, the distribution of attenuation coefficients throughout the imaging volume is needed. This distribution is called the attenuation map. The attenuation coefficient of a certain material (e.g. biological tissue) is related to the electron density of that material. In current PET or SPECT systems the attenuation map is usually derived from a X-ray computed tomography (CT) image or a transmission scan. This is straightforward as the signal obtained with those acquisitions is related to electron density. In PET-MRI or SPECT-MRI, the attenuation map should ideally be derived from the MRI image. This is much more difficult, as the MRI signal of a certain tissue is related to the proton density and relaxation properties of that tissue, not to its electron density. An additional problem is that lung and cortical bone, two important tissue types for attenuation, are not visible on images acquired with conventional MRI sequences. This problem is solved

in most currently available MRI-based attenuation correction methods by making assumptions on patient anatomy. However, these methods may fail when anatomic abnormalities are present. The purpose of this work is to derive a MRI-based attenuation correction method which derives the attenuation map from MRI image intensity alone, without assumptions on patient anatomy.

Before the design of a new method was started, the requirements for a MRI-based attenuation correction method were first investigated. Using simulation studies, the effect of errors or simplifications in the attenuation map on the reconstructed PET images was investigated. As the effect of attenuation depends on the size of the object under study, this was done for a rat study, a human brain study and a human whole-body study. The results indicated that for rat imaging, three tissue types need to be discriminated to obtain accurate quantification: air, lung and soft tissue. If bone is also discriminated, this yields even better quantification. It was also shown that a relatively high fraction (20 %) of classification errors in bone and lung tissue can be tolerated. For human brain imaging, air, soft tissue and bone should be discriminated. Classification errors which assign the attenuation coefficient of soft tissue to voxels containing bone can be tolerated, but assigning the attenuation coefficient of air to bone voxels should be avoided.

For human whole-body imaging, five tissue types should be discriminated to obtain accurate quantification: air, lung, soft tissue, spongeous bone and cortical bone. Additionally, the discrimination of adipose tissue can also be interesting but is not strictly necessary. It was also shown that inter-patient variability of the attenuation coefficient of lung tissue can lead to significant errors. As in the human brain study, we observed that limited classification errors from cortical bone to soft tissue can be tolerated, but classification errors from cortical bone to air or lung can not. We also showed that for lung tissue, misclassification into air is acceptable when less than 10 % of voxels are misclassified, but classification of lung voxels as bone or soft tissue should be avoided.

The results from the simulation study indicated that, apart from air, soft tissue and spongeous bone, a new MRI-based attenuation correction method should be able to discriminate cortical bone and lung as well. To that extent, ultrashort echo time (UTE) MRI sequences were introduced. UTE sequences use special fast acquisition schemes which allow recording the signal of tissues with very fast relaxation, such as tendons and ligaments.

Lung and cortical bone exhibit even faster relaxation. Therefore, the MRI properties of both tissue types were first investigated to determine if signal from lung and cortical bone could be acquired with a UTE sequence. It was shown that this was possible.

A general method for creating contrast between the different tissue types relevant for attenuation correction was then introduced. A UTE sequence usually acquires two images: the free inductive decay (FID) image, acquired as quickly as possible after RF excitation, and a normal gradient echo image. From these two images, the transverse relaxation map or R_2-map can be calculated. R_2 is a quantitative parameter, contrary to MRI image intensity which can change between different scans as it depends on scanner settings such as receiver gain. The R_2-map shows high values in tissues which have fast relaxation, such as cortical bone and lung, and low values in tissues with slower relaxation such as soft tissue. The R_2-map can also show high values in voxels containing air due to noise. Therefore, it needs to be corrected with a binary mask to set all voxels containing air to zero, yielding the corrected R_2-map. In this work, all UTE-MRI-based attenuation maps were derived from the corrected R_2-map. As a proof of principle, we first showed the feasibility of discriminating air, soft tissue and cortical bone on a segment of bovine femur bone.

Before testing our method on real animal or human data, it was tested on phantoms. As no suitable phantoms were available, two new phantoms were designed. The first was a pig head, used as a model for human brain imaging. Evaluation of the classification accuracy of our method versus a segmented CT image showed a classification accuracy of approximately 90 % in soft tissue and cortical bone and approximately 80 % in air. The results from the simulation study indicate that this should be sufficient to allow accurate quantification. To assess the feasibility of discriminating lung tissue with our method, a human thorax phantom was also designed. It consisted of a PMMA cylinder containing a segment of bovine femur bone and a lobe of a pig lung. The phantom was filled with activity and PET images reconstructed with CT-based and UTE-MRI-based attenuation correction were compared. A quantitative difference of 2 % was found in two hot spots and one cold spot inserted into the phantom. This showed that the discrimination of lung tissue was possible with our method.

Subsequently, our method was tested on small animal data. First, an extensive micro-SPECT study was described, using a total of 18 rats in-

jected with different ^{99m}Tc labeled tracers that targeted different organs. The images reconstructed with different MRI-based attenuation maps were compared to the images reconstructed with micro-CT-based attenuation correction. It was shown that good results can be obtained in most studies with a simple uniform attenuation map. However, when accurate quantification is required, a UTE-MRI-based attenuation map is preferred. Using our method, average quantitative errors below 1 % were obtained in the lung, kidney, liver and spleen and errors of 5 - 8 % were obtained in the brain. A more limited micro-PET study was also performed, acquiring images of three dead rats in which artificial ^{18}F-FDG lesions were implanted. The micro-PET images were again reconstructed with different attenuation maps. Comparable results as in the micro-SPECT study were obtained.

As a last step, our method was also tested on human data. A first study showed the feasibility of performing UTE-MRI-based attenuation correction for clinical brain imaging on 5 patient PET-CT-MRI data sets. The classification accuracy of our method was shown to be between 80 and 90 % for all patient data sets, with discrimination between tissue and air above 95 % for all cases. The reconstructed PET images showed an average relative error of 3 % in 12 clinically relevant volumes of interest (VOIs). No artificial hot or cold spots were observed in any of the data sets. These numbers are acceptable for clinical imaging.

Human thoracic imaging is a lot more difficult, as was shown on a single patient data set. The discrimination of air, lung, soft tissue and bone based on MRI image intensity alone was not possible, as too many classification errors were made. These classification errors led to significant errors in the reconstructed PET images, showing numerous artificial hot spots. Therefore, a more advanced algorithm was designed. It used Markov random fields (MRF) to accurately segment the lungs, and only attempts to detect bone in the spine region. Using this modified method, better results were obtained. Accurate quantification in the heart, lung and spine was possible. However, a single artificial hot spot was created in the lungs. Therefore, this method can only be used in thoracic imaging with caution.

No experiments were done on whole-body data sets. This is partly due to the fact that we did not have the possibility to acquire such data sets, but mostly because we believe further work is needed to allow the application of our method to whole-body data. Some of the issues that need to be solved include the difficulties in tissue discrimination as shown in the thoracic data set and the long acquisition time that is needed for UTE imaging. Also, the

method should first be tested and optimized for other regions of the body, such as the pelvis or abdomen. When good performance has been shown for all regions of the body, a method for whole-body imaging can be derived.

As a final conclusion, we have shown that air, lung, soft tissue and bone can be discriminated with the method developed in this work. Using this method, the feasibility of performing UTE-MRI-based attenuation correction in small animal (micro-PET and micro-SPECT) and human brain studies was shown. To evaluate the robustness of our method and the possibility of full automation for clinical use, it would be interesting to perform a clinical brain study with more subjects. More work is also needed on the subject of human thoracic or whole-body imaging.

Nederlandstalige samenvatting

Het onderzoek dat in dit proefschrift beschreven wordt is gesitueerd binnen de context van multimodale medische beeldvorming. Meerbepaald is het van toepassing op de combinatie van emissie tomografie met magnetische resonantie beeldvorming (*magnetic resonance imaging, MRI*). Emissie tomografie is gebaseerd op het speurstof principe, waarin een radioactief isotoop verbonden aan een biochemische molecule wordt toegediend aan de patient. Door de straling van het radioactief isotoop te detecteren kan men met behulp van gespecialiseerde reconstructie-algoritmes de distributie van de speurstof in het lichaam van de patient afleiden. Twee soorten isotopen worden gebruikt in emissie tomografie: *positron emitters* en *single photon emitters*, respectievelijk gebruikt in *positron emission tomography (PET)* en *single photon emission computed tomography (SPECT)*. Er wordt momenteel veel onderzoek gedaan naar de mogelijkheid om de functionele informatie die verkregen wordt met PET of SPECT te combineren met de anatomische informatie uit MRI beelden. MRI is een medische beelvormingstechniek die gebaseerd is op het detecteren van radiofrequente (RF) signalen van protonen. MRI maakt het mogelijk om anatomische beelden op te nemen met hoge resolutie en hoog zacht weefsel contrast.

In PET en SPECT zijn er verschillende effecten die de beeldkwaliteit verminderen. In het reconstructie-algoritme dient een correctie voor deze effecten geïmplementeerd te worden. Foton attenuatie is een belangrijk effect in zowel PET als SPECT. Om hiervoor te corrigeren dient de verdeling van attenuatiecoëfficienten binnen het beeldvolume gekend te zijn. Deze verdeling wordt de attenuatiemap genoemd. De attenuatiecoëfficient van een bepaald materiaal, bijvoorbeeld biologisch weefsel, wordt bepaald door de elektronendensiteit van dat materiaal. In huidige PET en SPECT systemen wordt de attenuatiemap meestal afgeleid van een X-stralen to-

mografie beeld (*X-ray computed tomography, CT*) of transmissiescan. Dit is eenvoudig aangezien het signaal dat verkregen wordt met die methoden direct gerelateerd is aan de elektronendensiteit. In PET-MRI of SPECT-MRI zou de attenuatiemap best uit de MRI beelden afgeleid worden. Dit is moeilijk aangezien het MRI signaal van een weefsel gerelateerd is aan de protondenstieit en relaxatie eigenschappen van dat weefsel, niet aan de elektronendensiteit. Een bijkomend probleem stelt zich doordat long en corticaal bot, twee weefsels die van belang zijn voor attenuatie, onzichtbaar zijn op conventionele MRI beelden. In de meeste momenteel beschikbare MRI-gebaseerde attenuatiecorrectie methodes wordt dit opgelost door bepaalde veronderstellingen te doen met betrekking tot de anatomie van de patiënt. Dergelijke methoden kunnen echter fouten maken indien de patiënt niet voldoet aan die veronderstellingen. Het doel van dit onderzoek is om een MRI-gebaseerde attenuatiecorrectie methode te ontwikkelen die de attenuatiemap afleidt van de informatie in de MRI beelden alleen, zonder veronderstellingen te doen met betrekking tot de anatomie van de patiënt.

Alvorens een nieuwe methode te ontwerpen, onderzochten we eerst de voorwaarden waaraan een MRI-gebaseerde attenuatiecorrectie methode moet voldoen. Met behulp van simulaties werd het effect van fouten en vereenvoudigingen in de attenuatiemap op de gereconstrueerde PET beelden onderzocht. Aangezien het effect van attenuatie afhankelijk is van de grootte van het object dat in beeld gebracht wordt, werd dit gedaan voor een rat studie, een humane hersenstudie en een humane studie van het volledige lichaam. Uit de resultaten kon afgeleid worden dat voor rat beeldvorming drie verschillende weefsels dienen te worden onderscheiden in de attenuatiemap: lucht, long en zacht weefsel. Indien bot ook in rekening gebracht wordt bekomt men nog betere resultaten. Er werd ook aangetoond dat een relatief grote fractie (20 %) van bot of long voxels verkeerd geclassificeerd mogen worden. Uit de humane hersenstudie konden we afleiden dat zowel lucht, zacht weefsel als bot dienen onderscheiden worden. Classificatie fouten van bot naar zacht weefsel kunnen getolereerd worden, maar men dient te vermijden dat de attenuatiecoefficient van lucht toegewezen wordt aan voxels die bot bevatten.

In de humane studie van het volledige lichaam werd gezien dat vijf verschillende weefsels moeten onderscheiden worden in dat soort studie: lucht, long, zacht weefsel, spongieus bot en corticaal bot. Eventueel kan vetweefsel ook in rekening gebracht worden. Er werd ook aangetoond dat de variabiliteit van de attenuatiecoefficient van de longen tussen verschillende patiënten een significant effect kan hebben. Net zoals in de humane hersenstudie

werd gezien dat beperkte classificatie fouten van bot naar zacht weefsel geen probleem vormen, maar classificatie van bot als lucht of long moet vermeden worden. Tot 10 % van de voxels met longweefsel mogen verkeerd geclassificeerd worden als lucht, maar fouten die long voxels classificeren als zacht weefsel of bot leiden snel tot significante afwijkingen.

Uit de resultaten van de simulatiestudies kon afgeleid worden dat een nieuwe MRI-gebaseerde attenuatiecorrectie methode naast lucht, zacht weefsel en spongieus bot ook long en corticaal bot dient te kunnen onderscheiden. Om dit mogelijk te maken werden ultrakorte echo tijd (*ultrashort echo time, UTE*) sequenties geïntroduceerd. Deze gebruiken speciale acquisitiemethoden om signaal op te nemen in weefsels met zeer snelle relaxatie, zoals pezen en ligamenten. Long en corticaal bot tonen nog snellere relaxatie dan deze weefsels. Daarom werden de MRI eigenschappen van long en corticaal bot eerst onderzocht om te zien of het mogelijk was om signaal uit die weefsels te detecteren met een UTE sequentie. De resultaten toonden dat dit het geval was.

Vervolgens werd een methode ontworpen om contrast te genereren tussen de verschillende weefsels die van belang zijn voor attenuatiecorrectie. Een UTE sequentie neemt gewoonlijk twee beelden op: een beeld van het vrij inductief verval (*free inductive decay, FID*) en een normaal gradient echo beeld. Uit deze twee beelden kan de transversale relaxatiemap of R_2-map berekend worden. R_2 is een kwantitatieve parameter, in tegenstelling tot MRI beeldintensiteit, die kan veranderen tussen verschillende acquisities omwille van scanner instellingen zoals signaalversterking. De R_2-map toont hoge waarden in weefsels die snel relaxeren, zoals corticaal bot en long, en lage waarden in weefsels die trager relaxeren zoals zacht weefsel. In voxels waarin lucht zit kan de berekende R_2 ook hoog zijn omwille van ruis. Daarom moet de R_2-map gecorrigeerd worden met een binair masker waardoor alle voxels met lucht op nul gezet worden. Dit geeft de gecorrigeerde R_2-map. In dit onderzoek werden alle attenuatiemappen afgeleid van de gecorrigeerde R_2-map.

In een volgende stap hebben we deze methode getest op fantomen. Aangezien geen bruikbare fantomen bestaan, werden twee nieuwe fantomen ontworpen. Het eerste fantoom was een varkenskop, en werd gebruikt als model voor beeldvorming van humane hersenen. De juistheid van de classificatie van onze methode werd geëvalueerd ten opzichte van een gesegmenteerd CT beeld. Deze was ongeveer 90 % in zacht weefsel en bot

en ongeveer 80 % in lucht. De resultaten van de simulatie studie doen vermoeden dat dit voldoende accuraat is om goede beelden te bekomen. Om te evalueren of longweefsel kon onderscheiden worden met de ontworpen methode werd ze ook getest op een humaan thorax fantoom. Dat fantoom was opgebouwd uit een PMMA cylinder waarin een segment bovien femurbot en een lobe van een varkenslong werden geplaatst. Het fantoom werd gevuld met radioactiviteit en de PET beelden werden gereconstrueerd met CT-gebaseerde en UTE-MRI-gebaseerde attenuatiecorrectie. Een kwantitatief verschil van 2 % werd gezien in drie lesies die in het fantoom waren aangebracht. Dit toont aan dat longweefsel onderscheiden kan worden met de methode.

Vervolgens werd de voorgestelde methode getest op data van kleine proefdieren. Eerst werd een omvangrijke micro-SPECT studie beschreven, waarin 18 ratten geïnjecteerd werden met speurstoffen voor verschillende organen. De micro-SPECT beelden gereconstrueerd met verschillende MRI-gebaseerde attenuatiemappen werden vergeleken met de beelden gereconstrueerd met micro-CT-gebaseerde attenuatiecorrectie. De resultaten toonden dat uniforme attenuatiecorrectie goede resultaten geeft in de meeste studies. Wanneer zeer accurate kwantitatieve beeldvorming vereist is, kan best een UTE-MRI-gebaseerde attenuatiemap gebruikt worden. Deze leidt tot gemiddelde fouten van 1 % in de longen, nieren, lever en milt en 5 - 8 % in de hersenen. Een kleinere micro-PET studie werd ook gedaan, waarin beelden werden opgenomen van drie dode ratten met geïmplanteerde artificiële lesies. De micro-PET beelden werden gereconstrueerd met verschillende attenuatiemappen. Er werden vergelijkbare resultaten bekomen als in de micro-SPECT studie.

Tenslotte evalueerden we onze methode op humane data. In een eerste studie werd aangetoond dat UTE-MRI-gebaseerde attenuatiecorrectie voor klinische beeldvorming van de hersenen mogelijk is. Dit werd gedaan op 5 PET-CT-MRI data sets van patiënten. De classificatie was juist voor 80 - 90 % van de voxels voor alle data sets. Het onderscheid tussen weefsel en lucht was juist in meer dan 95 % van de voxels. In de gereconstrueerde PET beelden werd een gemiddelde relatieve fout gezien van 3 % in 12 klinische relevante regio's. Er werden geen artificiële lesies gezien in de gereconstrueerde beelden. Deze resultaten zijn acceptabel voor klinische beeldvorming.

Beeldvorming in de humane thorax is veel moeilijker. Dit werd aangetoond op een enkele data set. Het onderscheid tussen lucht, long, zacht weefsel en

bot was niet mogelijk op basis van de MRI informatie alleen, aangezien dan teveel classificatie fouten gemaakt werden. Deze classificatie fouten leidden tot significante fouten in de gereconstrueerde PET beelden, met verschillende artificiële lesies tot gevolg. Daarom werd een meer geavanceerd algoritme ontwikkeld. Markov velden (*Markov random fields, MRF*) werden gebruikt om de longen te segmenteren, en de detectie van bot werd beperkt tot de wervelzuil. Met deze methode werden betere resultaten bekomen, met accurate quantificatie in het hart, de longen en de wervelzuil. Eén enkele artifiële lesie werd wel gezien. Daarom kan deze methode enkel gebruikt worden in humane thorax beeldvorming indien er zorgvuldig mee gewerkt wordt.

Er werden geen experimenten gedaan met beeldvorming van het volledige lichaam. Dit was deels omdat we niet de mogelijkheid hadden om dit soort data sets te verkrijgen, maar ook omdat we ervan overtuigd zijn dat er momenteel nog meer werk nodig is vooraleer onze methode kan toegepast worden op dat soort beeldvorming. Een aantal problemen dienen eerst opgelost te worden, zoals het feit dat verschillende weefsels moeilijk kunnen onderscheiden worden op basis van MRI informatie alleen en de lange acquisitietijd die nodig is om UTE beelden op te nemen. De methode moet ook eerst getest en geoptimaliseerd worden voor andere regio's van het lichaam, zoals het bekken of het abdomen. Van zodra aangetoond is dat de methode werkt in all regio's van het lichaam kan een gecombineerde methode ontwikkeld worden voor het volledige lichaam.

In dit proefschrift werd aangetoond dat lucht, long, zacht weefsel en bot kunnen onderscheiden worden met behulp van een nieuwe methode. De mogelijkheid om UTE-MRI-gebaseerde attenuatiecorrectie te gebruiken in beeldvorming van kleine dieren (micro-PET en micro-SPECT) en in humane hersenstudies werd aangetoond. Om de betrouwbaarheid van de methode te evalueren, zou het interessant zijn om een klinische hersenstudie op te zetten met meer patiënten. Er is ook nog extra onderzoek nodig met betrekking tot beeldvorming van het volledige lichaam.

Chapter 1

Introduction

1.1 Situation

The work presented in this dissertation is situated in the field of multimodal medical imaging, specifically in the combination of emission tomography with magnetic resonance imaging (MRI). Emission tomography is based on the tracer principle, in which a radioactive isotope is linked to a tracer molecule. After the tracer is administered to the patient, the radiation emitted by the isotope is recorded by the emission tomography scanner. Using specialized reconstruction algorithms, the distribution of the tracer within the body of the patient can be derived from this information. Two types of isotopes are used in emission tomography: positron emitters and single photon emitters, used in positron emission tomography (PET) and single photon emission computed tomography (SPECT) respectively. PET and SPECT provide information on the function of the body, contrary to anatomical imaging techniques such as X-ray computed tomography (CT) or MRI. MRI works by recording radiofrequency (RF) signals from protons in the body when the patient is inside the strong magnetic field in the scanner. Contrast between tissues can be created because protons in different tissues have a different chemical environment. Therefore they respond differently to the changes in magnetic field that are created by the scanner. By using various imaging sequences, different kinds of contrast can be created.

PET and SPECT have a very high sensitivity: tracer concentrations as low as picomolars can be visualized. Unfortunately, the resolution of PET and SPECT is limited and they can not provide a good anatomical background on which the tracer distribution can be situated. MRI has the advantage of acquiring high-resolution images, which accurately depict patient

anatomy. Therefore, there is currently much interest in combining either PET or SPECT with MRI. In part, this is inspired by the success of the combination of PET with CT. Combining PET and CT was quite straightforward, as both scanners can just be placed adjacent to each other and use the same bed. For PET-MRI or SPECT-MRI, the design is more difficult, especially if a fully integrated scanner is the goal. The main issue is the development of PET or SPECT detectors that can be used inside the high magnetic field of the MRI scanner. In the last 15 years, different small animal PET inserts for MRI systems have been designed. Most recently, the first human PET-MRI systems have become available.

Apart from the design issues related to constructing an integrated PET-MRI or SPECT-MRI scanner, other difficulties also need to be overcome before these new scanners can be routinely used. One of the important problems is the correction for different image-degrading effects that are present in emission tomography images. In PET and SPECT, one of the major effects is photon attenuation. To correct for photon attenuation, the distribution of the attenuation coefficients throughout the imaging volume needs to be known. This distribution is called the attenuation map and reflects the electron density distribution of the patient. In standalone PET or PET-CT, a transmission scan or a CT image is used to obtain the attenuation map. This is straightforward as the signal measured with a transmission scan or a CT is directly related to the electron density of tissue. In PET-MRI and SPECT-MRI, the attenuation map should ideally be derived from MRI images. However, this is difficult as MRI signal is related to proton density and relaxation properties of tissue, not to electron density. Additionally, lung tissue and cortical bone, which are two important tissue types for attenuation, exhibit no signal on images acquired with conventional MRI sequences. Therefore, it is difficult to create contrast between air (which also has no signal), lung and cortical bone based on images acquired with conventional MRI sequences alone. In most current MRI-based methods for deriving the attenuation map, this problem is solved by making certain assumptions on patient anatomy. However, this may lead to problems if the patient has anatomical abnormalities.

In this work, we have developed a MRI-based attenuation correction method which discriminates air, lung, soft tissue and bone based on MRI intensity alone. This is done by acquiring images with an ultrashort echo time (UTE) MRI sequence. This sequence enables the acquisition of MRI signal in lung and cortical bone. By performing a number of image processing steps, the attenuation map can be derived from images acquired with this sequence.

1.2 Outline

In chapter 2, the different imaging modalities that are used in this work are introduced. First the principles of PET and SPECT are described, followed by a brief discussion of image reconstruction methods. The different image-degrading effects that need to be corrected for in PET and SPECT are explained. An introduction to Monte Carlo simulations is also given, as well as a description of the most important clinical and preclinical applications of PET and SPECT. Then, the principles of MRI are introduced, from the description of spin physics to the general structure of MRI sequences. After an overview of MRI hardware, the different applications of MRI are also covered. Subsequently, multimodality imaging is introduced. The design issues of PET-MRI and SPECT-MRI scanners are explained, followed by an overview of systems that have been designed. The last part of chapter 2 is devoted to attenuation correction. The effect of attenuation on the reconstructed images is discussed as well as the implementation of attenuation correction into the reconstruction algorithm. Finally, the different methods that can be used to derive the attenuation map are described, with special attention for the MRI-based attenuation correction methods that have been proposed.

Before we derive our new method, the effect of errors in the attenuation map on the reconstructed PET images is evaluated. This is done using simulations in chapter 3. Using simulations of a rat, human brain and human whole-body phantom, the requirements for a MRI-based attenuation correction method are derived. These requirements are then used in the next chapters as a guideline.

In chapter 4, UTE imaging is introduced. After a description of the origin of short T_2 in tissues, UTE imaging principles are described along with a more detailed description of the Philips UTE sequence that will be used for most experiments described in this thesis. Next, the MRI properties of lung and cortical bone are investigated, to evaluate if visualization of those tissues with UTE sequences is possible. In the last section of chapter 4, the basic method which will be used throughout the rest of this work is introduced.

Before evaluating the proposed method on real animal and human data, we will test it on phantom data. As no suitable phantoms are currently available, we have designed new phantoms. The design of two phantoms, one for human brain imaging and one for human thorax imaging, is described in chapter 5. These phantoms are then used to evaluate the performance of our method.

In chapter 6, the UTE-MRI-based attenuation correction method will be tested on small animal data. Two studies will be described. The first is a micro-SPECT study using 18 rats injected with different tracers, which evaluates the feasibility of using the proposed method on micro-SPECT scans. A smaller micro-PET study, using 3 rats, will also be described.

The eventual goal of developing a UTE-MRI-based attenuation correction method is to use it in clinical practice. Therefore, we will test the developed method on human data in chapter 7. The performance in human brain imaging will be evaluated on 5 patient brain PET-CT-MRI data sets. To assess the feasibility of using our method for thoracic imaging, it is also tested on a single human thorax data set. In the last part of chapter 7, whole-body imaging will be discussed.

A summary of the results that are described in this thesis, along with the conclusions that can be drawn from them is given in chapter 8. A final conclusion is also presented there.

Chapter 2

Multimodal medical imaging

2.1 Introduction

In this chapter the different medical imaging modalities that are used throughout this work are described. In the first section, the principle of emission tomography is explained, as well as the methods used for acquisition of the data and reconstruction of the images. The image degrading effects are also described, and a brief overview of current applications of emission tomography is given. In the second section, magnetic resonance imaging (MRI) is introduced. First the principles of nuclear magnetic resonance are described, followed by the imaging principles. The main hardware components of a system are discussed, as well as the applications of MRI that are of interest for this work.

In the third section, multimodality imaging modalities and their applications are introduced. Special focus is given to the combination of MRI with emission tomography. Apart from the design issues relevant to that combination, the prototype systems that have been presented are also described, as well as the first clinical systems. As the subject of this work is attenuation correction, a detailed description of attenuation correction is given in the last section. It describes the effect of attenuation on (clinical interpretation of) the images, the methods for including attenuation correction into the reconstruction algorithm, and the methods for obtaining the attenuation map that are currently available.

2.2 Emission tomography

2.2.1 Early history

The earliest nuclear medicine experiments were done using naturally abundant radioactive isotopes. Cyclotron and reactor sources became available after World War II, in part due to technology developed in the Manhattan project. This enabled the use of fabricated radiotracers, but at that moment there were still too many technical limitations to develop an adequate imaging device. In 1957, Anger invented the Anger camera or gamma camera, which can be considered the start of modern nuclear medicine imaging[1]. Anger himself developed many modifications of his camera, such as pinhole collimators and images acquired at different projections by rotating the patient in front of the camera. Subsequent developments led to the design of rotating gamma cameras, allowing the reconstruction of tomographic images[2, 3]. These were the first single photon emission computed tomography (SPECT) images.

The development of positron imaging followed a different track than single-photon imaging. The first Anger camera with positron-imaging capability was presented by Anger and Rosenthal in 1959[4]. The first application was imaging of ^{52}Fe distributed in the bone marrow of patients with hematological diseases[5]. The first design that resembles the currently used scanners was designed by Robertson et al. in 1964, but computer systems were at that time not powerful enough to allow widespread use[6]. More than a decade later, and after several modifications, the device was used for brain imaging[7]. By the early 1980s, positron emission tomography (PET) was used in many major hospitals.

2.2.2 Tracer principle

Emission tomography is based on the tracer principle. An emission tomography tracer, consisting of a radioactive isotope linked to a specific biological molecule, is administered to an animal or a patient. The gamma photons emitted by the tracer when it decays are acquired by the emission tomography scanner. Using specialized reconstruction algorithms, the distribution of the tracer in the body can be derived from the acquired data. Hence emission tomography enables the evaluation of the function of the body. It provides different information than a purely anatomical medical imaging technique such as X-ray computed tomography (CT). While emission tomography does not achieve the same spatial or temporal resolution as most

anatomic imaging modalities, it does provide a sensitivity that is unmatched: concentrations as low as picomolars can be measured.

The tracers used in emission tomography can be divided into two categories, depending on the type of radiation emitted by the isotope: positron emitters and single photon emitters. Both types of isotopes are described in the next paragraphs. The principles of the acquisition of the photons emitted by these isotopes are discussed in the next section. It is important to keep in mind that radioactive decay is a random process, following a Poisson distribution. The data acquired by the scanner will therefore contain Poisson noise.

2.2.2.1 Positron emitters

The first category are the positron emitters, which are used in positron emission tomography (PET). When an unstable nucleus has an excess of protons, a proton can be converted into a neutron by emitting a positron or β^+ particle. The decay of ^{18}F to ^{18}O is an example of this transition:

$$^{18}\mathrm{F} \rightarrow {}^{18}\mathrm{O} + \beta^+ + \nu + 0.634\ \mathrm{MeV} \tag{2.1}$$

In which a positron and a neutrino (ν) are emitted. The positron emitted by ^{18}F has a kinetic energy of 0.634 MeV. Other isotopes can emit positrons with different kinetic energies. The positron then loses this kinetic energy in atomic collisions, traveling a random path until it has lost all kinetic energy. At that moment, it will annihilate by interacting with its antiparticle, an electron (β^-) from a nearby atom. The combined mass of the positron and the electron is converted into two gamma photons emitted in (almost) opposite directions. Each of the gamma photons has a photon energy of 511 keV, in accordance with Einstein's $E = mc^2$ equation.

Positron emitters are created in a cyclotron, by bombarding stable nuclei with charged particles. To obtain ^{18}F, water enriched with ^{18}O is bombarded with protons. The advantage of most positron emitters is that the stable isotopes of these elements are present in many molecules in the human body, and they can therefore be incorporated into many biological molecules. The downside is that most of them have a short half-life, which is not a hazard for ^{18}F (110 minutes) but makes studies with ^{11}C (20 minutes) and ^{15}O (2 minutes) very difficult. For studies with those isotopes, a cyclotron needs to be present close to the PET scanner, which is not possible in many hospitals.

2.2.2.2 Single photon emitters

The second category of isotopes used in emission tomography consists of the single photon emitters, used in planar scintigraphy and single photon emission computed tomography (SPECT). These isotopes only emit a gamma photon. This photon can arise from two different types of nuclear decay: isomeric transitions or electron capture. Most unstable nuclei that undergo α or β decay are in an unstable excited state after the emission of the α or β particle. The transition from this unstable state to a stable state of the same isotope, through emission of a gamma photon, is called an isomeric transition. Usually the emission of the gamma photon occurs very quickly after the emission of the particle (10^{-12} s on average). However, some excited states are called metastable, because the half-life of the excited state is much longer. The most used isotope in nuclear medicine is ^{99m}Tc, which is a metastable isotope of technetium. It is derived from the unstable mother isotope ^{99}Mo, which decays to ^{99m}Tc by β^- emission:

$$^{99}\mathrm{Mo} \rightarrow {}^{99\mathrm{m}}\mathrm{Tc} + \beta^- + \bar{\nu} \tag{2.2}$$

where an antineutrino $\bar{\nu}$ is also emitted. The metastable $^{99\mathrm{m}}$Tc then decays to the stable isotope through emission of one 140 keV gamma photon:

$$^{99\mathrm{m}}\mathrm{Tc} \rightarrow {}^{99}\mathrm{Tc} + \gamma \tag{2.3}$$

^{99}Mo has a half life of 66 hours and is usually obtained as a product of nuclear fission through neutron bombardment of a ^{235}U target. A generator with ^{99}Mo continuously produces ^{99m}Tc. Usually, the generator consists of ^{99}Mo in the form of molybdate (MoO_4^{2-}) adsorbed to a column of acid alumina (Al_2O_3). When molybdate decays to pertechnate (TcO_4^-), it becomes less tightly bound to the alumina because it only has a single charge. Pertechnate can therefore be extracted by pulling saline solution through the column. ^{99m}Tc has a half-life of 6 hours, which is very practical for emission tomography.

The other type of nuclear decay that produces a single gamma photon is electron capture. This happens when a nucleus with an excess of protons captures an electron and thereby converts a proton to a neutron. An example used in emission tomography is ^{123}I, which decays to ^{123}Te by capture of an electron and emission of a gamma photon:

$$^{123}\mathrm{I} + \beta^- \rightarrow {}^{123}\mathrm{Te} + \nu + \gamma \tag{2.4}$$

The most prominent gamma photon energy emitted by ^{123}I is 159 keV. ^{123}I is produced in a cyclotron through proton bombardment of ^{124}Xe, comparable to the production of ^{18}F from ^{18}O. It has a half-life of 13.2 hours. Another frequently used isotope, ^{67}Ga, is also produced in this manner.

Compared to positron emitters, single photon emitters have longer half lives, ranging from 6 hours (^{99m}Tc) to 76 hours (^{67}Ga). They are therefore easier to use than positron emitters, and do not require a cyclotron on-site. This makes imaging of single photon emitters much more accessible, also for smaller hospitals.

2.2.3 Imaging principles

2.2.3.1 Gamma detector

The photons emitted by PET and SPECT isotopes can not be acquired with normal optical cameras, as they have a much higher photon energy than optical photons. A special type of detector is therefore used in emission tomography, which converts gamma rays into electrical information[1]. A schematic drawing of such a detector is shown in fig. 2.1. In a gamma detector the photon is first absorbed by a scintillation crystal, which converts the gamma photon to a visible light pulse. The intensity of the pulse, i.e. the number of visible photons produced by the scintillation crystal, is proportional to the energy of the incident gamma photon. The most important properties of scintillation materials are a high stopping power, high light output and fast operating speed. A high stopping power is needed so that the crystal does not need to be too thick, as this would have a negative influence on spatial resolution. High light output is needed to obtain a high energy resolution. Fast operating speed, which requires a fast rise time of the light pulse and no afterglow, allows operation at high gamma count rates. Ideally a scintillation material is also cheap, easy to produce, robust and non-hygroscopic. Obviously, none of the available scintillation materials exhibit all these properties. Common scintillation materials are NaI, CsI, lutetium oxyorthosilicate (LSO) and lutetium-yttrium oxyorthosilicate (LYSO).

In a second step, the scintillation light is spread by a lightguide onto the next component, which converts the optical photons emitted by the scintillation crystal to an electric pulse. In most PET and SPECT scanners

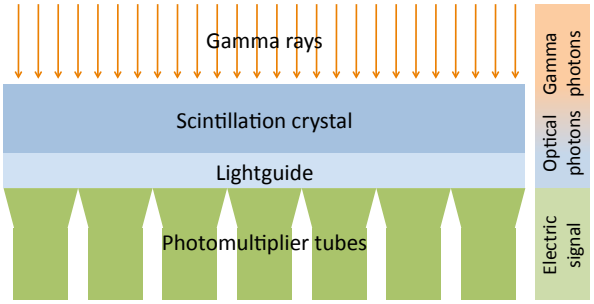

Figure 2.1: A gamma camera.

this is done using photomultiplier tubes (PMTs). These convert an incident optical light pulse into an amplified electric signal. This electric signal can then be recorded using electronic components. As PMTs are generally much larger than the size of a scintillation crystal, they are not coupled to a single crystal. Special positioning algorithms are therefore used to obtain the position of incidence of the gamma photon on the detector surface. This is done using Anger logic, named after the inventor of the gamma detector[1]. Using the relative signals of the different PMTs, a two-dimensional position can be obtained, which can then be mapped to one of the scintillation crystals. The total energy deposited in the crystal can be obtained from the total electric signal produced by all PMTs. Timing information is also obtained from the PMT signal.

In summary, a gamma detector will acquire three properties for each gamma photon:

1. the incidence location on the detector surface,
2. the energy deposited in the crystals,
3. the incidence time.

The ideal gamma detector will detect these properties with infinite resolution. Currently available detectors have limited spatial, energy and timing resolutions. These properties depend on the scintillation crystal, the light detector and the electronics that are used.

2.2.3.2 Positron emission tomography

PET imaging is based on the acquisition of both 511 keV photons that are emitted when a positron annihilates with an electron. If two 511 keV photons are detected by the scanner shortly after each other, they are assumed to have originated from the same positron emission. In that case, the detection of both photons is called a coincidence. By detecting both annihilation photons, the line along which the annihilation occured is determined. This line is called the line of response (LOR). By acquiring several millions of these coincidences, information is obtained on the distribution of the tracer inside the patient. The algorithm used for deriving the distribution image from the coincidence information is described in the section on image reconstruction below.

All current PET scanners consist of a full ring of acquisition modules (fig. 2.2). For simplicity's sake, suppose each of these modules can be seen as a gamma detector. The actual design is more complex, but this is described in more detail in the literature[8]. For PET imaging, the timing information provided by the module is important, as two incident photons can only be considered a coincidence if both photons are detected within a certain time window (the coincidence window). Coincidence detection is performed on-line by the coincidence electronics of the scanner. The coincidence window is determined by the size of the scanner and the timing resolution of the modules. In a scanner with a perfect timing resolution, the coincidence window should be set to the time it takes one photon to travel across the maximum distance between two crystals. In real scanners the timing resolution is never perfect, hence the coincidence window is larger.

For many years, full-ring PET scanners were operated in 2D-mode only, meaning that only coincidences that occur between crystals within the same ring were recorded. In theory, this means that in each ring, only data from the plane of the ring was acquired (called a slice). To avoid contamination of the data by photons from other slices, septa were placed between the rings. Although this avoids contamination, sensitivity is reduced by the septa, as all coincidence photons that are not emitted within a transaxial plane are not recorded. The sensitivity of 2D PET was approximately 0.2-0.3 %. Since the early 1990's PET scanners have been operated in 3D mode, acquiring coincidences between different rings[9]. This was done by retracting the septa. This yields a much higher sensitivity (up to 3 %) at the cost of a higher scatter fraction and random fraction, as discussed below. 3D reconstruction algorithms are also far more computationally demanding[10, 11]. Currently most PET scanners do not have septa anymore and operate in 3D mode

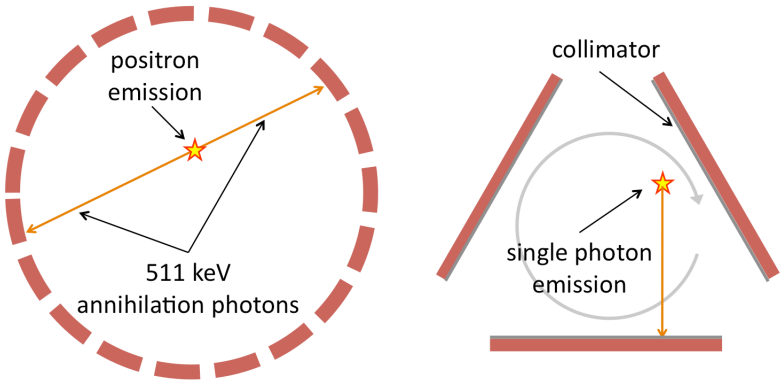

Figure 2.2: Schematic drawing of a PET (left) and SPECT (right) scanner.

only.

2.2.3.3 Single photon emission computed tomography

While two collinear photons are available per disintegration in PET imaging, only one photon is available in SPECT imaging, as SPECT tracers are single photon emitters. This means that, when the photon is detected in a gamma camera as described above, it is unclear where it originated from: the line along which it traveled from the emission towards the detector can not be determined. This line can be compared to a LOR in PET. Although the term 'LOR' is not used in SPECT in general, we will use it here to conserve analogy with PET imaging. To determine the LOR of a detected gamma photon, an extra component is added in a SPECT scanner: the collimator (fig. 2.2). A collimator is usually fabricated in a material with a high stopping power for gamma photons, e.g. tungsten or lead. The most frequently used collimator in clinical SPECT imaging is a parallel hole collimator, consisting of a thick lead plate with parallel cylindrical or hexagonal holes. When the collimator is placed in front of the gamma camera, only photons that are traveling perpendicular to the module surface will reach the scintillation crystal. This way a LOR can be determined, as the location of the incidence as well as the incidence angle is known.

Another type of collimator is a pinhole collimator, which has small pinhole openings[12]. A LOR can also be determined using a pinhole collimator, as two points on the LOR are known: the incident point on the scintillation crystal and the pinhole opening. Pinhole collimators provide the possibility of magnification of the object under study on the crystal surface, yielding a higher resolution. Therefore pinhole collimators are frequently used in small animal imaging, where resolution is very important[13].

SPECT scanners generally do not consist of a complete ring like PET scanners, but usually have 2, 3 or 4 heads that are rotated to sample a sufficient number of angles, as shown in fig. 2.2. Because the use of a collimator limits the acceptance angle for photons traveling towards the detector, the sensitivity of SPECT is much lower than PET[14]. In clinical SPECT imaging, a sensitivity of ≈ 0.03 % can be achieved with parallel hole collimators. There is also a trade-off between sensitivity and resolution in SPECT[15, 16]. For example, a parallel hole collimator with large holes will provide a higher sensitivity but will lead to resolution degradation and vice versa. In SPECT scanners different collimators are also needed for different isotopes. An isotope which emits high energy photons, such as ^{131}I (362 keV), requires a thicker collimator than isotopes which emit lower energy photons, such as ^{99m}Tc (140 keV).

2.2.4 Image reconstruction

The goal of image reconstruction in emission tomography is to derive a cross-sectional image from the acquired data, i.e. the counts on the LORs. This can be illustrated through the following equation:

$$E[p(\lambda)] = \int_{\lambda} f(x, y, z)\, dx\, dy\, dz \tag{2.5}$$

where $p(\lambda)$ is the projection along the LOR λ and $f(x, y, z)$ is the tracer distribution throughout the imaging volume. As radioactive decay is a random process, the acquisition of photons originating from radioactive decay is also a random process. The expectation operator $E[]$ is therefore needed in eq. 2.5. The purpose of tomographic image reconstruction is to obtain $f(x, y, z)$ from all acquired $p(\lambda)$. There are two general approaches to this problem: analytical and iterative image reconstruction. In this thesis only iterative image reconstruction methods were used, but a brief description of

analytical reconstruction methods is given below for completeness.

2.2.4.1 Analytical image reconstruction

Analytical reconstruction methods try to reconstruct the image directly from the acquired data, through a direct inversion of eq. 2.5[17]. This is only possible with a number of simplifying assumptions:

- continuous samples of $P(\lambda)$ are available,
- absence of physical data-degrading effects such as attenuation or scatter,
- absence of statistical noise, i.e. radioactive decay is a non-random process.

Analytical image reconstruction is based on the central section theorem, which states that the Fourier transform of a one-dimensional projection of an object is equivalent to a section through the the two-dimensional Fourier transform of that object:

$$P(v_{xr}, \phi) = F(v_x, v_y)|_{v_{yr}=0} \tag{2.6}$$

where v_x and v_y are the spatial frequency coordinates and x_r and y_r are the spatial coordinates in a cartesian system that is rotated over an angle ϕ. $P(v_{xr}, \phi)$ is then the one-dimensional Fourier transform of projection $p(x_r, \phi)$, which is obtained by projecting along the LORs at angle ϕ with distance from the origin defined by x_r. $F(v_x, v_y)$ is the two-dimensional Fourier transform of the tracer distribution $f(x, y)$.

Reconstruction can now be done by performing a backprojection of all acquired projections into the image. However, this will lead to overestimation at the center of the image as the center of the image was oversampled by the projection. Therefore, a filtering step is also needed. This leads to the best known analytical reconstruction algorithm: filtered backprojection (FBP):

$$f(x, y) = \int_0^{\pi} F_1^{-1}\{\, |v_{xr}|\, F_1[\, p(x_r, \phi)\,]\,\}\, d\phi \tag{2.7}$$

where the integration over ϕ represents the backprojection, F_1 and F_1^{-1} are the direct and inverse one-dimensional Fourier transforms and $|v_{xr}|$ represents filtering with the ramp filter.

2.2.4.2 Iterative image reconstruction

While analytical reconstruction is possible, many assumptions are needed to achieve a mathematically accurate result. This is because the model used for the imaging process in the analytical method described above is too simple. A better description of the model, allowing incorporation of physical effects such as attenuation, scatter, etc., would lead to a more accurate description of the imaging process. By including the statistical properties of the data into the model as well, even better results could be achieved. Unfortunately, incorporation of all these elements into the model inadvertently leads to a more complex model, for which an analytical solution in a closed form is either not available or impractical to compute. Therefore, these models can usually only be used to solve the reconstruction problem in an iterative manner[18]. As multiple forward- and backprojections are needed in iterative reconstruction algorithms, their development has only been possible from the moment sufficient computation power was available.

In iterative image reconstruction, the imaging volume is discretized into a two- or three-dimensional matrix. This matrix is called the image and each element from the matrix is called a pixel (in 2D) or a voxel (in 3D). Each value in the image represents the estimation of the tracer distribution in a single point, e.g. in the center of the voxel. After each iteration, the estimation of the tracer distribution in each point becomes more accurate.

A general model of an iterative algorithm is depicted in fig. 2.3. The algorithm starts with a first estimate of the image. This can be any image, but usually it is a uniform image. This estimate is then forward projected, meaning that the data that would be acquired by the scanner if the estimate was being imaged is derived. This projection is compared to the actual acquired data, e.g. by a division. The ratio between both projection sets (the error projection) is then backprojected into the image volume, yielding an error image. The image estimate is then multiplied by the error image, yielding a new estimate. The whole process is iterated a number of times until the algorithm converges.

In this work, all image reconstruction is done using the maximum-likelihood expectation maximization algorithm (ML-EM), therefore only that algorithm is described here[19, 20]. For a description of other iterative reconstruction

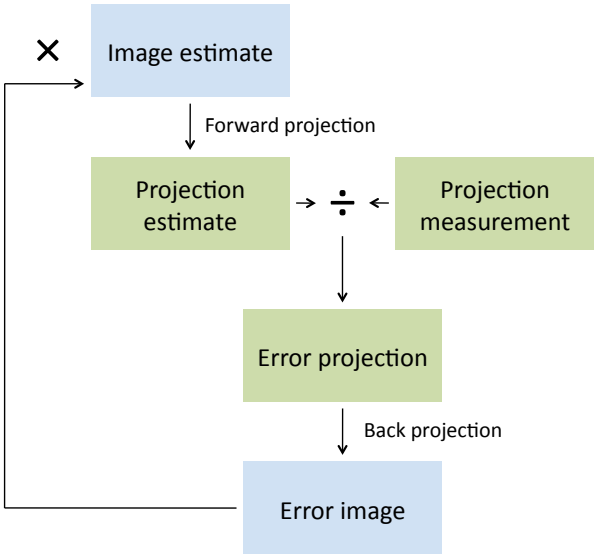

Figure 2.3: Schematic overview of an iterative reconstruction algorithm.

algorithms, the reader is referred to the literature on the subject[18]. The ML-EM algorithm is based on the maximum likelihood criterion, proposed by Fischer in 1921[21]:

$$\hat{\mathbf{f}} = \arg\max p(\mathbf{g}; \mathbf{f}) \tag{2.8}$$

which means that the reconstructed image $\hat{\mathbf{f}}$ should be chosen for which the measured data $\mathbf{g}$ has the largest probability. The ML-EM algorithm can be summarized in a single equation:

$$\hat{f}_j^{(n+1)} = \frac{\hat{f}_j^{(n)}}{\sum_{i'} h_{i'j}} \sum_i h_{ij} \frac{g_i}{\sum_k h_{ik} \hat{f}_k^{(n)}} \tag{2.9}$$

where $\hat{f}_j^{(n)}$ represents the image element j in estimation n, g_i is the number of counts in projection bin i and h_{ij} are the system matrix elements. The system matrix is the matrix that determines the projection: it defines for each

image element j what the probability is that an emission from this element will be detected in projection bin i. In this equation, the denominator of the last fraction is the forward projection, which is then compared to g_i. The sum over i represents the back projection, and the multiplication with $\hat{f}_j^{(n)}$ is the update step. The denominator of the first fraction is needed for normalization.

2.2.5 Image degrading effects

Apart from the noise in the data, which is inherent to the Poisson nature of radioactive decay, there are other effects that lead to lower quality PET and SPECT images. Image degrading effects can be divided into those mainly caused by the system and those mainly caused by the object or patient. As described above, they can be corrected for by incorporating them into the imaging model in iterative reconstruction algorithms. The most important effects are discussed here, together with common correction methods.

2.2.5.1 System-dependent image degrading effects

Sensitivity

The probability that an emission will be detected by the PET or SPECT scanner depends on the location of emission. This non-uniform sensitivity is in part due to the geometry of the scanner. This is corrected using geometric sensitivity correction, which can be calculated based on the system geometry[22]. It can also be due to non-uniformity of the detector response: there are variations in the responses of crystals and PMTs to a source. Normalization is used to correct for this effect, which requires normalization measurements[23, 24, 25].

Resolution

The scanners used in emission tomography have a limited resolution, which limits the capability of the system to discriminate two neighboring sources. Resolution in SPECT is affected by two components: the intrinsic resolution of the detector and collimator-dependent effects. In theory, there is no limit to the resolution that can be obtained with SPECT systems, but there is a trade-off between resolution and sensitivity for a certain field of view. There are currently micro-SPECT systems available for small animal research which enable sub-mm resolution[13]. In clinical SPECT imaging, current systems achieve resolutions of 7-10 mm[14].

As described above, the sensitivity of PET is much higher as no collimator is needed. However, there is a fundamental limit on resolution, determined by the positron range[26]. For low-energy positron emitters (such as ^{18}F) the positron range in water is small ($\approx$ 0.5 mm). The resolution in PET is also affected by the acollinearity of the emitted gamma photons, which can have a large effect in scanners with a large bore such as human whole-body scanners. Obviously, PET resolution also depends on the detector resolution. The resolution of current clinical PET scanners is in the range of 4-6 mm. By implementing resolution-recovery algorithms, the resolution of the reconstructed images can be improved[27]. However, this is not routinely used.

Random coincidences

Random coincidences are only relevant for PET. A random coincidence is a coincidence detected by the PET scanner within the coincidence window but in which both detected photons originated from a different positron emission. The detected coincidence does not contain any relevant information for the reconstruction process and even leads to incorrect information, as shown in fig. 2.4. Random coincidences can be limited by keeping the count rate low enough. In general, random coincidence correction is implemented by using a delayed coincidence window[28]. Regular coincidences ("prompts") are obtained by opening the coincidence window immediately after the first photon is detected. Delayed coincidences are obtained by opening a coincidence window of the same length a certain delay after the first photon was detected. As the delayed coincidences are all randoms, they provide an estimation of the randoms fraction. These delayed coincidences can be subtracted from the prompts to correct for random coincidences.

Other effects

Apart from the three effects discussed here, there are still other image-degrading effects in emission tomography. In both PET and SPECT, the system performance can decline when a lot of activity is present in the scanner. This determines the count rate performance of the scanner. In SPECT, there are additional effects related to collimator performance such as collimator penetration, scatter and X-ray production.

2.2.5.2 Object-dependent image degrading effects

Attenuation

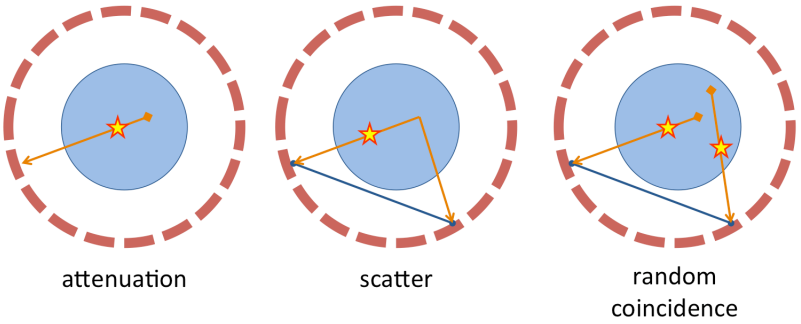

Figure 2.4: Illustration of attenuation, scatter and random coincidences in a PET scanner with a water phantom.

When a photon travels through matter for a certain distance, it has a probability of being absorbed (attenuated) and hence not reaching the detector. This is illustrated in fig. 2.4. The fraction of photons that penetrate through the tissue, the transmitted fraction TF, is determined by the attenuation coefficient of the tissue it travels through:

$$TF = e^{\int -\mu(s)\, ds} \tag{2.10}$$

where the line integral is taken over the path that is traveled by the photon. The attenuation coefficient μ depends on the material and the energy of the photon. It is clear that this effect is larger for photons that are emitted from the center of an object than for photons that are emitted from the border of the object. If no correction is performed, this will lead to image artefacts. This is clear on a non-corrected reconstruction of a uniform cylinder filled with ^{18}F-FDG and water, shown in fig. 2.5: the center of the cylinder appears darker whereas the border appears brighter. A comparable effect can be observed in a whole-body PET image, also shown in fig. 2.5: as the lungs are much less dense than soft tissue, they will appear much brighter on an uncorrected image. As attenuation correction is the subject of this work, it is discussed extensively in section 2.5.

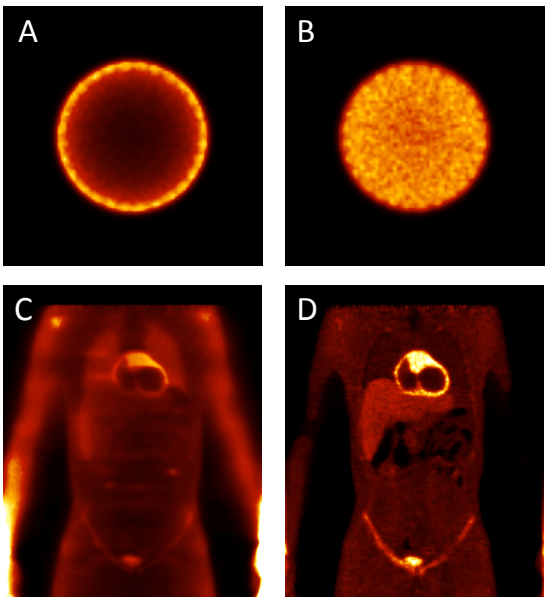

Figure 2.5: Example of the effect of attenuation. An uncorrected (A) and corrected (B) image of a water cylinder filled with a uniform ^{18}F-FDG concentration is shown. The effect of attenuation on whole-body imaging is also shown, with an uncorrected (C) and corrected (D) image.

Scatter

If an emitted photon is scattered along its path, it changes direction. When the photon is detected by a PET or SPECT scanner, the LOR that is attributed to the photon will be incorrect as illustrated in fig. 2.4. In most current systems, scatter is handled in two ways. The first way, used in PET and SPECT and aimed at reducing the amount of scatter in the acquired data, is based on the principle that scattering of a photon leads to a reduction of the energy of the photon. Therefore an energy window is set, and all photons that have a detected energy outside this window are disregarded as they were probably scattered. The amount of scatter inside the energy window can be estimated from the data outside the energy window using different methods, and can also be subtracted[29, 30, 31].

The second way of correcting for scatter is done by estimating the remaining amount of scatter in the acquired data. This information is then incorporated into the imaging model during reconstruction. Estimation of

the scatter can be done in different ways. Fast Monte Carlo simulations can be used to estimate the amount of scatter, which has been done in SPECT and PET[32, 33, 34, 35]. Currently, most PET system use an algorithm called single scatter simulation (SSS)[36], which is a model-based approach using the Klein-Nishina formula[37]. In SSS a crude estimation of the scatter is calculated based on the current image estimate and the attenuation map. This estimation of scatter is then subtracted from the original data.

Motion

In both PET and SPECT physiological motion of the organs (e.g. breathing or cardiac motion) or motion of the complete patient can lead to image blurring. Correcting for breathing motion can be done using gated acquisitions, in which only the data acquired at a specific point in the respiratory cycle is used for reconstruction[38, 39, 40]. This leads to a lower sensitivity but to higher resolution. Possible correction methods for patient motion have also been investigated, especially in brain PET imaging[41, 42, 43].

2.2.6 Simulation methods

Simulation techniques are very useful for research in emission tomography. A first application of simulations is in system design. Simulations allow to investigate the optimal configuration of different parameters, without the need for building numerous expensive prototypes. Possible parameters to be tuned include crystal size, scanner radius, collimator thickness, etc. Another advantage of simulations is that they allow the investigation of different effects with knowledge of the ground truth. As an example, this can be very useful in motion correction research. With real patient data, it is impossible to know the actual patient motion with 100 % certainty and hence the ground truth is unknown. With simulated data, the motion was included in the simulated model and the ground truth is therefore known. This allows accurate determination of the performance of the designed method. A similar approach can be used to assess performance of scatter correction or attenuation correction methods.

2.2.6.1 Principles of Monte Carlo simulation

The Monte Carlo (MC) method can be used to tackle statistical problems, and is currently used in many fields. The name was coined by Meteopolis and

Uman in 1949, and refers to the Monte Carlo casino in Monaco and to the random nature of the events modeled with the technique[44]. As radioactive decay as well as the detection of gamma radiation are stochastic processes, MC is ideally suited for use in emission tomography. The principles of MC simulation are described briefly here. For an extensive description of MC methods in emission tomography, the reader is referred to the literature[45, 46, 47, 48].

In order to use MC, there are a number of requirements. First of all, a complete description of the environment in which the simulation is taking place is needed. Secondly, a thorough understanding of all the physical processes that need to be modeled is required. In particular, a probability density function is needed for each possible phenomenon that can occur. Thirdly, a random number generator is required. MC simulation uses generated random numbers to sample stochastic variables from the probability density functions. These stochastic variables then determine the course of the simulation. This allows realistic simulation of the physical processes, if they are modeled accurately.

As a simple example, suppose one single photon emitting nucleus is simulated. First of all the emission needs to be simulated. As radioactive decay is a Poisson process, the time of decay can be sampled from the Poisson distribution determined by the half-life of the isotope. At the time of decay, the direction of the emitted photon is also sampled from a distribution, which is uniform in this case. As the photon travels along this path, it will encounter other particles. Suppose it encounters an electron of another atom. Then there is the possibility that the photon is scattered, and the angle under which it is scattered is also determined by a probability density function, which is also sampled, and so on.

2.2.6.2 GATE: Geant Application for Tomographic Emission

In this thesis, all simulations have been performed with the GATE simulation toolkit[49]. This was developed by the OpenGATE collaboration, and was built on top of the well-validated high energy physics package GEANT4[50]. Other simulation toolkits for emission tomography are also available, such as SimSET and EGS4[51]. GATE was chosen because of the extensive experience that exists within our research group. Also, validated models for different scanner geometries are available for GATE[52, 53, 54, 55].

2.2.6.3 Digital phantoms

To determine system characteristics such as resolution and sensitivity, simple analytical phantoms, such as point sources, spheres and cylinders, can be used. For realistic simulations, realistic digital phantoms are needed. Specifically, phantoms which represent the human body are required to realistically model object-based image degrading effects such as attenuation, scatter and motion. Since the development of simulation methods for tomographic imaging, these types of phantoms have been developed. The first antropomorphic phantoms were based on a composition of analytical shapes such as ellipsoids and cylinders. An example is the MIRD phantom, used for dosimetry[56].

A more detailed description of the human anatomy requires the possibility to use non-analytical shapes and hence requires the use of discrete, so-called voxellized phantoms. The first voxellized antropomorphic phantom was designed by Zubal and Harrell, based on a detailed CT study of a male[57]. We have used the XCAT phantoms in this work, which is based on the earlier design of the MCAT and NCAT phantoms[58, 59, 60]. These phantoms have been designed based on the data sets obtained from the visible human project. They allow the simulation of respiratory and cardiac motion. From the same developers, realistic digital rat (ROBY) and mouse (MOBY) phantoms are also available.

2.2.7 Applications

2.2.7.1 Clinical PET imaging

The specificity of the images obtained using emission tomography strongly depends on the tracer. ^{18}F is by far the most widely used isotope in PET, mainly in ^{18}F-fluorodeoxyglucose (FDG)[61]. FDG is a glucose analogue that is taken up by cells consuming glucose and gets blocked in the cell after the first enzymatic reaction. ^{18}F-FDG therefore enables the visualization of the metabolic (glycolytic) function of tissue. As most tumors are metabolically more active than normal tissue, ^{18}F-FDG is used to detect tumors[62]. It can also be used to determine regional brain activity[63]. An example brain PET image is shown in fig. 2.6. Other applications of PET in neurology include brain perfusion studies using ^{15}O and tracers that ligate specific neuroreceptors such as ^{11}C-raclopride for dopamine D2/D3 receptors.

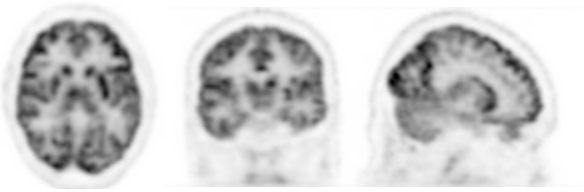

Figure 2.6: From left to right: a transverse, coronal and sagittal slice of a ^{18}F-FDG brain PET image.

2.2.7.2 Clinical SPECT imaging

^{99m}Tc is currently the most widely used isotope in nuclear medicine and accounts for 85 % of all diagnostic procedures. Bone scans, using ^{99m}Tc-labeled medronic acid (MDP) to visualize osteoblastic lesions in the bones, are one of the main applications of single photon emission. Myocardial perfusion SPECT, using either ^{99m}Tc-sestamibi or ^{99m}Tc-tetrofosmin, is widely used in cardiology to determine if there are significant stenoses in the coronary arteries leading to perfusion defects in the myocardium[64]. ^{99m}Tc-dimercaptosuccinic acid (DMSA) and ^{99m}Tc-mercaptoacetyltriglycine (MAG3) are used in urology for visualization of kidney function. Many other ^{99m}Tc-labeled radiotracers are available.

^{123}I is another single photon emitter that has been used in nuclear medicine for a long time. It can be used for visualization of the thyroid gland without linking to another molecule, as virtually all iodine in the human body is taken up in the thyroid gland[65]. It can also be linked to tracer molecules, such as metaiodobenzylguanidine (MIBG), which is used for visualization of adrenergic tumors such as phaeochromocytomas. It is also used in neurology for the confirmation of Parkinson's disease using ^{123}I-ioflupane (DaTSCAN®)[63]. Other commonly used single photon emitting isotopes include ^{67}Ga, ^{111}In and ^{201}Tl.

2.2.7.3 Quantitative PET and SPECT

In a clinical setting, both PET and SPECT are mostly used for lesion detection. This means that a physician will look at the images for qualitative differences. For example, a hot spot (region with high uptake) in a ^{18}F-FDG PET image could show a metastasis of a tumor. In cardiac SPECT imag-

ing, a cold region (region with low uptake) in the wall of the left ventricle could be related to a perfusion defect. However, emission tomography also provides the possibility to obtain quantitative images. With absolute quantification, the activity concentration (in Bq/ml) can be derived from the PET or SPECT images. This enables better longitudinal follow-up, e.g. for evaluation of response to therapy[66]. Absolute quantification is also needed for accurate kinetic modeling of tracer uptake[67].

For absolute quantification, accurate system calibration is needed as well as a very good image reconstruction algorithm, which takes into account all image degrading effects. For clinical PET, absolute quantification has been available for decades. The clinical advantage of quantitative PET for monitoring the response of tumors to chemotherapy and radiotherapy has been demonstrated in clinical studies[68, 69]. The applicability of quantitative PET to kinetic modeling has also been shown[70, 71].

While absolute quantification is definitely possible in SPECT, the corrections for image-degrading effects are more complex. Hence, quantitative SPECT is still a developing field[72, 73]. Nevertheless, there are important applications for quantitative SPECT, such as the use in individual dosimetry for targeted radionuclide therapy[74, 75, 76]. Although the number of studies showing absolute quantification with SPECT in a clinical setting is limited, the feasibility has been demonstrated[77, 78, 79].

2.2.7.4 Preclinical imaging

Many medical treatments, such as drugs, are first tested on laboratory animals before they are tested on humans. This stage of research is called preclinical research, as it is done before the clinical studies start. Emission tomography is widely used in preclinical research, as it enables the in-vivo visualization of functional information[80, 81]. Without imaging techniques, the laboratory animal needs to be sacrificed to obtain information on the internal effects of the treatment under study. This is very expensive, and it makes true longitudinal studies difficult or impossible. Most preclinical imaging is done in small rodents (rats or mice), but other animals can also be studied, such as rabbits, pigs, monkeys, etc.

Special scanners are needed to image small rodents, as they are much smaller than humans. Most importantly, a higher resolution is needed. Therefore, micro-PET and micro-SPECT scanners have been developed, which have a much higher resolution than clinical scanners[82, 83]. One of the main applications of preclinical imaging is their use in drug develop-

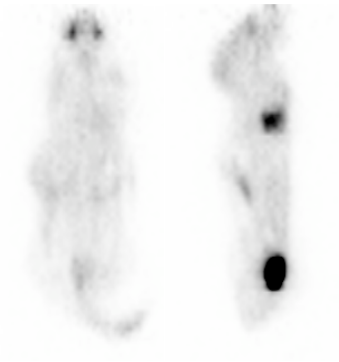

Figure 2.7: A coronal (left) and sagittal (right) slice of a micro-PET image of a mouse, injected with ^{18}F-FDG.

ment studies[84]. Micro-PET and micro-SPECT are used in those studies to investigate the distribution of drugs in the body after uptake, or to investigate the effect of drugs on functional parameters. An example of a micro-PET image of a mouse injected with ^{18}F-FDG is shown in fig. 2.7.

2.3 Magnetic resonance imaging

2.3.1 Early history

Contrary to what is usually stated, nuclear magnetic resonance (NMR) was not first demonstrated by Bloch and Purcell in 1946. Instead, it was Rabi who was the first to show the effect of a radiofrequency (RF) wave with the Larmor frequency on nuclear magnetic moments[85, 86]. His experiments were done on molecular beams. He received the Nobel prize in physics in 1944 "for his discovery of a resonance method for recording the magnetic properties of atomic nuclei". In 1946, Bloch and Purcell were the first to demonstrate NMR in condensed matter. Bloch did his experiments in liquid water[87, 88], while Purcell studied NMR in solid paraffin[89]. They received the Nobel prize in physics in 1946. Since then, NMR has been widely used to study the magnetic properties of molecules.

The step from NMR to magnetic resonance imaging (MRI) was made by the inventions of Lauterbur and Mansfield in 1973[90, 91]. Up to then, it had been accepted in physics that when images were obtained using elec-

tromagnetic waves, the size of the smallest object that could physically be discriminated (the resolution) was approximately the wavelength of the electromagnetic wave. In the case of MRI, this would mean that the highest possible resolution of MRI would be in the range of a few meters, which is the wavelength of the RF waves used in NMR. However, Lauterbur and Mansfield showed that, by manipulating the local magnetic field using gradient fields, a much higher resolution could be obtained. This enabled MRI, which has since then been a very successful imaging technique. For their work, Lauterbur and Mansfield received the 2003 Nobel prize in medicine and physiology.

There has been some controversy about the Nobel prize of Lauterbur and Mansfield, as a third researcher has claimed to have an equal or larger impact on the invention of MRI. Raymond Damadian was the first to show that the relaxation properties of tissue, which define the NMR signal, differ between cancer and normal tissue[92]. He was also the first to acquire a human body image, showing a transverse slice through the thorax in 1977[93]. However, his method used focused-field NMR, which is entirely different from the current method of MRI. It was also not the first human MRI image: the group of Mansfield had acquired transsectional images of a finger the year before[94].

2.3.2 Nuclear magnetic resonance: spin physics

Before the principles of MRI can be described, the physical description of the behavior of charged particles in a static magnetic field needs to be discussed. This is done in this section. First the concept of a spin angular momentum is introduced. Then the behavior of a single particle in a magnetic field is described, including energy quantization. Subsequently we discuss what happens when not a single particle but a collection of particles is observed. In the last parts of this section, the principles of excitation and relaxation, which are used to acquire the NMR signal, are described.

2.3.2.1 Angular momentum

The concept of angular momentum is used in classical mechanics when describing a rotating object. Different angular momenta exist. Take for example the motion of earth. The motion of earth around the sun is described by an orbital angular momentum. However, earth also rotates around its own axis. This momentum is called the spin angular momentum in classical mechanics. As an electron rotates around its nucleus, it also has an orbital

angular momentum. An electron is a charged particle, and therefore its motion describes a current loop and induces a magnetic moment. Electrons also possess a spin angular momentum[95]. However, relating this spin angular momentum to the classical phenomenon of an object rotating around its own axis is not correct, as the spin angular momentum of an electron does not have a classical analogue and is purely a quantum mechanic property.

Electrons are not the only elementary particles that have spin. Protons and neutrons also possess this property. The spin number of a nucleus is determined from the spins of its protons and neutrons. As a general rule, nuclei with an even number of protons and neutrons have no spin, nuclei with an odd number of protons and neutrons have an integer spin, and nuclei with an even number of neutrons and an odd number of protons or vice versa have half-integer spin. Only nuclei which possess spin can be used in NMR. We limit our description to nuclei with $1/2$ spin, such as a proton. The spin numbers of some nuclei frequently used in NMR are listed in table 2.1.

Nucleus	Spin number
^{1}H	1/2
^{13}C	1/2
^{19}F	1/2
^{31}P	1/2

Table 2.1: Spin numbers of isotopes frequently used in NMR.

2.3.2.2 Magnetic moment of a single particle

In this paragraph, we give the classical description of the behavior of the magnetic moment of a single charged particle, e.g. a proton, in an external magnetic field. The external magnetic field $\vec{B}$ is oriented along the Z-axis and has magnitude B_0. If $\vec{J}$ is the angular momentum of that particle, the magnetic moment associated with that angular momentum is:

$$\vec{\mu} = \gamma \vec{J} \tag{2.11}$$

with γ the gyromagnetic ratio, which depends on the nucleus. The behavior in time of $\vec{J}$ is now governed by the equation:

$$\frac{d\vec{J}}{dt} = \vec{\tau} \tag{2.12}$$

where $\vec{\tau}$ is the torque on $\vec{J}$, which is given by:

$$\vec{\tau} = \vec{\mu} \times \vec{B} \tag{2.13}$$

.

Combining these equations yields:

$$\frac{d\vec{\mu}}{dt} = \gamma\vec{\mu} \times \vec{B} \tag{2.14}$$

.

The solution to this differential equation in the time domain, assuming that $\vec{B}$ is constant, is:

$$\begin{aligned} \mu_x(t) &= \mu_x(0)cos(\omega_0 t) + \mu_y(0)sin(\omega_0 t) \\ \mu_y(t) &= -\mu_x(0)sin(\omega_0 t) + \mu_y(0)cos(\omega_0 t) \\ \mu_z(t) &= \mu_z(0) \end{aligned} \tag{2.15}$$

which describes a vector rotating clockwise about the Z-axis with angular frequency $\omega_0 = \gamma B_0$. If we now switch to a reference frame rotating around the Z-axis at angular frequency ω_0, the equations become:

$$\begin{aligned} \mu_x(t) &= \mu_x(0) \\ \mu_y(t) &= \mu_y(0) \\ \mu_z(t) &= \mu_z(0) \end{aligned} \tag{2.16}$$

which is a static vector.

2.3.2.3 The Zeeman effect

The potential energy of the single particle in an external magnetic field, described in the previous paragraph, is:

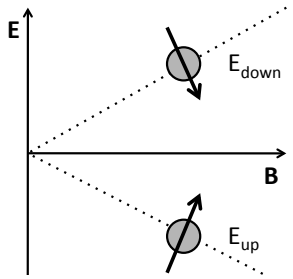

Figure 2.8: The Zeeman effect: in an external magnetic field B, the energy of a charged particle is quantized.

$$E = -\vec{\mu} \cdot \vec{B} = -\gamma J B_0 cos(\theta) \tag{2.17}$$

where θ is the angle between the external magnetic field and the magnetic moment $\vec{\mu}$. In classical mechanics, there is no limitation on the energy of the particle, and hence any value of E is possible. Unfortunately, this is not true, as quantum mechanics dictate that the energy of a charged particle in an external magnetic field is quantized. This means that the particle can only have discrete energy levels:

$$E = -m\gamma\hbar B_0, m = -j, -j+1, ..., j-1, j \tag{2.18}$$

where j is the spin quantum number and $\hbar$ is the reduced Planck constant. This effect, in which the energy of a particle is quantized in an external magnetic field, is called the Zeeman effect[96]. For protons, with $j = \frac{1}{2}$, it means that there are two energy levels:

$$\begin{array}{ll} E_{up} & = -\frac{1}{2}\gamma\hbar B_0 \\ E_{down} & = \frac{1}{2}\gamma\hbar B_0 \end{array} \tag{2.19}$$

.

These two energy levels are referred to as spin-up and spin-down, with spin-up meaning that the spin angular momentum is oriented in the direction of the $\vec{B}$ field, which has the lowest energy. The Zeeman effect for protons is

illustrated in fig. 2.8. A transition from spin-up to spin-down can now only be made by absorbing a photon with the correct energy. This is called the resonance condition:

$$E_{down} - E_{up} = \gamma \hbar B_0 \tag{2.20}$$

.

As the energy of a photon is $\hbar\omega_0$, this means that:

$$\omega_0 = \gamma B_0 \tag{2.21}$$

in which ω_0 is called the Larmor frequency. For protons, the Larmor frequency is approximately 42.6 Mhz in a magnetic field of 1T. An electromagnetic wave in this frequency range is called a radio-frequency (RF) wave.

2.3.2.4 Net magnetization vector

In NMR, not single particles, but collections of many particles are studied. For simplicity, we will from hereon refer to charged particles as spins. One would expect that, for the description of spins, the integration of the quantummechanical descriptions of all spins individually should be done. Fortunately, it has been shown that, for a large collection of spins, the classical description can be used[87]. This means that the total magnetization of a volume of matter can be described with a net magnetization vector, as illustrated in fig. 2.9:

$$\vec{M} = \Sigma \vec{\mu_i} \tag{2.22}$$

where μ_i are the magnetic moments of the spins in the volume. Each spin is either in the spin-up or the spin-down state, as described above. Because the spin-up state has the lowest energy, most spins will be in that state. The magnetic moments μ_i will also have a component in the XY-plane. However, in steady state these components are randomly distributed as the spins are not rotating about the Z-axis in phase. The net component of $\vec{M}$ in the XY-plane will therefore be 0. This means that $\vec{M}$ is oriented along the

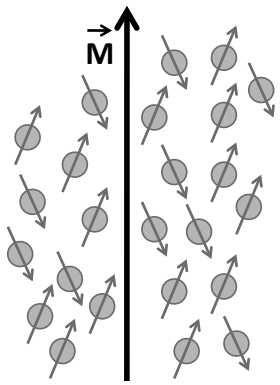

Figure 2.9: When observing a large collection of spins, the classical description can be used. This means that the total magnetization can be described using the net magnetization vector $\vec{M}$.

direction of the external magnetic field. In non-steady state conditions (see below) $\vec{M}$ can have a component in the XY-plane. The net magnetization vector satisfies:

$$\frac{d\vec{M}}{dt} = \vec{M} \times \gamma \vec{B} \tag{2.23}$$

and hence also precesses about the axis of the external magnetic field. In the rotating reference frame described above, $\vec{M}$ stands still.

2.3.2.5 RF excitation and flip angle

The state of equilibrium described in the previous paragraph can now be disturbed by transmitting photons with the Larmor frequency. Indeed, when such a photon is absorbed by a spin in the spin-up state, it will be brought to the spin-down state. This is done by transmitting an RF field ($\vec{B_1}$) with the Larmor frequency in the XY-plane. Next to the effect of bringing more spins in the spin-down state, the RF field will also force all individual spins to rotate in phase. This is called phase coherence, and makes it possible that the net magnetization vector has a transverse component. In the rotating reference frame, a RF wave will lead to a rotation of the net magnetization vector away from the Z-axis and towards the XY-plane. The angle of rotation, called the flip angle α, depends on the amplitude B_1 of the RF field and on

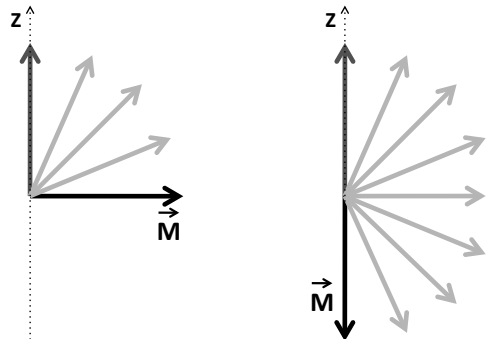

Figure 2.10: The effect of a 90° (left) and 180° pulse on the net magnetization vector $\vec{M}$.

the duration of the pulse t:

$$\alpha = \int_0^t \gamma B_1 d\tau = \gamma B_1 t \tag{2.24}$$

By modifying B_1 or t, any flip angle can be obtained. The most important RF pulses are the 90° and 180° pulse, which lead to a net magnetization vector oriented in the XY-plane (perpendicular to the Z-axis) and in the opposite direction of the static magnetic field respectively (fig. 2.10).

2.3.2.6 Relaxation

When the transmission of the RF field is stopped, the net magnetization vector will gradually return to its equilibrium state. It will do so by emitting an RF wave itself, also at the Larmor frequency. This wave is called the free inductive decay (FID). NMR is based on the recording of this RF wave in the XY-plane. The return to the equilibrium state is called relaxation and is governed by two physical phenomena: spin-spin relaxation and spin-lattice relaxation. Both phenomena are illustrated in fig. 2.11.

As described above, all spins are in phase while the RF field is being transmitted. Spin-spin relaxation leads to dephasing of the spins, and hence disappearance of the transverse component of the net magnetization vector. It is caused by the small differences in local magnetic field that are experienced by the spins. These small differences are caused by the chemical

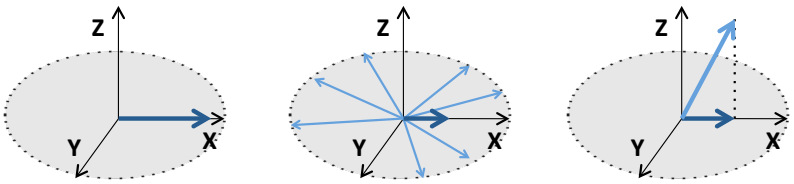

Figure 2.11: After the RF pulse, the net magnetization vector returns to its equilibrium. On the left, the situation just after the RF pulse is shown: all spins are in phase and the transverse component of $\vec{M}$ is maximal. The middle figure illustrates T_2 relaxation: the spins are dephasing in the transverse plane, leading to a smaller transverse component of $\vec{M}$. The right figure illustrates T_1 relaxation: as more spins return to the spin-up state, $\vec{M}$ rotates away from the transverse plane toward the Z-axis. This also leads to a smaller transverse component of $\vec{M}$

environment of the spins, i.e. the different atoms and binds surrounding the protons. This effect therefore depends on material composition. The transverse component of the net magnetization during spin-spin relaxation, in the rotating reference frame, can be described as:

$$\vec{M}_{tr}(t) = \vec{M}_{tr} e^{\frac{-t}{T_2}} \tag{2.25}$$

where T_2 is called the spin-spin or transverse relaxation time constant.

While spin-spin relaxation is purely a phenomenon of dephasing of the spins, spin-lattice relaxation is an energy phenomenon and describes the actual return to the energy equilibrium. As more spins return to the spin-up position, they will transfer their energy to the surrounding macro-molecules. This will lead to restoration of the longitudinal component of the net magnetization vector. Suppose a RF pulse with a flip angle of 90° was used. During relaxation, the longitudinal component of the net magnetization vector can then be described as:

$$M_l(t) = M_0(1 - e^{\frac{-t}{T_1}}) \tag{2.26}$$

where T_1 is the spin-lattice or longitudinal relaxation time constant. It is also dependent on material composition. The acquired NMR signal is

therefore dependent on the T_1 and T_2 of the material under study.

In non-homogeneous media, such as the human body, there is another effect that causes dephasing of the spins. It is caused by magnetic field inhomogeneities of the static magnetic field. These inhomogeneities can be related to the field itself (e.g. because the magnet does not provide a homogeneous field), or by materials present in the field. The inhomogeneities caused by materials are due to the different magnetic susceptibilities of the materials in the field. This effect is called the T_2^* effect.

2.3.3 Imaging principles

The NMR signal described above is obtained from the complete volume in the static field, and does not contain any position-dependent information. We need to add spatial encoding to the signal if images, either 2D or 3D, are to be acquired. By adding spatial encoding, we move from the field of NMR to the field of MRI. The principles of MRI are described in this section. The hardware that is necessary for MRI is described in the next section.

2.3.3.1 Volume selection

If the static field is the same everywhere in the imaging volume, a RF pulse with the Larmor frequency will excite all spins in the imaging volume. We can excite only a specific part of the imaging volume by changing the static field. This can be done using a linear magnetic gradient[90]. Consider a linear gradient G_z in the Z-direction. When switched on, the static magnetic field will now depend on the Z-position:

$$\vec{B}(z) = (0, 0, B_0 + G_z z) \tag{2.27}$$

which means that the Larmor frequency of the spins in the imaging volume also depends on the Z-position:

$$\omega(z) = \gamma(B_0 + G_z z) \tag{2.28}$$

.

When a RF pulse with a finite bandwidth is now transmitted, only the spins in a limited part of the imaging volume will be excited, namely a

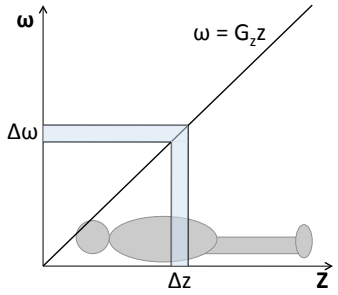

Figure 2.12: The principle of volume selection: by applying a gradient G_z in the Z-direction, the Larmor frequency of the spins becomes dependent on the Z-position. By applying a RF pulse with a finite bandwidth $\Delta\omega$, only the spins in a slice with thickness $\Delta z = \frac{\Delta\omega}{\gamma G_z}$ are excited.

slice perpendicular to the z-direction. The location of the center of the slice depends on the gradient. The principle is depicted in fig. 2.12. The thickness of the slice depends on the bandwidth of the RF pulse and the steepness of the gradient:

$$\Delta z = \frac{\Delta\omega}{\gamma G_z} \tag{2.29}$$

with $\Delta\omega$ the bandwidth of the RF pulse. In 2D imaging, a narrow-bandwidth pulse is used to excite only a limited slice. In 3D-imaging, a broad-bandwidth pulse is used to excite a larger volume. In 3D-imaging the excited volume is called a slab rather than a slice.

2.3.3.2 k-space theorem

Volume selection only allows position encoding in a single direction, and is therefore not sufficient for imaging. We now introduce an important concept in MRI: the k-space. First, recall that, after excitation, the transverse component of the magnetization vector describes a rotation around the Z-axis:

$$\vec{M_{tr}}(t) = M_{tr}(cos(\omega t), -sin(\omega t)) \tag{2.30}$$

which can be written in complex notation as:

$$\vec{M}_{tr}(t) = M_{tr} e^{-i\omega t} \tag{2.31}$$

.

Suppose that we now apply a 3D gradient $\vec{G}$. The Larmor frequency ω then depends on the position within the imaging volume, which is given by the position vector $\vec{r}$:

$$\omega(\vec{r}, t) = \vec{G}(t) \cdot \vec{r} \tag{2.32}$$

.

When the transverse component of the magnetization is recorded while the gradient is switched on, the signal from all the spins in the imaging volume is recorded. This can be seen as an integration in the space domain over the entire imaging volume:

$$s(t) = \iiint \rho(\vec{r})\, e^{-i\gamma \int_0^t \vec{G}(\tau)\cdot\vec{r}\, d\tau}\, d\vec{r} \tag{2.33}$$

where $\rho(\vec{r})$ is the position-dependent spin density. T_1 and T_2 relaxation effects can be included by multiplying the spin density with two relaxation functions:

$$s(t) = \iiint \rho(\vec{r})\, g(t, T_1(\vec{r}))\, h(t, T_2(\vec{r}))\, e^{-i\gamma \int_0^t \vec{G}(\tau)\cdot\vec{r}\, d\tau}\, d\vec{r} \tag{2.34}$$

.

It is well known that the Fourier transform of a 3D function is:

$$F(\vec{k}) = \iiint f(\vec{r})\, e^{-2\pi i \vec{k}\cdot\vec{r}}\, d\vec{r} \tag{2.35}$$

where $\vec{k}$ is the spatial frequency vector. Equations 2.35 and 2.34 are equivalent if the relaxation functions g and h are not time dependent. This implies that the distribution of T_1 and T_2 over the imaging volume does not

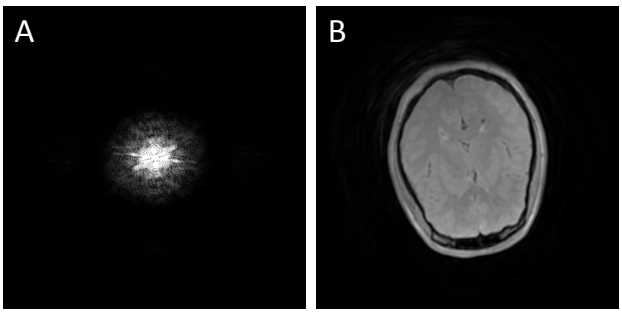

Figure 2.13: Based on the k-space theorem, a MRI image can be reconstructed from the measured signal by applying an inverse Fourier transform. (A) shows the 2D k-space raw data, and (B) shows the image reconstructed by applying the inverse 2D Fourier transform.

change over time. If there is no motion, which is assumed here for simplicity, this assumption is valid. $\vec{k}$ is then defined as:

$$\vec{k}(t) = \frac{\gamma}{2\pi} \int_0^t \vec{G}(\tau)\, d\tau \tag{2.36}$$

.

This shows that an image can be reconstructed from the recorded signal by applying an inverse 3D Fourier transform[91]. The spatial frequency domain is called k-space in MRI, a concept introduced independently by Ljunggren and Twieg in 1983[97, 98]. The sampling in k-space is determined by the time evolution of the magnetic gradient $\vec{G}$. By manipulating the gradients, any point in k-space can be sampled. An example of the reconstruction of a MRI image from raw data using the inverse Fourier transform is shown in fig. 2.13.

2.3.3.3 MRI sequences

The signal acquired during MRI thus depends on:

- The protons in the volume and their properties:
  - proton density,

  - relaxation properties: T_1 and T_2 time constants,
  - the local field inhomogeneities : T_2^* effects.

- The fields generated by the MRI system:
  - the static B_0 field, which aligns the spins,
  - the B_1 RF field, used for excitation of the protons (flip angle),
  - the gradient fields, used for position-encoding.

The static B_0 field can not be manipulated. However, the RF field and the gradient fields can be changed in time. By using different sequences of RF and gradient fields, different interactions with the spins in the imaging volume are induced and the result of these interactions is recorded. This is the source of contrast in MRI. The sequences are called MRI pulse sequences or in short MRI sequences. The programming of MRI sequences is very complex, but also enables the acquisition of images with many different kinds of contrast. This is a big advantage of MRI over e.g. CT where only contrast based on the electron density of tissue can be obtained.

The free inductive decay (FID) signal that is transmitted by the spins returning to the equilibrium quickly vanishes and therefore does not allow the complicated gradient switching that is needed to encode the k-space trajectory (an exception to this is ultrashort echo time imaging, see below). Therefore, MRI sequences use methods for rephasing the spins after the gradients have been applied. The coherent RF signal that is emitted after rephasing is called an echo. There are different ways to generate an echo. Below, the principles of spin echo and gradient echo sequences are explained, which are the two main acquisition schemes used in MRI.

Spin echo sequence

In a spin echo (SE) sequence, the refocusing of the spins is obtained by applying a 180° RF pulse after the 90° RF excitation pulse[99, 91]. The effect of the 180° pulse can be explained in the rotating reference frame. Consider one of the spins, after excitation with a 90° pulse. This spin is now oriented along the X-axis. Suppose it is dephasing in the clockwise direction, meaning that the rotational frequency of the spin is slightly higher than the expected Larmor frequency. In the rotating reference frame, it will move away from the X-axis. By applying a 180° pulse, the spin is rotated 180° about the Y-axis. If it continues to rotate in the clockwise direction, it is now moving towards the X-axis rather than away from it. The time it takes for the spin to align with the X-axis, and be in coherence, is exactly the time

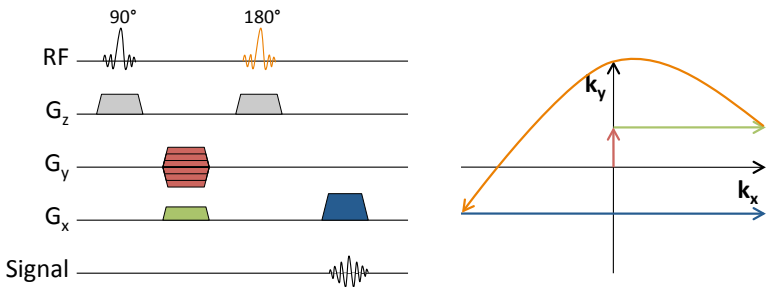

Figure 2.14: Schematic of a 2D spin-echo sequence (left), and the k-space trajectory in the k_x, k_y plane (right). The data is acquired while scanning the blue line in k-space.

between the 90° and the 180° pulses. This is half of the echo time T_E. In a spin echo, T_2 as well as T_2^* dephasing effects are compensated.

A schematic overview of a SE sequence is depicted in fig. 2.14, together with the trajectory that is sampled in k-space. The 90° RF excitation pulse is applied together with a slice selection gradient. After the RF excitation, a phase-encoding gradient is applied along the Y-axis. The amplitude of this gradient determines the k_y coordinate of the line that will be sampled in k-space. The 180° RF pulse is then applied, together with the same slice selection gradient, to flip the spins and make them rotate back towards coherence. The signal is then acquired around T_E, while a frequency-encoding gradient along the X-axis is switched on. This frequency-encoding gradient scans a line in k-space in the k_x direction. Usually, a frequency-encoding gradient with the same polarity is applied during the phase-encoding gradient in order to move the k-vector towards the beginning of the line that is to be acquired (negative k_x). The next line in k-space is acquired in the same manner after the repetition time T_R.

The contrast that is achieved by a SE sequence is now determined by T_E and T_R. In MRI, three main contrast types can be discriminated: proton density (PD) weighted, T_1-weighted and T_2-weighted. To obtain a T_1-weighted image, a short T_R is used: as the next excitation pulse follows before T_1 relaxation has been completed, the number of spins excited by the pulse will depend on the T_1 (a longer T_1 means less excited spins). If a long T_R is used, T_1 relaxation is finished before the next excitation. To obtain a T_2-weighted image, a long T_E should be used, allowing for a long T_2 dephasing time before the spins are refocused. To obtain a PD-weighted image (which has neither T_1 or T_2 contrast), a long T_R is combined with a

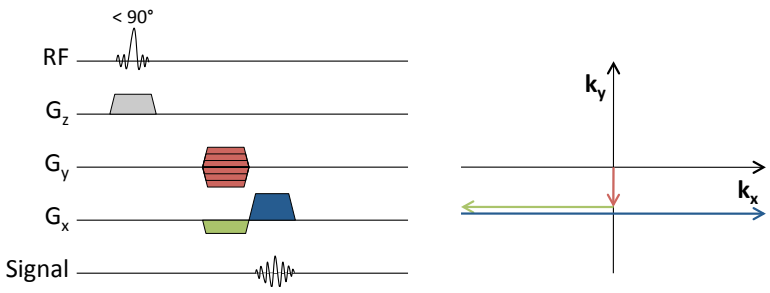

Figure 2.15: Schematic of a 2D gradient-echo sequence (left), and the k-space trajectory in the k_x, k_y plane (right). The data is acquired while scanning the blue line in k-space. Note the opposite polarities of the gradients along the X-axis and the RF pulse which can have a flip angle smaller than 90°.

short T_E.

Gradient echo sequence

While SE sequences are very flexible, as many kinds of contrast can be obtained by varying the T_E and T_R, they can lead to very long acquisition times. This is especially the case in T_2-weighted images, as the acquisition of the next line in k-space can only be acquired if T_1 relaxation of all spins is finished. Because a SE sequence always uses a 90° RF excitation pulse, T_1 relaxation can take a long time. This can be avoided by using a gradient echo (GE) sequence. As implied by the name, a GE sequence uses gradients with opposite signs to dephase and rephase the spins (fig. 2.15). No 180° pulse is used, allowing lower flip angles for RF excitation. A shorter T_R can therefore be achieved, leading to shorter total acquisition times.

There are some downsides to GE sequences. The main problem is that, as the refocusing of spins is purely based on gradients and not on a 180° pulse, the local field inhomogeneities due to susceptibility effects are not compensated by the echo. The signal is therefore governed by T_2^* rather than T_2. This leads to T_2^*-weighted images instead of T_2-weighted images. GE sequences are therefore mainly used for very fast imaging techniques in 2D or 3D.

2.3.4 MRI hardware

Three magnetic fields are used in MRI: the static B_0 field, the gradient field G and the RF field B_1. The components that are used to generate and/or

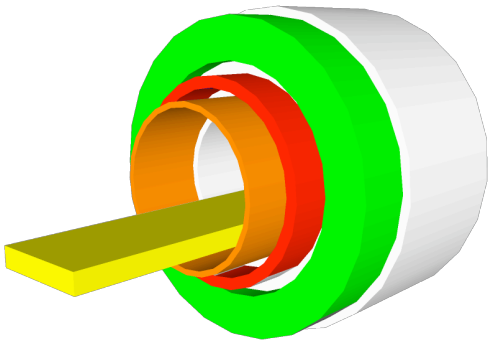

Figure 2.16: A cut-through of the hardware in a MRI scanner. The static magnet is depicted in green, the gradient coils in red and the RF coils in orange.

acquire these fields are discussed in this section. They are also depicted in fig. 2.16.

2.3.4.1 B_0-field

In MRI, the B_0 field strength can vary from 0.1T to 14.7T. Systems currently in use for clinical practice usually have a field strength of 3T or lower, most commonly 1.5T. In most systems the B_0 field is generated by a superconducting magnet, using a superconductor current loop. Usually niobium-tin or niobium-titanium superconductors are used, cooled with liquid helium. Resistive magnets can also be used, but they require more power and operate at lower field strengths ($\approx$ 0.2T). One of the advantages of resistive magnets is that they can be used in so-called open-magnet MRI systems, which are better tolerated by claustrophobic patients. In research, higher field strengths are used, which can only be generated by superconductor magnets. For human whole-body imaging, the maximum field strength currently used is 7T[100]. For brain imaging, there are 9.4T magnets[101]. For preclinical research, magnets of up to 14.7T are currently being made.

2.3.4.2 Gradient coils

For position encoding, 3 pairs of gradient coils are used. They enable the generation of linear magnetic gradient fields in the X, Y and Z directions. The principle of a gradient coil can be easily explained, and is illustrated in fig. 2.17. A magnetic gradient is created by placing two coils perpendicular

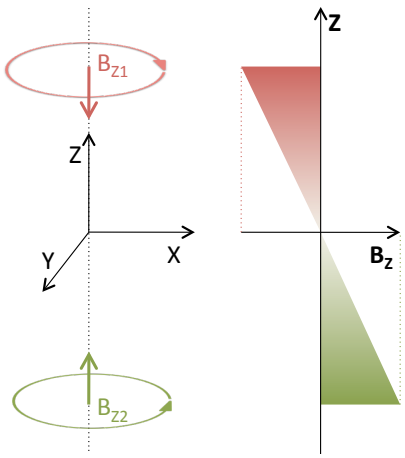

Figure 2.17: Principle of a gradient coil generating a linear gradient in the Z-direction. By using two coils perpendicular to the Z-axis on both sides of the imaging volume, in which opposing currents are induced (left), a linear gradient magnetic field is created in which the field depends on the Z-position (right).

to the axis along which the gradient needs to be created, on both sides of the imaging volume. By inducing currents with opposing directions in the coils, both coils will induce opposite magnetic fields along the axis. As the strength of the field created by a coil depends on the distance from the loop, the sum of the fields from both coils is a linear gradient.

2.3.4.3 RF coils

RF coils are used for both transmission and reception of signals in MRI. In all clinical MRI systems a large integrated RF body coil is present. It is mostly used for excitation of the spins. As the signal reception quality is strongly dependent on the distance between the spins and the coil, using the body coil for signal acquisition is not optimal. It is much better to have a coil that is as close to the body as possible. Therefore, different RF coils are used in MRI. Specific coils exist for the brain, head and neck, chest, spine, knee, etc. As these coils are much closer to the body, the obtained signal quality is much better. Some of these coils also have the possibility to transmit RF waves. Currently most coils used in clinical practice are multi-channel coils, which speeds up the acquisition process.

2.3.5 Applications

Because of the many possibilities of MRI, it is difficult to give a short overview of the applications of MRI. In this section, some applications of MRI in the fields relevant for this work are described. For a more extensive description of MRI applications, the reader is referred to the literature on the subject.

2.3.5.1 Neurology

MRI is the preferred imaging modality in neurology, as it has soft tissue contrast that is far superior to CT. The applications of purely anatomical MRI imaging in neurology are numerous[102]. MRI can be used to visualize large structural abnormalities, such as space-occupying lesions. It is also applied in epilepsy, when searching for hippocampal sclerosis as the cause of temporal lobe epilepsy. While CT is still the modality of choice for acute cerebrovascular imaging, MRI can also be used to visualize cerebral haemorrhages. In fact, it is superior in imaging cerebral micro-haemorrhages, which are the hallmark of hypertensive brain disease. Structural images of the brain are also used in the diagnosis of multiple sclerosis (MS), where the visibility of white matter lesions on MRI is necessary for a definitive diagnosis.

MRI allows more than just anatomical imaging. In diffusion tensor MRI imaging, the preferred diffusion direction of water is imaged[103]. In neurology, this can be used to assess white matter, as it consists of axons, which can be seen as fibers. This allows the visualization of structural connections in the brain using fiber tractography. It was mainly used in research, but clinical applications are now also available. Examples include MS and Alzheimers disease.

A special technique, which allows visualization of the functional activity of the brain, is functional MRI (fMRI)[104]. This is based on the blood oxygenation level dependent (BOLD) effect in brain tissue, leading to a different MRI signal in parts of the brain that are active, i.e. consuming oxygen. It can be used to map brain activity, for example during specific tasks. This allows investigation of the distribution of functions within the brain. It can also be used in pharmacological studies, where the effect of a neurotropic drug on brain activity is evaluated non-invasively.

2.3.5.2 Cardiology

MRI has many applications in cardiovascular imaging[105]. It can be used to determine the morphology of the ventricles as well as their function, e.g.

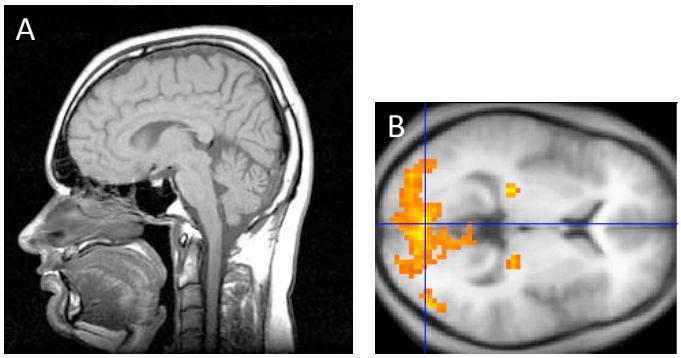

Figure 2.18: Example of a structural (A) MRI image of the brain as well as an fMRI activation image overlayed on a structural image (B).

by visualizing ventricular wall motion. In coronary artery disease, MRI can be used to assess the viability of heart tissue after an infarct using delayed contrast-enhanced imaging (DCE-MRI). Perfusion imaging, comparable to ^{99m}Tc-sestamibi-SPECT can also be done. MRI can be used for the evaluation of cardiomyopathy by visualizing fibrosis or iron overload. In congenital heart disease, cardiac MRI is used to visualize heart structures that can not be observed with echocardiography.

MRI can also be used to visualize vascular disease. Structural imaging of the aorta and great vessels can be done, e.g. for the detection of aortic dissection. A special MRI technique called MR angiography (MRA) enables the visualization of peripheral vascular disease, like X-ray angiography, but without the radiation dose.

2.3.5.3 Oncology

As MRI is the preferential imaging modality used in the brain, it is obvious that it is also the preferential imaging modality for the diagnosis of brain tumors[106]. MRI is also the best available technique for imaging multiple myeloma, and is more sensitive than bone scintigraphy in detecting skeletal metastases[107]. Whole-body MRI can also be used as a screening method, or to determine the total tumor load of a patient. Diffusion-weighted MRI is a specific technique that can be used to differentiate tumor tissue from healthy tissue[108]. In pregnant women with cancer, regardless of the type

of tumor, MRI is always preferred because of the absence of radiation dose. MRI is also the best imaging technique to discriminate different kinds of liver lesions[109].

2.3.5.4 Preclinical imaging

As emission tomography, MRI is also used in preclinical research. Imaging of large animals such as pigs or monkeys can be done on clinical MRI systems. Specialized MRI systems have been developed for small animals such as mice or rats. The smaller bore of these systems also enable the design of systems with much higher magnetic field strengths, up to 14.7T[110]. Specific RF coils have also been designed for imaging mice and rats[111]. The fact that no radiation dose is delivered to the animal is a big advantage in preclinical imaging, as the doses delivered by micro-CT, which is the other anatomic imaging modality available for small animals, can be relatively high[112]. Although it has not been demonstrated yet, it is conceivable that the radiation dose could influence the study outcome in longitudinal studies[113]. Small animal MRI is, among others, used in preclinical cancer research and neurological studies[114, 115].

2.4 PET-MRI and SPECT-MRI

2.4.1 Advantages of multimodality imaging

In the last decades a lot of research has lead to the development of combined imaging modalities. Especially the combination of functional imaging modalities, such as PET and SPECT, with anatomical imaging modalities, such as CT and MRI, has been investigated. While the first strategies for multimodality imaging involved acquiring images on both modalities separately and then combining them using coregistration techniques[116, 117], the focus is now on combining two modalities into a single system. This theoretically allows perfect registration, assuming the patient does not move between both acquisitions.

The combination of PET with CT into a sequential PET-CT scanner has been very successful[118]. Today, almost all PET scanners are sold in combination with a CT. PET-CT scans are mostly used in oncology, using ^{18}F-FDG as a tracer. The high sensitivity of PET for detecting tumor lesions is combined with the high resolution of CT, allowing accurate anatomic localization of the lesions detected on PET. The use of PET-CT in the stag-

ing and follow-up of different types of cancer has been shown to improve clinical outcome in a statistically significant way[119]. Although less prominent, SPECT-CT systems are becoming more popular[120]. SPECT-CT is interesting for oncology as well as cardiology[121, 122].

As MRI has superior imaging capabilities to CT for many applications, due to the superior soft tissue contrast of MRI, the combination of PET or SPECT with MRI is also very interesting[123, 124, 125]. Another advantage of this combination is that MRI does not deliver any radiation dose to the patient, contrary to CT which delivers a significant dose. MRI also allows other applications than simple anatomic imaging, such as MR angiography (MRA), functional MRI (fMRI) or even the use of MRI tracers. Furthermore, the total imaging time for a combined PET and MRI exam could be reduced with truly simultaneous imaging. While the CT in PET-CT takes much less time than the PET, in PET-MRI this would be the other way around as MRI exams generally take longer than PET exams. However, it has been argued by some authors that truly simultaneous imaging is only interesting for research purposes, mainly in neurology[126]. For most other applications, sequential imaging (comparable to a PET-CT) is sufficient. In addition to oncology, the possible applications of PET-MRI and SPECT-MRI include cardiology and neurology[127, 128, 129]. As described above, PET, SPECT and MRI are already preferred imaging modalities in those fields.

2.4.2 Design issues

Three general designs are possible for combining PET or SPECT and MRI. The first possibility is to use two separate scanners in different rooms. Although this is not a real multimodal scanner, multimodal images can be obtained if registration between both acquisitions is ensured. This can be done using markers, or in the case of small animal imaging, by using the same animal bed on both scanners. A second design is comparable to a PET-CT, where the PET and MRI acquisitions are done on the same gantry, but not simultaneously. The scanners can be mounted at a certain distance from each other to limit interference. The third possibility is a fully integrated scanner, which enables truly simultaneous imaging. The PET scanner then needs to be fit into the MRI system. This is also the most difficult to design, as it will lead to the most interference between both modalities.

There are many technical difficulties in designing a PET-MRI or SPECT-MRI system, especially if the third design is aimed for[130, 131]. These difficulties can be divided into problems with the PET or SPECT system caused by the presence of the MRI system, and vice versa. The difficul-

ties caused by the MRI system are mainly due to the presence of the high magnetic field of the MRI scanner. First and foremost, the PMTs that are used in most PET and SPECT scanners are extremely sensitive to magnetic fields. They can therefore not be used close to the MRI scanner, let alone inside the scanner. Another problem can be caused by the fast switching gradient and RF magnetic fields. If the electronic components in the PET or SPECT acquisition modules are not properly shielded, these fields may cause interference with their function. As for the effects of the PET or SPECT system on the MRI images, the main concern is that artefacts may be caused by the presence of the metallic components of the PET or SPECT system inside the MRI scanner. These components can cause inhomogeneities in the magnetic field, which makes MRI imaging very difficult, especially if the PET components are close to the object under study.

2.4.3 Prototypes and clinical systems

In this section a short overview of PET-MRI hardware development is given, with brief descriptions of the systems that have been designed and their innovations and challenges. The interested reader is referred to the review paper by Pichler et al. for more detail[131]. At the end of this section the (limited) current developments in SPECT-MRI are also discussed.

2.4.3.1 First images

The first simultaneous PET-MRI images were published by Shao et al in 1997, working with Paul Marsden and Simon Cherry[132]. They were acquired with a prototype PET insert for a clinical MRI system, based on the previous work of Cherry et al[133]. In this system, the interference between the PET insert and the MRI system was limited by putting all electronic components of the PET insert at a distance of 3 m from the center of the MRI magnet, which was a 0.2T open magnet system (fig. 2.19). At this distance, the fringe field of the magnet is limited to 10 mT. The only components of the PET system inside the magnet were the scintillator crystals (LSO). The scintillation light of the crystals was coupled to 4 m long optical fibers, which conduct the light out of the magnet and toward the electronic readout system. Readout was done with multi-channel PMTs, of which it was shown before that a 10 mT field did not interfere with their function. A line source phantom, consisting of 7 cylinders filled with a mixture of water, ^{18}F (for the PET signal) and $NiCl_2$ (for the MRI signal), was imaged. All cylinders could be discriminated on both the PET and the MRI images.

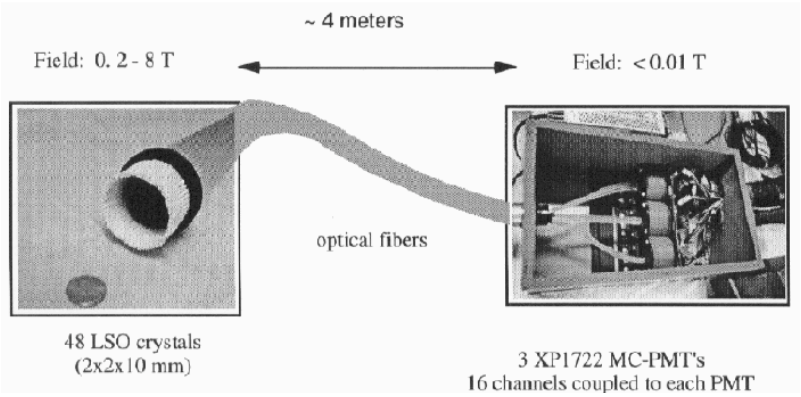

Figure 2.19: Overview of the system used to acquire the first simultaneous PET and MRI images. The LSO crystals are coupled to optical fibers, which guide the scintillation light towards the PMTs, which reside outside the strong magnetic field. Reproduced with permission from [132].

Images and magnetic resonance spectroscopy (MRS) spectra of isolated perfused rat hearts were also acquired[134]. The system is still being improved at the moment[135, 136]. Another system which uses light fibers and PMTs outside of the magnet was designed by Raylman et al[137]. Simultaneous PET and MRI images of a rat and mouse brain were acquired with that system, as well as simultaneous PET images and MRS spectra[138].

2.4.3.2 Modified MRI systems

Two designs in which a special MRI system was developed to allow operation of the PET system have also been proposed. The first uses a 1T MRI split-magnet MRI system, in which there is a 80 mm gap in the axial direction between the two parts of the magnet[139]. In this gap, LSO scintillator crystals were coupled to 1.2 m long optical fibers, which then guide the scintillation light out of the magnet in the radial direction. Readout was done with a slightly modified microPET Focus system[140]. The advantage of this set-up is that the optical fibers are much shorter than in the systems described above, and that they do not need to be bended from the radial to the axial direction, which preserves a lot of space.

A second system uses a field-cycled MRI magnet, which means that the PET and MRI acquisitions are not performed simultaneously[141, 142]. Instead, the MRI is switched of briefly while the PET data is acquired, and

then switched on again. The switching between PET and MRI occurs at a frequency of $\approx$ 1 Hz. The first images acquired with this system have been published in 2011[143].

2.4.3.3 APD-based systems

While it allows the use of large parts of older PET detector systems, the use of optical fiber coupling combined with PMTs outside of the magnet also imposes many limitations. The reduction of light output, caused by the attenuation of the optical fibers, leads to worsening of the energy and timing resolution of the PET detector. The optical fibers and the coupling of the optical fibers to the scintillation crystals also takes up a lot of space inside the MRI scanner. Therefore, the possibility of using other readout components, that were not so sensitive to magnetic fields, was investigated. Two components could be used: avalanche photodiodes (APDs) and silicon photomultipliers (SiPMs)[144, 145, 146]. SiPMs are very new and still being developed[147, 148, 149]. The first systems were therefore designed using APDs.

The first APD-based PET insert was designed by Catana et al[150]. In order to limit interference of the PET system with the MRI, the scintillation crystals were still coupled to optical fibers. However, these optical fibers were much shorter than in the other systems (10 cm), and were only used to allow moving all metallic PET detector components outside of the MRI field of view. The system is depicted in fig. 2.20. The PET insert was designed to be used inside a 7T preclinical MRI system, in combination with a 35 mm mouse coil. Simultaneous PET-MRI images of a mouse have been obtained and no significant interference between both imaging modalities was observed.

The first design in which a larger part of the PET system was located inside the MRI magnet was built by the group of Bernd Pichler[151]. In that setup, the APDs are coupled directly to the scintillation crystals. As no optical fibers are used, the performance of the PET imaging system is not reduced. The amplified APD signals are then conducted toward the digital PET electronics, located outside the magnet. The insert was designed to fit inside a 7T small-animal MRI scanner. Simultaneous PET and MRI images of a mouse have been acquired, and the presence of the APDs and the amplification does not influence MRI image quality.

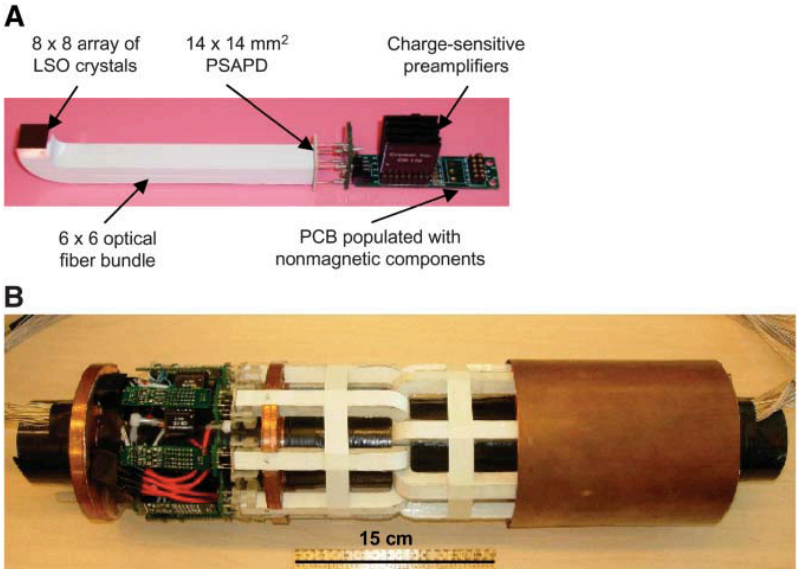

Figure 2.20: The first APD-based MRI-compatible PET insert was designed by Catana et al. It uses short optical fibers to guide the scintillation light out of the center of the magnet. This is done to limit influence of the electronic PET components on MRI field homogeneity. Reproduced with permission of the Society of Nuclear Medicine from [150].

2.4.3.4 Clinical systems

All systems described above can only be used for imaging mice or rats. Although this is very interesting for preclinical research, the end goal of PET-MRI integration is to obtain simultaneous PET and MRI images of humans. The first simultaneous brain PET and MRI images of human volunteers were acquired with the Siemens BrainPET insert in 2007, a APD-based PET detector ring that fits inside a Siemens clinical 3T MRI system[152, 153, 154]. A schematic overview of the system and images acquired with the system are shown in fig. 2.21 and fig. 2.22. It is also strictly a research system: no new BrainPET inserts will be produced.

The first clinical combined whole-body PET-MRI system was presented by Philips in 2009[155]. The Gemini PET-MRI is a sequential PET-MRI system, comparable to a PET-CT system, with the CT replaced by a MRI system. The PET system is located at approximately 3m from the MRI system. A standard Gemini TF PET system is used with conventional PMTs, but each

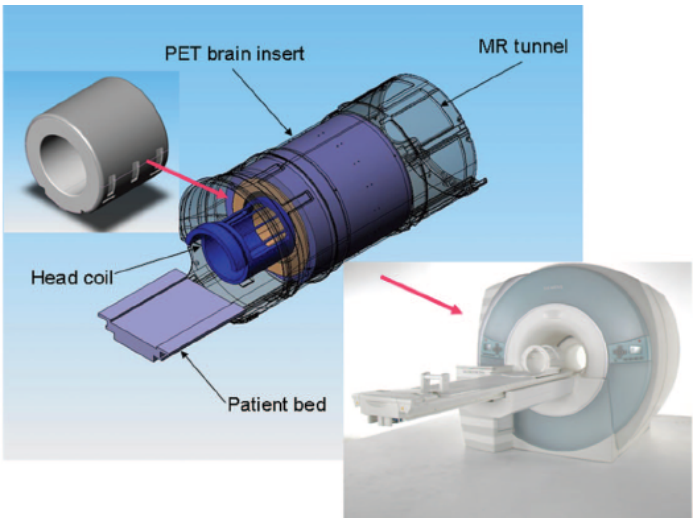

Figure 2.21: Schematic of the Siemens BrainPET insert, used to acquired the first simultaneous human PET-MRI images. Reproduced with permission from [154].

PMT is shielded additionally. Although this system does not provide the possibility to acquire truly simultaneous PET and MRI images, it is still an interesting system for research as well as clinical practice. The first clinical experience with PET-MRI was obtained with this system[156]. In 2011, Siemens presented the first fully-integrated whole-body PET-MRI system, the molecular MR (mMR). The mMR is an APD-based system, based in

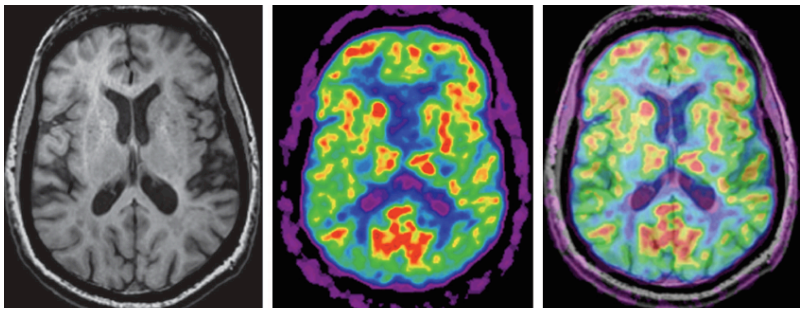

Figure 2.22: MRI (left), ^{18}F-FDG PET (right) and fused PET-MRI image (center) of a patient, acquired with the Siemens BrainPET insert. Reproduced with permission from [154].

part on the BrainPET insert. A whole-body PET ring is inserted into a wide-bore MRI system. Although not much data is currently available from this system, it will undoubtfully lead to very interesting research in the next few years.

Entirely new systems are also being developed. One example is the system that is being designed in the HYPERimage/SUBLIMA consortia, European collaborations led by Philips Research[157, 158, 159]. The aim of the consortium is to develop the first integrated whole-body PET-MRI that uses SiPMs as light detector. Because entirely new components are used, and the PET system is redesigned from scratch, the completion of such a system is still several years away.

2.4.3.5 SPECT-MRI

The field of SPECT-MRI is much less advanced than PET-MRI, and only prototype systems are being developed at the moment. This is in part because the development of SPECT-MRI is even more difficult. There are several reasons for this. Most importantly, a collimator needs to be added to perform SPECT imaging, which will require more space inside the MRI bore. The collimator also needs to be MRI-compatible.

The first combined SPECT-MRI images were acquired by Breton et. al in 2007[160, 161]. They were acquired with a sequential system, in which a small animal SPECT and a low-field (0.1T) MRI were moved close to each other and the animals were moved from one modality to the other. SPECT and MRI images of mice were acquired and showed no artefacts. However, the use of a low-field MRI limits the MRI imaging capabilities, especially for small animals. Therefore, truly MRI-compatible SPECT systems are being designed. Two prototypes have been built. Tan et al. tested the influence of a 3T MRI system on their SPECT insert using a ^{57}Co point source[162, 163]. Gamma Medica-Ideas is also designing a MRI-compatible CZT SPECT system, together with the group of Tsui at Johns Hopkins and the group of Nalcioglu at UC Irvine[164, 165]. The first truly simultaneous SPECT-MRI images of a water phantom filled with ^{99m}Tc were acquired with that system in 2010[166].

2.5 Attenuation correction

As attenuation correction is the subject of this work, it is described in more detail here. First, the effect of attenuation on the reconstructed PET and

SPECT images is discussed, together with the clinical evidence on the subject. The methods for including attenuation correction into the reconstruction algorithm are explained in the second part of this section. Then the different methods used for deriving the attenuation map are described. In the last section, the challenges and current state-of-the-art of MRI-based attenuation correction is discussed.

2.5.1 Effect of attenuation

The necessity of attenuation correction in PET or SPECT depends on the effect of attenuation on the reconstructed PET or SPECT images. For SPECT, there has been a long debate on whether or not attenuation correction was necessary or clinically important. It has been shown that attenuation correction is necessary to obtain absolute quantification[167], but does this also mean that it is beneficial to use attenuation correction for clinical interpretation? There have been studies which show no improvement with attenuation correction, in cardiac as well as oncologic imaging[168, 169]. However, it has also been shown that not performing attenuation correction on cardiac perfusion SPECT images can lead to significant artefacts, such as the creation of artificial perfusion defects in the posterior wall of the left ventricle due to liver attenuation[170]. From the current data, the clinical advantage of performing attenuation correction in cardiac perfusion SPECT is clear[171, 172]. The clinical effect of attenuation correction in oncologic imaging has not been studied as extensively, but a positive effect on tumor detection has also been shown[173, 174, 175].

The effect of attenuation in PET imaging is larger, as both annihilation photons need to reach the detectors to detect an emission. The effect of attenuation correction on PET quantification was studied already very early in the development of PET by Huang et al[176]. The effect of misregistration between the attenuation map and the emission data, of a bias in the attenuation coefficient, of nonuniform attenuation, etc. was investigated. The authors concluded that performing correct attenuation correction was necessary for quantification in PET. There has been a less extensive discussion on the clinical need for attenuation corrected PET images, compared to SPECT. However, a number of studies have shown the improvement of clinical accuracy when attenuation correction is used[177, 178, 179, 180].

As the magnitude of attenuation depends on the distance photons have to travel through matter, there is a difference in effect between human and small animal imaging. While the effect of attenuation in a rat or a mouse is much smaller, accurate quantification can be much more important in preclinical

imaging. This is, for example, the case in studies with inocculated tumors, which are often performed in small animals. As the location of the tumor is known, the researcher is not interested in lesion detection - which is generally more important in clinical imaging - but only in the uptake of the lesion. It was shown by Hwang et al. that not performing attenuation correction on rat micro-SPECT images of ^{99m}Tc labeled tracers leads to quantitative errors of up to 25 %[181]. When low-energy isotopes, such as ^{125}I are used, the error can amount to 50 %. Chow et al. have investigated the effect of attenuation correction in micro-PET imaging of rats. An underestimation of 40 % was seen in the reconstructed non-corrected image[182]. These results show that attenuation correction is needed for quantitative preclinical imaging.

2.5.2 Implementation

In analytical image reconstruction, the projection data needs to be corrected before the start of the reconstruction to account for attenuation. In iterative image reconstruction, correction for photon attenuation is implemented in the imaging model. For this, the distribution of attenuation coefficients across the imaging volume is needed in both PET and SPECT. This distribution, which can be considered an image itself, is called the attenuation map. As each patient has a specific body composition, a patient-specific attenuation map needs to be derived if accurate attenuation correction is to be performed. Below the implementation of attenuation correction into an iterative reconstruction algorithm is described. As the implementation is different for PET and SPECT, both are discussed separately.

2.5.2.1 PET attenuation correction

In PET, as a coincidence can only be detected when both photons are not attenuated, the probability of attenuation depends on the distribution of attenuation coefficients along the entire LOR connecting both detection points. The probability that both photons reach the detector, called the transmitted fraction, is:

$$TF = e^{\int \mu(r)dr} \tag{2.37}$$

where the line integral is calculated along the straight path connecting both detection points. Attenuation correction can then be implemented into the iterative reconstruction algorithm by multiplying the forward projection

by *TF* for each LOR. This represents the implementation of attenuation into the image acquisition model.

2.5.2.2 SPECT attenuation correction

In SPECT, attenuation correction can not be implemented as straightforward as in PET. When a photon is detected in SPECT, it is unclear from what point along the LOR it was emitted. Hence, it is also not certain what the total attenuation was along the path from the emission to the detector. The same method as in PET can therefore not be used. Two other methods have been proposed for SPECT attenuation correction. The first method, proposed by Chang in 1979, is performed in image space on the current estimate[183]. Although it was first developed for analytical reconstruction, it can also be used in iterative image reconstruction. For each voxel, a correction factor is calculated:

$$C(x,y) = \frac{1}{M}\Sigma_{i=1}^{M} TF(x,y,\theta_i) \tag{2.38}$$

where the sum is over a number of projection angles M, θ_i is the projection angle, (x,y) is the coordinate in the imaging matrix and $TF(x,y,\theta_i)$ is the transmitted fraction, calculated over the LOR from pixel (x,y) at projection angle θ_i towards the detector. $C(x,y)$ represents the average attenuation coefficient along all LORs coming from the pixel (x,y). In the estimate, each voxel is divided by $C(x,y)$ before forward projecting. This is an approximation, as the TFs can not be separated from the activity when summing over the angles.

The second method proposed for SPECT is more accurate. Instead of performing the correction in image space as in Chang's method, it is implemented in the forward projection. In that method, the actual total attenuation for each voxel is calculated along the line from the voxel towards the detector at a certain angle. This is done by multiplying the activity of each voxel by the total attenuation between the voxel and the detector at the current projection angle. This yields the same equation as before in PET:

$$TF = e^{\int \mu(r)dr} \tag{2.39}$$

but in this case, the line integral is not calculated between both detection

points, but from the voxel towards the detector. Hence, it yields a different *TF* for each voxel, whereas in PET the *TF* is the same for all voxels along a LOR. This method is more accurate, but computationally more expensive.

2.5.3 Methods for deriving the attenuation map

As discussed above, the attenuation map is needed to perform attenuation correction. A number of methods have been proposed to derive the attenuation map. A short overview of the most frequently used methods is given in this section. As this work concerns MRI-based attenuation correction, a separate section is dedicated to that subject.

2.5.3.1 Calculated attenuation map

The simplest way to obtain the attenuation map is to define the contour of the body without a specific measurement and then assign attenuation coefficients inside this contour based on general knowledge of anatomy. This method is generally referred to as "calculation" of the attenuation map. It can be done by manually defining an ellipse as the contour of the head or by automatically detecting the contour based on the emission sinogram[184, 185]. An advantage of these methods is that no extra time is needed for measurement of the attenuation map, and no extra dose is given to the patient.

2.5.3.2 Transmission measurements

On standalone PET or SPECT scanners the attenuation map is measured by a transmission scan. In PET, transmission measurements can be performed with either a coincidence or a singles source. In the first case one or more static rings or rotating rods containing a long-lived positron emitter such as ^{68}Ge are used[186, 187, 188, 189]. The annihilation photons are detected in two detectors: near to and far from the transmission source. A comparison is made between a blank scan (without the patient) and a scan with the patient in the bore to reconstruct the attenuation map. Acquisition after the patient was injected with the PET tracer is possible, but interference between the transmission and emission data will be present[190].

To achieve reasonable statistics for the transmission measurement a high activity level in the transmission source is needed. This rapidly leads to count rate problems in the near detector, definitely when using older (slower) detectors. Singles transmission data is therefore mostly used in PET[191,

192, 193]. In this configuration a rotating single photon source is used and it is shielded on the back to reduce counts on the near detector. The photons are detected in the opposite detector only and the attenuation map can then be derived provided the location of the source is known at all times. For PET singles transmission scanning, a singles source with high photon energy is used, usually ^{137}Cs (662 keV).

For SPECT coincidence-mode transmission imaging is obviously not possible. Therefore, only singles-mode transmission imaging is possible. The setup is also different, as a SPECT scanner does not consist of a full ring of detectors but rather a number of rotating heads. A rotating single photon source is therefore not a good design. Instead, different setups can be used[194]. Some of them can be used with a parallel-hole collimator (e.g. sheet source, scanning line source), others require a specific collimator (e.g. a fixed line source with converging collimation).

Transmission scans have some benefits, especially for PET, as attenuation values at 511 keV (in coincidence mode) or closer to 511 keV than with CT (in singles mode) are acquired. However, the statistical quality of the images remains low: noise levels of around 20 % are common. The resolution of the attenuation map is also quite low, making it difficult to detect small structures. Another disadvantage of transmission scans is that they require relatively long times to obtain low quality images. As the transmission scan can not be performed simultaneously with the acquisition of emission data, this leads to a significant increase in total acquisition time.

2.5.3.3 CT-based attenuation correction

Since the advent of PET-CT, and more recently SPECT-CT, CT images are used not only as an anatomic reference frame for the emission data but also to derive the attenuation map[118]. CT has some advantages over PET transmission data: the images contain less noise, have a higher resolution and can be acquired in a very short time span, at the expense of a much higher radiation dose. Some problems can also be encountered when using CT-based attenuation correction. The smaller field of view of the CT can lead to truncation of the attenuation map as the arms are not always inside the field of view. Due to the short acquisition time only part of the respiratory cycle may be acquired with CT, while the acquisition time for PET and SPECT is still too long for breathhold scans. The mismatch between attenuation map and emission data leads to motion artefacts in the reconstructed emission data[195]. CT uses X-rays with average energy around 60 keV. CT μ-values can therefore not be used directly as PET or SPECT attenuation coefficients.

Although segmentation of the CT into different tissue types followed by assigning the correct attenuation coefficients for the emission photon energy to this tissue types can easily be done, bilinear scaling is a more accurate method. It is now in general used in CT-based attenuation correction[196, 197]. Bilinear scaling works well with biological tissue[198], but problems can arise when contrast agents are used[199, 200] or metallic implants are present[201, 202].

2.5.4 MRI-based attenuation correction

2.5.4.1 Challenges

In a combined PET-MRI or SPECT-MRI scanner, no CT or transmission source is available. The attenuation map should therefore be derived using a different method. One option is to derive the attenuation map from MRI data. Contrary to CT, where the acquired signal is related to the electron density of the tissue, the MRI signal is determined by the proton density and relaxation properties of tissue, as described above. As there is no direct correlation between these properties and tissue electron density, a direct conversion from a MRI image to the attenuation map is not possible. Therefore, a different approach is needed.

An extra difficulty in MRI-based attenuation correction is that, in MRI images acquired with conventional MRI sequences, there is no signal in lung and cortical bone. This is caused by the low proton density and very short T_2 of these tissues, which makes the MRI signal of these tissues disappear very quickly after RF excitation. There is therefore no contrast between air (which also has no signal), lung and cortical bone. This may lead to problems, as these three tissue types can then not be discriminated based on the MRI data. As their attenuation coefficients are very different - especially the attenuation coefficient of cortical bone, which is much higher - this may lead to an inadequate attenuation map. This will in turn lead to errors in the reconstructed PET or SPECT images. As the quantitative effect of these errors has not been investigated, we have studied them in this work. These investigations are described in chapter 3.

2.5.4.2 Current methods

In the last few years a number of methods for MRI-based attenuation correction have been proposed. As most research has been done on PET-MRI rather than SPECT-MRI, none of these methods have been applied to

SPECT-MRI data sets. However, as the main difficulty in MRI-based attenuation correction is the derivation of the attenuation map, we can assume that these methods would also be applicable to SPECT-MRI. The methods can be divided into two main classes: template-based and segmentation-based[203]. In template-based methods, the MRI of the patient is coregistered to a template MRI using nonrigid coregistration[204]. The same transformation is then applied to a template of the attenuation map. This yields an attenuation map which theoretically predicts the attenuation map of the patient. Template-based methods have only been tested on brain data.

In segmentation-based methods the attenuation map is determined directly from the MRI image intensities. This is usually done in two steps. First, the voxels in the MRI image are classified into different tissue classes that are relevant for attenuation. In the second step predefined attenuation coefficients are assigned to these tissues. The first segmentation-based methods were only tested on brain data[205, 206]. The method proposed by Zaidi et al. uses a fuzzy-clustering-based segmentation on T_1-weighted MRI images. It was tested on 10 patient data sets for which MRI, PET and singles-mode transmission data was available. In the reconstructed PET images, an average relative difference of 7 % or less was found in VOIs in different brain structures. While this is a very good result, it is important to note that the average was taken over all ten patients. It is therefore unclear what the relative differences in individual patients were.

More recently, two segmentation-based methods have been proposed which are designed to work on whole-body data. The first method, proposed by Martinez-Moller et al., is based on a two-point Dixon method for MRI imaging[207]. Dixon methods use gradient echo acquisitions at different echo times to discriminate water and adipose tissue. The images acquired with a Dixon acquisition therefore allow easy segmentation into voxels containing soft tissue and adipose tissue. The lungs were defined using region growing. Cortical bone was not identified. Because of low signal intensity, some voxels containing cortical bone were classified as air. This was solved by applying a morphological closing operation on air voxels inside the body. The method was tested on two patient data sets, and no significant visual differences between images reconstructed with CT-based and MRI-based attenuation correction were observed.

A second segmentation-based method for whole-body MRI-based attenuation correction was designed for use on the Philips sequential PET-MRI system[208]. It only discriminates lung and soft tissue, and ignores bone. The method is based on connected-threshold region growing for segmen-

tation of the body contour and on a more specialized approach for lung segmentation. The algorithm was tested on 15 patient data sets, and relative differences of 5 - 10 % were seen in most patients.

A different method has also been proposed, which uses a combination of pattern recognition and atlas registration to predict the attenuation map from the MR image and a set of aligned MR-CT data sets[209]. In a first step, atlas MR data sets are coregistered to the MR image of the patient. The transformations are also applied to the corresponding CT atlas data sets. A pseudo-CT data set is then generated for each voxel as a weighted contribution of voxel values in the co-registered CT atlas images. The pseudo-CT is then rescaled to 511 keV attenuation coefficients to obtain the PET attenuation map. The method was tested on 17 brain data sets, and an average error of 3.2 % was found in specific regions of interest.

2.5.4.3 Limitations

A common property of all these methods is that they, in some form, take standard anatomical knowledge into account. This implies that they assume that the patient under study has a standard anatomy. In the registration-based or atlas-based method this is explicit, as the attenuation map is derived by transforming one or more standard attenuation maps. In the segmentation based methods the assumption lies in the region-based segmentation of the lungs. This imposes a limitation on the applicability of these methods, as they may fail when the patient has non-standard anatomic features. This could be the case e.g. when imaging head trauma patients. A method that can derive the attenuation map solely from the MRI data would not have this limitation. For that, a method must be derived which creates contrast between the relevant tissues based on the MRI data alone. In this work, the focus is on deriving such a method.

Chapter 3

The effect of segmented attenuation maps on PET quantification

3.1 Introduction

In this chapter, the effect of errors in the attenuation map on the reconstructed emission tomography images is investigated using Monte Carlo simulations. First the reasons for performing this study are explained. In the next sections the simulation setup and the reconstruction methods are described. Afterwards, the derivation of attenuation maps with different types of errors is discussed. This is followed by a description of the obtained results and a discussion on their interpretation. In the last section, a summarizing conclusion is given, which is used as a guideline for the development of MRI-based attenuation correction methods in the next chapter.

3.2 Research goal

As discussed in the last section of the previous chapter, there are some difficulties in performing MRI-based attenuation correction for emission tomography. Most importantly there is no direct correlation between MRI signal intensity and attenuation. In MRI images acquired with conventional MRI sequences, there is also no contrast between air, lung, and cortical bone. These problems are solved in most currently available MRI-based attenuation correction methods by incorporating some form of prior knowledge of

the anatomy of the patient (or animal). This may lead to problems if there are anatomic abnormalities.

Our goal is to develop an attenuation correction method which does not rely on assumptions about patient anatomy, and derives the attenuation map directly from the MRI data using segmentation. Before developing this method, one needs to know how accurate it needs to be. As the derivation of the attenuation map from MRI is inherently difficult, there can be different types of errors in the derived attenuation map. If a specific error has a significant effect on the reconstructed image, it needs to be avoided. However, if this is not the case, improving the method to avoid that kind of error is not interesting.

Different errors can arise with segmented MRI-based attenuation correction. Using a segmented attenuation map in itself yields an error as it uses a discrete representation of the attenuation map, whereas a realistic representation of the body should contain a continuous range of attenuation coefficients. In a segmented attenuation map, only a limited number of tissue classes are discriminated. Ignoring certain tissue types will also have an effect on the accuracy of the attenuation map. Furthermore, errors can be caused by a bias on the attenuation coefficient assigned to segmented tissues. For example, this can be the case when there is a large variability in actual attenuation coefficient of a certain tissue type between different patients. Additionally, there can be tissue misclassification. This can especially occur in bone and lung, as these tissues are difficult to discriminate on MRI images.

Some research has been done on the effect of using a segmented attenuation map on reconstructed image quality. This was mostly done in the context of segmented CT-based or transmission-based attenuation correction[196, 210]. Therefore these studies did not focus on the specific problems of MRI-based attenuation correction. Recently the search for MRI-based attenuation correction has led to investigations into the necessity of taking bone into account. It has been claimed that using a segmented attenuation map which ignores bone does not lead to clinically significant errors in the reconstructed image[207]. However, in that study a clinically significant error was defined as an error that led to a lesion not being seen by an experienced radiologist. Ignoring bone in the attenuation map did lead to average quantitative errors of 8 % in osseous lesions.

These results do not yield a complete answer on how accurate our MRI-based attenuation correction method needs to be. Therefore, we will thoroughly investigate the effect of attenuation map errors on the reconstructed

image. The results obtained in this investigation will then be used to define the requirements for the method that is developed in the next chapter. Specifically, the following questions need to be answered:

- Is it possible to achieve accurate results with a segmented, i.e. non-continuous, attenuation map?
- Which tissue classes need to be discriminated?
- Do we need to take into account inter-patient variability of tissue attenuation coefficients?
- Can tissue misclassification be tolerated? And if so, which fraction of voxels can be misclassified?

We will seek an answer to these questions using Monte Carlo simulations. A simulation study is ideally suited for this kind of investigation, as it allows to separate the effect of attenuation from other image degrading effects, such as motion or scanner count rate performance. As quantitative imaging is the most demanding application of emission tomography, our study will be focused on the effect of attenuation map errors on quantification. It could also be interesting to investigate the effect of attenuation map errors on lesion detection, but a study using clinical data and experienced clinical observers would be better suited for this. Also, it can be expected that an image that gives an accurate quantitative representation will also allow correct lesion detection.

As the magnitude of the effect of attenuation depends on object size, the effects of attenuation map errors will be different in human and small animal studies. In human studies, brain imaging is also different from whole-body imaging. Therefore we have performed three simulation studies: a rat study, a human brain study and a human whole-body study. The investigation was limited to PET alone for two reasons. First of all, the effect of attenuation in PET is larger in most cases. This is due to the fact that two photons need to be detected in PET, and hence the total distance over which photons have to travel through tissue is larger for each detection than in SPECT. Although the linear attenuation coefficients of human tissues are larger at the energies of the gamma photons emitted by SPECT isotopes than at 511 keV, the effect of the distance is much larger in PET. Therefore, if an attenuation correction method is accurate enough for PET quantification, it should also be accurate enough for SPECT quantification with most SPECT isotopes. This does not apply for SPECT isotopes which emit very low energy

gamma photons, such as ^{125}I (35 keV), where the attenuation coefficient is so much higher that the effect of distance does not dominate. Secondly, PET simulations can be run faster than SPECT simulations. This is mainly due to the simpler nature of PET physics, especially the absence of a collimator. In SPECT simulations, tracking of photons through the collimator requires significant computation time.

3.3 Simulations

All simulations were done using the GATE Monte Carlo simulation framework[49]. As back-to-back gamma emission was simulated, positron range and acollinearity were ignored. This was done to reduce the simulation time. Although the digital phantoms that were used allow the simulation of physiological motion, static simulations were performed. This was done to avoid motion artefacts in the reconstructed images. Also, the investigation of the effects of motion is outside the scope of this thesis.

3.3.1 Rat study

For the small animal simulation, the digital ROBY phantom was used[60]. This is a digital representation of a rat, containing all relevant organs. A scanner model for the LabPET micro-PET system (Gamma Medica-Ideas, Sherbrooke, Canada) was used[55], as this scanner is also available in our lab. The axial field of view of the scanner is 76 mm. To perform a whole-body acquisition of the ROBY phantom, 6 bed positions were simulated. There was 50 % overlap between consecutive bed positions, yielding a total axial field of view of 267 mm. The ROBY phantom was simulated as a voxelized phantom in a 128 x 128 x 550 matrix with 0.5 mm isotropic voxel dimensions. Five different tissue types were simulated: air, lung, soft tissue, spongeous (soft) bone and cortical (hard) bone.

The activity distribution of a rat injected with ^{18}F-FDG was simulated. The relative activity distribution in the organs of the ROBY phantom was obtained from human data[211]. A total activity of 74 MBq was simulated. As quantification is best evaluated on lesions within a background, fifteen spherical lesions with 4 mm diameter were added to the phantom. All lesions had the same activity level, which was 8 times higher than the activity level in muscle tissue. The lesions all had the density of soft tissue. They were placed in the brain, lung, liver, spine, colon and femur, with different locations in the organs, as listed in table 3.1. Fig. 3.1 shows a maximum intensity

projection of a reconstructed image to illustrate the extent of the field of view and the location of the lesions.

	Organ	Specific location
1	Brain	Center
2	Brain	Border - close to skull
3	Lung	Center
4	Lung	Apex
5	Lung	Base - close to liver
6	Liver	Center
7	Liver	Lateral border
8	Spine	Thoracic vertebra
9	Spine	Lumbal vertebra
10	Spine	Sacral vertebra
11	Colon	Ascending part
12	Colon	Transverse part
13	Colon	Descending part
14	Rectosigmoid	
15	Femur	Neck

Table 3.1: Locations of the simulated lesions in the ROBY phantom used for the small animal simulation.

3.3.2 Human brain study

For the human brain simulation a different phantom and a different scanner model were used. The digital XCAT brain phantom was used[60], which provides the possibility to distinguish many small structures in the brain. We used a scanner model for the Philips Gemini TF scanner (Philips Medical Systems, Cleveland, USA), which has an axial field of view of 180 mm. A single bed position was simulated. The simulated phantom matrix was 128 x 128 x 90 matrix with 2 mm isotropic voxel dimensions. The voxelized phantom contained 3 different tissue types: air, soft tissue, and cortical (hard) bone. The ^{18}F-FDG activity distribution was obtained from [212], in which the average uptake in different regions for two healthy volunteers is given.

Figure 3.1: Maximum intensity projection of the a reconstructed image of the ROBY phantom, illustrating the field of view and the location of the lesions.

No lesions were inserted in the brain phantom. Fig. 3.2 shows a transverse, coronal and sagittal slice of a reconstructed PET image, illustrating the field of view.

Figure 3.2: A transverse (left), coronal (middle) and sagittal (right) slice of a PET image of the human brain study, reconstructed with the correct attenuation map.

3.3.3 Human whole-body study

The setup of the human whole-body simulation was similar to the small animal simulation, using a different phantom and a different scanner model. The XCAT whole-body phantom was used[60], representing a male subject with a body weight of 85 kg and a height of 1.90 m. This can be considered an average adult body constitution. The same scanner model as for the brain study was used. 7 bed positions were simulated with 90 mm overlap between bed positions, yielding an axial field of view of 70 cm. The simulated phantom matrix was 350 x 350 x 400 matrix with 2 mm isotropic voxel dimensions. The voxelized phantom contained 7 different tissue types: air, lung, adipose tissue, soft tissue, liver, spongeous (soft) bone and cortical (hard) bone.

The average activity distribution of a normal healthy patient injected with ^{18}F-FDG was simulated[211]. Fifteen spherical lesions with 20 mm diameter were placed inside the phantom to simulate clinically relevant pathologies in the lung, liver, spine, colon, prostate and femur. As the brain was simulated separately, no brain lesions were investigated here. All lesions had the same density (soft tissue) and activity level, providing a contrast of 8 : 1 to the activity in muscle tissue. Fig. 3.3 illustrates the field of view and the location of the lesions. The specific locations of the lesions are listed in table 3.2.

3.4 Reconstruction

For all three simulation studies, reconstruction was performed with attenuation-corrected listmode ML-EM reconstruction, as described in the previous chapter[213]. For the rat simulation, the reconstructed matrix was 64 x 64 x 256 with 1 mm isotropic voxel size. For the human brain simulation, the matrix was 128 x 128 x 90 and the voxel dimensions were 2 mm. For the human whole-body study, a matrix of 144 x 144 x 200 was used with 4 mm voxel size. In the human whole-body simulation, scatter correction was performed based on scatter sinograms obtained with single scatter simulation[36]. As the effect of scatter was deemed much smaller in the case of small animal and human brain imaging, scattered coincidences were removed from the data before reconstructing the images.

Geometric sensitivity correction was used in all studies. The sensitivity map for a single bed position was generated by a single backprojection of all available lines of response (LORs) in the scanner[22]. As only one bed position was acquired for the human brain study, reconstructing the data

	Organ	Specific location
1	Lung	Center
2	Lung	Apex
3	Lung	Base - close to liver
4	Lung	Lateral border
5	Liver	Center
6	Liver	Lateral border
7	Spine	Thoracic vertebra lung level (T8)
8	Spine	Thoracic vertebra liver level (T11)
9	Spine	Lumbal vertebra (L4)
10	Colon	Ascending part
11	Colon	Transverse part
12	Colon	Descending part
13	Rectosigmoid	
14	Prostate	
15	Femur	Neck

Table 3.2: Locations of the simulated lesions in the XCAT phantom used for the human simulation.

with this sensitivity map yielded a corrected image. However, the situation is more complex for the rat and human whole-body studies, as multiple bed positions were acquired. First, all bed positions were reconstructed separately using the sensitivity map of a single bed position. The whole-body image (containing all bed positions) was then obtained by summing the individual images, all shifted 38 mm (ROBY) or 90 mm (XCAT) from the previous one. The reconstructed value in each voxel of the whole-body image was calculated as a weighted average of the different bed positions contributing to that voxel. The weighing factor was obtained from the single bed position sensitivity map. With this method, reconstructed values acquired with a higher sensitivity (e.g. in the axial center of the scanner) will have a larger influence on the whole-body reconstructed image than reconstructed values acquired with a lower sensitivity (e.g. at the edge of the axial field of view).

To investigate the effect of attenuation map errors the data was recon-

Figure 3.3: Maximum intensity projection of the a reconstructed image of the XCAT phantom, illustrating the field of view and the location of the lesions.

structed using different attenuation maps. The generation of these attenuation maps is discussed in the next section. All reconstructions were stopped after 25 iterations. The number of iterations was determined from the contrast-to-noise curve of the reconstruction with the correct attenuation map, showing convergence after 25 iterations.

3.5 Derivation of attenuation maps

Attenuation maps for all three simulated data sets were generated in a comparable way. First a reference attenuation map was derived from the tissue map of the ROBY, XCAT brain and XCAT whole-body phantoms. This tissue map (dimensions 128 x 128 x 550, 0.5 mm, 128 x 128 x 90, 2 mm and 350 x 350 x 400, 2 mm for ROBY, XCAT brain and XCAT whole-body respectively) determines the tissue that is simulated by GATE inside each voxel. The 511 keV attenuation coefficients for the simulated tissues are listed in table 3.3. These attenuation coefficients were derived from [214] and verified on 10 whole-body CT based attenuation maps acquired at our hospital. As lung tissue of rats is denser than lung tissue of humans, a different attenuation coefficient is used for lung in the ROBY simulation. This attenuation coefficient was derived from 5 micro-CT based attenuation

maps of rats acquired in our lab.

All derived attenuation maps had the same dimensions as the reconstruction matrix (64 x 64 x 256, 1mm, 128 x 128 x 90, 2 mm and 144 x 144 x 200, 4 mm for ROBY, XCAT brain and XCAT whole-body respectively). First a reference attenuation map is derived. For each voxel in the reconstruction matrix the average of the attenuation coefficients of the tissues inside the voxel was calculated. The reference map contains a continuous range of attenuation coefficients and can be considered the gold standard. All attenuation maps described below were directly or indirectly derived from the reference attenuation map. Table 3.4 gives an overview of the attenuation maps that are derived.

Tissue	511 keV μ (cm^{-1})
Lung (human)	0.0267
Lung (rat)	0.0600
Adipose tissue	0.0927
Soft tissue	0.0968
Liver	0.0977
Spongeous (soft) bone	0.1100
Cortical (hard) bone	0.1300

Table 3.3: Attenuation coefficients of the simulated tissues.

3.5.1 Number of tissue classes

Attenuation maps segmented into different numbers of tissue classes were derived from the reference attenuation map to investigate the effect of the number of tissue classes considered. Based on histograms of whole body CT images one can discriminate 7 tissue types which have clearly different attenuation coefficients: air, lung, adipose tissue, soft tissue, liver, spongeous bone and cortical bone. The regions containing these tissue types were segmented using simple thresholding on the reference attenuation map. The attenuation coefficients listed in table 3.4 were used for the segmented values. As the tissue map for the ROBY phantom did not provide separate values for the liver or adipose tissue, it was de facto a 5-class attenuation map. In the XCAT brain phantom only 3 tissue types are discriminated (air, soft tissue, cortical bone), so in that case was actually a 3-class attenuation map.

	Attenuation map	Compared to
	Reference	(None)
1	Number of tissue classes	
	7 class	Reference
	Liver replaced by soft tissue*†	7 class
	Adipose tissue replaced by soft tissue*†	7 class
	Spongeous bone replaced by soft tissue*†	7 class
	Lungs replaced by air†	7 class
	Cortical bone replaced by soft tissue	7 class
	Cortical bone replaced by air*§	7 class
	Contour map§	7 class
2	Inter-patient variability	
	Lung segmented value + 1SD, 2SD*†	4 class
	Cortical bone segmented value + 1SD, 2SD*	4 class
3	Tissue misclassification	
	3.1 Random tissue misclassification	
	5, 10 and 20% lung => air†	4 class
	5, 10 and 20% lung => soft tissue†	4 class
	5, 10 and 20% lung => cortical bone†	4 class
	5, 10 and 20% cortical bone => soft tissue	4 class
	5, 10 and 20% cortical bone => lung	4 class
	5, 10 and 20% cortical bone => air	4 class
	3.2 Distance-to-interface dependent tissue misclassification	
	5, 10 and 20% lung => air*†	4 class
	5, 10 and 20% lung => soft tissue*†	4 class
	5, 10 and 20% lung => cortical bone*†	4 class
	5, 10 and 20% cortical bone => soft tissue*	4 class
	5, 10 and 20% cortical bone => lung*	4 class
	5, 10 and 20% cortical bone => air*	4 class

Table 3.4: Attenuation maps used for reconstruction and the attenuation map they are compared to. The attenuation maps that were not used in the rat, human brain and whole-body study are marked with a *, † and § respectively.

Eight different attenuation maps were then created. In the first all 7 tissue types were assigned the correct attenuation coefficient. In the second the liver was assigned the soft tissue attenuation coefficient. The third atten-

uation map was derived by replacing the attenuation coefficient of adipose tissue by the value for soft tissue. The attenuation coefficient of soft bone was replaced by the soft tissue attenuation coefficient in the fourth map. In the fifth map the attenuation coefficient of air was assigned to voxels containing lung. In the sixth map the attenuation coefficient of cortical bone was replaced by the value for soft tissue, in the seventh map it was replaced by the value for air. The eight map was a contour map, i.e. a map in which everything inside the body contour was replaced by soft tissue. The second and third map were not derived for the rat study, as no separate tissue class for liver and adipose tissue was available in the ROBY phantom. For similar reasons, the second, third, fourth and fifth map were not derived for the human brain study. The seventh map, in which cortical bone is set to air, was only derived for the human brain study, as this is the only situation in which air and bone occur close to each other.

3.5.2 Inter-patient variability

When segmentation is used to derive the attenuation map the same attenuation coefficient will usually be assigned to a certain tissue type in all patients. However, it is well known that there can be considerable inter-patient variability in the attenuation coefficients of specific tissue types. We have investigated if this inter-patient variability can also lead to significant differences in the reconstructed PET image. For this, a quantitative measure of the inter-patient variability is needed. We have obtained this from 20 clinical whole-body CT based attenuation maps. In each data set, the cortical bone and lungs were segmented using connected-threshold region growing. The segmentation was verified visually. Then, the average attenuation coefficient in the lungs and cortical bone was calculated for each patient, as shown in fig. 3.4. In a last step, the standard deviations of both sets of attenuation coefficients were calculated. We found a standard deviation of 0.004 cm^{-1} and 0.002 cm^{-1} for the average attenuation coefficient of lung and cortical bone respectively.

To evaluate the effect of using a biased attenuation coefficient in the lung two attenuation maps were derived where the attenuation coefficient of lung was increased by 1 and 2 inter-patient standard deviations of the attenuation coefficient of lung. The same was done for cortical bone. As the same data was not available for rats, these attenuation maps were not derived for the rat study. The effect of attenuation coefficient variability on the reconstructed images will also be much smaller for rats. The attenuation

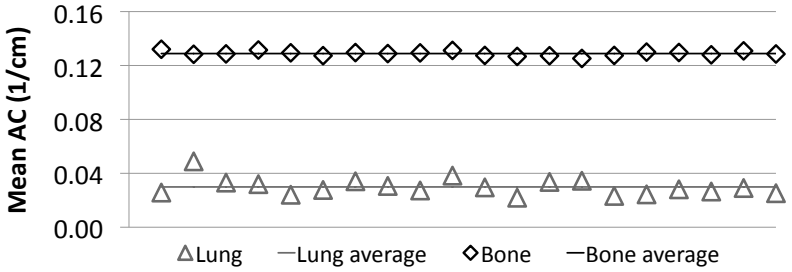

Figure 3.4: The average attenuation coefficient in lung and cortical bone for 20 patients, obtained from whole-body CT based attenuation maps. This data was used to derive the inter-patient variability of the attenuation coefficients of lung and cortical bone.

maps with a variation on the attenuation coefficient of lung were not derived for the human brain study as there is no lung tissue in the brain.

3.5.3 Tissue misclassification

To investigate the effect of tissue misclassification, i.e. detecting the wrong tissue class in a voxel, attenuation maps with classification errors were derived. These attenuation maps were derived from an attenuation map segmented into 4 tissue types: cortical bone, soft tissue, lung and air. As lung and cortical bone are the most difficult to detect on MRI images misclassification will most likely occur in those tissues. Therefore attenuation maps with errors in lung and cortical bone classification were derived. The attenuation maps with lung misclassification were not derived for the human brain study for obvious reasons.

The distribution of tissue classification errors throughout the attenuation map can depend on the segmentation algorithm and the image quality of the image that is used for segmentation. When segmenting an image with a high noise level, the errors will be randomly distributed over the image. This will also be the case if a clustering method is used for segmentation. If the accuracy of the segmentation is mainly limited by the resolution of the image, classification errors will more likely occur at the interfaces between tissues, due to partial volume effects. This will happen if a contour-based segmentation method is used. As the distribution of tissue classification errors can have an effect on the reconstructed PET image, both types of

errors were investigated.

3.5.3.1 Random tissue misclassification

Nine attenuation maps were derived with random lung misclassification. This was done by assigning air, soft tissue and bone attenuation coefficients to a fraction (5, 10 and 20 %) of voxels containing lung. The voxels in which errors were made were distributed randomly. For random cortical bone misclassification nine attenuation maps were derived in the same way, replacing 5, 10 and 20 % of the attenuation coefficients of voxels containing bone by the attenuation coefficient of soft tissue, lung and air.

3.5.3.2 Distance-to-interface dependent tissue misclassification.

To derive attenuation maps with tissue classification errors that are distributed non-randomly, the distribution of classification errors is needed. As described above, we assume that the probability that a classification error occurs can depend on the distance to the tissue interface. This has not been investigated in the past. Therefore, we have derived the error probability distribution from 5 patient data sets. For each patient a segmented CT-based attenuation map and a segmented MRI-based attenuation map were available. The attenuation maps contained 3 tissue types (air, soft tissue and bone). The CT-based attenuation map was used as a reference to determine classification errors on the MRI-based attenuation map. For classification errors between each of these tissue types, a histogram showing the fraction of misclassified voxels for each distance to the tissue interface was derived. As the shape of the obtained histograms was comparable, we assume that the error probability distribution could be derived by normalizing the histograms to a maximum value of 1 and taking the average of all histograms. The obtained distribution is shown in fig. 3.5. It shows a strong dependence of the error probability on the distance to the tissue interface.

Attenuation maps with distance-to-interface dependent tissue misclassification in lung and cortical bone were then derived using this distribution. This was done in three steps for each point. First, the distance to the tissue interface was calculated. Then, a random number was generated. In the last step a classification error was assigned only if the random number was smaller than the error probability for that distance, obtained from the distribution. The same types of classification errors as for the random classi-

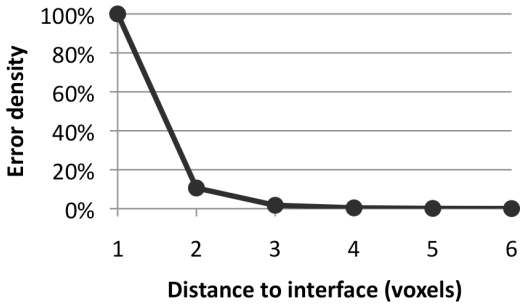

Figure 3.5: Normalized error probability distribution used to derive attenuation maps with classification error density dependent on the distance to the tissue interface.

fication errors were used. The distribution was scaled to obtain attenuation maps in which 5, 10 and 20 % of lung or bone voxels were misclassified. These attenuation maps were not derived for the rat study, as it can be assumed that only minor differences with random tissue misclassification will be observed because the organs of a rat are quite small.

3.6 Evaluation of the reconstructed images

The image reconstructed with the attenuation map using 7 tissue types (5 in the rat study, 3 in the human brain study) was compared to the image reconstructed with the reference attenuation map. The images obtained with the other segmented attenuation maps (using only 6 (4, 2) tissue types) were compared to the image obtained with the 7 (5, 3) tissue map. This was done to show the actual effect of not taking the considered tissue type into account. For the maps with segmentation errors the images were compared to the image reconstructed with an attenuation map segmented into bone, soft tissue, lung and air (bone, soft tissue and air for the human brain study). This was done because these 4 tissue types are the most important to be discriminated, as is discussed below. All attenuation maps and the maps they are compared to are listed in table 3.4.

For some reconstructed images visual evaluation was performed to provide insight into the location of the differences in the reconstructed images. This was done in three steps. First a difference image was calculated by

subtracting both reconstructed images being compared. Then the ratio of the difference between both images to the value in the reference image was calculated in each voxel, yielding a percent difference image. A maximum intensity projection was then obtained by taking the percent difference with the highest absolute value for each line in the anterior-posterior direction. The images are depicted in color scale: red means that the modified attenuation map yielded an overestimation of the activity in that location, blue indicates an underestimation.

For quantitative evaluation spherical volumes of interest (VOIs) were defined. The diameter of the VOIs were 4 mm, 10 mm and 20 mm in the reconstructed images of the ROBY, XCAT brain and XCAT whole-body phantoms respectively. The percent difference between the activity in the VOIs in the images reconstructed with different attenuation maps was calculated:

$$\Delta_{m,i}(\%) = \frac{N_{m,i} - N_{c,i}}{N_{c,i}} \times 100 \tag{3.1}$$

where $N_{m,i}$ and $N_{c,i}$ are the total number of counts in VOI i on the image reconstructed with the attenuation map under evaluation (m) and the attenuation map used for comparison (c) respectively. In the rat and human whole-body studies, the VOIs were drawn on the location of the lesions described above. In the human brain study, the VOIs were drawn in clinically relevant regions of the brain, listed in table 3.5.

	Location
1	Dorsal cortex
2	Frontal cortex
3	Lateral cortex
4	Putamen
5	Thalamus
6	White matter

Table 3.5: Locations of the VOIs defined in the brain for evaluation of the human brain study.

As all changes to the attenuation map will lead to changes in the reconstructed image, it is important to define what is a relevant difference. As we

have compared the total activity in VOIs, a difference is relevant if it is larger than the variation in the total counts in VOIs of the same size in a region of homogeneous uptake. To determine this variation, 5 VOIs were drawn on the image reconstructed with the reference attenuation map in a soft tissue region with homogeneous uptake. The total counts in each of these VOIs was calculated. The average of the total counts was then calculated:

$$\mu_N = \frac{\Sigma_{k=1}^{5} N_k}{5} \tag{3.2}$$

where N_k is the total counts in VOI k. The lower level of significance was then set to:

$$\Delta_{sig} = \frac{\sqrt{\frac{\Sigma_{k=1}^{5}(N_k - \mu_N)^2}{4}}}{\mu} \tag{3.3}$$

This is the ratio of the standard deviation on the total counts to the average total counts. For the ROBY simulation, this was 3.1 %. For the XCAT brain and XCAT whole-body simulations, values of 4.2 % and 4.7 % were obtained respectively. All results that have a relative difference less than 3.1 %, 4.2 % or 4.7 % in the respective studies were therefore defined as non-relevant.

3.7 Results

In this section, a description of the most important results obtained from all three simulation studies is given. For clarity, the results of the different studies are discussed separately. Not all results are described here but the complete list of results can be found in appendix A.

3.7.1 Rat study

In the rat study, only very few relevant errors were observed. The quantitative evaluation of the effect of segmenting into different numbers of tissue classes is shown in fig. 3.6. Replacing spongeous bone with soft tissue yielded errors smaller than 1 % and hence no results are displayed for that

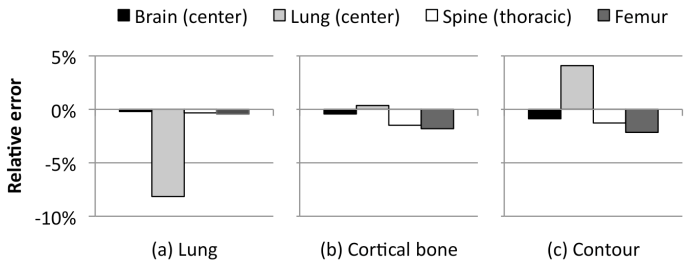

Figure 3.6: Relative errors in total activity in 4 lesions in the rat study, induced by ignoring a certain tissue type in the segmented attenuation map: (a) lung (replaced by air) and (b) cortical bone (replaced by soft tissue) and (c) contour attenuation map (all tissue inside the body replaced by soft tissue).

case. The largest errors were found when lung tissue was ignored and replaced by air, which led to an underestimation of 8 % in the center of the lungs. Replacing cortical bone by soft tissue did not lead to relevant errors (2 % in the spine and femur). When a contour map is used, errors of 4 - 5 % are seen in the lungs and errors of $\approx$ 2 % in the spine and femur. In the abdomen, no relevant errors were found with any of the attenuation maps.

Random tissue misclassification did not lead to any relevant errors. In fact, even lung misclassification into cortical bone only yielded errors of 1.7 % or less. As inter-animal variability was not investigated, no results were available. The same applies to distance-to-interface dependent tissue misclassification.

3.7.2 Human brain study

3.7.2.1 Number of tissue classes

The quantitative effect of using different numbers of tissue classes in the attenuation map is shown in fig. 3.7. When cortical bone is replaced by soft tissue, underestimations of 7 % or less are seen. Larger errors are observed if cortical bone is replaced by air: over 20 % in the dorsal cortex and the thalamus. When a contour map is used, which replaces bone as well as air voxels inside the head with soft tissue, the largest error is seen in the frontal cortex, with an overestimation of 27 %. An error of almost 15 % is also observed in the thalamus.

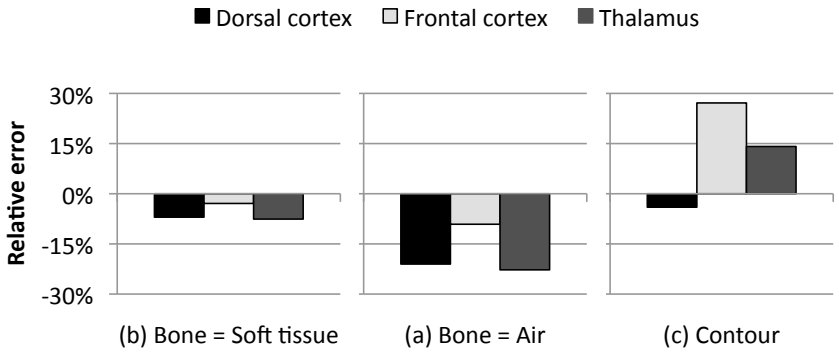

Figure 3.7: Relative errors in total activity in 3 lesions induced by ignoring a certain tissue type in the segmented attenuation map in the human brain study: (a) cortical bone (replaced by soft tissue), (b) cortical bone (replaced by air) and (c) contour map (all voxels inside the body set to soft tissue).

3.7.2.2 Inter-patient variability

When the attenuation coefficient of cortical bone is increased by one or two standard deviations, no relevant errors were observed. The maximum error was 0.6 %, which is very small.

3.7.2.3 Tissue misclassification

Misclassification of cortical bone voxels into soft tissue did not lead to relevant effects, even if 20 % of bone voxels were misclassified. There was no noticeable difference between random and distance-to-interface dependent classification errors for those errors. When a fraction of cortical bone voxels is classified as air, different results are observed. Random bone/air misclassification of up to 10 % does not lead to relevant errors. When 20 % of cortical bone voxels are randomly misclassified, the error in the thalamus is borderline relevant (-4.4 %). The errors in all other VOIs are smaller.

When misclassification of cortical bone into air is not random but depends on the distance to the bone/air interface, larger errors are observed. When 10 % of cortical bone voxels are misclassified, a relevant error can already be observed in the thalamus (-6.7 %). When the misclassified fraction amounts to 20 %, the error in the frontal cortex also becomes relevant (-4.6 %).

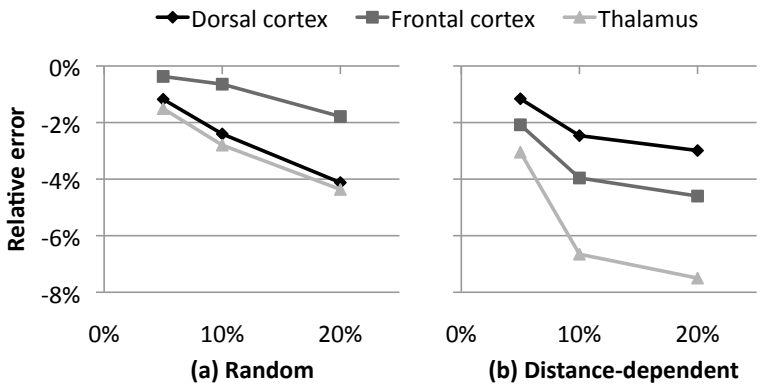

Figure 3.8: Quantitative evaluation of the effect of bone misclassification into air in the human brain study. The relative difference in total activity in three different lesions is shown for 5, 10 or 20 % bone misclassification. The misclassification was random (a) or distance-to-interface dependent (b).

3.7.3 Human whole-body study

3.7.3.1 Number of tissue classes

A visual representation of the errors induced by not taking adipose tissue, spongeous bone, lung or cortical bone into account is shown in fig. 3.9. The

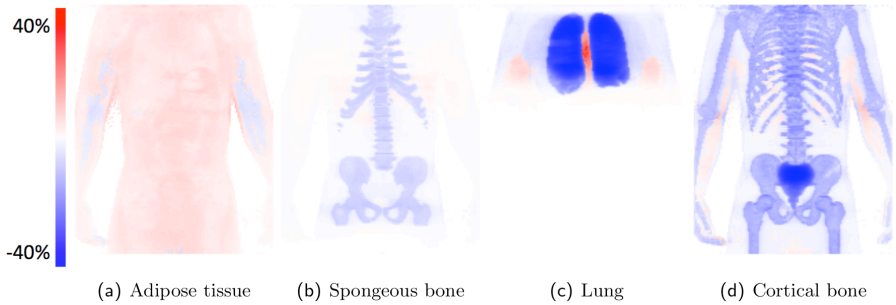

Figure 3.9: Maximum intensity projections of the relative errors induced by ignoring a certain tissue type in the segmented attenuation map (human whole-body study): (a) adipose tissue, (b) spongeous bone (both replaced by soft tissue), (c) lung (replaced by air) and (d) cortical bone (replaced by soft tissue). Red indicates an overestimation, blue indicates an underestimation.

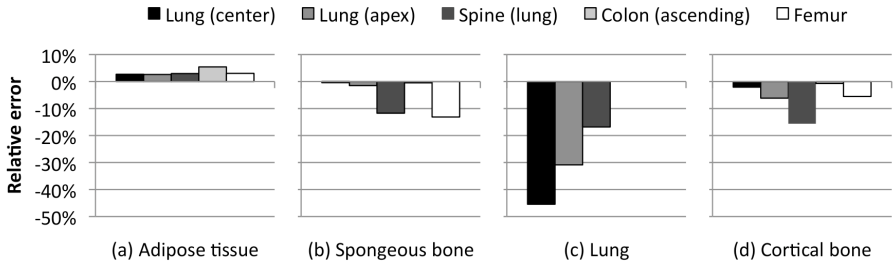

Figure 3.10: Relative errors in total activity in 5 lesions in the human whole-body study, induced by ignoring a certain tissue type in the segmented attenuation map: (a) adipose tissue, (b) spongeous bone (both replaced by soft tissue), (c) lung (replaced by air) and (d) cortical bone (replaced by soft tissue).

most important quantitative results are depicted in fig. 3.10. Segmenting into all 7 tissue classes yields very small errors compared to the reference attenuation map ($<$ 2 %) and hence no results are displayed for that case. The same applies for the attenuation map where liver tissue is ignored. Ignoring adipose tissue leads to errors of 5 - 7 % in the colon and the prostate but no other relevant errors. Ignoring soft bone yields errors of 10 - 15 % in the spine and the femur but non-relevant differences elsewhere. Assigning the attenuation coefficient of air to lung tissue leads to errors of 25 - 45 % in the lung but also a 17 % error in the spine at the level of the lung. The effect of not taking cortical bone into account is smaller: 10 - 20 % in all segments of the spine and the femur. A 7 % error was also found at the apex and lateral border of the lung. The contour map yielded very high errors, e.g. an overestimation of more than 200 % in the lungs.

3.7.3.2 Inter-patient variability

An increase of the segmented attenuation coefficient of lung by one or two standard deviations led to relevant effects, as visible in fig. 3.11: errors of 6 % - 12 % in the lung with a bias of one (0.004 cm^{-1}) standard deviation. With a bias of two standard deviations relevant errors are also seen in the spine at the level of the lung. An increase of the segmented attenuation coefficient of cortical bone by one or two standard deviations did not lead to relevant differences.

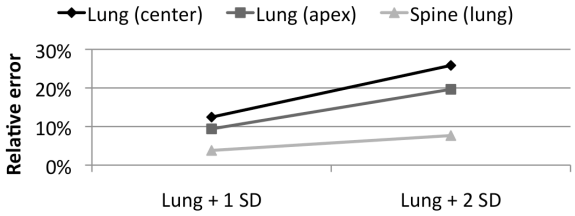

Figure 3.11: Quantitative evaluation of the effect of inter-patient variation on the attenuation coefficient of lung (human whole-body study). The relative error in total activity in three different lesions is shown for an overestimation of the lung attenuation coefficient by 1 and 2 standard deviations.

3.7.3.3 Tissue misclassification

Random tissue misclassification

The effect of random lung misclassification is depicted in fig. 3.12. Lung misclassification where lung tissue is assigned the attenuation coefficient of air does not yield relevant errors if less than 10 % of the voxels are misclassified. If errors are made in more voxels, a relevant underestimation can be seen in the lung (5 - 10 %). Misclassification where the attenuation coefficient of soft tissue is assigned to lung tissue yields relevant errors even if there are only 5 % errors. The errors are largest at the center, lateral border and apex of the lung, followed by the base of the lung and the part of the spine behind the lung. Lung / cortical bone misclassification shows results with comparable trends but the errors are even larger.

Fig. 3.13 shows the effect of random cortical bone misclassification. Misclassification of cortical bone where the cortical bone is assigned the attenuation coefficient of soft tissue does not lead to relevant errors, even if 20 % of bone voxels are misclassified. 10 % or more bone / lung and bone / air misclassification can lead to relevant errors in the thoracic and lumbar spine. The lateral border of the lung is also affected.

Distance-to-interface dependent tissue misclassification

If the tissue classification errors are not randomly distributed, slightly different results can be seen for lung / soft tissue misclassification, as shown in fig. 3.14. As expected, the error in the center of the lung is smaller,

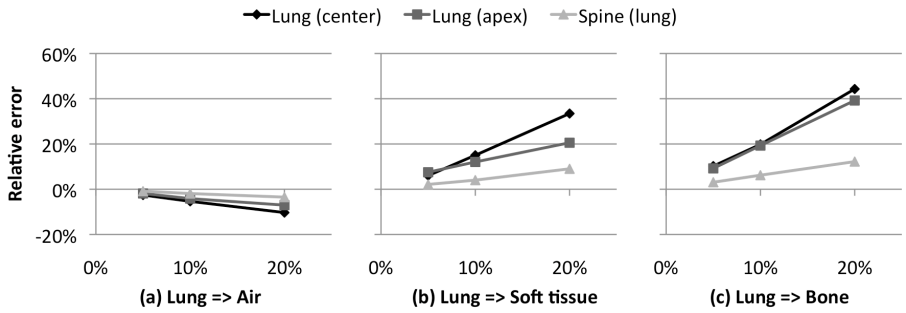

Figure 3.12: Quantitative evaluation of the effect of random lung misclassification (human whole-body study). The relative difference in total activity in three different lesions is shown for 5, 10 or 20 % lung misclassification. The effect of misclassification where lung tissue is assigned the attenuation coefficient of air (a), soft tissue (b) and cortical bone (c) is shown.

but the errors at the borders of the lung are increased. This still leads to relevant errors even if only 5 % of lung voxels are misclassified. For lung / bone errors, the difference with random misclassification is larger. In that case, non-relevant errors are observed at the center and the bottom border of the lung if 5 % of voxels are misclassified. The error at the apex of the lung is increased compared to random misclassification.

Small differences with random misclassification are observed for bone clas-

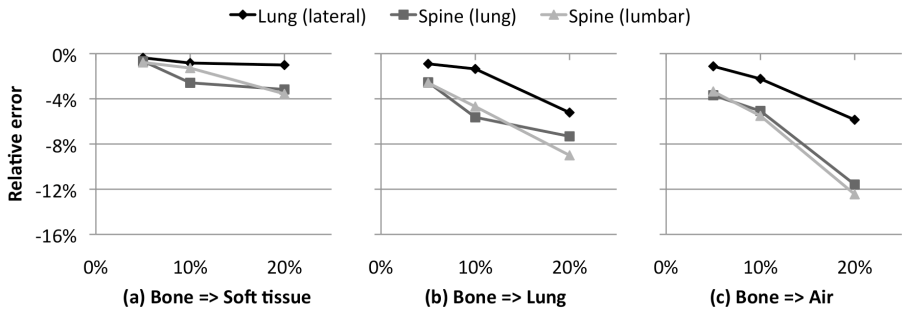

Figure 3.13: Quantitative evaluation of the effect of random bone misclassification (human whole-body study). The relative difference in total activity in three different lesions is shown for 5, 10 or 20 % bone misclassification. The effect of misclassification where cortical bone is assigned the attenuation coefficient of soft tissue (a), lung (b) and air (c) is shown.

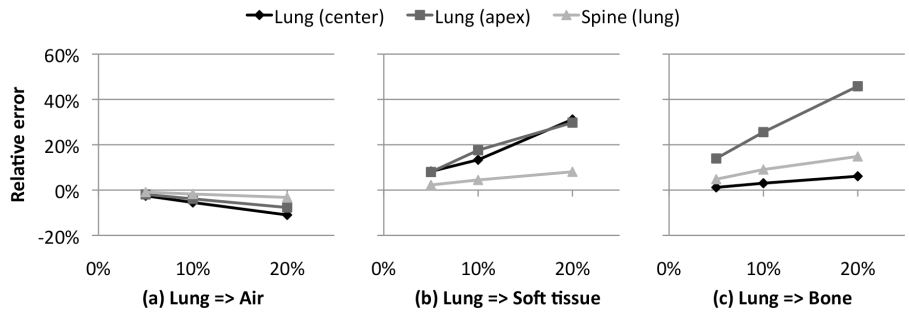

Figure 3.14: Quantitative evaluation of the effect of lung distance-to-interface dependent misclassification (human whole-body study). The relative difference in total activity in three different lesions is shown for 5, 10 or 20 % lung misclassification. The effect of misclassification where lung tissue is assigned the attenuation coefficient of air (a), soft tissue (b) and cortical bone (c) is shown.

sification errors. Bone / soft tissue misclassification still leads to non-relevant errors, even if 20 % of bone voxels are misclassified. Bone / lung non-random misclassification yields slightly higher errors than random misclassification in the apex and lateral border of the lung, leading to significant errors if 20 % of voxels are misclassified. Bone / air non-random misclassification leads to comparable results as bone / air random misclassification.

3.8 Discussion

3.8.1 Rat study

In the rat study, only small errors were found. This is related to the small size of the animal under study. Although it has been shown in the past that attenuation correction for small animal PET is necessary for accurate quantification[182, 215], the results presented in this chapter show that the requirements on the attenuation map are not so stringent. In fact, the results indicate that an attenuation map that discriminates air, lung and soft tissue is sufficient to achieve accurate results. If the lungs are not treated as a separate tissue type, it is better to assign the attenuation coefficient of soft tissue to them than to treat them as air. This is different from human imaging, and is related to the higher density of rat lungs compared to human lungs.

Spongeous bone and cortical bone can be treated as soft tissue without

leading to relevant errors. This is also related to the size of the bone structures in a rat. To achieve the highest accuracy, they should also be treated as separate tissue types. If the attenuation map is derived from images in which they can be easily discriminated, such as a micro-CT, this can be done. However, as the segmentation of cortical bone in MRI images is difficult, it is probably not interesting to put a lot of effort into the discrimination of cortical bone in MRI-based attenuation correction. The small size of the bone structures also adds an extra difficulty for segmentation.

As different levels of tissue misclassification do not lead to relevant errors, even if 20 % of bone or lung voxels are misclassified, it seems that random tissue classification errors can be tolerated up to a certain level. This is interesting for MRI-based attenuation correction, as it means that the noise in the images used for segmentation can be relatively high. As small animal imaging is usually done at high resolution, long acquisition times are needed to achieve images with a high signal-to-noise ratio. Our results indicate that the images that will be used for deriving the attenuation map do not need very low noise levels. Hence, the total acquisition time can possibly be reduced.

Only micro-PET simulations have been performed, and the effect of the errors in the attenuation map on micro-SPECT data is therefore not clear. However, as was explained in the introduction of this chapter, the effect of attenuation in SPECT is smaller than in PET. Therefore, it can be expected that an attenuation map that is sufficient for micro-PET imaging will also be sufficient for micro-SPECT imaging. The methods derived for micro-PET attenuation correction will therefore also be used for the micro-SPECT study described in chapter 6.

3.8.2 Human brain study

In the human brain study, relevant errors were found when cortical bone was replaced with a different tissue type. When it was replaced with soft tissue, the errors were modest ($\approx$ 7 %) but still too high to be tolerated. When the attenuation coefficient of air is assigned to cortical bone voxels, large underestimations are seen. The errors are largest in the dorsal cortex and the thalamus, as both regions are located close to the skull. The contour map, in which soft tissue is assigned to all voxels inside the body and hence nor cortical bone nor air are discriminated, also shows large errors, especially in the frontal cortex. This is explained by the proximity of the frontal sinus, which is a large air structure. From these results it is clear that all three

tissue types present in the human brain need to be discriminated to allow accurate quantification.

20 % classification errors from cortical bone to soft tissue can be tolerated. Random misclassification of cortical bone into air can also be tolerated, as long as the fraction of misclassified voxels remains below 20 %. When the misclassification is not random but depends on the proximity of the air/cortical bone interface, larger errors are seen. This is especially the case in the frontal cortex and the thalamus. The large difference between the effect of random and distance-to-interface dependent misclassification in the thalamus is related to the location of the thalamus. It is located close to the base of the skull, where complex combinations of cortical bone and air are present. These results are interesting when designing a segmentation algorithm: one should keep the probability of misclassifying cortical bone as air low, even if this means increasing the fraction of cortical bone voxels that are misclassified as soft tissue.

3.8.3 Human whole-body study

The results of the human whole-body study show that the most important tissue type that needs to be discriminated, apart from soft tissue and air, is lung tissue. The large effect is mainly caused by the large volume covered by the lungs. This implies that if a positron annihilation takes place in the middle of this volume, the 511 keV photons will be affected by a wrong attenuation coefficient over a long distance (at least 10 cm for the lungs), independent of the direction in which they travel. When ignoring the attenuation of lung tissue, voxels containing lung tissue should be classified as air, as the difference with soft tissue attenuation coefficients is much larger. However, the difference between lung and air attenuation coefficients is still substantial (0.027 cm^{-1}). A quick calculation shows that a photon traveling through 10 cm of lung tissue has a 24% chance of being attenuated. This important effect is not taken into account when lung tissue is ignored.

The second most important tissue type to take into account is cortical bone. The difference in attenuation coefficient between cortical bone and soft tissue is comparable to the difference between lung and air (0.028 cm^{-1}). However, the effect is smaller compared to lung because the total volume of cortical bone in the body is much smaller. Cortical bone is also not concentrated in one region as is the case for lung tissue. This does make the effect also more difficult to predict as cortical bone can be present in many regions throughout the body. The fact that cortical bone is difficult to visualize on MRI images, which could ideally be used to derive segmented

attenuation maps in the context of PET-MRI, adds to the difficulty. The most important clinical context for this is cancer that has metastasised to the spine or other bone structures, as can be seen from the results.

Not taking spongeous bone into account leads to errors of comparable magnitude in the bone structures. Although the difference in attenuation coefficient between soft tissue and spongeous bone is much smaller, most bones contain a much larger volume of spongeous bone compared to cortical bone. When possible it should also be taken into account, as it also has a considerable effect on the quantification of uptake in the bone. To our knowledge, no research has been done up to this point into MRI-based attenuation correction methods that discriminate spongeous bone.

The effect of ignoring adipose tissue will depend on patient constitution. In this study we have modeled a patient of average size, and the effects of adipose tissue on attenuation correction are only slightly relevant. It is therefore more important that tissue classes discussed above are taken into account. However, as the segmentation of adipose tissue on MRI images is quite straightforward, we would suggest taking adipose tissue into account when using segmented MRI images.

When a segmented attenuation map is used the same attenuation coefficients will be assigned to the different tissue types for all patients. It is well known that there is inter-patient variability on the actual attenuation coefficient of lung or cortical bone. Our results show that the inter-patient variability of cortical bone is not relevant for attenuation correction. The inter-patient variability of lung tissue can produce relevant effects, even if the attenuation coefficient only deviates from the mean by one standard deviation. Ideally a segmented attenuation map should thus also provide a custom lung attenuation coefficient for each patient. In MRI-based attenuation correction it would be interesting if the density of lung tissue could be determined from the MRI image. Currently this possibility has not been demonstrated. Another option would be to determine if there are other predictors of lung density (e.g. age, constitution, smoking) that could be used.

Segmentation algorithms can assign the wrong tissue type to a voxel. We have shown that up to 10 % misclassification that assigns the attenuation coefficient of air to voxels containing lung tissue can be tolerated as well as up to 20 % misclassification that yields the attenuation coefficient of soft tissue in bone voxels. Other errors (lung / soft tissue, lung / bone, bone / lung and bone / air) do lead to relevant errors and should therefore be

avoided. This is the case when misclassified voxels are distributed randomly over the image as well as when classification errors are more prominent close to tissue interfaces. As mentioned in the previous section, this can be interesting when designing a segmentation algorithm. It is better to design the algorithm so that classification of lung to air and of bone to soft tissue is more likely.

Apart from influencing attenuation correction, the attenuation map also has an effect on scatter correction. As current scatter correction algorithms use a combination of the attenuation map and a preliminary reconstructed image to estimate the amount of scatter, it is clear that using an incorrect attenuation map will lead to incorrect scatter correction. The results described in this chapter were obtained from data containing scattered coincidences, using the single scatter simulation algorithm to perform scatter correction. As it is possible to remove scattered coincidences from the simulated data prior to reconstruction, we have also performed all reconstructions described above with scatterless data. The results were very similar to those described above, apart from slightly smaller errors in the lungs ($\approx$ 5 % smaller in most cases). Therefore these additional results are not described in detail.

A final remark can be made concerning the simulated voxel size in all three simulation studies. In the rat and human simulations, the voxel sizes of the simulated phantoms were 0.5 mm and 2 mm respectively. These voxel sizes were chosen because they are well below the measured resolution of the simulated scanners, which are $\approx$ 1.4 mm and $\approx$ 4.7 mm respectively[216, 217]. However, some features relevant for attenuation correction have dimensions smaller than the chosen voxel sizes. Therefore, these features were not represented accurately in the simulation. This can, for example, be the case for the cortical shell of some bones. The effect of errors in the attenuation map in such small features can not be assessed from these results. However, it is unlikely that these errors would be large, especially because of the limited resolution of the scanners. It would also be very time consuming to perform a Monte Carlo simulation with much smaller voxel size. Therefore, we did not investigate this in more detail.

3.9 Conclusion

We will use the results presented in this chapter as a guideline for the requirements of the algorithms that will be developed in the next chapter.

The results indicate that for small animal attenuation correction, a method which discriminates air, lung and soft tissue is needed. As lung tissue is not visible on conventional MRI images, this means that a new method needs to be developed. Discrimination of cortical bone can also be interesting, but is not explicitly necessary.

For human brain imaging, all tissue types that are present in the head should be discriminated: air, soft tissue and cortical bone. As classification errors from cortical bone to soft tissue of up to 20 % can be tolerated while this is not the case for cortical bone/air misclassification, an algorithm should be designed which is more likely to misclassify bone voxels as soft tissue than as air.

The results of the human whole-body study lead to much more stringent requirements. In human whole-body imaging, at least 5 tissue types should be discriminated: air, lung, soft tissue, spongeous bone and cortical bone. As current methods for whole-body attenuation correction only discriminate air, lung and soft tissue (and sometimes adipose tissue), this means that a completely new method also needs to be derived for human imaging. Special effort is needed to discriminate air, lung and cortical bone, as this is not possible with conventional MRI images.

The results also indicate that classification errors in the lung should be avoided, as even a low fraction of misclassified voxels leads to relevant errors. Limited classification errors in cortical bone can be tolerated, at least if the algorithm is designed so that it is more likely that cortical bone will be misclassified as soft tissue than as air or lung. In the next chapter, the development and testing of an algorithm that fulfills these requirements is described.

3.10 Original contributions

The results of the human whole-body study presented in this chapter was published in a A1 journal paper[218]. The investigation of inter-patient variability of the attenuation coefficients of lung and cortical bone was presented at the SNM conference in 2010[219].

Chapter 4

Derivation of attenuation maps from ultrashort echo time images

4.1 Introduction

In the previous chapter it was shown that, in order to achieve accurate quantification in human whole-body imaging, 5 different tissue classes need to be discriminated in the attenuation map: air, lung, soft tissue, spongeous bone and cortical bone. In human brain imaging, air, soft tissue and cortical bone are needed. In small animal studies, the discrimination of air, lung and soft tissue is sufficient. As MRI has superior soft tissue contrast to any other imaging modality, the segmentation of soft tissue from MRI images is not difficult. As spongeous bone also contains a large fraction of bone marrow, which can be considered soft tissue, the segmentation of spongeous bone from MRI images should also be possible.

The discrimination of air, lung and cortical bone is more difficult on MRI images. In fact, lung and cortical bone exhibit practically no MRI signal in images acquired with conventional MRI sequences. Consequently, there is no contrast between air, lung and cortical bone in those images. The low signal of lung and cortical bone is caused by the low proton density and short T_2 relaxation time of these tissues. Due to these properties, the MRI signal of these tissues disappears very quickly after RF excitation, before it can be acquired by the scanner.

This problem can be solved by using an MRI sequence that acquires the

signal very fast after RF excitation, before the signal has disappeared. For this purpose, special MRI sequences called ultrashort echo time (UTE) sequences have been developed. In this chapter, the principles and applications of UTE sequences are first described. Then, the MRI properties of lung and cortical bone are investigated to assess the feasibility of using UTE sequences to visualize them. In the last section, a method is proposed which allows the derivation of attenuation maps from images acquired with UTE sequences.

4.2 Ultrashort echo time imaging

4.2.1 Imaging of short T_2 components

4.2.1.1 Origin of short T_2

As described in chapter 2, T_2 is the transverse relaxation time of tissues and is defined by the chemical environment of the protons in the tissue. In general, protons in a highly organized chemical environment (e.g. in solids) have extremely short T_2s (≈ 1 μs), whereas protons in liquid water have very long T_2s ($\approx$ 4000 ms). Protons in other materials can have T_2s anywhere in between those values. In biological tissue, the T_2 of protons strongly depends on the organization of the protein matrix[220, 221]. The best example in the mammalian body, and also most relevant for this thesis, is collagen[222]. Collagen molecules provide structural support in many tissues, and are especially abundant in hard tissues such as tendons, ligaments, cartilage and cortical bone. The protons in the collagen have T_2s in the order of 10 μs, but protons in water molecules that are in the vicinity of collagen molecules have longer T_2s.

4.2.1.2 Imaging problems

The imaging of short T_2 components is impeded by two specific phenomena[223]. The first is related to the short T_2 itself and involves the RF pulses. In materials with a long T_2, the T_2 is much longer than the duration of the RF pulse. Hence, transverse relaxation during application of the RF pulse can be ignored. This means that a 90° RF pulse will indeed lead to complete flipping of the magnetization vector into the transverse plane. However, this assumption does not apply to short T_2 components. The transverse relaxation of short T_2 components occurs so fast, that the relaxation during the application of the RF pulse can not be neglected. The longer the RF pulse, the more transverse relaxation will take place during

application of the RF pulse and hence the smaller the obtained flip angle will be. RF pulses therefore need to be very short to excite short T_2 components. To obtain the same flip angle in a shorter time span, the power of the RF pulse needs to be increased, as determined by eq. 2.24. However, the output power of the RF coils is limited by the hardware as well as safety regulations. Also, short RF pulses will inherently have a broad bandwidth and lead to poor slice selection. Another problem related directly to the short T_2 is that the acquisition of short T_2 components also requires very fast sampling of the signal, which relies on very fast switching from transmit to receive mode, which is also limited by the hardware.

The second phenomenon that leads to problems in imaging of short T_2 components is their broad resonance peak compared to long T_2 components. This means that they are not only affected by RF pulses exactly at the Larmor frequency, but may also be affected by RF pulses at slightly different frequencies. This can cause problems with fat saturation pulses, which are applied at the resonance frequency of adipose tissue (slightly different from water) to reduce the signal from fat in the image. Fat saturation pulses do not affect long T_2 components, but may affect short T_2 components and hence lead to a lower signal from those components.

4.2.2 Principles of UTE imaging

The goal of UTE imaging is to start the acquisition of the MRI signal as quickly after the start of RF excitation as possible. Therefore, there are three key differences between UTE sequences and conventional sequences[224]:

1. **FID sampling**: in conventional MRI sequences, the spins are refocused after RF excitation by forming a gradient or spin echo. This makes it impossible to acquire MRI signal very quickly after RF excitation, as a 180° pulse (SE) or the application of gradients (GE) is needed to produce the echo. In UTE sequences, the FID is sampled instead of an echo[225]. This makes it possible to start acquiring the signal directly after RF excitation, with only a delay from the hardware switching time.

2. **Short RF pulse**: a normal 90° RF pulse can take up to 0.40 ms, depending on system specifications. During this period, short T_2 components will already exhibit significant transverse relaxation. In UTE sequences, special truncated RF pulses are used[226]. Using low flip angles ($\approx 10°$) also limits RF pulse duration. As mentioned earlier,

truncated RF pulses have large bandwidths, leading to a broad slice selection profile. This limits resolution in the axial direction with 2D imaging.

3. **Radial sampling of k-space**: if k-space is sampled in the conventional way, i.e. on a cartesian grid, the application of a gradient is needed to move the k-space vector to the start position of a line. This also requires time. Therefore, UTE sequences sample k-space radially, starting in the center of k-space and moving outwards using gradients[227]. This allows the start of acquisition without first applying any gradients. Other sampling schemes are also possible, e.g. spiral sampling[228].

4.2.3 Philips UTE sequence

The UTE sequence used in most experiments in this thesis was available on a Philips Achieva 3T system (Philips Medical Systems, Best, The Netherlands). It was developed by Rahmer et al. and is described in detail in [229]. In the following paragraphs the most important features of the sequence are clarified. A simplified schematic overview of the sequence is shown in fig. 4.1. First of all, the RF pulse is applied. It is a hard block pulse with low flip angle ($\leq 10^{\circ}$). With these properties, the RF pulse duration can be kept much shorter than 100 μs. However, this does lead to a very broad bandwidth of the pulse, which makes accurate slice selection difficult. Therefore, no slice selection is performed: the complete imaging volume is excited. This is called a 3D acquisition (contrary to 2D acquisitions with slice selection).

After the RF pulse, the energy stored in the RF coils must ring down to allow tuning of the receive coils. This also leads to a delay on the start of acquisition. If the coils are switched to receive mode too quickly while there is still too much energy in the coil, this may destroy the coil. Ring down of the energy only takes a few μs, but tuning of the coils can be more time consuming. With fast coils - which are generally the simplest in design - it is possible to be ready for acquisition within less than 100 μs from the end of the RF pulse.

Sampling of the FID signal starts from the moment the gradients are switched on. This means that signal is also sampled while the gradients are ramping up to their intended strength. This also provides a few μs of time gain. Using gradients in three dimensions, the k-space vector is moved radially outward from the center of k-space during sampling. Each radial line in k-space is called a spoke. By acquiring spokes with different directions,

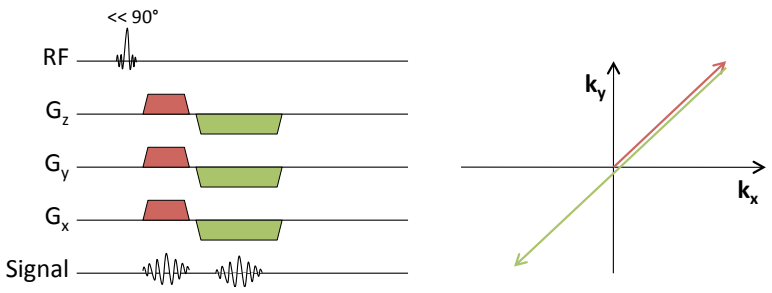

Figure 4.1: Schematic of a 3D UTE sequence (left), and the k-space trajectory in the k_x, k_y plane (right). The k_z direction is not shown for simplicity, but the sequence does acquire in 3 dimensions. The RF pulse is very short, with flip angle well below 90°. Acquisition of the FID starts as quickly as possible after the RF pulse. The gradients are used to traverse k-space from the center outward. The data is acquired on the red line. To acquire the gradient echo image, the gradients are inverted and data is acquired while traveling along the green line. Note that twice as much data is sampled for the gradient echo.

a spherical sampling pattern of k-space is obtained. As the sampling time is usually in the order of several hundred μs, this is the main limitation on the T_2 of tissues that can be visualized. Rahmer et al. have investigated in their paper that, in order to have an optimal signal-to-noise ratio (SNR) for tissues with a specific T_2, the following equation should be used to define the sampling time:

$$T_s = 0.69\ T_2 \tag{4.1}$$

where T_s is the sampling time and T_2 is the transverse relaxation time of the tissue that needs to be visualized. This shows that the sampling time is shorter than T_2, leading to a very short sampling time for short T_2 components. This requires high gradient strengths, and fast sampling. The latter inherently leads to a large bandwidth for the sampled data and more noise in the data.

The FID image will contain signal from short T_2 components, but also from long T_2 components. To provide contrast between short and long T_2 components, a second image is acquired using the UTE sequence. This is a normal gradient echo image, for which the echo time can be set. The

data for this image is also sampled radially, and each spoke is sampled after the sampling of the FID. The difference with the FID sampling is that the sampling of the gradient echo is done from the end of the spoke reached by FID sampling, over the origin of k-space, towards the other end of the spoke. This means that the double amount of data is sampled for the gradient echo image. This will lead to better image quality in the gradient echo image.

4.3 MRI properties of relevant tissues

UTE sequences have mainly been used in clinical practice to study tendons, ligaments, menisci, etc. However, for attenuation correction, we want to specifically visualize lung and cortical bone using a UTE sequence. As these tissues are generally considered to have even shorter T_2s than the tissues currently visualized with UTE sequences, it is uncertain if it is possible to acquire signal in lung and cortical bone using a UTE sequence. In this section, we therefore investigate the MRI properties of lung and cortical bone.

4.3.1 Lung

4.3.1.1 Origin of short T_2

The parenchyma of mammalian lungs is composed of millions of alveoli, which can be seen as small spheres of tissue filled with air (fig. 4.2). Although the tissue itself does not have an especially short T_2 ($\approx$ 35 ms), the complex structure of the lungs does lead to an apparent short T_2^*[225]. This is caused by susceptibility effects, which appear at the border between tissue and air. The magnetic susceptibility χ_ν of a material, e.g. a biological tissue, describes its response to an applied magnetic field. It defines the magnetization of the material when it is placed in an external magnetic field:

$$\vec{M} = \chi_\nu \vec{H} \tag{4.2}$$

where $\vec{M}$ is the magnetization of the material and $\vec{H}$ is the external magnetic field. The magnetization can be interpreted as the magnetic field that is produced by the material itself in response to an applied field. Diamagnetic materials will produce a magnetic field that is opposed to the external field ($\chi_\nu < 0$), whereas paramagnetic materials will produce a magnetic field

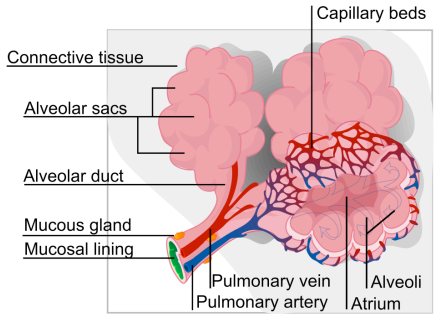

Figure 4.2: Schematic illustration of a lung alveolus. Reproduced from the Wikimedia Commons library (http://commons.wikimedia.org/wiki/File:Alveolus_ diagram.svg).

that has the same direction as the external magnetic field ($\chi_\nu < 0$). The total local magnetic field $\vec{B}$ is then given by the equation:

$$\vec{B} = \mu_0(\vec{H} + \vec{M}) = \mu_0(1 + \chi_\nu)\vec{H} \tag{4.3}$$

The interface between two materials with different susceptibilities, e.g. tissue and air, is therefore also an interface between two local magnetic field strengths. At this interface, there exists a small magnetic field gradient. This gradient will accelerate the dephasing of the spins at the interface, and lead to faster relaxation[230]. Susceptibility effects are larger if the applied field is larger, as the magnetization of the material is proportionate to the external magnetic field. As the lungs can be seen as a collection of many tissue/air interfaces, the susceptibility effects in the lungs have a very large effect on the apparent T_2^*[231].

Apart from the low T_2^* due to susceptibility effects, lung tissue also has a much lower proton density than other tissues, as a large fraction is occupied by air. The proton density in lung tissue has been shown to be approximately 20 % of the proton density of soft tissue[232]. This is also the reason for the lower density of lungs on CT and the lower attenuation coefficient of lungs. As a lower proton density means that less MRI signal is available, this adds an extra difficulty to the MRI imaging of lung tissue.

As the low signal in lung tissue is mainly a T_2^* effect, it should be possible to visualize lung tissue with UTE sequences. In fact, several authors have

demonstrated the feasibility of lung imaging with MRI. Lung imaging with UTE sequences has been shown[225], as well as imaging with normal gradient echo sequences[233, 232], as long as the echo time is kept low. We have investigated the UTE imaging properties of lung tissue below, to obtain insight into the optimal sequence settings.

4.3.1.2 Methods

The ideal method for determining the MRI properties of a material is by NMR relaxometry, as will be done in the next section for cortical bone. This requires a number of small samples of the material that needs to be investigated. For lung tissue, this would require performing relaxometry of small pieces of lung. However, a lung is kept open in the body by the negative pressure inside the chest cavity. When a lung is removed from the chest cavity, it collapses immediately under the normal atmospheric pressure. As a consequence, it is impossible to obtain a small sample of lung tissue in the same state as when inside the body. Hence, relaxometry of lung tissue is not possible. The MRI properties of lung tissue were therefore investigated by acquiring MRI images of healthy volunteers.

UTE-MRI images of 3 healthy volunteers were acquired on a Magnetom Trio 3T system (Siemens Healthcare, Erlangen, Germany), with a 3D radial UTE sequence comparable to the Philips sequence. Two images were obtained by this sequence: a FID at 0.08 ms and a gradient echo at 2.3 ms. To investigate the effect of resolution on the available MRI signal in the lungs, data was acquired at three different isotropic resolutions: 2 mm, 4 mm and 6 mm. The acquisition times were approximately 6 min, 2 min and 1 min. Coronal slices of one of the data sets are shown in fig. 4.3. For each volunteer five spherical volumes of interest (VOIs) with a diameter of 20 mm were drawn on the lungs. The volunteers stayed on the bed between different acquisitions. Therefore, we assume that all images of a volunteer were registered to each other and the same VOIs could be used for the 2 mm, 4 mm and 6 mm images. For each patient and resolution, the average amplitude over all 5 lung VOIs was calculated for the FID and gradient echo image and compared to each other. As MRI image intensity as such is not a quantitative measure, and there is no guarantee that the MRI receiver settings did not change between the different scans, the image intensities at different resolutions can not be compared directly. Therefore, all intensities were normalized to the noise level of the image. The noise level was calculated as the average intensity in five spherical VOIs drawn outside the body. The normalized intensity is then calculated as:

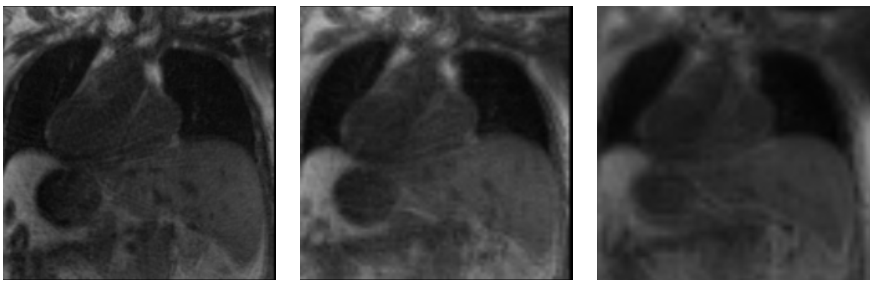

Figure 4.3: Coronal slice through the FID images of a healthy volunteer acquired at 2 mm (left), 4 mm (middle) and 6 mm (right) resolution.

$$I_{L,N} = \frac{I_L}{I_A} \tag{4.4}$$

where $I_{L,N}$ is the normalized amplitude in the lungs and I_L and I_A are the average image intensities measured in lungs and air respectively.

4.3.1.3 Results

Fig. 4.4 depicts the normalized signal amplitude in the lungs in the FID image for different resolutions. It shows that the relative amplitude in lung parenchyma is always higher than unity. This means that the UTE sequence enables the acquisition of a signal higher than the noise level from lung tissue. Fig. 4.4 also shows that the normalized amplitude is considerably higher in images acquired at 4 mm and 6 mm resolution than at 2 mm resolution. This is explained by the fact that SNR increases with voxel size[234]. Acquisition at a resolution of 4 mm or more should therefore be preferred, or longer acquisition times should be used to achieve a higher SNR.

The relation between image intensity in the FID and gradient echo images is depicted in fig. 4.5. For 2 mm resolution, the signal in both images is comparable. For a resolution of 4 mm, the gradient echo image shows considerably less signal than the FID image. With 6 mm resolution, the difference in signal intensity between the gradient echo image and the FID image is further increased. It is not entirely clear what the explanation is for this dependence of the lung signal in the gradient echo image on resolution. It could be explained using the theory of susceptibility effects described above. If images are acquired at a high resolution (e.g. 2 mm),

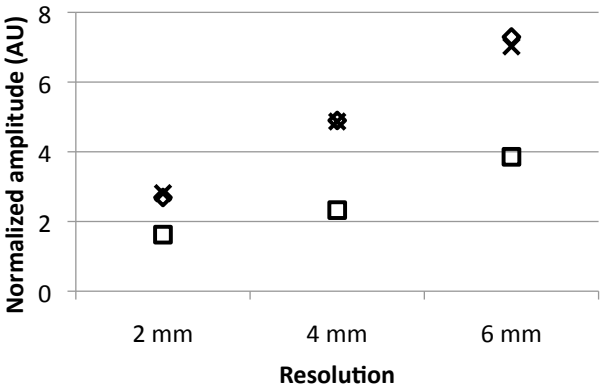

Figure 4.4: Normalized signal amplitude in the lungs in the FID image acquired with a UTE sequence for three volunteers and three different resolutions. The different symbols represent three different volunteers.

there are much less tissue/air interfaces per voxel than at low resolution (e.g. 6 mm). Therefore, the susceptibility effects within the same voxel are much lower at a higher resolution. This could lead to a longer apparent T_2^* when imaging at a higher resolution. However, as the alveoli in human lungs have average diameters of approximately 150 μm[235], there are already over 1000 alveoli in a single 2 x 2 x 2 mm voxel. It seems unlikely that an increase of this number will still lead to larger effects.

These results show that, at high resolution, the imaging of lung tissue with normal gradient echo sequences is therefore possible. However, the SNR in images acquired at a high resolution is relatively low. This could be solved by acquiring for a longer time, but this should be avoided as the imaging time used to derive the attenuation map should be limited to allow enough time for other MRI acquisitions. Therefore, these results indicate that acquisition of UTE images at a resolution of 4 mm would be the best option to visualize lung tissue.

4.3.2 Cortical bone

4.3.2.1 Origin of short T_2

Cortical bone has a short T_2 because of the highly organized matrix it consists of. Cortical bone has three main components: hydroxyapatite, collagen and water. Hydroxyapatite is a mineral form of calcium, with chemical for-

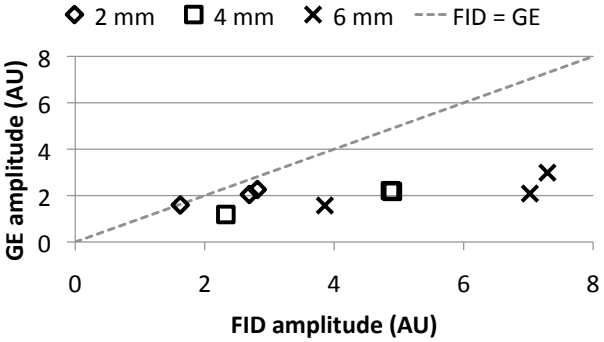

Figure 4.5: Relative image intensity acquired with a UTE sequence in lung tissue for three volunteers and three different resolutions. The image intensity in the FID image (acquired at 0.08 ms) is compared to the image intensity in the gradient echo image (acquired at 2.3 ms).

mula $Ca_5(PO_4)_3(OH)$. It is organized in a hexagonal crystal system, and constitutes approximately 50 % of cortical bone. Therefore, it is also called bone mineral. The calcium atoms in hydroxyapatite are the cause of the high density of cortical bone.

Collagen is a structural protein and forms the main component of mammalian connective tissue. There are different types of collagen, and up to now 24 different collagen genes have been identified. In cortical bone, collagen I is predominant and accounts for 30 % of the tissue. Collagen macromolecules are made up of smaller collagen molecules, which are all formed by three polypeptide strands wound around each other to produce a triple helix (fig. 4.6). Assembly of the macromolecules leads to a structural matrix, which is then mineralized with hydroxyapatite. The third component of cortical bone, water, is located throughout the collagen matrix as water molecules bound more or less closely to the collagen.

The protons in hydroxyapatite and collagen have extremely short T_2s, due to their immobility and the strong dipolar interactions between atoms in such organized structures. They can therefore most likely not be visualized with MRI[224]. However, the protons in the water molecules that are distributed throughout the collagen matrix will have longer T_2s. Due to the presence of the collagen matrix they are also relatively immobile. Hence, the T_2 of these protons will still be much shorter than the T_2 of protons in free water[236]. Nevertheless, it may be possible to visualize these protons using UTE sequences. As only 20 % of cortical bone consists of water, the proton

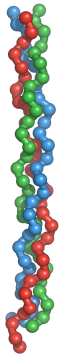

Figure 4.6: A collagen molecule is a triple helix of three polypeptide strands. Reproduced from the Wikimedia Commons library under the Creative Commons - Share Alike license (http://commons.wikimedia.org/wiki/File:Collagen triplehelix.png).

density of cortical bone is also much lower than that of soft tissue. This may also cause problems for visualization.

4.3.2.2 Methods

To investigate the MRI properties of cortical bone relaxometry measurements were performed on samples of bovine cortical bone. 5 samples were taken from the shaft of a bovine femur bone obtained from a local slaughterhouse. The bovine femur bone was chosen because it has a very thick cortical shell so that large sample sizes could be obtained. The samples are shown in fig. 4.7. The samples were analyzed with a Bruker 0.5 T relaxometer (Minispec mq20, Bruker Optics, Ettlingen, Germany). The proton density was quantified as a value relative to the proton density of water. The signal amplitude 170 μs after RF excitation of different volumes of water was measured. Subsequently the signal amplitude of the bone samples was measured with the same receiver gain settings. The volume of the samples was derived from a micro-CT scan.

The T_2 relaxation time of each sample was measured with an in-house developed multi spin-echo sequence with Carr-Purcell-Meiboom-Gill phase alternation[237]. With this sequence 50 consecutive echoes are acquired after excitation with a 90° RF pulse, yielding 50 data points on the transverse relaxation curve. By fitting an exponential decay function ($exp(-\frac{t}{T_2})$) to the acquired data points, the sample averaged transverse relaxation time T_2 is

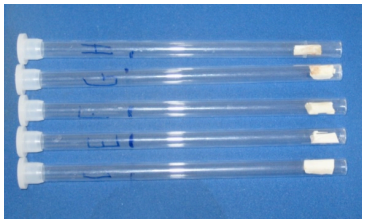

Figure 4.7: 5 cortical bone samples, taken from a bovine femur bone and used to evaluate the MRI properties of cortical bone.

determined. The inter-echo time spacing was 170 μs.

4.3.2.3 Results

Fig. 4.8 shows measured signal amplitude versus volume of the cortical bone samples and 5 samples of distilled water. Linear regression was performed on both sets, yielding approximate expressions for the signal intensity I as a function of the sample volume V:

$$I_{water} \approx 0.175\ V_{water} \tag{4.5}$$

$$I_{bone} \approx 0.051\ V_{bone} \tag{4.6}$$

A unit volume of cortical bone will thus provide approximately 29% (=

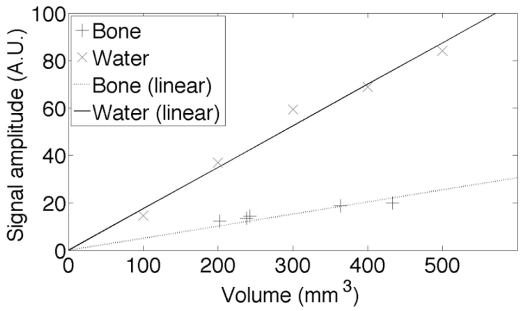

Figure 4.8: Measured signal amplitude versus volume of 5 samples of bovine cortical bone and 5 samples of distilled water. A linear fit on both data sets is also shown.

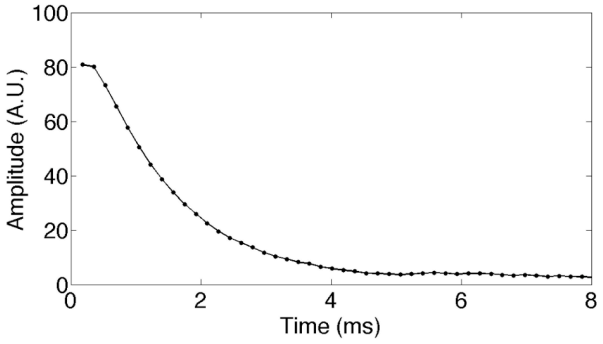

Figure 4.9: Transverse relaxation curve of one of the bovine cortical bone samples.

$\frac{0.051}{0.175}$) of the signal intensity of a unit volume of water. The signal intensity in cortical bone is significantly lower than in water, but it should still be detectable.

A T_2 relaxation curve of one of the samples is shown in fig. 4.9. The T_2 values measured in the samples were in the range of $1.37 - 1.70$ *ms*, with an average over 5 samples of 1.51 *ms*. This is much shorter than soft tissue, but with current UTE sequences echo times below 0.1 ms can easily be reached. These results therefore indicate that the visualization of cortical bone with UTE sequences should be possible.

4.4 Proposed method

In the previous sections of this chapter, we have introduced UTE sequences and shown that it is feasible to visualize lung tissue and cortical bone with those sequences. The question is now how an attenuation map can be derived from the images acquired with a UTE sequence. In this section, a method to achieve this is introduced. In the next chapters, the method for deriving the attenuation map will be slightly modified for each specific study. For example, the method will be different for human brain studies than for rat whole-body studies. Therefore, only the basic features that all investigations in the next chapters have in common are introduced here.

The different steps that have led to the development of our method are described and illustrated using UTE images of a segment of bovine femur bone. A segment of bovine femur bone was chosen because it has a very

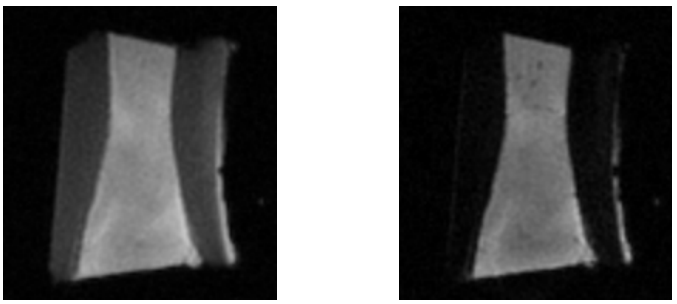

Figure 4.10: Slice through the FID (left) and gradient echo (right) image of the bovine femur bone.

thick cortical shell, which limits interference of partial volume effects. The center of the bone was yellow bone marrow, which is spongeous bone with a very low bone content, and hence comparable to soft tissue. As no lung tissue was present in the bone segment, the method is not evaluated on lung tissue in this section. However, the method presented here can be easily extended to segmentation of lung tissue, as is described in the next chapter.

The segment of bovine femur bone was obtained from a local slaughterhouse. It was approximately 8 cm long with a diameter of 5 cm and a cortical shell with 1 cm thickness. UTE-MRI images were acquired on a Philips Achieva 3T system (Philips Medical Systems, Best, The Netherlands), using the UTE sequence described in section 4.2.3. A standard head coil was used, and the echo times for the FID and gradient echo images were 0.09 ms and 1.7 ms respectively. T_R was 4.8 ms and the total acquisition time was approximately 4 minutes. The resolution was 1 mm in a reconstructed matrix of 152 x 152 x 152. As CT is currently the best method to discriminate tissue density, the images were compared to a CT of the same segment of bone. The CT was acquired on a Philips Gemini PET-CT system (Philips Medical Systems, Cleveland, USA). The standard protocol used for CT-based attenuation correction was used: 50 mAs, 120 kVp. The CT data set was coregistered to the MRI data set using rigid mutual-information based registration and resampled to the same matrix as the MRI. A slice through the FID and gradient echo is shown in fig. 4.10. The same slice through the CT and segmented CT based attenuation map is depicted in fig. 4.11.

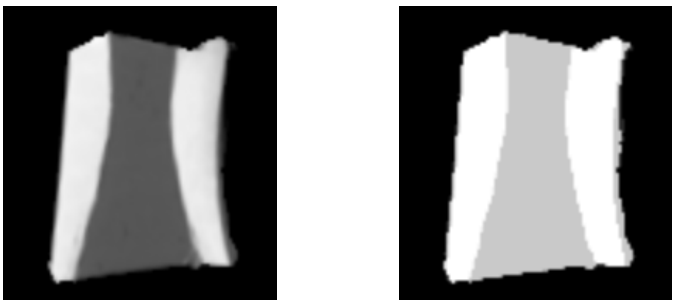

Figure 4.11: Slice through the CT (left) and segmented CT based attenuation map (right) of the bovine femur bone.

4.4.1 Image intensity-based segmentation

The simplest method for segmenting the UTE images into air, soft tissue and cortical bone is by segmentation using a combination of thresholds on the FID and gradient echo images. Due to the T_2s of cortical bone and soft tissue, cortical bone will have a medium to high image intensity in the FID image and a low image intensity on the gradient echo image, whereas soft tissue will have a high signal on both images. Therefore, segmentation can be done using table 4.1:

		Gradient echo	
		Low	High
FID	Low	**Air**	(Impossible)
	High	**Cortical bone**	**Soft tissue**

Table 4.1: Segmentation matrix for segmentation based on image intensities of the FID and gradient echo images.

Fig. 4.12 shows the result of segmentation based on the image intensities in the FID and gradient echo images. The resemblance with the segmented CT based attenuation map in fig. 4.11 is very good.

4.4.2 Derivation of the R_2-map

Although segmentation based on image intensities is possible, as shown above, this is not a very practical method in MRI. The reason for this is that the image intensities in MRI are not a quantitative measure, and can vary

Figure 4.12: Slice through the attenuation map derived from the FID and gradient echo images using thresholding on the image intensities.

greatly between different acquisitions. This is mainly caused by changes in the receiver gain settings, which are automatically adapted to the water content of the object in the scanner. As the user has no control over these settings, this means that for image intensity based segmentation, the thresholds would have to be set for each acquisition separately. This could be done manually or automatically based on the histograms. However, another problem with image intensity based segmentation is that inhomogeneities in the images could lead to segmentation errors. This can not be solved by adapting the thresholds for each acquisition. Therefore, it would be better to use a quantitative parameter as a base for segmentation.

In this work we propose the use of the quantitative parameter R_2, the transverse relaxation rate. It is the inverse of the transverse relaxation time T_2. Recall the transverse relaxation equation, described in section 2.3.2.6:

$$\vec{M}_{tr}(t) = \vec{M}_{tr} e^{\frac{-t}{T_2}} \tag{4.7}$$

Suppose two images are acquired at T_{E1} and T_{E2} with the same receiver gain settings, then the transverse magnetization vector in each of these images is defined by the T_2 of the tissue and the echo times:

$$\vec{M}_{tr}(T_{E1}) = \vec{M}_{tr} e^{\frac{-T_{E1}}{T_2}} \tag{4.8}$$

$$\vec{M}_{tr}(T_{E2}) = \vec{M}_{tr} e^{\frac{-T_{E2}}{T_2}} \tag{4.9}$$

If the MRI signal only depends on T_2 relaxation, which can be assumed for short echo times, the image intensity in a voxel will be proportional to the transverse magnetization defined in this equation. An image which represents the transverse relaxation rate, called the R_2-map, can then be derived from both images by a voxel-by-voxel calculation:

$$R_2 = \frac{\ln(I_1) - \ln(I_2)}{T_{E2} - T_{E1}} \tag{4.10}$$

where I_1 and I_2 are the image intensities in both images. As the FID and gradient echo images obtained from the UTE sequence are acquired with the same receiver gain settings, we can derive the R_2-map from those images. The first image is then the FID image and the second image is the gradient echo image.

R_2 does not depend on receiver gain, and should not be affected by image inhomogeneity. It can therefore be used as a quantitative parameter for segmentation. In the R_2-map, we expect tissues with a long T_2 to have a low value and tissues with a short T_2 to have a high value. This means that cortical bone will have a higher value than soft tissue in the R_2-map.

Fig 4.13 shows the R_2-map obtained from the segment of bovine femur bone, showing high intensity in cortical bone and low intensity in soft tissue. However, voxels outside the piece of bone, which contain air, exhibit low as well as high R_2 values. The joint histogram of the R_2-map and the CT image is shown in fig. 4.14. This shows that, although cortical bone and soft tissue can be perfectly separated, air voxels can not be discriminated from cortical bone or soft tissue based on R_2 alone. This is explained by the logarithms used in the definition of R_2 in eq. 4.10 and the low quality of the FID image. The numerator of eq. 4.10 is equal to:

$$\ln I_1 - \ln I_2 = \ln \frac{I_1}{I_2} \tag{4.11}$$

when the denominator of the argument of the logarithm is small, a small absolute change in the value of the numerator will have a large effect. This is the case in voxels containing air, where the image intensity is very low in the gradient echo image. However, due to its lower quality the FID image contains more noise. Therefore, there will be a larger variation in I_1 than in

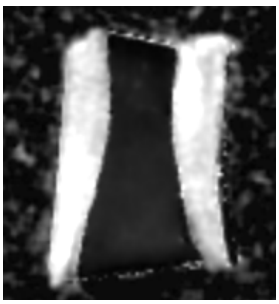

Figure 4.13: Slice through the uncorrected R_2-map of the bovine femur bone.

I_2. This leads to a large variation in R_2 for voxels containing air, as shown in fig. 4.14. This causes problems for segmentation, as voxels containing air could be segmented as soft tissue or cortical bone. In the next paragraph, a solution to this problem will be proposed.

4.4.3 Air mask

To allow direct segmentation from the R_2-map into air, soft tissue and cortical bone, a step is needed in which R_2 in voxels containing air is corrected. This would allow perfect separation of these tissue types. In our method,

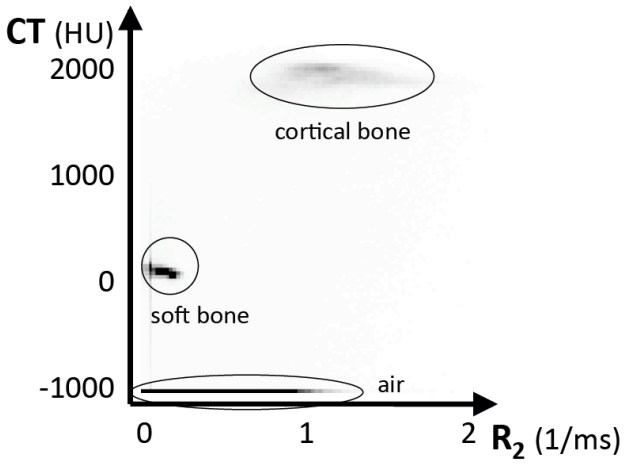

Figure 4.14: Joint histogram of the uncorrected R_2-map and the CT of the bovine femur bone.

Figure 4.15: Slice through the corrected R_2-map (left) and attenuation map derived from the corrected R_2-map (right) of the bovine femur bone.

this is done by multiplying the R_2-map with a binary mask, in which all voxels containing air are set to zero and all other voxels are set to 1. As there is almost no contrast between air and cortical bone in the gradient echo image, this mask can only be derived from the FID image.

The mask is derived in two steps. First a region-growing approach is used to determine the outer contour of the patient (or phantom). Eight seeds are used, placed at the outer corners of the image. Starting from these seeds all neighboring voxels which have an intensity below a certain value (outer threshold intensity, $I_{th,o}$) are set to 0. Next all voxels which have an intensity below a different threshold (inner threshold intensity, $I_{th,i}$) but are not necessarily connected to the region that was grown in the first step are also set to 0. All remaining voxels are set to 1. The mask is derived in two steps because the high intensity of the border of the patient, mainly caused by fat in the skin, allows for a higher threshold outside than inside the patient.

Fig. 4.15 shows the corrected R_2-map and fig. 4.16 shows the joint histogram of the corrected R_2-map and the CT. As all air voxels are set to zero in the R_2-map, perfect separation of air, soft tissue and cortical bone is now possible based solely on the corrected R_2-map. The derivation of the attenuation map from the corrected R_2-map can now be done using a simple mapping:

$$\begin{array}{lcll} \mu(R_2) & = & 0\ cm^{-1} & R_2 = 0\ ms^{-1} \quad \text{(air)} \\ & = & 0.097\ cm^{-1} & 0\ ms^{-1} < R_2 < 0.5\ ms^{-1} \quad \text{(soft tissue)} \\ & = & 0.13\ cm^{-1} & R_2 \geq 0.5\ ms^{-1} \quad \text{(bone)} \end{array}$$

The threshold value 0.5 ms was obtained from the measurement of the

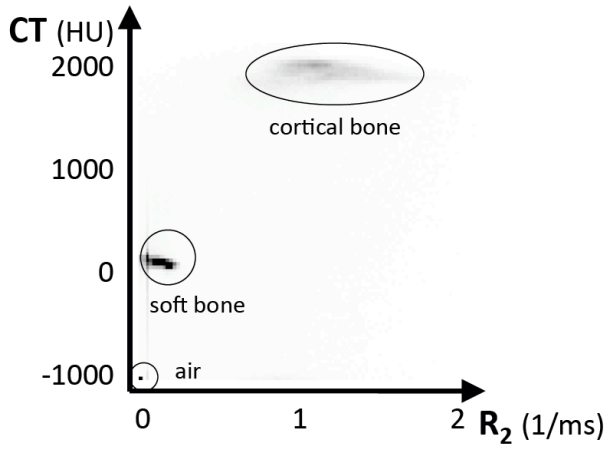

Figure 4.16: Joint histogram of the corrected R_2-map and the CT of the bovine femur bone.

T_2 of cortical bone, described above. Fig. 4.15 shows the segmented attenuation map derived from the corrected R_2-map. It resembles the CT-based attenuation map in fig. 4.11 very well.

4.5 Conclusion

In this chapter, UTE sequences were introduced as a possibility to visualize lung and cortical bone using MRI. The feasibility of acquiring measurable signal was evaluated for lung and cortical bone separately. For lung, the results indicate that lung tissue is best imaged using a UTE sequence with moderate resolution ($\approx$ 4 mm). The proton density and T_2 of cortical bone was investigated using relaxometry. Although the proton density of cortical bone is significantly lower and its T_2 much shorter than most tissues, visualization using UTE sequences should be possible.

In the last section of this chapter, a method was proposed which allows the discrimination of air, soft tissue and cortical bone based on images acquired with a UTE sequence. As image intensities can vary between different MRI studies, the quantitative parameter R_2 was used for segmentation. The R_2-map, which is derived from the FID and gradient echo images, needs to be corrected to set all voxels containing air to zero. From this corrected R_2-map, an attenuation map can be derived using a simple mapping. This basic method will be modified in the next chapters to allow the derivation of

attenuation maps in different situations. For example, it will be modified to discriminate lung as well for studies where lung tissue is present in the field of view.

4.6 Original contributions

The evaluation of the MRI properties of cortical bone was presented at the IEEE NSS/MIC conference in 2008[238] and was also included in a A1 journal paper[239]. The UTE-MRI-based method using the corrected R_2-map was first presented at the ISMRM conference in 2009[240]. A patent application was also submitted for that method[241].

Chapter 5

Phantom experiments

5.1 Introduction

In the previous chapter a method was proposed to derive the attenuation map from MRI images acquired with a UTE sequence. The feasibility of generating contrast between air and bone was shown using a very simple object, i.e. part of bovine femur bone. However, the method is intended to be used to derive the attenuation map for animals and humans, which are far more complex structures. Therefore, the question can be posed if the method will also work on more realistic objects. Before testing our method on real animal (chapter 6) and real human (chapter 7) data, it is tested on different phantoms in this chapter.

In medical imaging, phantoms are often used to evaluate the performance of scanners. There are a number of advantages to using phantoms instead of real patients for this. Most importantly, phantom experiments are reproducible. This allows comparing different scanners or different scanner settings while imaging exactly the same object. Second, phantoms themselves can also be reproduced. This enables the possibility of using comparable phantoms in different locations, allowing comparison of results obtained by different groups. Third, phantoms are rigid structures. This allows easy coregistration, contrary to patient imaging where small registration errors are unavoidable. Phantom experiments are also simple to organize and perform. Finally, there is also the advantage that the radiation dose delivered to the phantom is of no concern. When imaging with modalities that use ionizing radiation, such as CT, PET or SPECT, this means that phantom experiments can be repeated as much as needed.

Phantoms can consist of mathematical shapes, such as cylinders and

Figure 5.1: The Alderson phantom, a good example of an antropomorphic phantom used in PET, SPECT and CT.

spheres. These phantoms are mostly used to evaluate image quality properties, such as contrast, noise, uniformity, etc. In emission tomography, the Jaszczak phantom is used very often. More realistic phantoms can also be made, which are intended to resemble the human or animal body. The Alderson phantom, depicted in fig. 5.1, is a good example. It can be used for CT, PET and SPECT. As it is shaped like the human body, it is called an antropomorphic phantom. Such an antropomorphic phantom allows a more realistic evaluation of how the scanner will perform in a real imaging situation.

Phantoms are usually constructed of synthetic material, such as different kinds of plastics, and filled with water to resemble the human body. For CT, PET and SPECT, other structures such as bone or lung can be mimicked by inserting materials with different densities into the phantom. In an MRI phantom, different tissues or pathological processes can be simulated by doping water with specific compounds that change the relaxation properties[242]. However, as far as we know, there are currently no materials that mimic the behavior of protons in tissues with special relaxation properties, such as lung and cortical bone. Rubber has a short T_2 and can be used to evaluate the performance of UTE sequences[229]. The origin of the short T_2 of rubber lies in its molecular structure, and the mechanism is therefore comparable to the fast relaxation of cortical bone. However, the specific relaxation behavior of protons in the lung, mostly due to the inhomogeneous structure of the lung, can not be modeled with rubber. As cortical bone

and lung are two important tissues in attenuation correction, this poses a problem for our investigation. Also, there is the added difficulty that we are working in a multi-modal setting, and a phantom therefore needs to appear realistic on MRI, CT and PET or SPECT. There are currently no phantoms available that are realistic on all modalities. There are even no materials available that mimic cortical bone or lung realistically.

Therefore, we have designed different multimodality phantoms to evaluate our method. Due to the lack of realistic synthetic materials, biological materials were used in these phantoms. First, the head of a pig is used as a phantom for human brain imaging. Afterwards a human thorax phantom is presented. For both phantoms, the description of the design of the phantom is followed by the evaluation of the performance of our method on the phantom.

5.2 Human brain imaging: pig head phantom

5.2.1 Materials and methods

5.2.1.1 Phantom construction

The human head contains mostly soft tissue, but also bone structures (skull, facial bones) and air cavities (sinuses, nasal cavity). A realistic phantom for human brain imaging should therefore contain air, soft tissue and bone. The head of a pig was chosen for this, as it contains all three tissue types and has a complexity that is roughly comparable to that of the human head. It is also rigid, as is the human head. The pig head was obtained from a local slaughterhouse, and stored in the freezer in between acquisitions to prevent decomposition. As freezing can alter MRI signal, it was always defrosted before a MRI acquisition. A sagittal slice of a MRI image of the pig head is shown in fig. 5.2 to illustrate its structure. As the pig head is completely filled with tissue, no activity can be added to the phantom. For this reason, no PET or SPECT images were acquired but only CT and MRI images.

5.2.1.2 CT and MRI acquisitions

MRI acquisitions were done on an Achieva 3T system (Philips Medical Systems, Best, The Netherlands). The UTE sequence described in section 4.2.3 was used. A combination of Philips Flex coils was used to achieve a field-of-view large enough to cover the entire phantom. The flex coils are very simple coils, which allow very fast switching to receive mode, and hence

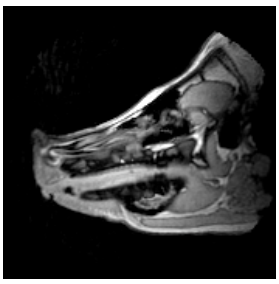

Figure 5.2: Sagittal slice of a gradient echo MRI image of the pig head phantom.

yield a very short echo time for the FID. For the FID, the shortest possible echo time was used (0.072 ms). The echo time for the gradient echo was 1.747 ms. The repetition time was chosen as short as possible ($T_R = 4$ ms) to reduce total image acquisition time. The images were reconstructed to a 176 x 176 x 176 voxel matrix with 1.875 mm isotropic voxel dimension. This resulted in a field of view covering a sphere with 165 mm radius. CLEAR (Constant LEvel AppeaRance) coil sensitivity correction was used to correct for the highly non-uniform sensitivity of the Flex coils. The total imaging time was approximately 3.5 minutes.

A CT scan of the pighead phantom was acquired on a Philips Gemini TF PET-CT scanner (Philips Medical Systems, Cleveland, USA) using the following parameters: 120 kVp, 200 mAs and 1.5 mm slice thickness. The in-plane resolution was 1.17 mm. The size of the reconstructed matrix was 512 x 512 x 264 voxels.

5.2.1.3 Derivation of attenuation maps

Before the attenuation maps were derived from the CT and MRI images, the CT images were registered to the MRI images. This was done using rigid 3D registration based on an optimization of the mutual information metric, as implemented in the Insight Toolkit[243]. The CT images were then resampled to the matrix of the MRI images. Two attenuation maps were derived: CT-based and UTE-MRI-based. As no activity can be injected into the phantom, the performance of the algorithm can only be evaluated by assessing the ability of the algorithm to discriminate air, soft tissue and bone. Therefore, segmented attenuation maps were used. The segmented CT-based attenuation map was obtained by mapping CT Hounsfield units (HU) to linear attenuation coefficients at 511 keV:

$$\begin{array}{lll} \mu\,(cm^{-1}) = 0 & HU \leq -800 & \text{(air)} \\ = 0.097 & -800 < HU \leq 200 & \text{(soft tissue)} \\ = 0.13 & HU > 200 & \text{(bone)} \end{array} \tag{5.1}$$

For the UTE-MRI-based attenuation map, the corrected R_2-map was first derived using the algorithm described in section 4.4. The attenuation map was then derived from the corrected R_2-map by mapping R_2 to linear attenuation coefficients:

$$\begin{array}{lll} \mu\,(cm^{-1}) = 0 & R_2 = 0 & \text{(air)} \\ = 0.097 & 0 < R_2 \leq 0.5 & \text{(soft tissue)} \\ = 0.13 & R_2 > 0.5 & \text{(bone)} \end{array} \tag{5.2}$$

This yields an attenuation map in which air, soft tissue and bone are discriminated.

5.2.1.4 Analysis

The accuracy of the UTE-MRI-based attenuation map was evaluated by performing a voxel-by-voxel comparison to the segmented CT-based attenuation map. For each tissue class on the CT-based attenuation map, the percentage of voxels that was assigned to the correct and incorrect tissue classes was calculated. A region of interest was chosen inside the head to avoid deterioration of the results by the oversegmentation of skin, as explained below.

5.2.2 Results

Transverse slices of the FID and gradient echo image are shown in fig. 5.3. In areas of cortical bone (the jawbone is indicated) the signal intensity is medium to high in the first echo image and much lower in the second echo image. Soft tissue has a medium to high signal content in both images, whereas air has a low signal intensity in both images. These observations agree with the expectations. The quality of the first echo image is not very good, showing a lot of artefacts. The reasons for this are described in chapter 4. The uncorrected R_2-map is shown in fig. 5.4A. The high R_2 value of cortical bone is clear, but cavities containing air also show voxels

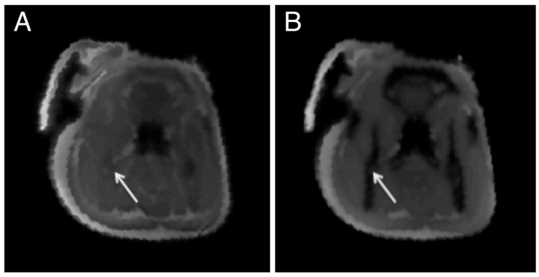

Figure 5.3: Transverse slice of the FID (A) and gradient echo (B) image of the pig head phantom.

with a high R_2. The corrected R_2-map shown in fig. 5.4B shows distinctive intensity values in bone, soft tissue and air regions.

The same transverse slice of the segmented UTE-MRI is shown in fig. 5.5A together with the segmented CT (fig. 5.5B). The results of the quantitative evaluation of the classification accuracy of our method are depicted in fig. 5.6. A large majority of the voxels is assigned to the correct tissue class: 89 % for bone, 91 % for soft tissue and 82 % for air. The discrimination between tissue (either soft or bone) and air is correct in 97 % of the voxels.

5.2.3 Discussion

In the UTE-MRI-based attenuation map it is clear that major bone structures such as the jawbones are correctly segmented. The air cavity in the middle is also detected. Some segmentation errors are visible, mainly an overdetection

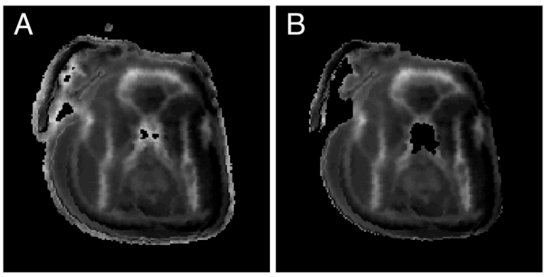

Figure 5.4: Transverse slice of the uncorrected (A) and corrected (B) R_2-map of the pig head phantom.

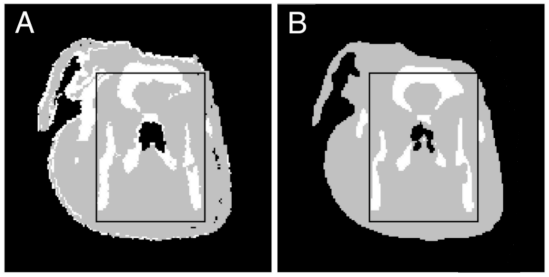

Figure 5.5: Transverse slice of the segmented UTE-MRI-based (A) and segmented CT-based (B) attenuation map of the pig head phantom. Air is depicted in black, soft tissue in grey and bone in white.

of bone in the central part of the phantom and in the skin. The latter is possibly in part related to the high collagen content and thick constitution of porcine skin. Collagen is also present in cortical bone and is in part responsible for the short T_2 of cortical bone. Although the human skin also contains a lot of collagen, it is thinner so it is expected not to cause the same amount of error. This will also be shown in the clinical brain images in chapter 7.

The quantitative results show that our method is quite accurate in dis-

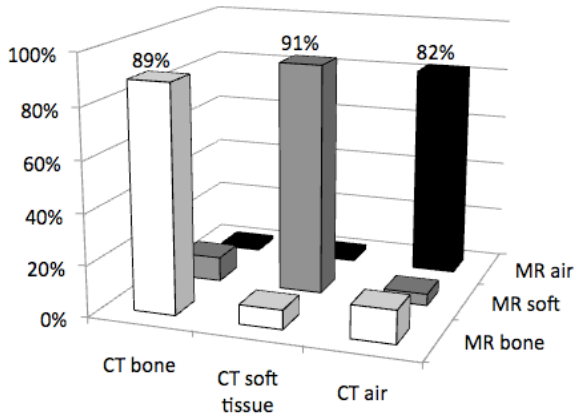

Figure 5.6: Results of the voxel-by-voxel comparison of the segmented UTE-MRI and segmented CT.

criminating air, soft tissue and bone. The tissue/air discrimination is very accurate, which is most important. As was shown in the simulation study in chapter 3, a segmentation algorithm should be designed so that bone is more likely to be misclassified as soft tissue rather than as air. This is clearly the case with our algorithm. As no PET images are available it is not possible to say what the effect of these errors on the reconstructed PET images would be. However, with an overall segmentation accuracy of around 90 % for bone and soft tissue and around 80 % for air, the results from the simulation study indicate that it should be possible to obtain quantitatively accurate images.

5.3 Human thorax phantom

5.3.1 Materials and methods

5.3.1.1 Phantom construction

The human thorax contains air, lung, soft tissue, spongeous bone and cortical bone. Hence, a good thorax phantom should contain these tissue types. Water is a good equivalent for soft tissue on PET, CT and MRI. For lung and bone, it is more difficult to find a simple equivalent. Therefore, biological tissue was used. To allow evaluation of the effect of attenuation on the reconstructed PET or SPECT images, a fillable phantom is needed.

For the lung part of the phantom, a lobe of a pig lung was used. It was obtained from an adult female pig sacrificed after a cardiac surgery experiment. As the lung was maintained open inside the body by the negative pressure within the chest cavity, it collapsed once it was exposed to normal atmospheric air pressure. Therefore it had to be reinflated mechanically. A cannula was inserted into the main bronchus of the lobe and fixed air-tight. The lung was inflated using a positive pressure ventilator available in the lab (fig. 5.7). Once the lung was inflated the cannula was sealed air-tight and the lung was submersed in 4 % formaldehyde solution for 48 hours to allow fixation. This is necessary to allow long-term storage of biological tissue.

For the bone part of the phantom, only cortical bone was modeled. Spongeous bone was not taken into account, as it is usually visible on conventional MRI sequences and hence it is not needed to evaluate the accuracy of our method. A section of a bovine femur bone was used, comparable to the one used in the previous chapter. A bovine femur bone was obtained from a local slaughterhouse. A piece from the middle of the shaft was cut out. The bone

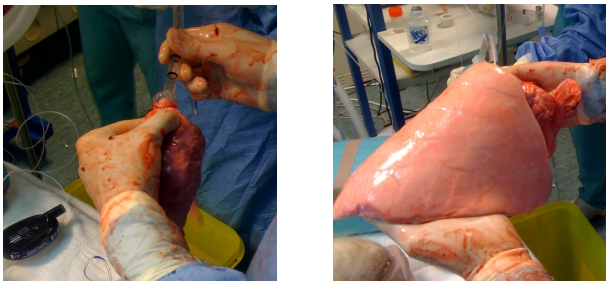

Figure 5.7: The collapsed (left) and reinflated (right) lobe of pig lung.

has a thick cortical layer ($\approx$ 10 mm) and a center filled with yellow bone marrow, which can be considered adipose tissue. The marrow was removed from the cylinder as it is not relevant for this experiment. This yielded a piece of cortical bone approximately cylindrically shaped with inner radius $\approx$ 10 mm, outer radius $\approx$ 20 mm and height $\approx$ 80 mm. The cylindrical shape of the bone allows it to be used as a rough model for the spine, which is the most important bone in thoracic imaging. It was also stored in 4 % formaldehyde solution.

The container of a Jacszak phantom was used as a base for the phantom. This is a PMMA cylinder with height 200 mm and diameter 220 mm. 4 CT-MRI markers were attached to the surface of the cylinder to allow coregistration between CT and MRI. The bone was screwed to the floor of the cylinder with a plastic screw. The lung was fixed to three plastic rods inserted in the floor of the cylinder using suture wire. Two hot spheres with 10 mm radius were filled with ^{18}F-FDG and inserted. A cold sphere was also inserted. The phantom was then filled with water containing a lower activity concentration of ^{18}F-FDG. The ratio of the activity concentration in the hot spheres to the background was 8:1. The total activity inside the phantom was approximately 2 mCi. There was no activity in the lung. Fig. 5.8 shows a picture of the assembled phantom, before it was filled. The color of the lung has changed from pink in fig. 5.7 to grey-brown in fig. 5.8. This is due to the fixation with formaldehyde.

5.3.1.2 Acquisitions

CT, PET and MRI images of the phantom were obtained. First a standard low-dose CT (50 mAs, 120 kVp), usually used to derive the attenuation map in clinical studies, was acquired on a Gemini TF system (Philips Medical Sys-

Figure 5.8: The assembled thorax phantom, containing a segment of bovine cortical bone and a lobe of pig lung.

tems, Cleveland, USA). The slice thickness was 5 mm with 1.18 mm in-plane resolution. The reconstructed matrix was 512 x 512 x 36. Subsequently, a PET was acquired on the same system. The acquisition time for the PET was 5 minutes.

The phantom was then moved to the MRI facility. A UTE-MRI scan was acquired on a Siemens Magnetom 3T system (Siemens, Erlangen, Germany). The UTE sequence was comparable to the one described in section 4.2.3. FID and gradient echo times were 0.08 ms and 3.2 ms respectively. The images were reconstructed to a 122 x 122 x 32 matrix with 4 mm isotropic voxel size. The MRI acquisition time was approximately 2 minutes.

5.3.1.3 Derivation of attenuation maps

UTE-MRI images were coregistered to the CT images with AMIDE by using the 4 CT-MRI markers as fiducial markers[244]. As the PET and CT images were acquired on the same bed, the UTE-MRI images are automatically coregistered to the PET images. CT-based and UTE-MRI-based attenuation maps were derived. The CT-based attenuation map was derived using bilinear scaling of CT Hounsfield units to linear attenuation coefficients at 511 keV, as is the gold standard in human whole-body imaging[198]:

$$\begin{aligned} \mu\,(cm^{-1}) &= 0.097\,\tfrac{HU+1000}{1000} && HU \leq 0 \\ &= 0.097 + 0.057\,\tfrac{HU}{1000} && HU > 0 \end{aligned} \tag{5.3}$$

The derivation of the UTE-MRI-based attenuation map can be done using a method comparable to the one presented in the previous section, modified to discriminate lung tissue as well. This can be done based on the R_2 as well. First the corrected R_2-map is derived as described in section 4.4. Then, a mapping from R_2 to μ is performed:

$$\begin{array}{lll} \mu\,(cm^{-1}) = 0 & R_2 = 0 & \text{(air)} \\ = 0.097 & 0 < R_2 \leq 0.5 & \text{(soft tissue)} \\ = 0.03 & 0.5 < R_2 \leq 0.9 & \text{(lung)} \\ = 0.13 & R_2 > 0.9 & \text{(bone)} \end{array} \tag{5.4}$$

This yields an attenuation map which discriminates air, lung, soft tissue and bone.

5.3.1.4 PET reconstruction

The PET images were reconstructed with the CT-based and UTE-MRI-based attenuation map. This was done using the ML-EM algorithm and based on the raw PET data obtained directly from the scanner. Apart from attenuation correction, geometric sensitivity correction was performed using the same method as described in section 3.4. Scatter correction was not implemented as the phantom was relatively small. Random coincidences were not corrected as the total activity in the phantom was low so the random fraction should be limited.

5.3.1.5 Analysis

A spherical volume of interest (VOI) with 10 mm radius was drawn in the lung and in the bone. The average values inside these VOIs on the CT and the R_2-map were calculated to verify if the materials in the phantom have realistic values on both modalities. To evaluate the quantitative accuracy of the PET images reconstructed with the UTE-MRI-based attenuation map, 3 VOIs with 10 mm radius were drawn over the hot and cold spheres. The total activities in the spheres with UTE-MRI-based attenuation correction were compared to the total activities in the spheres with CT-based attenuation correction.

5.3.2 Results

A sagittal slice of the CT image is shown in fig. 5.9. The same slice of the FID and gradient echo images is depicted in fig. 5.10. The density of the

Figure 5.9: A sagittal slice of the CT image of the thorax phantom.

lung and bone on the CT image is comparable to what is seen in clinical data sets. The average values of lung and bone were -630 HU and 1300 HU respectively. The corrected and uncorrected R_2-maps are shown in fig. 5.11. The average R_2 value of lung and bone was 0.70 ms^{-1} and 1.05 ms^{-1} respectively.

Fig. 5.12 shows the attenuation maps used for PET reconstruction. A transverse slice through both reconstructed PET images at the location of the spheres is shown in fig. 5.13. A coronal slice is also shown in fig. 5.14. Quantitative evaluation showed that there was an average underestimation of the activity in the hot spots of 2 % using the UTE-MRI-based attenuation correction. In the cold spot there was also an underestimation of 2 %.

5.3.3 Discussion

The average HU and R_2 values that are found in the lung are comparable to what is seen in clinical data sets. This shows that the pig lung used in the phantom is a realistic representation of human lung. The values observed in cortical bone are also realistic. The phantom can therefore be used to evaluate the performance of our method, in particular to determine if our method can discriminate air, lung, soft tissue and bone based on UTE-MRI signal alone. Although the bone and lung are realistic, the phantom does not model the composition of the human body accurately. For example, a real thorax contains two lungs and contains a spine that runs along the complete axial length. Because of this limitation, the phantom can not

Figure 5.10: A sagittal slice of the FID (left) and gradient echo (right) image of the thorax phantom.

Figure 5.11: A sagittal slice of the uncorrected (left) and corrected (right) R_2-map of the thorax phantom.

Figure 5.12: A sagittal slice of the CT-based (left) and UTE-MRI-based (right) attenuation map used for reconstructing the PET images of the thorax phantom.

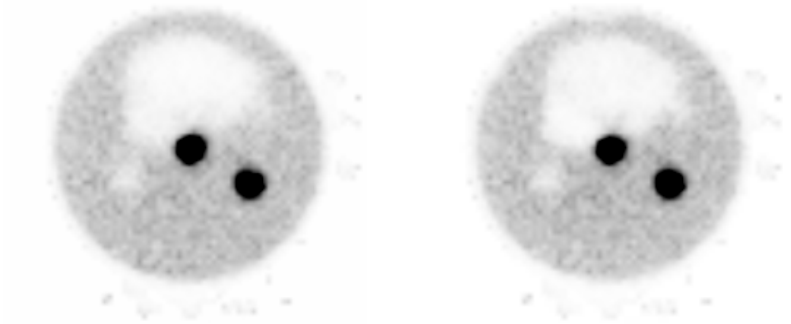

Figure 5.13: A transverse slice of the PET image of the thorax phantom reconstructed with CT-based (left) and UTE-MRI-based (right) attenuation correction.

Figure 5.14: A coronal slice of the PET image of the thorax phantom reconstructed with CT-based (left) and UTE-MRI-based (right) attenuation correction.

be used to test methods that rely on assumptions about patient anatomy. All current methods that have been proposed for whole-body MRI-based attenuation correction methods fall into this category. Designing a phantom that is more antropomorphic would allow evaluation of those methods as well, enabling comparison of the performance of different methods.

The UTE-MRI images show that there is signal in the bone and the lung in the FID image. In the gradient echo image, most of this signal has disappeared, as was expected. The signal in the water is comparable in both images. The R_2-maps show that the bone and lung have very high R_2 compared to the water. The uncorrected R_2-map also shows a high R_2 outside the phantom, due to the noise in the air surrounding the phantom. This is fixed in the corrected R_2-map.

Comparison of both attenuation maps shows that our method can discriminate air, lung, soft tissue and bone quite well. There are a few segmentation errors in the bone, which lead to bone being segmented as lung tissue, but these are limited. This happens because the R_2 in some voxels is just below the threshold for bone. These voxels are segmented as lung tissue in the attenuation map. Both reconstructed PET images are comparable, and no visual differences can be seen. The quantitative evaluation also reflects this, as only a very small deviation in total counts in the spheres is found.

These results indicate that our method could be used to derive an attenuation map which discriminates air, lung, soft tissue and bone. Although small classification errors are made, these have only a minor effect on the reconstructed PET images. However, one should keep in mind that these results only prove that these tissue types can be discriminated in an ideal situation. In a real imaging situation, there will be different effects which may pose extra problems. First of all there can be physiological motion of the heart and lungs in the thorax. Second, the field of view in clinical imaging will be larger, which will increase acquisition time. A last remark is that the bone structures in a real body are much more complex and usually smaller than the segment of bone that was used here. Bone may therefore be much more difficult to discriminate in a real data set.

5.4 Conclusion

In this chapter our method was tested on two phantoms. The data obtained with the pig head phantom, used as a model for human brain imaging, show that classification of UTE-MRI images into air, soft tissue and bone can be

done with our method. Limited classification errors are made, but mostly between bone and soft tissue. This is much better than classification errors between air and tissue (either soft tissue or bone). As it was not possible to fill the pig head phantom with activity, we could not evaluate the effect of reconstructing with the UTE-MRI-based attenuation map on a reconstructed PET image. However, from the data of the simulation study we expect that the effect of the classification errors will be limited.

A thorax phantom was presented in the second part of this chapter. It contains bovine bone and pig lung to model bone and lung realistically on PET, CT and MRI. The results indicate that our method enables the discrimination of air, lung, soft tissue and bone based solely on MRI data. Because the phantom could be filled with activity, the effect of the limited errors in the UTE-MRI-based attenuation map on the reconstructed PET images could be tested. The results indicate that the errors cause only small quantitative differences. However, the thorax phantom is structured much simpler than a real human thorax, and does not exhibit any motion. Application of our method to real animal and human data may therefore be more difficult. This will be investigated in the next chapters.

5.5 Original contributions

The use of a pig head as a phantom for evaluation the performance of MRI-based attenuation correction was first presented at the IEEE NSS/MIC conference in 2008[238] and also at the annual meeting of the ISMRM Benelux chapter[245]. The evaluation of the classification accuracy of our method on the pig head phantom was included in a A1 journal paper[239]. The design of the thorax PET-CT-MRI phantom was accepted for presentation at the IEEE NSS/MIC conference in 2011[246].

Chapter 6

Preclinical imaging experiments

6.1 Introduction

In the previous chapter our UTE-MRI-based attenuation correction method was tested on phantom data. The eventual goal of developing a MRI-based attenuation correction method is to use this method to perform attenuation correction in real emission tomography studies. As was described in chapter 2, micro-PET and micro-SPECT are important tools in current preclinical research, and attenuation correction is also necessary for quantitative small animal imaging. As micro-PET inserts for MRI scanners are already available and micro-SPECT-MRI is being developed, a MRI-based attenuation correction method for small animal studies is also needed.

The current gold standard for attenuation correction in small animal imaging is micro-CT-based attenuation correction. As was already described, the derivation of an attenuation map from CT images is straightforward. However, there are two specific disadvantages to the use of micro-CT for attenuation correction in preclinical imaging. First, micro-CT delivers soft tissue contrast which is even poorer than clinical CT. For vessel imaging, this can be solved by using large amounts of contrast agent. This leads to problems in the attenuation map, as the attenuation coefficients of the contrast agents can not be rescaled in the same way as biological tissue. Bonta et al.[247] have shown that this leads to significant errors in the reconstructed image for clinical SPECT studies, but the effect on preclinical imaging has not been studied. It should be noted that high doses of contrast agent can also be toxic for the animals. Second, the dose delivered to

the animal can be quite high ($>$ 0.1 Gy). It has been proposed that this could effect study outcome in longitudinal studies which use many micro-CT scans[112, 113, 248, 249]. The dose could have an effect on e.g. tumor metabolism or on the immune system of the animal. These two reasons provide additional motivation to develop a MRI-based attenuation correction method for small animal imaging.

In this chapter the feasibility of MRI-based attenuation correction for emission tomography of small animals is investigated. This is done for micro-SPECT as well as for micro-PET. First a large micro-SPECT study, comprising a total of 18 rats, is described. Four different tracers, each targeting a different organ, were used to evaluate the effect of MRI-based attenuation correction throughout the complete body of the rat. The images reconstructed with different MRI-based attenuation correction methods are compared to the images reconstructed with micro-CT-based attenuation correction. A smaller micro-PET study was also performed, to illustrate the applicability of the method to micro-PET. For that study 3 dead rats were used, and artificial lesions were implanted in different regions of the rat body.

6.2 Rat micro-SPECT-MRI

6.2.1 Materials and Methods

6.2.1.1 Acquisitions

Animal preparation

18 Hsd:Wistar rats were imaged in total. All rats weighed approximately 300 g and were no older than 8 weeks. Different radiotracers were used for micro-SPECT imaging. All radiotracers were administered via the tail vein. For the brain study, five rats were injected with 330 MBq of ^{99m}Tc-labeled hexamethylpropyleneamine oxime (HMPAO). A total of 13 rats were imaged for the body studies. Five rats were injected with 110 MBq of ^{99m}Tc-labeled dimercaptosuccinic acid (DMSA, kidney tracer), five rats were injected with 300 MBq of ^{99m}Tc-labeled colloids (liver and spleen tracer) and five rats were injected with 150 MBq of ^{99m}Tc-labeled macro-aggregated albumin (MAA, lung tracer). Of the rats injected with colloids two died before the MRI acquisition could be finished, so results from only 3 colloid scans will be presented here. The rats were anesthetized with an intraperitoneal dose of 115 μl pentobarbital per 100 g body weight. This dose was slightly higher

than the normal dose (100 μl per 100g body weight) to keep the animals anesthetized long enough to perform all acquisitions.

Micro-SPECT and micro-CT acquisitions

Micro-SPECT imaging was done on a dual-head Siemens e.cam clinical gamma camera (Siemens Medical Systems, Erlangen, Germany) using two multipinhole collimators. Each collimator had three pinholes with 1.5 mm knife-edge pinhole apertures. The total micro-SPECT acquisition time was 30 minutes. The system is described in more detail in [250]. The rats were then moved to the micro-CT scanner in the adjacent room while remaining on the same bed. A micro-CT was acquired on a SkyScan 1178 high-throughput in vivo micro-CT system (Skyscan, Kontich, Belgium). The CT settings were 50 kV and 615 μA. The acquisition time for the micro-CT was 2 min. The images were reconstructed with the software provided by the scanner manufacturer into a 1024 x 1024 x 1024 matrix with 0.083 mm isotropic voxel size.

MRI acquisitions

MRI acquisitions were performed on a clinical MRI system (Achieva 3T, Philips Medical Systems, Best, The Netherlands). A standard wrist coil was used for the brain scans. A standard knee coil was used for the body scans. Images were acquired with the UTE sequence described in section 4.2.3. For the brain scans, UTE-MRI images were acquired at an isotropic resolution of 0.5 mm and with FID and gradient echo times (T_{E1} and T_{E2}) set to 0.15 and 2.4 ms respectively. Two averages were acquired to improve signal to noise, yielding a total acquisition time of 35 minutes for a field of view of 75 mm x 75 mm x 75 mm. For the body scans the resolution was 0.7 mm and a larger field of view was acquired to include almost the complete body of the rat (75 mm x 75 mm x 177 mm). To allow acquisition of a non-spherical FOV, a modified version of the UTE sequence was used which performs non-isotropic radial sampling[251]. Only one average was used to keep the acquisition time acceptable (40 minutes).

6.2.1.2 Registration

Micro-SPECT, micro-CT and MRI images were registered using rigid registration methods. To restrict movement when moving the rats between different scanners, the rats were placed inside a plastic tube before the start of the experiment. Two small syringes filled with water were also placed inside

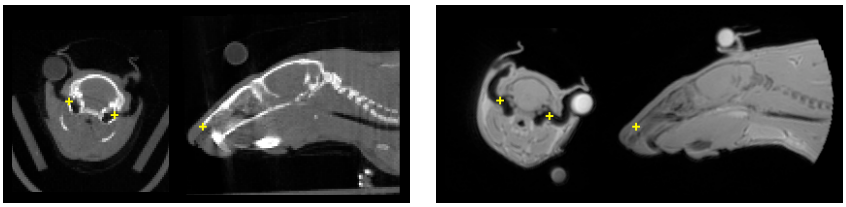

Figure 6.1: Illustration of the fiducial markers used for coregistration of the MRI images to the micro-CT images for the micro-SPECT brain studies. Three anatomical markers were used: the tip of the nose and the entrances of the left and right ear canal. The markers (yellow +) are illustrated on transverse and sagittal slices of a micro-CT (left) and MRI (right) image.

the plastic tube to help with the registration. The registration of micro-SPECT and micro-CT images was done using two circular discs placed on the bed used for both modalities. Each disc contained three 3.7 MBq ^{57}Co point sources. The method is described and validated in [252].

As the ^{57}Co point sources are not visible on MRI images, the same method could not be used to for the MRI images. The MRI images were registered to the micro-CT images using A Medical Image and Data Examiner (AMIDE)[244] by selecting fiducial markers on both CT and MRI images and applying the implemented alignment wizard. Different fiducial markers were used for the brain scans and the body scans. For the brain scans 3 anatomical fiducial markers were used: the tip of the nose and the entrances of the left and right ear canal, as shown in fig. 6.1. Four fiducial markers were used for registration of the body scans: both ends of the water syringes placed inside the plastic tube, depicted in fig. 6.2. After registration the micro-CT and MRI images were resampled to the same matrix as the micro-SPECT images. This was a matrix of 128 x 128 x 128 voxels with isotropic voxel size of 0.5 mm for the brain scans and a matrix of 128 x 128 x 256 with the same isotropic voxel size for the body scans.

6.2.1.3 Attenuation maps

The goal of this study is to evaluate the performance of different methods of MRI-based attenuation correction, compared to the currently used attenuation correction on the system (micro-CT-based attenuation correction). Therefore different attenuation maps were derived. All attenuation maps described in this section, derived for one of the DMSA (kidney) scans, are shown in fig. 6.5C-F. As all micro-SPECT imaging was done with ^{99m}Tc,

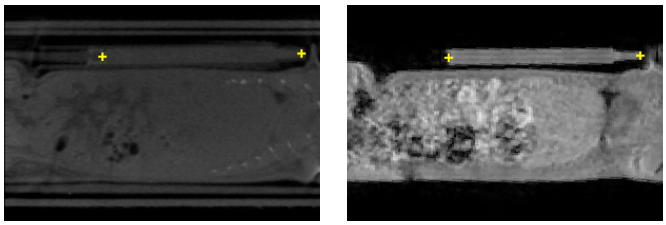

Figure 6.2: Illustration of the fiducial markers used for coregistration of the MRI images to the micro-CT images for the micro-SPECT body studies. Four markers were used: both endpoints of two syringes filled with water. The two endpoints of one syringe are shown on a sagittal slice of a micro-CT (left) and a MRI (right).

attenuation coefficients for 140 keV photons were used. First of all, the micro-CT-based attenuation map is derived. As micro-CT-based attenuation correction is currently the best available method for attenuation correction in micro-SPECT imaging, we can consider this attenuation map as the reference. The micro-CT image is first downsampled to the resolution of the micro-SPECT image by summing several neighbouring voxels together. This also acts as a smoothing operator and reduces noise in the micro-CT. The attenuation map is then derived from the micro-CT image by rescaling the micro-CT value in each voxel according to the formula:

$$\mu\,(cm^{-1}) = 0.15\,\frac{I}{I_{water}} \tag{6.1}$$

where I is the micro-CT value in the voxel and I_{water} is the micro-CT value of water, which is calibrated daily. The micro-CT values obtained from the scanner are positive values with air = 0 and increase with measured tissue density. As 0.15 cm^{-1} is the linear attenuation coefficient of water at 140 keV, this formula yields a linear scaling from the attenuation measured by CT to the attenuation coefficient for 140 keV photons. A linear scale was used rather than a bilinear scale (used e.g. in CT-based attenuation correction for clinical PET) as Brown et al. showed that the relationship between CT values and attenuation coefficients is linear to a good approximation for low energies up to 140 keV[253].

Three attenuation maps were derived from the MRI images, each using a different segmentation approach. Two of them can be derived from a conventional (non-UTE) MRI image. In our study the second (gradient echo) image of the UTE acquisition was used for this, as it is a normal

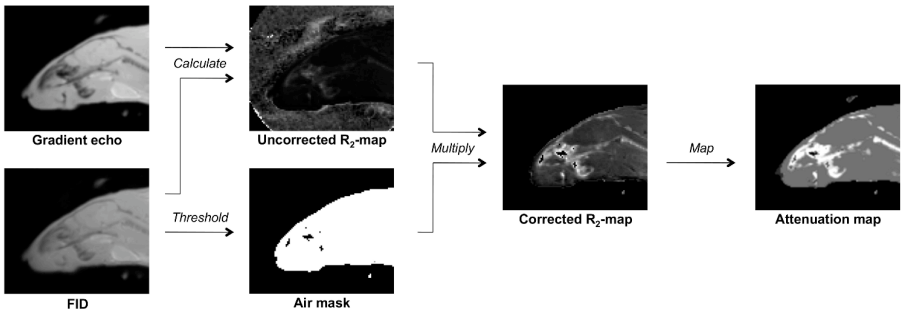

Figure 6.3: Image processing steps used to derive an attenuation map from UTE-MRI images of a rat.

T_1-weighted MRI image. A uniform (contour) attenuation map was derived by using region growing to determine the contour of the animal and setting the attenuation coefficient inside the contour to 0.15 cm^{-1}. A second attenuation map discriminating only soft tissue and air was extracted from the gradient echo image by simple thresholding. As there is no signal in the lungs in this image, this means that voxels in the lungs will be assigned air attenuation coefficients (0 cm^{-1}). Theoretically this should also happen in voxels containing bone, but this was not the case as is discussed in section 6.2.3. The second attenuation map was not derived for the brain scans, as there is no lung tissue in the head. Consequently, this attenuation map would be identical to the contour attenuation map.

In the small animal simulation study described in chapter 3, it was shown that air, lung and soft tissue should be discriminated in the attenuation map in rat studies. Discrimination of bone is not strictly necessary, but can provide even more accurate results. As described in chapter 4, information about bone and lungs can be extracted from the UTE images. An extra attenuation map which discriminates air, lung, soft tissue and bone was therefore also derived. This was done in three steps, which are summarized in Fig. 6.3. The first two steps consist of the derivation of the R_2-map and multiplication with the air mask, as described in section 4.4. This yields a corrected R_2-map. In this corrected R_2-map different tissues are discriminated based on their R_2 value. Lung has the highest R_2, followed by bone. Soft tissue has a low R_2 and the R_2 in air is set to 0 by the binary mask. The UTE-MRI-based attenuation map was derived from the corrected R_2-map by applying a mapping to the R_2 values:

$$\begin{array}{lll} \mu\,(cm^{-1}) = 0 & R_2 = 0 & \text{(air)} \\ = 0.15 & 0 < R_2 \leq 0.5 & \text{(soft tissue)} \\ = 0.15 + (0.25 - 0.15)\frac{R_2 - 0.5}{0.1} & 0.5 < R_2 \leq 0.6 & \text{(bone)} \\ = 0.08 & R_2 > 0.6 & \text{(lung)} \end{array} \tag{6.2}$$

The attenuation coefficient for voxels containing lung tissue was set to the average attenuation coefficient of lung tissue in the micro-CT-based attenuation maps. The R_2 thresholds of bone and lung were determined empirically. With this mapping, the highest R_2 values are segmented as lung whereas the R_2 of bone is assumed to be lower. This is different from the mapping used for the thorax phantom described in section 5.3, where bone has the highest R_2. This was done because we observed that the R_2 of the bone structures of the rats appeared to be lower than the R_2 of lung. This can be explained by considering the size of the bones of the rats. These bones are much smaller than the bone used in the thorax phantom. Consequently, the cortical shell of these bones is also very thin and far below the resolution of the system. Hence, voxels that contain cortical bone also always contain soft tissue or spongeous bone. As the protons in those tissues relax much slower than the protons in cortical bone, partial volume effects lead to a lower R_2 in such voxels. In fact, the R_2 is so much lower that it is even below the R_2 of lung tissue.

In eq. 6.2, voxels which have an R_2 value between lung and soft tissue are not just assigned a single bone attenuation coefficient. This is done for two reasons. First, due to the mechanism described above, the contrast between (partial) bone voxels and soft tissue voxels is not always high enough to clearly discriminate both tissue types. Second, not all voxels containing bone have the same attenuation coefficient: on the micro-CT a large range of values can be seen in bone. To compensate for both effects the R_2 values between 0.5 and 0.6 are rescaled to the range of values between the attenuation coefficient of soft tissue (0.15 cm^{-1}) and the maximum attenuation coefficient of bone on the micro-CT-based attenuation maps (0.25 cm^{-1}). The linear scale that is used is a working assumption and has not been verified experimentally.

The bed used for micro-CT and micro-SPECT and the plastic tube used to fixate the animals also cause some attenuation. As the bed is not MRI-compatible it was not used for the MRI scans and hence not visible on the MRI images. The plastic tube was used in the MRI scans but was also not visible on the MRI images as it provides no MRI signal. Therefore, an

attenuation template was made of the bed and tube from a micro-CT scan of the bed and tube without an animal. The template was then included in every MRI-derived attenuation map.

6.2.1.4 Micro-SPECT reconstruction

The SPECT projections were reconstructed using an iterative reconstruction algorithm based on the Ordered Subsets Expectation Maximization (OSEM) algorithm[250, 254], which is a modified version of the ML-EM algorithm described in section 2.2.4.2. The reconstructed matrix was 128 x 128 x 256 with an isotropic reconstructed voxel size of 0.5 mm. The algorithm models the system geometry as accurately as possible, taking into account the pinhole geometry, the collimator response, the angular variation of the sensitivity for each pinhole aperture, the intrinsic spatial resolution of the gamma camera, attenuation and scatter. It is described in detail in [252]. The non-uniform attenuation correction was implemented in the iterative reconstruction as proposed by Gullberg et al. [255]. A triple energy window (TEW) scatter correction was used. The SPECT images were reconstructed with four different attenuation maps: micro-CT-based, MRI uniform (contour) map, MRI map with air and soft tissue and a UTE-MRI map with air, lung, bone and soft tissue. A fifth reconstruction with no attenuation correction was also done.

6.2.1.5 Analysis

It has been shown that the reconstruction algorithm yields absolutely quantitative results when using a non-uniform micro-CT based attenuation map in [252]. Therefore the micro-SPECT images reconstructed with micro-CT based attenuation map can be considered the reference. In this study, we have thus compared the images reconstructed with the micro-CT based attenuation correction and the other images to prove that quantification is also possible with MRI-based attenuation correction. This was done in two ways. First the average percent difference Δ_X in a volume of interest (VOI) was calculated:

$$\Delta_X\,(\%) = 100\frac{1}{N}\sum_i \frac{|S_{X,i} - S_{CT,i}|}{S_{CT,i}} \tag{6.3}$$

where i is the voxel index, $S_{CT,i}$ and $S_{X,i}$ are the reconstructed SPECT activity concentrations in the image corrected with the micro-CT based at-

tenuation map and other image respectively and N is the total number of voxels in the VOI. For the body scans the VOI was automatically defined by thresholding on the micro-SPECT image reconstructed with the micro-CT based attenuation map, taking into account only voxels that have a significant SPECT image intensity. This was done to avoid corruption of the results by voxels that have only very low tracer uptake. The threshold was set to 10 % of the maximum micro-SPECT value. This was not done for the brain scans as HMPAO is a less specific tracer than the others. For the brain scans the VOI was manually defined by a box which contained the complete brain.

Second, the average activity concentrations in the VOIs in the different micro-SPECT images reconstructed with MRI-based attenuation maps were compared to the images reconstructed with micro-CT based attenuation map. The significance of the difference between the average activity concentrations was tested using a paired Student's t-test. The same VOI's as above were used for the evaluation. A significant difference was defined as a p-value smaller than 0.05.

6.2.2 Results

6.2.2.1 Attenuation maps

Fig. 6.4 shows images of one of the brain scans. The UTE-MRI images (FID and gradient echo), the micro-CT-based attenuation map, the uniform MRI-based attenuation map and the UTE-MRI-based attenuation map are depicted. Fig. 6.5 shows the same images for one of the DMSA (kidney) scans, but also includes the MRI-based (non-UTE) attenuation map which discriminates only air and soft tissue. The uniform MRI-based attenuation maps (Fig. 6.4D, 6.5D) are easy to derive and the contour of the body is correctly defined. The same applies to the non-UTE-MRI map where lung tissue is assigned air attenuation coefficients (Fig. 6.5E). The bones in this image are segmented as soft tissue, because of the issues discussed below.

The UTE-MRI map of the brain shows resemblance to the micro-CT-based attenuation map. Although the segmentation is not perfect, the large bone structures are discriminated in this attenuation map. The skull, jaw and spine can be seen. The attenuation map derived from the body UTE-MRI image shows good resemblance to the micro-CT in the lungs and soft tissue. The segmentation of the bones is more difficult. Although bone is detected in the ribs, the detected volume of bone is much smaller than on the micro-CT.

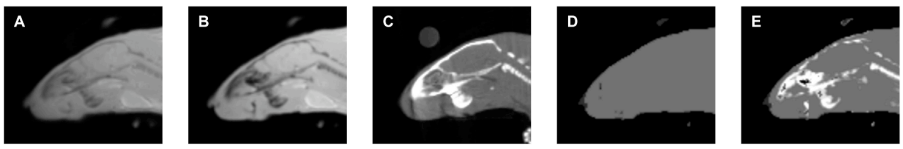

Figure 6.4: FID image (A), gradient echo image (B), micro-CT-based attenuation map (C), uniform MRI-based attenuation map (D) and UTE-MRI-based attenuation map (E) for one of the brain micro-SPECT-MRI scans.

6.2.2.2 Reconstructed micro-SPECT images

For each type of scan a slice of all micro-SPECT images of a single rat reconstructed with different attenuation maps is shown in Fig. 6.6. The greyscale window was the same within each scan type. Only very small visual differences can be seen between the micro-SPECT images reconstructed with the different attenuation maps. The quantitative comparison in fig. 6.7 shows more differences. The results for the brain scans should be interpreted separately from the body scans, as the setting is clearly different. In the brain scans, the UTE-MRI-based attenuation correction performs best in all rats, yielding an average error in all rats of 5 - 8 %. Uniform attenuation correction gives slightly larger errors, leading to errors above 10 % in two subjects. No attenuation correction gives errors of around 15 %. In the body scans the average errors are much smaller. All UTE-MRI-based attenuation maps have an average percent difference of 3 % or less. The non-UTE-MRI maps have an average percent difference of at most 6 %. Large average errors between

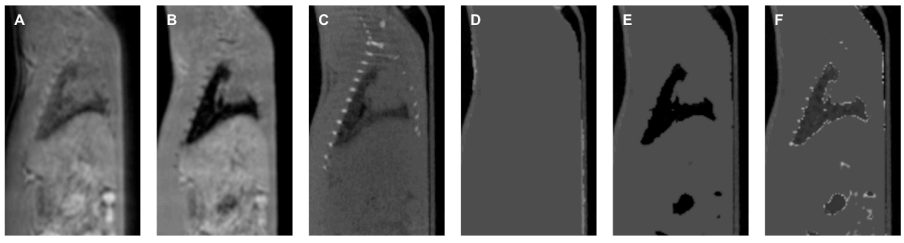

Figure 6.5: FID image (A), gradient echo image (B), micro-CT-based attenuation map (C), uniform MRI-based attenuation map (D), MRI-based attenuation map discriminating air and soft tissue (E) and UTE-MRI-based attenuation map discriminating air, lung, soft tissue and bone (F) for one of the body micro-SPECT-MRI scans.

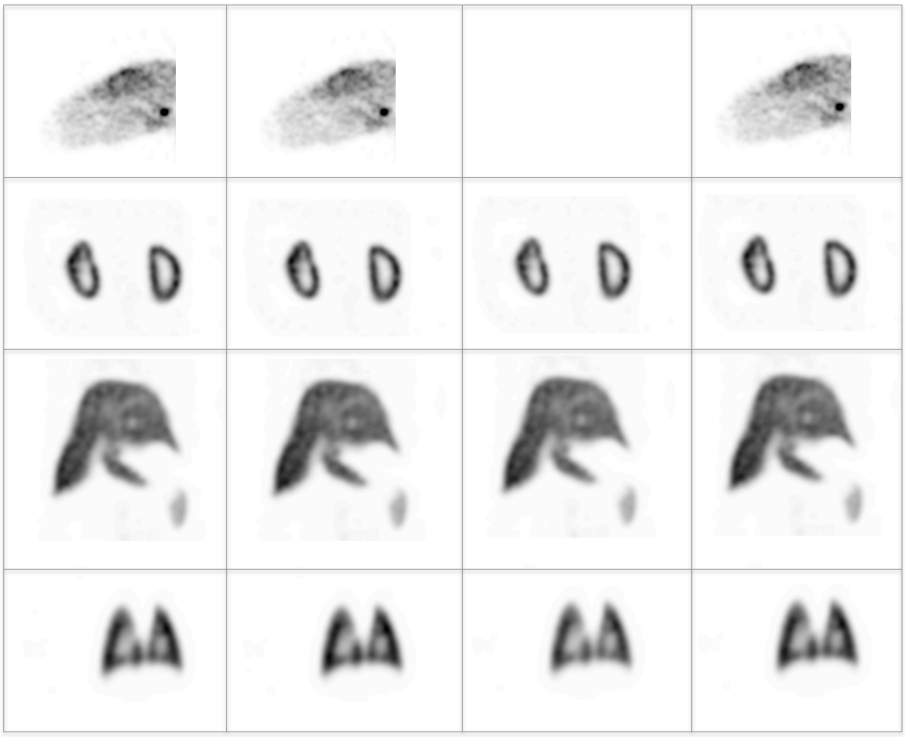

Figure 6.6: Micro-SPECT images from different tracers reconstructed with different attenuation maps. Tracers from top to bottom: HMPAO (brain), DMSA (kidney), colloids (liver and spleen), macro-aggregated albumin (lung). Attenuation map from left to right: micro-CT-based, uniform MRI-based, NON UTE MRI-based (air and soft tissue), UTE MRI-based (air, lung, soft tissue and bone). The third attenuation map was not available for the brain scans.

25 % and 45 % are found when no attenuation correction is done.

The average difference in activity concentration between the different MRI-based attenuation correction methods and the micro-CT-based attenuation correction is shown in table 6.1. For the brain scans, all MRI-based attenuation correction methods yield significant differences. For the body scans, the UTE-MRI-based attenuation correction yields a non-significant difference for all different tracers. The non-uniform non-UTE-MRI-based attenuation correction shows significant errors for all tracers. The uniform MR-based attenuation correction leads to significant differences for all tracers except colloids.

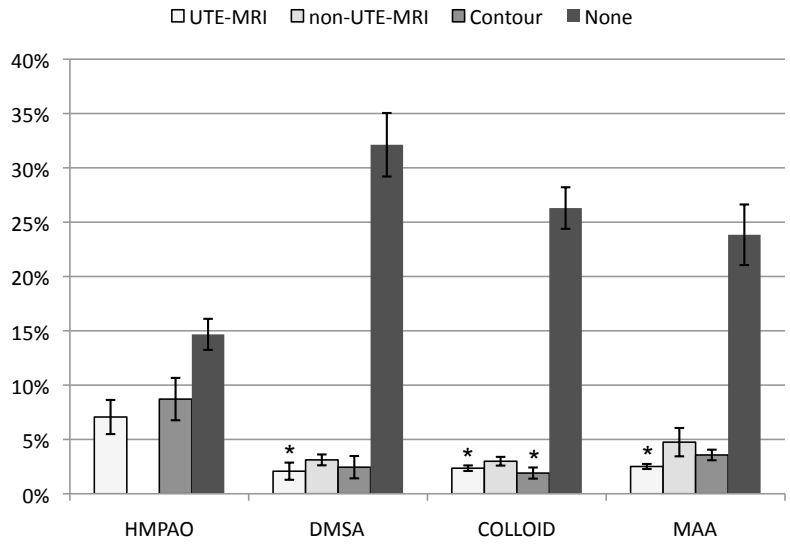

Figure 6.7: Average percent difference with micro-CT-based attenuation correction in the reconstructed micro-SPECT images, per scan type. The different attenuation maps are color-coded (* = non-significant difference).

6.2.3 Discussion

When looking at both UTE images it is clear that the FID image is of lower general quality than the gradient echo. Especially the FID body image (Fig. 6.5A) looks more blurred and exhibits more noise. This can be seen clearly around the edges of the body. The reasons for the lower quality of the FID image are discussed in chapter 4. As with the phantom images, these images also show why applying the binary mask is necessary. If the R_2-map would be used in its uncorrected form, there would be a lot of voxels with a high R_2 surrounding the body. By applying the binary mask, these voxels are set to 0 in the corrected R_2-map.

The UTE acquisition provides signal in bone and lung as the image intensity in the FID image in these tissues is well above the noise level. This is in clear contrast with the gradient echo image. The image intensity in the lungs in Fig. 6.5B is almost zero. In the brain image (Fig. 6.4B) the drop in signal is also apparent in the bones of the skull, spine and jaw. This will

	UTE MRI	Non-UTE MRI	Uniform MRI	None
DMSA	0.59 % *	2.23 %	1.55 %	32.32 %
Colloids	0.61 % *	1.75 %	1.08 % *	26.56 %
MAA	0.60 % *	4.34 %	2.34 %	22.79 %
HMPAO	6.34 %		9.60 %	17.66 %

Table 6.1: Average difference between activity concentration yielded by different MR-based attenuation correction methods and micro-CT based attenuation correction (* = difference is non-significant).

lead to high R_2 values. There is also a signal drop in bone in the body image (Fig. 6.5B), but it is much smaller than in the brain image. This is because the bones are smaller than the MRI resolution, which was explained above. As this leads to a lower R_2, close to the R_2 of soft tissue, bone will thus be segmented as soft tissue from these images. For the attenuation correction this is much better than segmenting bone as air as the attenuation coefficient of bone is much closer to soft tissue than to air. Bone is also detected in regions where no bone is present. The most obvious is the contour of the lungs. Partial volume effects comparable to what happens with bone and soft tissue will lead to lower R_2 values at the border of the lungs, where lung and soft tissue are contained in the same voxel. This leads to R_2-values between lung and soft tissue, comparable to the R_2 of voxels which contain bone.

These partial volume effects demonstrate that, to obtain a very accurate MRI-based attenuation map, UTE-MRI based images with a higher resolution should be acquired. In fact, the resolution of the acquired UTE-MRI images should be high enough to resolve the smallest structures with a difference in attenuation coefficient, which are probably the cortical shells of the bones. This is necessary because there is no direct correlation between MRI signal intensity and attenuation. Therefore, if a voxel contains tissues with different attenuation coefficients, the signal that is measured is the average of the MRI signals of these tissues. The calculated R_2 in the voxel will not necessarily be the R_2 that is expected from a tissue which has an attenuation coefficient equal to the average attenuation coefficient of the tissues in the voxel. Unfortunately, acquiring at such a high resolution would lead to unacceptably high acquisition times. We have also shown in the rat simulation study in chapter 3 that the discrimination of cortical bone is not strictly necessary to achieve accurate quantification.

In the non-uniform body MRI images (Fig. 6.5E, 6.5F) an air bubble can be seen in the abdomen. In the UTE-MRI-based R_2-map, a very high R_2 is in general seen in these bubbles. This is probably caused by fast relaxation within the bubbles because of susceptibility effects, comparable to what happens in the lungs. It leads to the segmentation of the air bubbles as lung tissue. In the gradient echo the image intensity is low in these bubbles, leading to segmentation as air. In the uniform attenuation map the bubble can not be seen as it is assigned the attenuation coefficient of soft tissue. The effect of air in the abdomen is very difficult to evaluate, as the air can shift to a different position. This can happen not only between different modalities but also within the same scan. It is therefore unclear which of the three attenuation maps is more correct at the moment of micro-SPECT acquisition. Only truly simultaneous micro-SPECT-MRI could compensate accurately for this.

These results indicate that attenuation correction should be performed in all situations. The statistically significant errors of over 25 % that are seen in the uncorrected reconstruction of the body images are unacceptable for quantitative studies.These figures were also found by other authors[181, 252]. As the head is smaller than the body the overall attenuation is lower and the effect of attenuation correction is smaller. However, the effect is still significant and attenuation correction should still be included in the reconstruction to keep the average error below 10 %.

In the colloid scans, the uniform attenuation map performs only slightly worse than the UTE-MRI-based map. Both maps yield a non-significant difference in activity concentration from micro-CT based attenuation correction. This can be understood as the spleen and liver are large homogeneous soft tissue structures and are not surrounded by many bones, so the effect of bone and lung attenuation will be very small. The attenuation of the lungs will have a small effect on the top part of the liver, but the liver is such a big structure that this does not significantly influence the average activity concentration. For the DMSA scans the uniform attenuation correction yields slightly larger errors, which are significant. This can be explained by the fact that the kidneys are smaller in size and close to the spine and ribs. This leads to a slightly larger effect of ignoring bone in the attenuation map, and so only the UTE-based attenuation map leads to non-significant errors.

In the lung scans (MAA) the errors between the different MRI-maps are larger than in the other body scans. This is conceivable as the attenuation of the lungs is only implemented correctly in the UTE-MRI map. In four out

of five rats the non-UTE MRI map discriminating air and soft tissue performs worst. The uniform map, where the lungs have soft tissue attenuation coefficients, performs better. This is explained by the fact that the attenuation coefficient of the lung tissue of the rats was closer to the attenuation coefficient of soft tissue than to air. However, only the UTE-MRI-based attenuation correction leads to a non-significant difference with micro-CT based attenuation correction.

In the brain the average differences with micro-CT based attenuation correction are larger. The difference between non-UTE and UTE-based attenuation correction is also larger. The head contains a lot of bone structures (skull, jaw, part of the spine) which are quite large compared to the total volume of the head. This is different in the body, where in most areas there is relatively little bone present. This leads to higher effect of not taking bone into account in the brain. It also leads to a higher effect of small errors in the attenuation map on the measured activity concentration. This explains why none of the MRI-based attenuation maps yield a non-significant difference with the micro-CT based attenuation correction.

Overall most of these results agree with what was derived in chapter 3, although those results were only directly applicable to micro-PET. If air, lung and soft tissue would be discriminated, errors of 3 % or less would be obtained in the body scans. This would be qualified as a non-relevant error in the simulation study. In the study presented in this chapter, the statistical significance of the errors was also evaluated. This leads to the requirement of a complete UTE-MRI-based attenuation map, which also discriminates bone. As described above, this will only be necessary if the quantification needs to be very accurate, e.g. within 1 %.

The results for the brain studies differ somewhat from the results obtained in the micro-PET simulation study. This could be related to the difference between micro-PET and micro-SPECT. In micro-PET, the attenuation coefficient of cortical bone is approximately 30 % higher than the attenuation coefficient of soft tissue (0.13 cm^{-1} versus 0.097 cm^{-1}), whereas in micro-SPECT the attenuation coefficient of cortical bone is up to 65 % higher (0.25 cm^{-1} versus 0.15 cm^{-1}). This may lead to a larger effect of ignoring the skull in the brain micro-SPECT scans.

From these results it seems that uniform (contour) attenuation correction can be used in most micro-SPECT studies. It can always be used for liver studies. For brain, lung and kidney studies it can be used if the quantification

criteria are not too stringent. This has a number of advantages. The biggest advantage is that no time is lost with the relatively slow UTE acquisition. The MRI scan time is often limited for different reasons: the animal can not be anesthetized for too long, limited experimental availability of the MRI system, etc. This means that the available MRI time should be used as good as possible to acquire interesting MRI images, e.g. images with high contrast in the organ under study. Apart from providing signal in bone and lung the UTE sequence does not provide interesting contrast. Therefore it is only acquired to derive the attenuation map and if that can be derived from the other MRI images, this is a more efficient use of scan time. Another advantage is the stability of the uniform attenuation map: apart from the anticipated errors in the lungs and bone the attenuation map is correct. The derivation of the attenuation map can also be done fast and is easy to implement. The only parameter that needs to be tuned is the threshold for the contour detection.

In brain, lung and kidney scans the UTE-MRI-based attenuation correction performs better. It should be preferred if absolute quantification is important, as it is the only MRI-based method that leads to non-significant errors (for lung and kidney scans). It is the best approximation of micro-CT-based attenuation correction. However, there are some downsides to using UTE-MRI-based attenuation correction. First of all, there is the long acquisition time of the UTE sequence as discussed above. Second, the UTE images can be difficult to acquire and sufficient care should be taken to assure the highest possible quality. Finally, the UTE-MRI-based attenuation correction is much more difficult to implement and requires a lot more parameters to be tuned. This can lead to errors if the image quality is lower than normal or the parameters are not tuned well. These errors can be larger than the benefit that is achieved by taking bone and lung into account. All of this should be kept in mind when making the trade-off between uniform and UTE-MRI-based attenuation correction.

All micro-SPECT scans in this study were performed using ^{99m}Tc-labeled tracers. In micro-SPECT many other isotopes can be used. If imaging is done with a lower-energy isotope, such as ^{125}I the effect of attenuation correction will be larger. This has been demonstrated in phantom studies by Hwang et al[181], showing that the quantitative error can be up to 50 % if no attenuation correction is performed. In this context, attenuation correction is even more important.

6.3 Rat micro-PET-MRI

In this section a smaller micro-PET study, using only 3 rats, is described. It was not possible to perform a large study, such as the micro-SPECT study described above. This was in part due to the limited availability of the micro-PET scanner. Also, such a large study comes with a considerable cost. Therefore, the idea of the micro-PET study described here was to demonstrate that the performance of our method in micro-PET is comparable to the performance in micro-SPECT.

6.3.1 Materials and methods

6.3.1.1 Acquisitions

Animal preparation

Spherical artificial lesions were created for the experiment. This was done by submersing small spheres in a ^{18}F-FDG solution. The spheres were 10 Å carbon molecular sieves, with a diameter of approximately 2 mm. After leaving the spheres in the ^{18}F-FDG solution for approximately 15 minutes, they were placed on a hard surface to dry for 5 minutes. Subsequently they were coated with plastic glue, to prevent leaking of the activity. A total of 24 artificial lesions were created, with activities ranging from 1 to 3 MBq.

Three rats that were sacrificed after previous experiments and stored in the lab freezer were used. All rats weighed approximately 300 g. The rats were taken out of the freezer the day before the experiment. In each rat, 8 spherical lesions were implanted in different locations: mouth, neck, shoulder, lung, kidney, abdomen, bladder, lumbar spine.

Micro-PET and micro-CT acquisitions

All acquisitions were done on a Triumph (Gamma Medica-Ideas, Sherbrooke, Canada) system. This tri-modality system consists of a micro-PET (LabPET), micro-CT (X-O) and micro-SPECT (X-SPECT) scanner. The LabPET scanner is an APD-based scanner with 50 % LYSO and 50 % LGSO crystals (2 x 2 x 13 mm)[256]. It is made up of modules of 4 (tangential) by 2 (axial) crystals. There are 48 modules in the tangential direction and 16 modules in the axial direction. There are gaps between the modules ($\approx$ 2.5 mm and $\approx$ 0.8 mm tangential and axial respectively). A model for the LabPET scanner was also used in the rat simulation study in chapter 3. The X-O is a micro-CT scanner with adjustable magnification, which can be

achieved by moving the source closer or further away from the animal. The X-SPECT scanner was not used for this study.

First a micro-CT scan was performed by acquiring 256 projections into a 1184 x 1120 matrix with 50 μm pixel size and magnification 1.3. The CT settings were 75 kVp and 140 μA. The micro-CT acquisition time per bed position was approximately 2 minutes. Three bed positions were acquired for each rat, with 50 % overlap. The total axial field of view (FOV) was approximately 220 mm. The micro-CT images were reconstructed with the software provided by the scanner manufacturer. The reconstructed matrix for a single bed position was 512 x 512 x 512 with 0.25 mm isotropic voxel size. All three bed positions were joined to obtain a CT image of the complete rat. This image was then downsampled to 1 mm isotropic resolution by summing together neighboring voxels. This acts as a smoothing operator and also reduces noise.

Five micro-PET bed positions were needed to cover the complete rat. All bed positions were acquired with 50 % overlap, yielding a total axial FOV of 228 mm. Ten minutes were acquired per bed position, leading to a total PET acquisition time of 50 minutes. The reconstruction of the micro-PET images was not done with the software provided by the scanner manufacturer but is described below.

MRI acquisitions

MRI acquisitions were performed on a clinical MRI system (Magnetom Trio 3T, Siemens Healthcare, Erlangen, Germany). A standard knee coil was used, and images were acquired with a UTE sequence comparable to the one described in section 4.2.3. The echo times for the FID and gradient echo images were set to 0.08 and 2.3 ms respectively. The reconstructed matrix was 224 x 224 x 224 with 1 mm isotropic voxel size, covering the complete rat. The MRI acquisition time was approximately 25 minutes.

6.3.1.2 Registration

As the micro-CT and micro-PET images were acquired on the same scanner using the same bed, no coregistation was needed to align those data sets. However, the MRI images were acquired on a clinical system in a different building. Coregistration of the MRI images to the micro-CT images was done using a comparable method as for the micro-SPECT study described in section 6.2. To restrict movement, the rats were placed inside a plastic tube before the start of the experiment. For coregistration between MRI and

micro-CT, two small syringes filled with water were also placed inside the plastic tube. After the micro-CT and micro-PET acquisitions, the plastic tube with the rat inside was moved to the MRI scanner. Afterwards, the MRI images were coregistered to the micro-CT images with the implemented alignment wizard of AMIDE, using both ends of the water syringes as fiducial markers.

6.3.1.3 Attenuation maps

As in the micro-SPECT study described above, the goal of this study is to compare the performance of MRI-based attenuation correction to micro-CT-based attenuation correction. The same attenuation maps as in the micro-SPECT study were therefore derived from the micro-CT and MRI images. However, as a positron emitter was used rather than ^{99m}Tc, different absolute values for the attenuation coefficients were used. Bilinear scaling was also used to derive the attenuation map from the micro-CT, as this is the most accurate method for 511 keV photons. The attenuation coefficient in each voxel using the following equation:

$$\begin{aligned} \mu\,(cm^{-1}) &= 0.097\,\frac{I}{I_{water}} && I \leq I_{water} \\ &= 0.097 + 0.096\,\frac{I - I_{water}}{I_{water}} && I > I_{water} \end{aligned} \tag{6.4}$$

where I is the micro-CT value in the voxel and I_{water} is the micro-CT value for a voxel containing water. This equation was obtained from [198].

The three MRI-based attenuation maps were derived using the same method as in the micro-SPECT study. The uniform MRI-based attenuation map and the non-UTE MRI-based attenuation map discriminating air and soft tissue were obtained from the gradient echo image. The correct 511 keV attenuation coefficient for soft tissue was assigned (0.097 cm^{-1}). For the UTE-MRI-based attenuation map the method illustrated in fig. 6.3 was also used. The mapping from R_2 to μ was changed to apply to 511 keV photons:

$$\begin{aligned} \mu\,(cm^{-1}) &= 0 && R_2 = 0 && \text{(air)} \\ &= 0.097 && 0 < R_2 \leq 0.5 && \text{(soft tissue)} \\ &= 0.097 + (0.13 - 0.097)\,\frac{R_2 - 0.5}{0.1} && 0.5 < R_2 \leq 0.6 && \text{(bone)} \\ &= 0.06 && R_2 > 0.6 && \text{(lung)} \end{aligned} \tag{6.5}$$

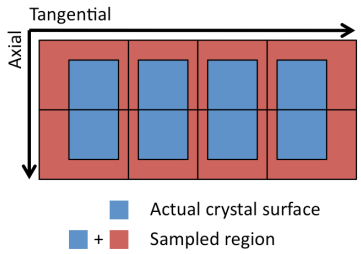

Figure 6.8: Illustration of the gap correction for a single module of the LabPET scanner. The actual crystal surface is depicted in blue. The position on the crystal surface is randomly sampled from the red + blue region. This yields a scanner with virtually no gaps.

6.3.1.4 Micro-PET reconstruction

The reconstruction software available from the scanner manufacturer is a 2D MLEM algorithm with single slice rebinning (SSRB). It is well known that SSRB generates artefacts for points that are not in the transaxial center. The manufacturer software also does not include attenuation correction. Therefore we developed our own 3D MLEM reconstruction algorithm including corrections for the gaps between modules, geometric sensitivity and attenuation. Attenuation correction was implemented into the forward projection of the algorithm. Scatter correction was not implemented as it was deemed to have a small effect in micro-PET.

The reconstruction is LOR histogram based. A LOR histogram contains the number of measured counts for each crystal pair. For each histogram bin the three-dimensional position of each of the crystals is calculated. To avoid sampling artefacts, random sampling on the crystal surface is used to calculate the position inside the crystal. As the gaps between the modules are quite large relative to the module dimensions, a gap correction is needed to avoid artefacts in the reconstructed images. This was done by performing random sampling on a region larger than the crystal surface, as shown in fig. 6.8. As the crystals at the tangential border of a module are made virtually larger than the others with this method, the number of counts in these crystals were multiplied with a correction factor. This method is a form of nearest neighbor interpolation of the data that was lost inside the gaps. The calculated points are then used to forward- and backproject the number of counts in the LOR.

Although the gaps are corrected for, correction for geometric sensitivity

is still necessary, as the solid angle coverage of the scanner will still vary between points inside the field of view. A geometric sensitivity map was calculated by performing a single backprojection of all available LORs. This method is comparable to the sensitivity correction described in section 3.4, except that crystals which are defective and are not measuring at the time of the scan are not backprojected and hence do not contribute to the calculated sensitivity. This is necessary as a real scanner is used rather than a simulation, and some crystals may be defective. The active crystals were determined from a normalization scan with a ^{68}Ge rod source performing a full rotation close to the crystal surfaces.

Using this reconstruction algorithm all bed positions were reconstructed separately with the different attenuation maps. The reconstructed matrix for each bed position was 100 x 100 x 64 with 1 mm isotropic voxel dimensions. The reconstruction was stopped after 50 iterations. The bed positions were then merged by calculating the reconstructed value in each voxel as a weighted average of the different reconstructed images contributing to that voxel. The weighing factor was obtained from the geometric sensitivity map, comparable to what was done in section 3.4.

6.3.1.5 Analysis

To evaluate the accuracy of MRI-based attenuation correction, the relative difference between the activity in the lesions in the micro-PET images reconstructed with micro-CT-based attenuation correction and MRI-based attenuation correction was calculated. This was done by drawing 8 spherical VOIs on the artificial lesions. The diameter of the spherical VOIs was 10 mm. The relative difference was then calculated using the following equation:

$$\Delta_{X,k}\,(\%) = 100\,\frac{\sum_i (P_{X,i} - P_{CT,i})}{\sum_i P_{CT,i}} \tag{6.6}$$

where $\Delta_{X,k}$ is the relative difference in VOI k, $P_{X,i}$ and $P_{CT,i}$ are the micro-PET values in voxel i reconstructed with MRI-based attenuation map X and micro-CT-based attenuation map respectively. The sums are taken over all voxels i in the VOI.

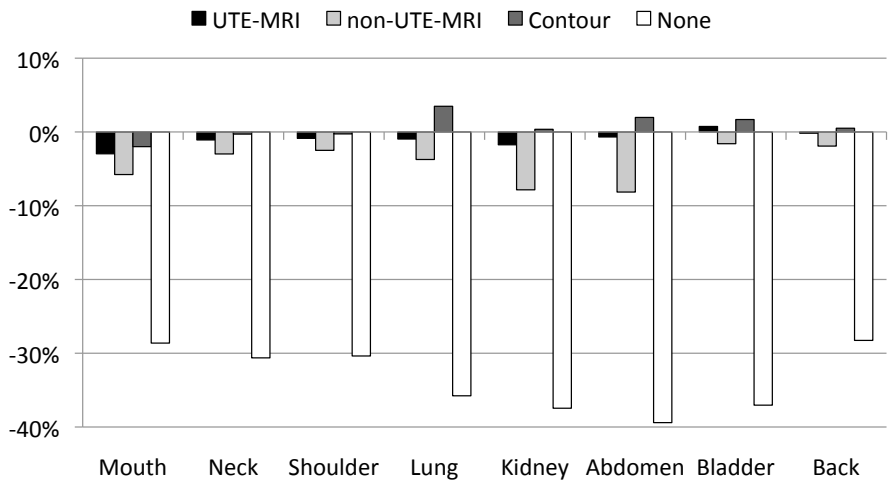

Figure 6.9: Average percent difference with micro-CT-based attenuation correction in the reconstructed micro-PET images, per lesion location. The different attenuation maps are color-coded.

6.3.2 Results

As the attenuation maps obtained from the rats in this study were comparable to the attenuation maps obtained in the micro-SPECT study, they are not depicted separately. The relative differences in all VOIs, averaged over all 3 rats, are shown in fig. 6.9. All results in fig. 6.9 are also listed in table 6.2. Large underestimations of 25 - 40 % are seen in all lesions when no attenuation correction is performed. Uniform MRI-based attenuation correction yields errors smaller than 2 % in most lesions, except for overestimations in the lung (3.5 %) and abdomen (2 %) and an underestimation in the mouth. Non-uniform non-UTE MRI-based attenuation correction, which discriminates air and soft tissue inside the body, leads to larger errors. Especially the underestimations in the abdomen, kidney, mouth and lung (3.7 - 8.1 %) are high. UTE-MRI based attenuation correction yields errors of less than 2 %, except for the lesion in the mouth, which is underestimated by 3 %.

6.3.3 Discussion

The results from the micro-PET study also show that attenuation correction should be performed at all times. In all lesions, the relative error made

	UTE MRI	Non-UTE MRI	Uniform MRI	None
Mouth	-3.0 %	-5.8 %	-2.0 %	-28.6 %
Neck	-1.1 %	-3.0 %	-0.3 %	-30.6 %
Shoulder	-0.9 %	-2.5 %	-0.3 %	-30.4 %
Lung	-1.0 %	-3.7 %	3.5 %	-35.8 %
Kidney	-1.7 %	-7.8 %	0.4 %	-37.5 %
Abdomen	-0.7 %	-8.1 %	2.0 %	-39.4 %
Bladder	0.7 %	-1.6 %	1.7 %	-37.0 %
Back	-0.2 %	-1.9 %	0.5 %	-28.3 %

Table 6.2: Average relative difference between the total activity in the lesions in the micro-PET images reconstructed with different MRI-based attenuation correction methods and micro-CT based attenuation correction.

by ignoring attenuation is much too high to allow quantitative micro-PET studies. The errors in the mouth, neck, shoulder and back are slightly smaller than in the lung, kidney, abdomen and bladder. This is related to the depth at which the lesions were implanted. In the latter the lesions were implanted deeper into the body, leading to a higher effect of attenuation.

When performing MRI-based attenuation correction, the results of the micro-PET study indicate that a uniform attenuation map leads to small errors in general. Errors are specifically small in soft tissues, such as the kidney. The quantification error in the liver will also be small with this method. This was also observed in the rat simulation study discussed in chapter 3, as well as in the micro-SPECT study. A slightly larger error is seen in the lungs, which is due to the fact that this method ignores the difference between the attenuation coefficients of lung and soft tissue.

A non-uniform non-UTE-MRI-based attenuation correction method, where lung and air inside the body are given the attenuation coefficient of air, should not be used. It leads to underestimations of up to 3.7 % in the lungs and up to 8.1 % in the abdomen. The relatively large error in the abdomen is probably caused by air bubbles, as discussed already in the micro-SPECT study. If these bubbles actually contain a certain amount of water or food, but have a low MRI signal in a gradient echo image because of susceptibility effects, the attenuation coefficient of air will be assigned to them.

Overall, a non-uniform UTE-MRI-based attenuation correction performs the best. An underestimation of 3 % in the mouth is the largest error that is

observed. All other errors are small, most even below 1 %. This attenuation correction method is also the only method that leads to a small error in the lungs, as it is the only method that takes the real attenuation coefficient of lung tissue into account. It will also assign the attenuation coefficient of lung tissue to air bubbles in the abdomen, which is a better approximation of the real attenuation coefficient than soft tissue (in the uniform map) or air (in the non-uniform non-UTE map).

As with the results obtained from the micro-SPECT study described above, these results support the conclusion that a uniform MRI-based attenuation correction is generally sufficient for rat micro-PET studies. Especially if soft tissue studies are performed this is the case. When the focus of a study is in the lung or close to the lungs, a UTE-MRI-based attenuation correction can be considered. This is, however, far more challenging and time-consuming, and only leads to small improvements. The same remarks as above therefore apply to micro-PET studies. The results also agree quite well with the results obtained in the rat simulation study. The errors in the mouth are smaller than those observed in the brain in the micro-SPECT study and resemble the simulated errors in the brain closer. However, as this is not exactly the same location, it is uncertain if the error in a brain lesion would not be larger in the real micro-PET study.

As a last remark, one could question how realistic this study is. There are two main limitations. First of all, the animals are dead. Therefore, there are no additional image-degrading effects such as physiological motion. However, the effect of physiological motion in rats is probably small. This is supported by the fact that no motion effects were observed in the micro-SPECT study, where the animals were alive during imaging. Secondly, only small spherical lesions were imaged, without a background. This is a different situation than a whole-body scan of an animal injected with ^{18}F-FDG. This is partly compensated by the dispersion of the lesions throughout the complete body. If a large error would be made in a specific part of the body, this would lead to errors in one or more of the lesions. In a real imaging situation, partial volume effects would also play an important role. The lesions used here had a diameter of 2 mm. This is quite close to the resolution of the scanner ($\approx$ 1.4 mm). Therefore, if the lesions would be imaged with background activity, it would be more difficult to discriminate them.

6.4 Conclusion

In this chapter, the feasibility of MRI-based attenuation correction for micro-SPECT and micro-PET studies of rats was demonstrated. For micro-SPECT, scans of the brain, kidneys, spleen, liver and lungs were evaluated. For micro-PET, artificial lesions were implanted into the body of the rat in 8 locations: mouth, neck, shoulder, lung, kidney, abdomen, bladder, back. The different study types cover most areas of the rat body. In most cases uniform attenuation correction can be applied. This leads to errors of less than 5 % in the body and less than 12 % in the brain for micro-SPECT, and errors of less than 4 % for micro-PET. It can be implemented quickly, provides stable results and the attenuation map can be derived from different types of MRI images.

When accurate quantification is important a UTE-MRI-based attenuation correction should be applied in the brain and lungs, and perhaps also in soft tissues close to bone structures such as the kidneys. This technique discriminates air, lung, soft tissue and bone and yields the best performance. However, it is much more difficult to implement and requires a long acquisition time on the MRI system. In many cases the small improvement obtained with UTE-MRI-based attenuation correction will not justify the additional effort that is needed.

6.5 Original contributions

The results of the micro-SPECT study were presented at the WMIC conferences in 2009 and 2010[257, 258]. A paper with these results has also been accepted for publication in a A1 journal[259]. The validation of the reconstruction that was implemented for the LabPET scanner was accepted for presentation at the IEEE NSS/MIC conference in 2011[260].

Chapter 7

Clinical imaging experiments

7.1 Introduction

As the first clinical PET-MRI systems are now available, a MRI-based attenuation correction method for human imaging is also needed. The fact that attenuation correction has a much larger effect in human studies than in small animal studies has already been discussed in the introductory chapter. It has also been shown in the simulation studies described in chapter 3. We have demonstrated that there are more stringent requirements for a human MRI-based attenuation correction method, as more tissue types need to be discriminated to allow accurate quantification. The field of view in human imaging is also a lot larger. This may lead to an increase in imaging time.

The application context in human imaging is different from that of small animal imaging. It can be expected that current clinical PET-MRI systems will be used almost exclusively for research. This means that quantification can be important, comparable to small animal imaging. It also means that many different situations may be encountered, e.g. different regions of the body can be imaged. A method should be able to adapt to that. On the other side, a research context also allows closer follow-up of a new method, and does not necessarily require full automation. Although imaging time for the acquisition of the attenuation map should always be kept short, research protocols are usually lengthy so a few extra minutes for the acquisition of the attenuation map may not pose a big problem.

Over the next few years, it is likely that PET-MRI scanners will also evolve

into clinical practice. In that case, different requirements will apply. In clinical practice, standard protocols are used. Full automation of MRI-based attenuation correction will therefore be necessary. Quantification is used more and more in clinical situations, and this would require a very accurate attenuation correction method. Nevertheless, the most important requirement of a clinical MRI-based attenuation correction will be its robustness. In a clinical situation it is more acceptable to make small errors that can be predicted and accounted for, than having the possibility of a large error which can not be predicted. The best example is lesion detection: if a clinical MRI-based attenuation correction can lead to the disappearance of a lesion on the reconstructed PET image, this is completely unacceptable. The same applies when an artificial lesion is created. As throughput is also very important in a clinical situation, the imaging time used for the acquisition of the attenuation map should be kept as low as possible.

After testing our method on phantoms and small animals, it will be tested on human data in this chapter. In human imaging, the effect of attenuation and the requirements for the attenuation map depend on the region that is being imaged. As was discussed before, the most important future applications for PET-MRI are probably neurology, cardiology and oncology. In the first part of this chapter a clinical brain study with 5 patients is described. In the second part a method is proposed for use in thoracic imaging, such as cardiac imaging. This method is evaluated on a single data set, and the limitations and difficulties in thoracic imaging are extensively discussed. The thorax was chosen because it contains the lungs, which are very important for human body attenuation correction, as described in chapter 3. To test our method in the context of oncological studies, whole-body data sets would be needed. No whole-body data is presented in this thesis for two reasons. First, we did not have the possibility to acquire these data sets. Second, the application of UTE-MRI-based attenuation correction to clinical whole-body imaging may not be feasible. The reasons for this and other considerations regarding to whole-body MRI-based attenuation correction are discussed in the third part of this chapter.

7.2 Brain

7.2.1 Materials and methods

7.2.1.1 Acquisitions

Five epilepsy patients who were planned to receive a brain PET-CT and MRI exam also received a UTE-MRI scan. The PET-CT was acquired on a Philips Gemini TF PET-CT (Philips Medical Systems, Cleveland, USA). A low-dose CT suitable for attenuation correction was acquired with standard settings (50 mAs, 120 kVp). The slice thickness was 5 mm. The in-plane resolution was 1.17 mm. The reconstructed matrix was 512x512x40 voxels. ^{18}F-FDG PET images were acquired with the standard brain PET protocol. The acquisition time was 7 minutes. The images were reconstructed to a 128 x 128 x 90 matrix with 2 mm isotropic voxel dimension. After the PET-CT exam the patient was transferred to the MRI department.

UTE images were acquired with a Philips 8-channel SENSE head coil. The FID echo time was set to the minimum achievable echo time, i.e. 0.140 ms. The gradient echo time was 1.8 ms. T_R was 4 ms. This yielded a total acquisition time of 6 minutes. The images were reconstructed to a 224 x 224 x 224 matrix with 1.3 mm isotropic voxel dimension. The field-of-view was a sphere with 145.6 mm radius.

7.2.1.2 Derivation of attenuation maps

A comparable method as described in section 5.2 was used for the derivation of the attenuation maps. First, a segmented CT-based attenuation map was derived from the CT data sets. This was done by mapping CT Hounsfield units (HU) to linear attenuation coefficients at 511 keV:

$$\begin{array}{lll} \mu\,(cm^{-1}) = 0 & HU \leq -800 & \text{(air)} \\ \quad = 0.097 & -800 < HU \leq 200 & \text{(soft tissue)} \\ \quad = 0.13 & HU > 200 & \text{(bone)} \end{array} \qquad (7.1)$$

The different steps used in the derivation of the attenuation map from the UTE-MRI images are shown in fig. 7.1. First, the corrected R_2-map was first derived from the FID and gradient echo image, as described in section 4.4. The attenuation map was then derived from the corrected R_2-map, by the same mapping from R_2 to μ as described in section 5.2:

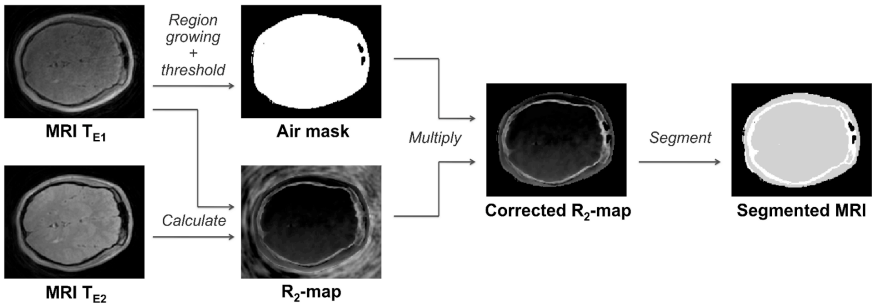

Figure 7.1: Image processing workflow used for the clinical brain PET study. The uncorrected R_2-map is calculated from the UTE FID and gradient echo images. The R_2-map is masked with the air mask derived from the first echo image to yield the corrected R_2-map. The corrected R_2-map can be segmented into bone, soft tissue and air.

$$\begin{array}{lll} \mu\,(cm^{-1}) = 0 & R_2 = 0 & \text{(air)} \\ \quad = 0.097 & 0 < R_2 \leq 0.5 & \text{(soft tissue)} \\ \quad = 0.13 & R_2 > 0.5 & \text{(bone)} \end{array} \tag{7.2}$$

This yields CT-based and UTE-MRI-based attenuation maps for each patient, which are then resampled to the matrix of the PET acquisition: 128 x 128 x 90 voxels with 2 mm isotropic voxel dimensions. As the CT and PET were acquired on the same system, those images were automatically coregistered. However, coregistration of the MRI images to the PET-CT data set was needed. This was done in two steps: first approximate coregistration was done manually using visual guidance. In a second step, optimization of the coregistration was done using automatic rigid 3D registration with a mutual information metric. The mutual information metric was calculated on the CT image and the corrected R_2-map, as the corrected R_2 map has 0 image intensity in air, medium intensity in soft tissue and high intensity in bone, comparable to the CT.

7.2.1.3 PET simulation

As described below, the classification accuracy of our method will be evaluated against the segmented CT, showing the amount of voxels of different tissue types that are misclassified. However, this does not allow intuitive derivation of the effect of these misclassified voxels on the reconstructed

PET image, as an error in the attenuation map will not only have an effect locally, but will also affect all voxels on LORs that are passing through the error. The ideal method for evaluating the performance of a MRI-based attenuation correction method on clinical data sets is to reconstruct the original raw PET data with a CT-based and a MRI-based attenuation map. Unfortunately, the raw PET data was not available for all patient data sets. Therefore, a simplified simulation of the PET acquisition/reconstruction process was done to evaluate our method.

For each patient, the PET data set was first forward projected along all LORs in a clinical PET scanner. As the data was acquired on a Philips Gemini TF scanner, a model for this scanner was used. For each LOR, the projected data was attenuated by the total attenuation factor for that LOR in the CT-based attenuation map. This yields a LOR histogram, comparable to the data format of the LabPET systems described in section 6.3. The data in this histogram represent the data that would be obtained by a perfect acquisition of the activity distribution in the PET data set, without randoms, scatter or noise. Attenuation is taken into account, with the assumption that the CT-based attenuation map represents the exact attenuation coefficient distribution of the patient.

The reconstruction was then performed twice: once using the CT-based and once using the UTE-MRI-based attenuation map. An attenuation corrected ML-EM algorithm was used and the reconstruction was stopped after 20 iterations. As the simulation process depends on the geometry of the scanner, geometric sensitivity correction was needed. This was implemented as described in section 3.4. The differences between the simulated PET images reconstructed with the CT-based and UTE-MRI-based attenuation will be similar to the differences that would be obtained if the real PET data was reconstructed with both data sets. In fact, as attenuation is the only image-degrading effect that is modeled, the errors introduced by the UTE-MRI-based attenuation correction will be the only errors present in the reconstructed images. This allows evaluation of the effect of attenuation by itself.

7.2.1.4 Analysis

The evaluation of the classification accuracy of the UTE-MRI-based attenuation map was evaluated by performing a voxel-by-voxel comparison with the segmented CT-based attenuation map. For each tissue class on the segmented CT, the fraction of voxels that were assigned to the correct tissue class in the UTE-MRI-based attenuation map and the fractions that were

assigned to the other tissue classes was determined.

The effect of the UTE-MRI-based attenuation map on the reconstructed PET images was also evaluated. This was done by calculating the relative difference between the images reconstructed with the CT-based and UTE-MRI-based attenuation maps in 12 volumes of interest. The VOIs were spherical with 10 mm diameter and were located in the left and right dorsal cortex, frontal cortex, lateral cortex, putamen, thalamus and white matter. The relative difference was calculated in each VOI:

$$\Delta_k\,(\%) = 100\,\frac{\sum\limits_i (P_{MRI,i} - P_{CT,i})}{\sum\limits_i P_{CT,i}} \tag{7.3}$$

where Δ_k is the relative difference and $P_{MRI,i}$ and $P_{CT,i}$ are the image intensities in voxel i in the PET images reconstructed with UTE-MRI-based and CT-based attenuation correction respectively. The sum is taken over all voxels in the VOI. To give a visual impression of the location of the errors in the reconstructed images, a percent difference image was also generated. This was done by calculating the relative difference in each voxel, and assigning a color intensity proportional to the percent difference to that voxel. Red was used for underestimation, blue for overestimation.

7.2.2 Results

Fig. 7.2 shows transverse slices of the FID and gradient echo images through the eye sockets of one subject. This region was chosen because it contains complex bone structures as well as air cavities (the ethmoidal sinuses) and hence is the most challenging for the classification algorithm. As was already observed in UTE images shown in the previous chapters, there is signal in the bone in the FID image. In the gradient echo image, this signal has practically disappeared. In the air cavities, there is no signal in the FID or in the gradient echo image.

The same transverse slice of the uncorrected and corrected R_2-maps are shown in fig. 7.3. The segmented UTE-MRI-based and CT-based attenuation maps are depicted in fig. 7.4. The voxel-by-voxel comparison of the segmented MRI and segmented CT yielded an overall accuracy of between 85 % and 95 % for all subjects. The tissue/air discrimination was at least 95 % in all cases. Approximately 95 % of air voxels are classified correctly. There are significantly more classification errors in voxels containing bone or soft tissue: up to 25 % of bone voxels are assigned the attenuation coeffi-

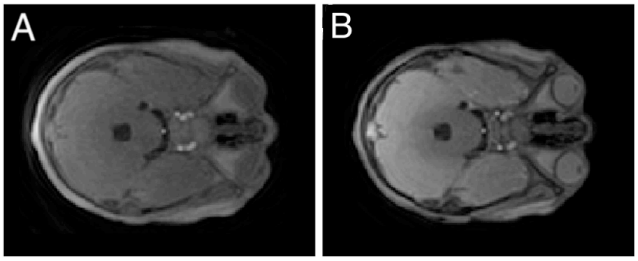

Figure 7.2: Transverse slices of the FID (A) and gradient echo (B) images of one of the data sets of the brain study.

cient of soft tissue. Approximately 20 % of soft tissue voxels are classified as bone. Fig. 7.5 shows a summary of the results per tissue type, averaged over all patients. Fig. 7.6 shows a summary per individual patient.

The same transverse slice as in fig. 7.2 is shown for the simulated PET images reconstructed with UTE-MRI-based and CT-based attenuation correction in fig. 7.7. A summary of the quantitative evaluation is shown in fig. 7.8. The average relative error over all VOIs was 3 %. Most VOIs showed relative errors between 0 and 5 %. The largest error in a single VOI was 9 %. Fig. 7.9 shows a transverse (A) and a sagittal (B) slice of the percent difference map of that subject. The largest deviation in a single voxel in the complete brain of this patient was an overestimation of 34 % in the border of the right eyesocket. Maximum deviations in other data sets were also between 20 and 40 %.

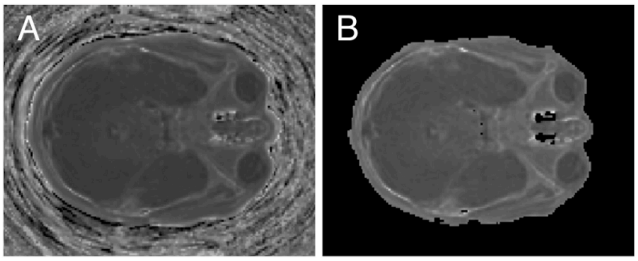

Figure 7.3: Transverse slices of the uncorrected (A) and corrected (B) R_2-maps of one of the data sets of the brain study.

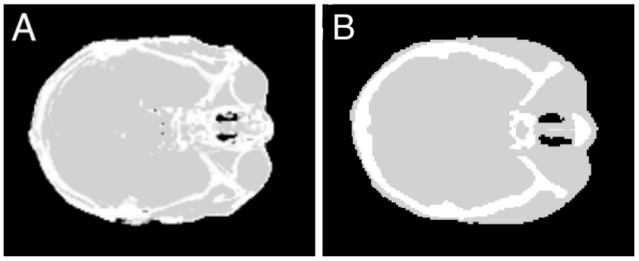

Figure 7.4: Transverse slices of the UTE-MRI-based (A) and CT-based (B) attenuation maps of one of the data sets of the brain study.

7.2.3 Discussion

As was observed in the previous chapters, the uncorrected R_2-map shows significant artefacts and can not be used to derive the attenuation map directly. The R_2 in the air surrounding the head is especially high. However, the corrected version shows a much better image. The ethmoidal sinuses are detected, showing that air inside the head can be discriminated from bone. It shows contrast between bone and soft tissue. However, this contrast seems

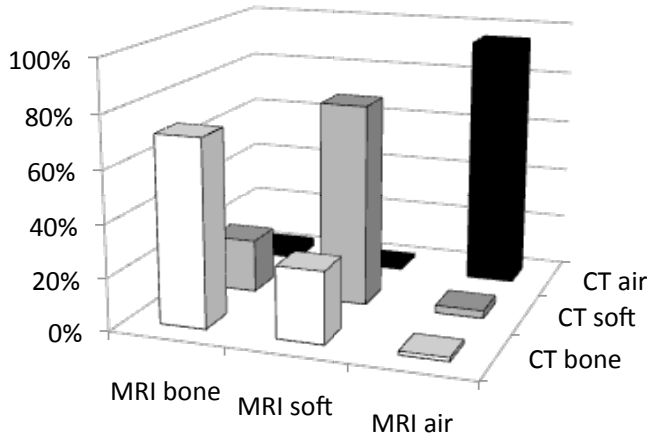

Figure 7.5: Evaluation of the classification accuracy of the UTE-MRI-based attenuation map (overview per tissue type). For each tissue type on the CT images, the fraction of voxels that were assigned to the correct and other tissue types were determined per patient. The average of these fractions was then taken and shown in this graph.

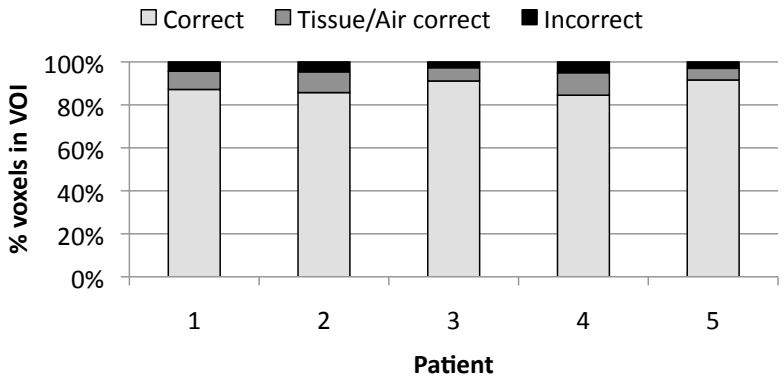

Figure 7.6: Evaluation of the classification accuracy of the UTE-MRI-based attenuation map (overview per patient). For each patient, the fraction of voxels that is assigned to the correct tissue class is shown, as well as the fraction of voxels that are misclassified from bone to soft tissue or vice versa (tissue/air correct) and the fraction of voxels that are misclassified from tissue (bone or soft tissue) to air.

lower than in the R_2-map of the pig head phantom, discussed in section 5.2. Several reasons can be proposed for this. First of all, the FID time was shorter in the phantom acquisitions (0.08 versus 0.14 ms). This may lead to more relaxation in the bone before acquisition, and hence less signal in the FID image. However, as R_2 is a quantitative measure which should not be influenced by the echo times, this should not have an effect. A lower R_2 can also be caused by partial volume effects. As explained before, the R_2 in voxels which contain bone as well as soft tissue will be lower than the R_2 in

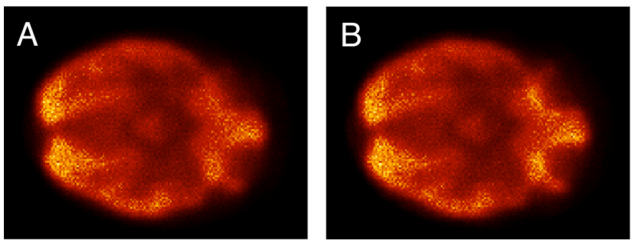

Figure 7.7: Transverse slices of the simulated PET images reconstructed with UTE-MRI-based (A) and CT-based (B) attenuation correction of one of the data sets of the brain study.

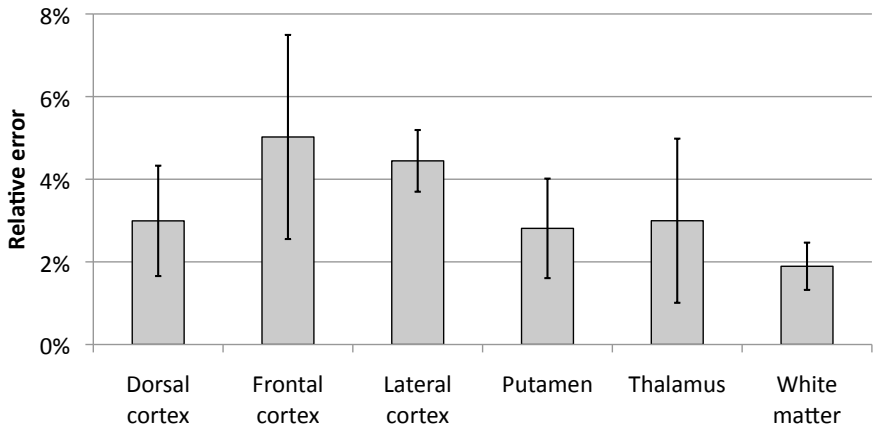

Figure 7.8: Average relative error in different VOIs between PET images reconstructed with CT-based and UTE-MRI-based attenuation correction. For each VOI location, the average was taken over the left and right side and the 5 patients. The error bars show the standard deviation on the error.

voxels which contain only bone. However, as the skull is quite thick, and the reconstructed resolution was quite high, this will probably only have minor effects on the brain UTE images. It is therefore not clear what is causing this lower contrast.

Even with a lower contrast between bone and soft tissue, an attenuation map discriminating air, soft tissue and bone can still be derived from the corrected R_2-map. The segmented UTE-MRI-based attenuation map shows that the same large bone structures as in the CT-based attenuation map are

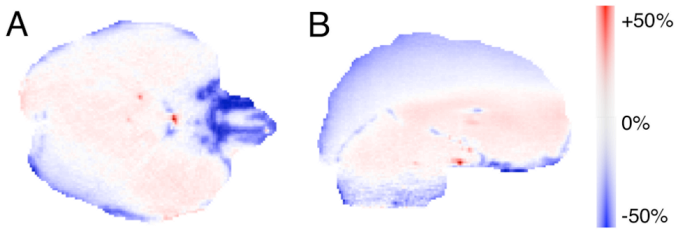

Figure 7.9: Transverse (A) and sagittal (B) slice of the percent difference image between PET images reconstructed with CT- and UTE-MRI-based attenuation correction.

detected. In the depicted slice, the skull is the most important. Some differences can be seen between both attenuation maps. The most obvious is that the skull seems thicker in the CT-based attenuation map. In part, this could be caused by the coarse axial resolution of the CT (slice thickness 5 mm) compared to the MRI. This can also explain the fact that some structures are only seen on the MRI-based attenuation map, such as the bony back of the eye sockets. As the ethmoidal sinuses also consist of bone structure with air cavities, it is possible that the UTE-MRI-based attenuation map, which shows bone near the sinuses, is actually a more accurate representation than the CT-based attenuation map. There are also some voxels that are clearly misclassified in the MRI-based attenuation map. Most obvious are the bone voxels in the center of the brain, which are definitely errors. There are also some segmentation errors at the border of the head, where bone is detected.

The quantitative evaluation of the classification accuracy shows very good tissue/air discrimination. The discrimination between bone and soft tissue is less accurate. However, as shown in the simulation studies in chapter 3, it is much better to confuse bone with soft tissue than bone or soft tissue with air. Overall, the fraction of classification errors between tissue and air is less than 5 %. The classification errors between bone and soft tissue amount to 20 - 25 %. In the simulation study, classification errors between bone and soft tissue of up to 20 % did not cause any relevant errors. We therefore expect that no large errors will be seen in the reconstructed PET images.

The comparison between PET images reconstructed with CT-based and UTE-MRI-based attenuation correction suggest that the segmentation errors do not cause large errors in the resulting PET image. Visual comparison of the PET images did not show large differences. Evaluation of the quantitative difference in different clinically relevant VOIs showed only small differences. The largest errors in the VOIs are found in the frontal cortex, which is explained by the presence of the frontal sinus. Although the frontal sinus was detected in all data sets, there may be some classification errors there, which lead to a slightly larger error. These results agree with the results obtained from the human brain simulation study in chapter 3.

The percent difference image shows that most errors in the reconstructed image can be found at the borders of the skull, which is where segmentation is most difficult. Nevertheless, these errors mostly remain below 15 %. Higher errors are seen in the vicinity of the ethmoidal sinuses and the eye sockets. However, this is compared to the CT-based attenuation map. As described above, the UTE-MRI images were acquired at higher resolution

than the CT images. It is therefore possible that the bone in the region of the eye sockets and the ethmoidal sinuses is more accurately classified in the UTE-MRI-based attenuation map.

Nevertheless, one should always be careful when looking at the reconstructed PET images in the vicinity of bone. Overestimation or underestimation of bone content could respectively cause artificial hotspots or cause tumors to become invisible in extreme cases. This is important in a clinical situation, as this may lead to under- or overdiagnosis and hence to incorrect patient treatment. None of the evaluated clinical data sets exhibited artifactual hot or cold spots. This is also visible in the reconstructed PET images: the 34 % difference in the vicinity of the orbits did not yield artifactual appearances on the PET images reconstructed with the UTE-MRI-based attenuation map.

These results therefore indicate that our method can be used for attenuation correction of human brain PET studies. As the derivation of the attenuation map is done without intervention of the operator, it can be fully automated. This would allow use of our method within a standardized clinical protocol, which is executed by a radiological technician. In the 5 data sets that were evaluated, no large errors were seen. However, this does not suffice to conclude that the method is robust, as 5 data sets can only be regarded as an extended proof of concept. To demonstrate clinical robustness, a larger study should be done, which also involves radiologists which evaluate the clinical interpretation of the images.

For implementation into a clinical protocol, the imaging time should also be as short as possible. In the described study UTE-MRI imaging time was 6 minutes. Considering that the total scanning time of a clinical MRI protocol is mostly between 30 and 60 minutes, this can be considered borderline acceptable. There are different options to reduce imaging time. First of all, the images could be acquired at a coarser resolution. However, this is difficult in the brain where many small bone structures and air cavities are present. A different option would be to reduce the number of spokes sampled in k-space. This will lead to a lower quality images, with more noise, which will probably not be tolerated as the FID image already has a low quality. As a last option, the acquisition scheme of the sequence could also be improved. As MRI sequence development is not the focus of this thesis, we have not investigated this. However, after this study was performed, a new UTE-MRI sequence, designed for Siemens systems, was installed at our hospital. It allows acquisition of UTE images with the same quality as

shown here in an acquisition time of 3 minutes. This would definitely be acceptable for clinical practice.

7.3 Thorax

7.3.1 Materials and methods

7.3.1.1 Acquisitions

A SPECT-CT of a single patient was acquired on a Symbia S SPECT-CT system (Siemens Medical Solutions, Malvern, USA). The patient had been treated with ^{131}I radio-ablation therapy for thyroid cancer. As the SPECT images showed only a very small region with uptake, they were not usable for evaluation of attenuation correction. The CT was a low-dose CT used for attenuation correction, acquired with settings 130 kVp, 70 mAs. The slice thickness was 5 mm. The reconstructed matrix was 512 x 512 x 73, with 1 mm in-plane resolution.

UTE-MRI images were acquired on a Philips Achieva 3T system with a Torso XL chest coil. The UTE sequence described in section 4.2.3 was used. The FID and gradient echo times were 0.14 ms and 2.3 ms respectively. The reconstructed matrix was 125 x 125 x 100, with 4 mm isotropic voxel dimensions. This yielded a field of view of 500 x 500 x 400 mm, which comprised the complete chest and part of the neck axially. Transaxially, part of the arms were outside the maximum field of view of the MRI scanner and hence not visible. The total acquisition time was 2 minutes.

7.3.1.2 Derivation of attenuation maps

Registration of the MRI images to the CT images was done manually with AMIDE[244]. Different attenuation maps were then derived. First, the reference CT-based attenuation map was derived. As bilinear scaling is currently the gold standard for derivation of the attenuation map in whole-body PET-CT studies, this method was used. The CT Hounsfield units (HU) were scaled to linear attenuation coefficients at 511 keV using the following equations:

$$\begin{aligned} \mu\,(cm^{-1}) &= 0.097\,\tfrac{HU+1000}{1000} && HU \leq 0 \\ &= 0.097 + 0.057\,\tfrac{HU}{1000} && HU > 0 \end{aligned} \tag{7.4}$$

This equation is comparable to the one used in section 6.3, but a different scaling factor is used as different CT settings apply for this study. The basic equation was obtained from [198].

Three MRI-based attenuation maps were derived from the UTE-MRI images. As was demonstrated in the simulation studies in chapter 3, accurate thoracic imaging requires the discrimination of 5 tissue types: air, lung, soft tissue, spongeous bone and cortical bone. Ideally, an attenuation map should therefore be obtained which accurately discriminates these 5 tissue types. However, cortical bone can not be discriminated accurately with a resolution of 4 mm. As the cortical shell of the spine vertebrae and the ribs is only 1 - 2 mm thick, partial volume effects make it impossible to discriminate cortical bone from the surrounding soft tissue and spongeous bone. Therefore we will not aim to discriminate cortical bone, but aim to discriminate 4 tissue types: air, lung, soft tissue and bone, the latter representing a combination of cortical and spongeous bone.

Threshold-based UTE-MRI attenuation map

The first UTE-MRI-based attenuation map was derived with a method comparable to the one used in the rat micro-PET and micro-SPECT studies described in chapter 6. The first two steps comprise the calculation of the R_2-map and the correction with an air mask, as described in section 4.4. The attenuation map was then derived using a mapping of R_2 values to linear attenuation coefficients at 511 keV as follows:

$$\begin{array}{lll} \mu\,(cm^{-1}) = 0 & R_2 = 0 & \text{(air)} \\ \quad = 0.097 & 0 < R_2 \leq 0.5 & \text{(soft tissue)} \\ \quad = 0.097 + (0.13 - 0.097)\frac{R_2 - 0.5}{0.1} & 0.5 < R_2 \leq 0.6 & \text{(bone)} \\ \quad = 0.03 & R_2 > 0.6 & \text{(lung)} \end{array} \tag{7.5}$$

where air, lung, soft tissue and bone are discriminated. As simple thresholds on the R_2-map are used to discriminate different tissue types, this attenuation map is called the threshold-based map in what follows.

Theoretically, this should yield an accurate attenuation map. Unfortunately, the image quality of UTE images is not optimal. This will lead to two problems in the attenuation maps:

1. Large local variations in the apparent R_2 of lung tissue. This yields highly inhomogeneous lungs in the R_2-map, and difficulties segmenting

the lungs based on the R_2 value of a single voxel. It will lead to the segmentation of voxels in the lungs as bone and soft tissue.

2. Significant inhomogeneity of the images, especially at the outer parts of the FID image. This will lead to changes in the apparent R_2, which make segmentation of the complete image with the same R_2 thresholds difficult. It will lead to errors between bone and soft tissue in the outer parts of the image.

Possible explanations for these problems are discussed in section 7.3.3. A solution to these problems needs to be found in order to derive a more accurate attenuation map. The solution consists of employing more advanced segmentation methods than simple thresholding, and is described below.

MRF-based UTE-MRI attenuation map

Both issues that lead to problems in the threshold-based attenuation map are solved by modifying the derivation of the attenuation map from the R_2-map in two ways. First, the segmentation of the lungs can be improved by using a segmentation algorithm that performs classification of voxels not only based on the value in the current voxel, but also on the values of the surrounding voxels. This can be done using Markov random field (MRF) segmentation with a Gibbs prior. The extensive description of MRF segmentation is outside the scope of this thesis. We have used the MRF segmentation method that is implemented in the Insight Toolkit[243]. It suffices here to say that MRF segmentation attempts to classify each voxel into the tissue class to which the voxel has the smallest distance. The distance is calculated based on local (the value of the current voxel) and regional (the values of the neighboring voxels) information. MRF classification will allow segmentation of the lungs as a homogeneous structure, as local variations will be compensated by regional information.

MRF segmentation can not be used for the bones, as they are too small to allow taking regional information into account. Therefore, a different method is needed for this. Due to the global inhomogeneity of the R_2-map, it is difficult to derive a classification method which will correctly classify bone in all regions of the thorax. However, if a region is homogeneous in itself, simple classification method will work there. Therefore, we modified our method so that bone is only detected in a single region. In all other regions, only air, lung and soft tissue are detected. As one of the possible applications of PET-MRI is cardiac imaging, we decided to focus on bone segmentation in the spine. This was done because the spine is the most important bone

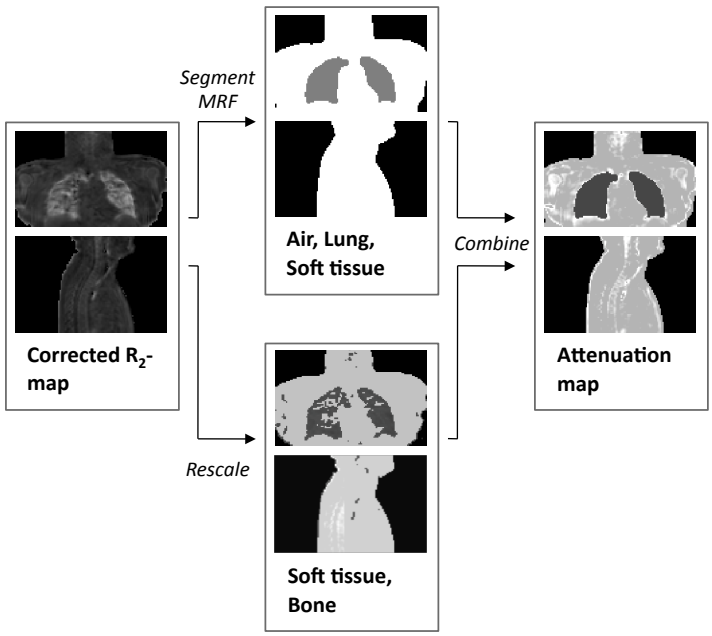

Figure 7.10: Modified algorithm for the derivation of the attenuation map from UTE-MRI images, using Markov random field segmentation to classify lung voxels.

structure close to the heart. Attenuation of the other bones in the thorax has a smaller effect on cardiac imaging as they are either further removed from the heart (such as the arm bones) or smaller than the spine (such as the ribs). The spine also has the advantage that it is quite easy to locate, as it is concentrated in a cylinder parallel to the longitudinal axis of the body.

To include these modifications, the algorithm was changed as shown in fig. 7.10. The first steps comprise the derivation of the corrected R_2-map as described already and are not shown in the image. Then, two operations are performed on the corrected R_2-map. The first is a MRF segmentation, which classifies the voxels in the image into air, lung or soft tissue. The second is a modified version of the mapping described in eq. 7.5. In a cylinder paralell to the longitudinal axis of the body, which contains the spine, the same mapping as in eq. 7.5 is used. This means that air, lung, soft tissue and bone are discriminated in that region. In all other regions of the body, bone tissue is not discriminated and the following mapping is used:

$$\begin{aligned} \mu\,(cm^{-1}) &= 0 \quad R_2 = 0 \quad \text{(air)} \\ &= 0.097 \quad 0 < R_2 \leq 0.6 \quad \text{(soft tissue)} \\ &= 0.03 \quad R_2 > 0.6 \quad \text{(lung)} \end{aligned} \tag{7.6}$$

Then, both derived images were combined into the UTE-MRI-based attenuation map in a final step. In each voxel, the tissue class obtained with the MRF segmentation was determined. If the voxel was classified as lung or air, the attenuation coefficient of lung or air was assigned in the final attenuation map. If the voxel was classified as soft tissue by the MRF segmentation, the value of the voxel in the final attenuation map was set to the value in the second derived image. This can then be the attenuation coefficient of soft tissue or bone. To evaluate the effect of the regional bone segmentation separately, an attenuation map which does not contain bone was also derived, directly from the segmented MRF attenuation map.

7.3.1.3 PET simulation

As the SPECT images were not useable for the evaluation of attenuation correction, a simulated PET was generated. This was done with the same method as in the brain study described above. However, as the field of view in this study was larger than in the brain study, the axial field of view of the scanner was doubled by simulating a scanner with twice as many rings. The simulated activity distribution was obtained by segmenting the CT into air, lung, soft tissue and bone and assigning the activity distribution of a healthy patient injected with ^{18}F-FDG[211]. The images were then reconstructed with 4 attenuation maps:

- CT-based,
- threshold-based UTE-MRI attenuation map,
- MRF-based UTE-MRI attenuation map with discrimination of bone in the spine,
- MRF-based UTE-MRI attenuation map without discrimination of bone.

7.3.1.4 Analysis

The reconstructed PET images were compared quantitatively by calculating the total counts in volumes of interests in different organs. 10 VOIs were

drawn in the lungs (5 left, 5 right), 5 in the heart and 4 in the spine. The VOIs were spherical with a diameter of 20 mm. In each VOI, the relative difference in total counts with the CT-based reconstruction was calculated:

$$\Delta_{X,k}\,(\%) = 100\,\frac{\sum\limits_{i}\left(P_{X,i} - P_{CT,i}\right)}{\sum\limits_{i} P_{CT,i}} \tag{7.7}$$

where $\Delta_{X,k}$ is the relative difference in VOI k, $P_{X,i}$ and $P_{CT,i}$ are the reconstructed PET values in voxel i reconstructed with MRI-based attenuation map X and CT-based attenuation map respectively. The sums are taken over all voxels i in the VOI. For each organ, the average absolute relative difference was calculated:

$$\Delta_{X,O}\,(\%) = \frac{1}{N_O}\sum_{k\in O}\left|\Delta_{X,k}\right| \tag{7.8}$$

where O is the organ and N_O is the number of VOIs in the organ.

7.3.2 Results

Fig. 7.11 shows coronal and sagittal slices of the FID and gradient echo images acquired. The uncorrected and corrected R_2-maps are shown in fig. 7.12, and the attenuation maps that were used are depicted in fig. 7.13. The UTE-MRI-based attenuation map derived by simple mapping from R_2 to μ shows that the general contour of the lungs is segmented correctly. The structure of the spine and parts of the shoulder bones can also be seen. However, many differences with the CT-based attenuation map can be observed. Especially the oversegmentation of bone on one side of the body, and detection of bone voxels inside the lungs and at the border of the lungs are seen.

The third attenuation map, which was derived with the modified algorithm and determines the lungs using MRF segmentation and only detects bone in the spine region, shows a better image. The segmentation of the lungs by the MRF method is accurate, except for the large bronchi in the middle of the lungs, which are classified as soft tissue. The detection of the structure of the spine is also adequate. Obviously, other bones such as the shoulder bones are not detected. Small soft tissue structures in the lungs, such as the vessels, are also not detected. The last attenuation map shows a comparable image but without the spine.

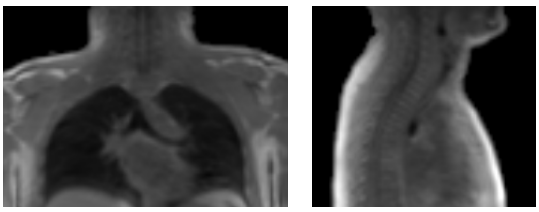

(a) FID

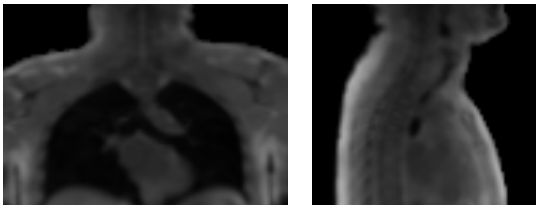

(b) Gradient echo

Figure 7.11: Coronal (left) and sagittal (right) slices of the FID (a) and gradient echo (b) images acquired in the thorax study.

The reconstructed PET images are shown in fig. 7.14. Reconstruction with the CT-based attenuation map shows uniform activity distributions in the lungs, soft tissue and bones. Reconstructing with the first, threshold-based UTE-MRI attenuation map shows many differences with the CT-based reconstruction. Especially remarkable are the artificial hot spots that are created in the lungs. The acivity distribution in the rest of the body is also not uniform. Less artefacts are seen when reconstructing with the attenuation maps derived using MRF segmentation. In the map that discriminates air, lung, soft tissue and bone, the activity in the lungs is quite uniform, with the exception of small underestimations at the border of the heart and a significant overestimation in the region where the large bronchi are normally found. The activity distribution in soft tissue and the lower part of the spine is also quite uniform, but clear underestimations are observed in the upper part of the spine and in the other bones. Reconstruction with the last attenuation map shows comparable images, but with larger underestimations in the spine.

The quantitative evaluation of the differences between the PET images reconstructed with the CT-based and the three UTE-MRI-based attenuation maps is depicted in fig. 7.15. The threshold-based UTE-MRI attenuation map shows errors of over 10 % in the lung and spine VOIs. In the heart the average error remains below 5 %. The MRF-based UTE-MRI attenuation

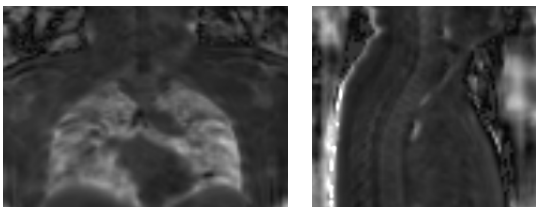

(a) Uncorrected R_2-map

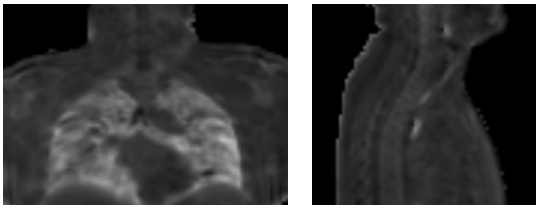

(b) Corrected R_2-map

Figure 7.12: Coronal (left) and sagittal (right) slices of the uncorrected (a) and corrected (b) R_2-map of the thorax study.

map with bone discrimination yields average errors of less than 5 % in the lung, spine and heart. The MRF-based map without bone shows comparable results in the lung and heart but leads to much larger errors ($\approx$ 26 %) in the spine.

7.3.3 Discussion

Although the threshold-based UTE-MRI attenuation map shows that most of the lung tissue is detected and large bone structures are also detected, it also displays many local errors. The bone/soft tissue segmentation errors in one side of the body are mainly caused by inhomogeneity in the FID image. This leads to a higher apparent R_2 in the voxels in that region, which is comparable to the R_2 of bone in other regions of the image. It is unclear how the inhomogeneity could be corrected, especially since it mostly affects the FID image. Homogeneity corrections such as CLEAR (Constant LEvel AppeaRance) can be used, but they will affect the FID and gradient echo image comparably, and will therefore most probably not fix this problem.

The errors in the lung, where local variations in the R_2 values lead to misclassification of some lung voxels into bone and soft tissue, are even more problematic. These can be caused by different effects. One possibility is high noise due to the low signal in the lungs, but the UTE sequence is

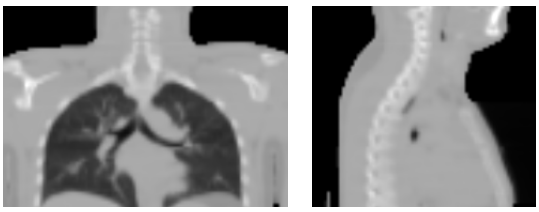

(a) CT-based

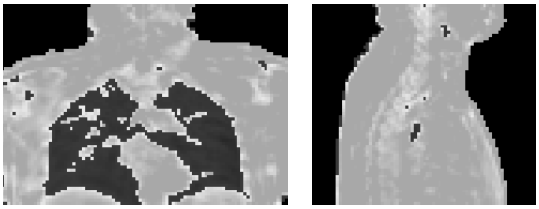

(b) Threshold-based UTE-MRI

(c) MRF-based UTE-MRI with bone

(d) MRF-based UTE-MRI without bone

Figure 7.13: Coronal (left) and sagittal (right) slices of the attenuation maps used in the thorax study. The CT-based (a) and three UTE-MRI-based (b-d) attenuation maps are shown.

used to obtain higher signal in the lungs so this should not be a problem. Secondly, there is also a lot of motion in the lungs, which may lead to complex effects. A third possible reason is that the lungs have a highly inhomogeneous structure, composed of a combination of alveoli, air ducts

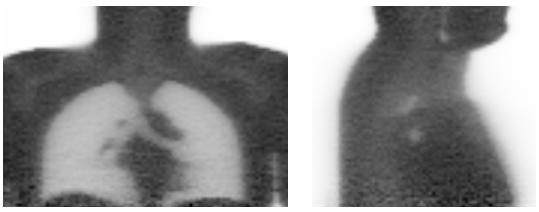

(a) CT-based

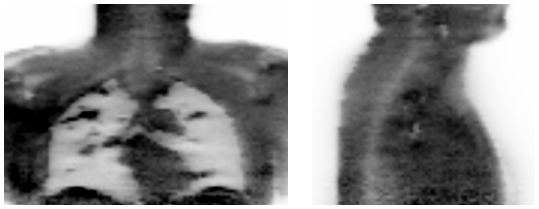

(b) Threshold-based UTE-MRI

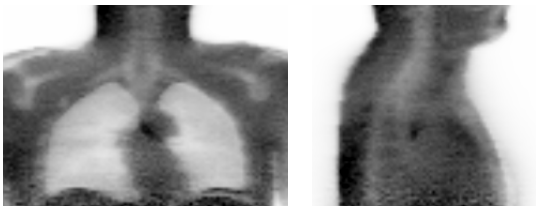

(c) MRF-based UTE-MRI with bone

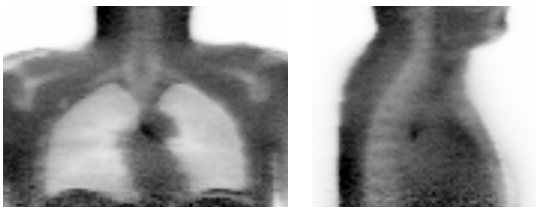

(d) MRF-based UTE-MRI without bone

Figure 7.14: Simulated PET images of the thorax study, reconstructed with different attenuation maps (a-d). Coronal (left) and sagittal (right) slices are shown.

and small vessels. This in itself may also lead to inhomogeneity, and even more so when motion is added. The inhomogeneous R_2 in the lungs is probably caused by a combination of these factors.

Another difference between the CT-based and threshold-based UTE-MRI attenuation map can be observed. In the CT-based attenuation map, some

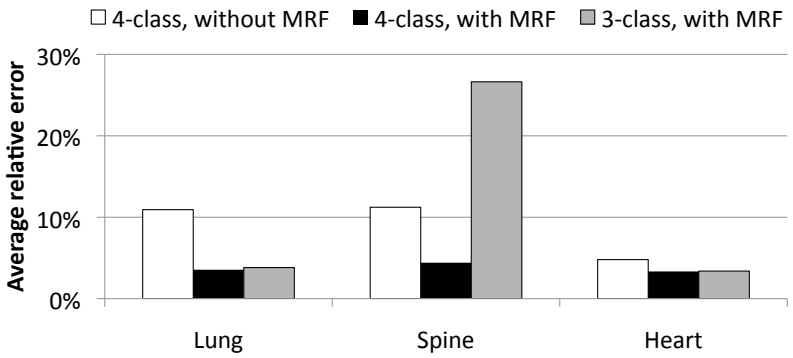

Figure 7.15: Average relative error in the VOIs in the lung, spine and heart in the PET images reconstructed with three different UTE-MRI-based attenuation maps. 4-class = air, lung, soft tissue, bone and 3-class = air, lung, soft tissue.

vessels can be seen, especially close to the heart. In the MRI images, these vessels are very difficult to visualize. This can be related to flow artefacts, which are caused by the flow of blood through the vessels. The protons in the blood are moving through the imaging volume instead of remaining at the same location as other protons. Therefore, they are influenced by the RF pulses and gradient fields in a different way, rendering them difficult to visualize. Breathing motion can also have an effect. As the acquisition time of the MRI is much longer than the CT, the MRI image is acquired over multiple breaths. Therefore, the vessels also move during the MRI acquisition and their signal is smoothed over different voxels.

The different errors in this attenuation map lead to many errors in the reconstructed PET image. Especially the creation of artificial hot spots in the lungs is a big problem for interpretation of the images. If only a MRI image and a PET image with so many artefacts are available, it is not possible for the radiologist to decide if a pathological process, such as a lung tumor, is present or if the hot spots are caused by errors in the attenuation map. The inhomogeneity in the lateral parts of the body can also cause problems for the same reasons. The main problem is that this method leads to unpredictable errors, which may be present in one image but not in another. This may lead to an incorrect clinical diagnosis. This can be either a diagnosis of a tumor if none is present, which may lead to unnecessary medical or surgical therapy, or a tumor that is missed, which leads to undertreatment. Both situations are unacceptable in clinical practice. The quantitative evaluation also shows errors that are too large, which

can be expected when looking at the images qualitatively.

The MRF-based UTE-MRI attenuation map, derived with the modified algorithm in which the lungs are segmented using MRF segmentation and bone is only detected in the spine region, is much better. The general contour of the lungs is accurately detected, and the spine is also discriminated. No other bone is detected, as intended. This causes an error in itself, but also has the advantage that no erroneous bone voxels are assigned in other parts of the body. For example, there is no bone/soft tissue misclassification on one side of the body. We can also see that the entire content of the lungs is homogeneous, without bone or soft tissue voxels. This shows that the MRF method works well and enables classification of voxels not only based on their own value but also on the values of neighboring voxels. There is a downside to MRF segmentation of the lungs, as it also leads to small structures being ignored. Two examples are seen in the lung region. First, none of the lung vessels are detected. However, as already discussed, the long acquisition time of the MRI images probably makes it impossible to visualize these vessels anyway, due to motion. Second, the large bronchi, which are situated just above the heart, are classified as soft tissue whereas they should actually be classified as air. This does cause problems, as discussed below.

The PET images reconstructed with this attenuation map are much better than with the first UTE-MRI-based attenuation map. The lungs and the soft tissue regions show relatively homogeneous activity uptake, as in the images reconstructed with the CT-based attenuation map. The heart also shows uniform uptake. Underestimation of activity is seen in the periferal bones, which were not detected by the algorithm. However, this is a predictable effect, which will be present in all images and can be taken into account by the radiologist when interpreting the images. Limited underestimation is also seen in the part of the lungs close to the mediastinum, where lung vessels are seen on the CT but not on the MRI. However, this does not lead to real cold spots. The segmentation error at the large bronchi, which leads to segmentation as soft tissue instead of air, do lead to a big problem. A clear artificial hot spot is created, which may cause problems in clinical interpretation.

The quantitative evaluation of this method in VOIs in the lung, heart and spine shows good results. As all average errors are below 5 %, this seems acceptable for quantification. This was also the limit that was used for evaluation of the simulation study in chapter 3. Evaluation of the last attenuation map, in which the spine is not discriminated, shows that it is

useful to detect bone in the spine. Indeed, an average error of over 25 % is seen in the spine, which is far too high to allow quantification. As quantification in the spine is accurate in the reconstruction where bone is discriminated, we can conclude that merging cortical bone and spongeous bone into a single class does not cause any problems. As the thickness of the cortical bone layers is mostly smaller than the scanner resolution, this is understandable. In this way, the recommendations derived in chapter 3 are partially fulfilled: only 4 tissue classes are distinguished, but the fourth tissue class actually comprises a combination of spongeous and cortical bone.

Overall these results indicate that our method could be used for attenuation correction of thorax PET images, but with caution. There is probably no problem for cardiac imaging, which is an important possible application of PET-MRI, as the heart and lungs are segmented accurately. However, there is still the possibility of important classification errors, as was shown with the artificial hotspot in the large bronchi in these results. Also, we have only evaluated our method in a data set from a single patient here. In order to claim feasibility, a more extensive study should be done, comparable to the brain study presented in the first part of this chapter. However, this was not done, in part for the reasons described in the next section.

7.4 Whole-body

As already mentioned in the introduction to this chapter, no evaluation of our method for whole-body imaging was done. The motivation for this is discussed here, together with other considerations regarding whole-body MRI-based attenuation correction. There are several reasons why the application of UTE-MRI-based attenuation correction to whole-body imaging will be very difficult. First of all, there is the intrinsic difficulty of discriminating all five tissue types that are important for attenuation correction based on the MRI image alone. This was shown in the previous section, and leads to various problems. First, the discrimination of cortical bone is impossible with limited resolution, as cortical bone is too thin. Therefore a compound tissue class, containing cortical and spongeous bone, was created. Second, a very inhomogeneous R_2 was observed in the lungs. Therefore, MRF segmentation was used to determine the contour of the lungs. And third, the inhomogeneity of the images can cause large problems and requires different segmentation thresholds for different regions of the body. This was solved by only detecting bone in the spine region, which was defined as a cylinder

parallel to the axis of the body. However, these last two methods already take into account some anatomical information and determine the attenuation map not solely from the MRI image anymore. This partly counteracts the primary reason for using UTE sequences.

A second reason why UTE-MRI-based attenuation correction for whole-body studies will be difficult, is the long acquisition time of the UTE images. For the single data set presented in the previous section, MRI acquisition time was 2 minutes. This can be acceptable for a cardiac study, where the complete attenuation map may be acquired with a single bed position. However, in a whole-body study multiple bed positions of the attenuation map will need to be acquired. For a normal adult at least 5 bed positions will be needed, yielding a MRI acquisition time of 10 minutes or more for acquisition of the attenuation map alone. This can be considered quite long. The acquisition time for the UTE-MRI could be reduced by acquiring at a coarser resolution, but this would lead to even more segmentation difficulties.

Thirdly, motion is not compensated in the UTE sequence at the moment. Therefore, it is unclear what the effect of motion is, especially in the thorax. It will definitely lead to blurring of the heart and lung borders. However, one can argue that this is not a problem for PET attenuation correction, as PET images are also acquired over many cardiac and respiratory periods. In fact, as was discussed in chapter 2, one of the issues with CT-based attenuation correction is that the CT is acquired much faster and hence shows only part of the respiratory period. This can lead to reconstruction artefacts in the PET image, such as a cold liver dome. Nevertheless, it is not sure if the effect of motion on the PET and MRI images is the same. Therefore, the acquisition of a static attenuation map would be interesting. By implementing cardiac and respiratory gating into the UTE sequence, this could be done. However, this would again lead to an increase of the acquisition time, which is already too long as it is.

A fourth problem is that, for whole-body imaging, the method must be tested and validated in different regions of the body. For example, for thoracic imaging the segmentation of the spine is probably most important. However, for other parts of the body, different bones should be taken into account. In the pelvis, e.g. for prostate imaging, the hip and sacral bones will have a much larger effect than the spine. In the legs and arms, other bones will also be more influential. Implementing a region-based segmentation for all these bones can be possible, but will lead to many assumptions on patient anatomy which we want to avoid. Derivation of the attenuation map in the abdomen will also require a different focus. In that part of the

body, discrimination of adipose tissue may be important.

All these considerations lead to the conclusion that our UTE-MRI-based method for deriving the attenuation map is currently not applicable to whole-body PET-MRI imaging. To allow this in the future, different improvements need to be made. The most important improvement can be made by optimizing the UTE sequence, possibly improving image quality and shortening acquisition time. Furthermore, investigations need to be done into different regions of the body. When the feasibility of UTE-MRI-based attenuation correction has been shown on all body regions separately, an algorithm could be derived which combines different methods to obtain a whole-body UTE-MRI-based attenuation map.

Apart from the issues that are specific to UTE-MRI-based attenuation correction, there are also other difficulties in whole-body MRI-based attenuation correction in general. First, there is the problem of field-of-view truncation in MRI. In general, the field of view of the MRI scanner will not contain the complete body in the transaxial plane. Usually, the arms are not completely included in the image. However, PET attenuation is not limited to the FOV as it is a physical effect. Therefore, the attenuation map also needs to include the arms. This problem could also be avoided by asking the patient to place the arms behind the head. Unfortunately this is quite uncomfortable for a long PET-MRI exam.

Another problem in whole-body MRI-based attenuation correction is caused by the MRI coils. These coils are usually developed to be invisible on MRI images, but do cause attenuation. Coil attenuation may even be quite high, as they often contain metal parts. Therefore, coils need to be included in the attenuation map. For rigid coils, such as brain coils, this is not a big problem: a template can be derived and added to the attenuation map, comparable to what was done for the bed and plastic tube in the micro-PET and micro-SPECT studies described in chapter 6. However, in whole-body imaging, flexible coils are often used, such as the torso coil that was used in the thorax study. As these coils usually have a different location and orientation for each patient, inclusion in the attenuation map is more difficult. If the location and orientation of the coil could be determined, this could be solved. It may be possible to do this using UTE sequences, as they allow visualization of the plastic of the coils.

A last remark can be made about the usability of the MRI images acquired to derive the attenuation map for other purposes than attenuation correction. In PET-CT, the CT is not only acquired to obtain the attenuation map but

also serves as an anatomical reference. If the MRI images that are used for attenuation correction could also serve as a general anatomical reference, this would be interesting. This would also place a less severe constraint on the acquisition time that can be used to acquire the attenuation map. Some authors have proposed the use of Dixon-based methods for the derivation of the attenuation map[207]. This involves a whole-body acquisition with a Dixon sequence, which yields images that can also be used as a general anatomic reference.

7.5 Conclusion

In this chapter, we have demonstrated the feasibility of applying our UTE-MRI-based attenuation correction method to human brain imaging. This was done by testing the method on 5 patients, and evaluating the classification accuracy of the attenuation map as well as the quantitative accuracy of the reconstructed PET images. The distinction between tissue (bone or soft tissue) and air showed an accuracy of 95 % or more in all patients. The average quantitative error in different clinically relevant VOIs was 3 %. The maximum error observed in a VOI was 9 %. These numbers are acceptable for clinical imaging. Most importantly, no artificial hot spots or cold spots were observed in the images.

We also evaluated our method on one single human thorax data set. It was shown that derivation of the attenuation map for thoracic imaging is a lot more cumbersome. While no such assumptions were made in all other studies presented in this thesis, limited assumptions on patient anatomy were needed to obtain a relatively accurate attenuation map from the UTE images. Visual evaluation showed mostly limited differences with the PET images reconstructed with CT-based attenuation correction, but a single artificial hot spot was created. Therefore, this method can only be used in a clinical context with caution. The attenuation correction is probably accurate enough to allow quantitative cardiac imaging, which is one of the possible applications of PET-MRI. However, a more extensive validation should be done to reliably evaluate feasibility.

The application of UTE-MRI-based attenuation correction to whole-body imaging was not evaluated. In our opinion, there are still a lot of limitations that need to be overcome in order to allow application of our method to whole-body imaging. Most importantly these limitations include the image quality of the UTE images and the total acquisition time needed to acquire a whole-body attenuation map. Also, different algorithms may be needed in

different regions of the body, such as the thorax, abdomen, or pelvis.

7.6 Original contributions

The clinical brain study, presented in the first part of this chapter, was published in a A1 journal paper[239]. It was also presented at the second PET-MR workshop in Juelich, Germany in 2010[261]. The evaluation of our method on a single thorax data set was presented at the EANM conference in 2010[262].

Chapter 8

General conclusions

In this chapter, a general overview of the work presented in this thesis is given. For each chapter, the most important results are summarized together with the conclusions that can be drawn from them. Afterwards, an overall conclusion is presented.

8.1 Summary

In chapter 2, a number of concepts and methods that are used throughout this work were introduced. In the first part, emission tomography was discussed. Emission tomography is based on the tracer principle, in which a radioactive isotope is linked to a tracer molecule and the radiation emitted by the isotope is recorded by a scanner. Two types of isotopes are used: positron emitters (used in PET) and single photon emitters (used in SPECT). The imaging principles of PET and SPECT were explained, starting from the gamma detector invented by Anger in 1957. Next, a brief overview of reconstruction methods was given. Special attention was devoted to the ML-EM iterative reconstruction algorithm, which was extensively used in this thesis. In PET and SPECT there are different physical effects that degrade image quality, such as sensitivity, resolution, attenuation and scatter. These effects and the correction methods that are mostly used to correct for them were also described. Subsequently the basics of Monte Carlo simulation in emission tomography were explained. In the last section on emission tomography, the clinical and preclinical applications of PET and SPECT were discussed.

In the second part of chapter 2, magnetic resonance imaging was intro-

duced. After describing the principles of spin physics and nuclear magnetic resonance, the imaging principles were discussed. Particular attention was given to the k-space theorem and the principles of spin echo and gradient echo sequences. A brief description of MRI hardware was also given. Finally, the most important current clinical and preclinical applications of MRI were discussed.

Multimodality imaging was introduced in the third part of the introductory chapter. The advantages of combining information from different medical imaging modalities were explained. The design of PET-MRI and SPECT-MRI systems raises quite a few difficulties, which were also discussed. Subsequently, an overview was given of the different PET-MRI and SPECT-MRI systems that have been designed, from the first prototype systems to the currently available human scanners.

As this thesis concerns MRI-based attenuation correction, the last part of chapter 2 was devoted to this topic. First an overview was given of the results that have been presented on the effect of attenuation on the reconstructed images. Next, the implementation of attenuation correction into the reconstruction algorithm was explained. Subsequently, the different methods that have been used historically to derive the attenuation map were discussed. In the last section, the challenges of MRI-based attenuation correction are explained, along with the current methods that have been proposed and their limitations. The goal of our work was also introduced: to develop a method which allows the derivation of the attenuation map based on MRI image intensity alone.

Before designing a new MRI-based attenuation correction method, it is important to determine how accurate this method needs to be. This was done using simulations in chapter 3. As the effect of attenuation depends on the size and constitution of the object under study, it will be different in small animal imaging, human brain imaging and human whole-body imaging. Therefore, 3 simulation studies were done with the ROBY, XCAT brain and XCAT whole-body phantom respectively. The GATE simulation toolkit was used. The simulated PET data was reconstructed with different attenuation maps, to evaluate the effect of different errors in the attenuation map on the reconstructed PET images. Attenuation maps were derived to determine the effects of ignoring different tissue classes, the effect of inter-patient variability, and the effect of tissue classification errors. The quantitative difference in VOIs between the images reconstructed with the correct and the modified attenuation maps were calculated.

The results indicated that discriminating air, lung and soft tissue is sufficient in small animal studies. Cortical bone can also be discriminated for a higher accuracy, but is not explicitly necessary. Tissue classification also does not need to be extremely accurate: tissue classification errors in bone and lung of up to 20 % did not show relevant changes in the quantitative accuracy of the reconstructed PET images.

In human brain studies, the three tissue classes present in the head should be included to allow quantitative imaging: air, soft tissue and cortical bone. Classification errors from cortical bone to soft tissue did not lead to relevant effects even if 20 % of voxels were misclassified. More care should be taken with classification errors from cortical bone to air. They may lead to significant effects, even if only 10 % of voxels are misclassified. A MRI-based attenuation correction method for human brain imaging should therefore be designed so that it is more likely that cortical bone will be misclassified as soft tissue than as air.

For human whole-body imaging, even more stringent requirements were derived from the simulation results. Five tissue types need to be discriminated to allow accurate quantification: air, lung, soft tissue, spongeous bone and cortical bone. Additionally, adipose tissue may also be included when possible. Although the effect of the inter-patient variability of the attenuation coefficient of cortical bone was negligible, this was not the case for lung. Therefore, it would be interesting if the attenuation coefficient of lung tissue of a specific patient could be derived from the MRI images of that patient. Misclassification of lung to air was tolerable if 10 % or less of the lung voxels were misclassified. If lung is misclassified to soft tissue or cortical bone, even 5 % errors lead to relevant effects. Classification errors of cortical bone to soft tissue were acceptable, even if 20 % of cortical bone voxels were set to soft tissue. Classifying cortical bone as air or lung was not acceptable. Therefore, a whole-body attenuation correction method should be designed so that lung is more likely to be misclassified as air, and cortical bone is more likely to be misclassified as soft tissue.

In chapter 4, UTE sequences were introduced. UTE sequences are used in MRI imaging to visualize tissues with very short T_2, such as tendons and ligaments, which can not be visualized with conventional MRI sequences. Lung and cortical bone, two tissue types which are important for attenuation, also have a very short T_2. Therefore, we propose using UTE sequences for derivation of the attenuation map. The principles of UTE imaging were first introduced, along with the properties of the Philips UTE sequence that is

used for most experiments in this thesis. This sequence acquires two images: one of the FID, which is acquired as shortly as possible after RF excitation, and one normal gradient echo image. The MRI properties of lung and cortical bone were investigated in the next section. The results indicated that it was possible to visualize lung and cortical bone using UTE sequences.

In the last section of chapter 4, the development of the basic method that was used throughout this thesis was described and tested on a segment of bovine femur bone. It was shown that UTE sequences allow the visualization of cortical bone. MRI image intensity is not a quantitative parameter and depends on receiver gain settings. Therefore, it can not be used reliably for automatic segmentation. We introduced the R_2-map, which represents the transverse relaxation rate in each voxel, and can be calculated from both images acquired by the UTE sequence. As voxels containing air may have a high R_2 due to artefacts in the FID image, the images need to be masked with a binary mask to set all voxels containing air to zero. This yields the corrected R_2-map, which shows distinctive intensities in air, soft tissue and cortical bone.

Before moving on to real animal or human imaging, we tested our method on phantom data in chapter 5. As no phantoms are currently available that have a realistic appearance on PET, CT and MRI, new phantoms were designed. There are also no synthetic materials available that realistically mimic lung or cortical bone on all three modalities. Therefore, biological tissue was used in the phantoms. The first phantom was a pig head, obtained from a local slaughterhouse. It was used as a model for human brain imaging, as it contains the same tissue types (air, soft tissue and bone) and has a comparable complexity. The classification accuracy of the segmented UTE-MRI-based attenuation map was compared to the segmented CT-based attenuation map. The accuracy was approximately 90 % for cortical bone and soft tissue and 80 % for air. The results from the simulation study indicated that this was sufficient for accurate quantification.

A human thorax phantom was also created, to evaluate the feasibility of discriminating air, lung, soft tissue and cortical bone with our method. For the bone part of the phantom a segment of bovine femur bone was used. For the lung part a lobe of pig lung was used, obtained from a pig sacrificed after a cardiac surgery experiment. The phantom was assembled in a PMMA cylinder and filled with water with ^{18}F-FDG. Two hot spheres and one cold sphere were also inserted. A CT-based and UTE-MRI-based attenuation map were derived, and the PET images reconstructed with both

attenuation maps were compared. The difference in reconstructed activity between both images was small ($\approx$ 2 %), demonstrating the feasibility of discriminating lung with our method. However, the thorax phantom was a simplification of the human thorax. Therefore, these results do not prove that our method will also be applicable to in-vivo human thoracic imaging.

The applicability of our method to preclinical small animal imaging was tested in chapter 6. First a large micro-SPECT study was presented, including a total of 18 rats. Different ^{99m}Tc-labeled tracers were used to target the brain, lung, kidney, liver and spleen. UTE-MRI images of the rats were acquired. The reconstruction with different MRI-based attenuation maps was compared with the current gold standard, micro-CT-based attenuation correction. For the brain images, errors of 5 - 8 % were found when reconstructing with the UTE-MRI-based attenuation map. For the images of other organs, UTE-MRI-based attenuation correction yielded errors of 3 % or less. This demonstrates the feasibility of using UTE-MRI-based attenuation correction for micro-SPECT imaging. However, performing uniform MRI-based attenuation correction leads to only slightly higher errors, and is much easier to implement. Therefore, it can be used in most studies.

A smaller micro-PET study was also performed. In that study, artificial ^{18}F-FDG lesions were implanted in 3 dead rats in specific locations: mouth, neck, shoulder, lung, kidney, abdomen, bladder and lumbar spine. Micro-PET images were reconstructed with different MRI-based attenuation correction methods. The reconstructed activity in the lesions was compared to the reconstructed activity in micro-PET images reconstructed with micro-CT-based attenuation correction. UTE-MRI-based attenuation correction leads to errors of 2 - 3 % in all spheres, demonstrating the feasibility of using this method for micro-PET attenuation correction. As in the micro-SPECT study, uniform MRI-based attenuation correction only led to slightly larger errors. It can be used in most studies as a simpler alternative.

In chapter 7, we applied our method to human data. As described in chapter 2, the most important applications of clinical PET-MRI will probably be situated in neurology, cardiology and oncology. In the first part of the chapter, a human brain PET study with 5 patients is described. PET, CT and MRI data sets were available for all patients. Segmented UTE-MRI-based and CT-based attenuation maps were derived. The classification accuracy of the UTE-MRI-based attenuation maps was 85 - 95 % in all patients, with tissue/air discrimination of 95 % or higher. As the PET raw data was

not available, simulated PET data was obtained and reconstructed with CT-based and UTE-MRI-based attenuation correction. Visual comparison of the reconstructed PET images did not show artificial hot spots or cold spots. Quantitative evaluation in clinically relevant VOIs showed an average error of 3 % and a maximum error of 9 %. These results indicate that our method could be used for clinical brain PET imaging.

We also evaluated the feasibility of using our method for thoracic imaging, such as cardiac imaging. This was done on a single human thorax data set. As only CT and UTE-MRI images were available, PET images were simulated. First, a UTE-MRI-based attenuation map was derived by using a simple mapping, as was done in the previous studies. However, due to the local and regional inhomogeneity of the UTE-MRI images, there were too many errors in this attenuation map. A more sophisticated method was therefore developed, which used Markov random field (MRF) segmentation to segment the lungs and only detected bone in the spine region. Reconstruction of the PET images with this attenuation map showed average quantitative errors in VOIs in the lung, heart and spine of approximately 5 %. Visual comparison of the reconstructed PET images showed quite good results in the lungs and soft tissue, apart from an artificial hot spot that was created in the center of the lungs. Although these results indicate that quantification in the heart is quite accurate with our method, they also show it can only be used for cardiac studies with caution.

To evaluate the applicability of our method to oncology, whole-body data sets are needed. This was not done for two reasons. First, we did not have the possibility to obtain such data sets. Second, and more important, the application of our method to clinical whole-body imaging is not feasible at the moment. In the last section of chapter 7, the reasons for this were given. The most important problems with our method include the difficulty of discriminating all five relevant tissue types on MRI image intensity alone, the long acquisition time of UTE sequences and the fact that motion is currently not compensated in the UTE sequence. Our method has also not been evaluated in other regions of the body, such as the pelvis or the abdomen. Apart from these limitations specific for UTE, some general issues also need to be considered for whole-body MRI-based attenuation correction. Two specific problems are field-of-view truncation and MRI coil attenuation. These considerations lead to the conclusion that more work is needed to allow whole-body UTE-MRI-based attenuation correction.

8.2 Final conclusion

In this thesis, we have first determined the requirements for MRI-based attenuation correction in human and small animal imaging. Based on these requirements, a method was proposed which uses MRI images acquired with UTE sequences to allow the discrimination of all tissue types relevant for attenuation correction. We have shown that air, lung, soft tissue and bone can be discriminated with our method. We have also shown that using the attenuation map derived with our method, accurate quantification can be achieved in small animal studies (micro-PET and micro-SPECT) and human brain PET studies. It would be interesting to perform a clinical brain study with more subjects, in which the reliability of our method could be evaluated better. This would also allow to test if the method can be fully automated, which will be necessary if it is to be used in clinical practice. More work is also needed on the subject of human thoracic or whole-body imaging.

Appendix A

Detailed results of the simulation studies

In this appendix, the relative quantitative differences calculated in the simulation studies described in chapter 3 are listed. This is done for all three simulation studies, all lesions and all attenuation maps that were described.

A.1 Rat study

		Brain		Lung			Liver	
	Lesion	1	2	3	4	5	6	7
1	Number of tissue classes							
	5 class	0.3	-0.3	-1.0	-0.4	-0.1	1.1	0.0
	Lung replaced by air	-0.2	-0.1	-8.2	-2.7	-8.3	0.2	-0.3
	Cortical bone replaced by soft tissue	-0.4	-0.2	0.4	0.3	-0.2	-0.5	-0.8
	Contour	-0.9	-0.8	4.1	1.5	4.8	0.1	-1.2

Table A.1: Relative error (in %) in lesions 1 - 7 of the rat study in images reconstructed with all attenuation maps: part 1 (number of tissue classes). The location of the lesions is listed in table 3.1. The attenuation maps used for comparison are listed in table 3.4.

		Spine			Colon				Femur
	Lesion	8	9	10	11	12	13	14	15
1	Number of tissue classes								
	5 class	0.3	-0.4	0.3	0.2	0.1	1.3	0.4	-0.3
	Lung replaced by air	-0.3	0.3	-0.1	0.6	0.0	0.0	0.3	-0.4
	Cortical bone replaced by soft tissue	-1.5	-1.1	-0.8	0.7	-0.1	0.1	-0.8	-1.8
	Contour	-1.3	-2.9	-1.5	-0.7	-0.1	0.4	-0.1	-2.2

Table A.2: Relative error (in %) in lesions 8-15 of the rat study in images reconstructed with all attenuation maps: part 1 (number of tissue classes). The location of the lesions is listed in table 3.1. The attenuation maps used for comparison are listed in table 3.4.

		Brain		Lung			Liver	
	Lesion	1	2	3	4	5	6	7
3.1	Random tissue misclassification							
	5 % errors lung => air	0.1	-0.1	-0.8	-0.5	-0.9	-0.3	-0.4
	10 % errors lung => air	-0.2	-0.4	-1.4	0.5	-0.8	0.1	-0.2
	20 % errors lung => air	-0.4	-0.5	-1.6	-0.2	-2.4	0.6	0.1
	5 % errors lung => soft tissue	0.2	-0.1	-0.2	0.4	0.2	0.4	-0.1
	10 % errors lung => soft tissue	-0.4	0.0	0.9	0.2	1.3	-0.5	-0.4
	20 % errors lung => soft tissue	-0.2	-0.3	1.1	1.7	0.2	-0.3	-0.5
	5 % errors lung => cortical bone	-0.4	-0.2	-0.3	0.8	0.6	-0.6	-0.3
	10 % errors lung => cortical bone	-0.3	0.0	1.0	1.0	1.7	0.3	0.1
	20 % errors lung => cortical bone	-0.4	-0.2	1.7	0.7	1.6	-0.4	-1.2
	5 % errors cortical bone => soft tissue	-0.4	0.1	-0.5	0.0	-0.3	-0.8	-0.9
	10 % errors cortical bone => soft tissue	0.5	-0.7	0.0	1.3	-0.2	-0.4	-1.0
	20 % errors cortical bone => soft tissue	0.1	-0.1	-0.3	-0.5	-0.2	0.0	-0.7
	5 % errors cortical bone => lung	-0.1	-0.3	-0.3	0.7	-0.4	-0.2	-0.3
	10 % errors cortical bone => lung	-0.2	-0.1	-0.7	0.3	0.1	0.3	-0.6
	20 % errors cortical bone => lung	-0.7	-0.1	-0.7	0.8	0.6	-0.4	-0.3
	5 % errors cortical bone => air	-0.4	0.3	-0.3	0.1	0.1	-0.8	-0.7
	10 % errors cortical bone => air	-0.3	-0.2	0.1	0.7	0.3	-0.4	-1.4
	20 % errors cortical bone => air	-0.2	-0.2	-0.1	0.1	0.5	-0.8	-0.6

Table A.3: Relative error (in %) in lesions 1 - 7 of the rat study in images reconstructed with all attenuation maps: part 2 (random tissue misclassification). The location of the lesions is listed in table 3.1. The attenuation maps used for comparison are listed in table 3.4.

		Spine			Colon				Femur
	Lesion	8	9	10	11	12	13	14	15
3.1	Random tissue misclassification								
	5 % errors lung => air	0.0	0.0	-0.1	0.7	0.2	0.1	-0.2	-0.7
	10 % errors lung => air	0.1	0.3	-0.1	0.4	0.2	0.6	0.5	-0.7
	20 % errors lung => air	0.0	0.2	0.2	0.4	-0.2	0.8	0.4	-0.3
	5 % errors lung => soft tissue	0.5	0.3	0.3	0.9	-0.4	-0.4	0.5	-0.6
	10 % errors lung => soft tissue	-0.4	-0.1	-0.1	0.6	0.5	0.0	0.3	-0.4
	20 % errors lung => soft tissue	0.4	-0.9	-0.1	0.4	0.2	0.1	-0.4	-0.3
	5 % errors lung => cortical bone	0.0	-0.1	-0.2	0.6	0.5	0.7	0.6	-0.5
	10 % errors lung => cortical bone	0.3	-0.7	0.3	0.1	0.2	0.2	0.3	-0.7
	20 % errors lung => cortical bone	0.4	-0.2	-0.3	0.6	0.6	0.2	0.9	-0.7
	5 % errors cortical bone => soft tissue	0.1	-0.1	0.2	0.9	0.1	-0.1	1.0	-0.4
	10 % errors cortical bone => soft tissue	-0.3	0.1	-0.5	0.9	0.1	0.1	0.8	-0.8
	20 % errors cortical bone => soft tissue	-0.2	-0.4	-0.5	0.6	0.2	0.6	0.2	-0.6
	5 % errors cortical bone => lung	-0.3	-0.5	0.2	0.1	0.4	0.1	0.2	-0.8
	10 % errors cortical bone => lung	-0.3	-0.4	0.0	0.3	0.4	0.4	0.4	-1.0
	20 % errors cortical bone => lung	-0.1	-0.7	-0.4	0.4	0.3	0.2	-0.1	-1.5
	5 % errors cortical bone => air	-0.1	-0.6	-0.6	0.8	0.2	0.1	0.8	-1.0
	10 % errors cortical bone => air	-0.6	-0.7	-0.6	0.9	-0.1	0.4	-0.2	-1.0
	20 % errors cortical bone => air	0.0	-1.6	-0.4	0.7	0.7	0.4	0.5	-1.4

Table A.4: Relative error (in %) in lesions 8-15 of the rat study in images reconstructed with all attenuation maps: part 2 (random tissue misclassification). The location of the lesions is listed in table 3.1. The attenuation maps used for comparison are listed in table 3.4.

A.2 Human brain study

	Lesion	1	2	3	4	5	6
1	Number of tissue classes						
	Cortical bone replaced by soft tissue	-7.0	-2.9	-6.7	-3.8	-7.6	-3.6
	Cortical bone replaced by air	-21.0	-9.1	-20.2	-11.5	-22.8	-11.1
	Contour	-4.0	27.2	-4.1	2.4	14.1	-1.2
2	Inter-patient variability						
	Cortical bone segmented value + 1SD	0.3	0.1	0.3	0.1	0.3	0.1
	Cortical bone segmented value + 2SD	0.6	0.2	0.6	0.3	0.6	0.3
3.1	Random tissue misclassification						
	5 % errors cortical bone => soft tissue	-0.5	-0.2	-0.3	-0.2	-0.5	-0.2
	10 % errors cortical bone => soft tissue	-0.7	-0.2	-0.7	-0.4	-0.8	-0.4
	20 % errors cortical bone => soft tissue	-1.5	-0.7	-1.4	-0.7	-1.3	-0.7
	5 % errors cortical bone => air	-1.2	-0.4	-1.6	-0.5	-1.5	-0.5
	10 % errors cortical bone => air	-2.4	-0.6	-2.6	-1.3	-2.8	-1.1
	20 % errors cortical bone => air	-4.1	-1.8	-3.9	-2.4	-4.4	-2.5
3.2	Distance-to-interface dependent tissue misclassification						
	5 % errors cortical bone => soft tissue	-0.4	-0.2	-0.6	-0.3	-0.3	-0.2
	10 % errors cortical bone => soft tissue	-0.8	-0.3	-0.8	-0.5	-0.8	-0.5
	20 % errors cortical bone => soft tissue	-1.5	-0.9	-1.7	-1.0	-1.7	-0.9
	5 % errors cortical bone => air	-1.2	-2.1	-0.4	-0.6	-3.0	-0.5
	10 % errors cortical bone => air	-2.5	-4.0	-1.0	-1.5	-6.7	-1.1
	20 % errors cortical bone => air	-3.0	-4.6	-1.0	-1.6	-7.5	-1.4

Table A.5: Relative error (in %) in all lesions of the human brain study in images reconstructed with all attenuation maps. The location of the lesions is listed in table 3.5. The attenuation maps used for comparison are listed in table 3.4.

A.3 Human whole-body study

		Lung				Liver		Spine		
	Lesion	1	2	3	4	5	6	7	8	9
1	Number of tissue classes									
	7 class	0.3	0.3	0.2	0.2	0.5	0.4	1.0	1.9	0.9
	Liver replaced by soft tissue	-0.5	-0.4	-1.2	-0.4	-2.0	-1.1	-0.2	0.0	-0.4
	Adipose tissue replaced by soft tissue	2.7	2.6	3.1	3.5	2.9	3.4	3.0	4.1	3.7
	Spongeous bone replaced by soft tissue	0.0	-1.5	0.0	-0.1	-0.3	-0.2	-11.7	-11.9	-10.8
	Lung replaced by air	-45.5	-30.9	-25.4	-36.9	-0.1	0.1	-16.8	0.0	-2.6
	Cortical bone replaced by soft tissue	-2.1	-6.2	-2.7	-7.2	-2.2	-3.2	-15.6	-8.1	-17.5
2	Inter-patient variability									
	Lung segmented value + 1SD	12.4	9.4	5.9	9.8	0.0	0.0	3.8	0.0	0.6
	Lung segmented value + 2SD	25.8	19.6	11.8	20.1	0.1	0.0	7.7	0.0	1.3
	Cortical bone segmented value + 1SD	0.1	0.4	0.2	0.5	0.1	0.2	1.0	0.5	1.1
	Cortical bone segmented value + 2SD	0.2	0.8	0.3	0.9	0.3	0.4	2.0	1.0	2.2

Table A.6: Relative error (in %) in lesions 1 - 9 of the human whole-body study in images reconstructed with all attenuation maps: part 1 (number of tissue classes and inter-patient variability). The location of the lesions is listed in table 3.2. The attenuation maps used for comparison are listed in table 3.4.

		Colon				Prostate	Femur
	Lesion	10	11	12	13	14	15
1	Number of tissue classes						
	7 class	1.0	1.1	1.1	1.0	0.3	0.0
	Liver replaced by soft tissue	-0.4	-0.3	-0.3	-0.3	-0.3	0.0
	Adipose tissue replaced by soft tissue	5.4	6.5	5.9	4.1	5.4	3.0
	Spongeous bone replaced by soft tissue	-0.1	-0.2	-0.4	-0.7	-1.7	-13.1
	Lung replaced by air	0.0	0.0	0.0	0.0	0.0	0.0
	Cortical bone replaced by soft tissue	-0.7	-0.9	-1.3	-3.5	-4.2	-5.5
2	Inter-patient variability						
	Lung segmented value + 1SD	0.0	0.0	0.0	0.0	0.0	0.0
	Lung segmented value + 2SD	0.0	0.0	0.0	0.0	0.0	0.0
	Cortical bone segmented value + 1SD	0.0	0.1	0.1	0.2	0.3	0.3
	Cortical bone segmented value + 2SD	0.1	0.1	0.2	0.4	0.5	0.7

Table A.7: Relative error (in %) in lesions 10 - 15 of the human whole-body study in images reconstructed with all attenuation maps: part 1 (number of tissue classes and inter-patient variability). The location of the lesions is listed in table 3.2. The attenuation maps used for comparison are listed in table 3.4.

		Lung				Liver		Spine		
	Lesion	1	2	3	4	5	6	7	8	9
3.1	Random tissue misclassification									
	5 % errors lung => air	-2.5	-1.9	-1.4	-2.2	0.0	0.0	-0.9	0.0	-0.2
	10 % errors lung => air	-5.3	-4.1	-2.3	-4.2	0.0	0.0	-1.9	0.0	-0.3
	20 % errors lung => air	-10.3	-7.0	-5.4	-8.7	0.0	0.0	-3.5	0.0	-0.6
	5 % errors lung => soft tissue	6.0	7.5	3.3	5.5	0.0	0.0	2.1	0.0	0.4
	10 % errors lung => soft tissue	15.0	12.1	7.5	12.3	0.0	0.0	4.0	0.0	0.7
	20 % errors lung => soft tissue	33.5	20.5	13.9	21.8	0.1	-0.1	9.0	0.0	1.4
	5 % errors lung => cortical bone	10.2	9.2	5.4	8.6	0.0	0.0	3.1	0.0	0.5
	10 % errors lung => cortical bone	19.8	19.3	12.1	18.9	0.1	0.0	6.2	0.0	1.3
	20 % errors lung => cortical bone	44.3	39.2	18.8	31.8	0.1	0.0	12.2	0.0	2.0
	5 % errors cortical bone => soft tissue	-0.1	-0.3	-0.1	-0.4	-0.1	-0.1	-0.7	-0.3	-0.8
	10 % errors cortical bone => soft tissue	-0.2	-0.7	-0.3	-0.8	-0.3	-0.2	-2.6	-0.8	-1.3
	20 % errors cortical bone => soft tissue	-0.4	-1.1	-0.6	-1.0	-0.4	-0.7	-3.2	-1.8	-3.6
	5 % errors cortical bone => lung	-0.4	-0.9	-0.4	-0.9	-0.3	-0.2	-2.5	-1.6	-2.6
	10 % errors cortical bone => lung	-0.5	-1.6	-0.8	-1.4	-0.6	-0.7	-5.6	-2.2	-4.7
	20 % errors cortical bone => lung	-1.5	-3.9	-1.7	-5.2	-1.3	-1.6	-7.3	-5.9	-9.0
	5 % errors cortical bone => air	-0.4	-1.0	-0.6	-1.1	-0.4	-0.3	-3.7	-1.4	-3.3
	10 % errors cortical bone => air	-0.7	-3.4	-1.1	-2.2	-0.8	-1.9	-5.1	-3.4	-5.5
	20 % errors cortical bone => air	-1.8	-4.3	-2.1	-5.9	-1.8	-2.1	-11.6	-5.8	-12.5

Table A.8: Relative error (in %) in lesions 1 - 9 of the human whole-body study in images reconstructed with all attenuation maps: part 2 (random tissue misclassification). The location of the lesions is listed in table 3.2. The attenuation maps used for comparison are listed in table 3.4.

		Colon				Prostate	Femur
	Lesion	10	11	12	13	14	15
3.1	Random tissue misclassification						
	5 % errors lung => air	0.0	0.0	0.0	0.0	0.0	0.0
	10 % errors lung => air	0.0	0.0	0.0	0.0	0.0	0.0
	20 % errors lung => air	0.0	0.0	0.0	0.0	0.0	0.0
	5 % errors lung => soft tissue	0.0	0.0	0.0	0.0	0.0	0.0
	10 % errors lung => soft tissue	0.0	0.0	0.0	0.0	0.0	0.0
	20 % errors lung => soft tissue	0.0	0.0	0.0	0.0	0.0	0.0
	5 % errors lung => cortical bone	0.0	0.0	0.0	0.0	0.0	0.0
	10 % errors lung => cortical bone	0.0	0.0	0.0	0.0	0.0	0.0
	20 % errors lung => cortical bone	0.0	0.0	0.0	0.0	0.0	0.0
	5 % errors cortical bone => soft tissue	0.0	0.0	-0.1	-0.1	-0.3	-0.3
	10 % errors cortical bone => soft tissue	-0.1	-0.1	-0.1	-0.4	-0.4	-0.5
	20 % errors cortical bone => soft tissue	-0.1	-0.2	-0.3	-0.7	-0.8	-1.1
	5 % errors cortical bone => lung	-0.1	-0.1	-0.2	-0.6	-0.8	-0.9
	10 % errors cortical bone => lung	-0.2	-0.2	-0.3	-1.1	-1.4	-1.7
	20 % errors cortical bone => lung	-0.6	-0.6	-0.9	-2.1	-2.4	-4.0
	5 % errors cortical bone => air	-0.2	-0.2	-0.3	-0.5	-0.9	-1.5
	10 % errors cortical bone => air	-0.1	-0.4	-0.4	-1.4	-1.7	-2.4
	20 % errors cortical bone => air	-0.4	-0.7	-1.0	-2.8	-3.6	-3.8

Table A.9: Relative error (in %) in lesions 10 - 15 of the human whole-body study in images reconstructed with all attenuation maps: part 2 (random tissue misclassification). The location of the lesions is listed in table 3.2. The attenuation maps used for comparison are listed in table 3.4.

		Lung				Liver		Spine		
	Lesion	1	2	3	4	5	6	7	8	9
3.2	Distance-to-interface dependent tissue misclassification									
	5 % errors lung => air	-2.5	-1.9	-1.4	-2.0	0.0	0.0	-0.9	0.0	-0.1
	10 % errors lung => air	-5.5	-3.9	-2.6	-4.7	0.0	0.0	-1.7	0.0	-0.3
	20 % errors lung => air	-11.0	-7.7	-5.0	-8.6	0.0	0.0	-3.2	0.0	-0.4
	5 % errors lung => soft tissue	8.2	8.0	4.1	6.2	0.0	0.0	2.3	0.0	0.6
	10 % errors lung => soft tissue	13.4	17.6	12.3	12.6	0.1	0.0	4.5	0.0	1.2
	20 % errors lung => soft tissue	31.2	29.8	20.9	28.5	0.2	0.0	8.1	0.0	2.6
	5 % errors lung => cortical bone	1.2	13.9	2.7	7.1	0.1	0.0	4.8	0.0	1.1
	10 % errors lung => cortical bone	3.0	25.6	5.6	12.9	0.2	0.0	9.1	0.0	2.1
	20 % errors lung => cortical bone	6.1	45.8	8.6	23.0	0.3	-0.1	14.8	0.0	4.0
	5 % errors cortical bone => soft tissue	-0.1	-0.3	-0.1	-0.3	-0.1	-0.2	-0.8	-0.6	-0.9
	10 % errors cortical bone => soft tissue	-0.2	-0.6	-0.3	-0.5	-0.2	-0.4	-1.4	-0.8	-1.2
	20 % errors cortical bone => soft tissue	-0.4	-1.1	-0.6	-1.7	-0.5	-1.0	-3.5	-2.0	-3.4
	5 % errors cortical bone => lung	-0.1	-2.0	-0.6	-1.0	-0.1	0.0	-2.2	-1.4	-2.0
	10 % errors cortical bone => lung	-0.5	-3.2	-1.3	-3.3	-0.2	0.0	-3.7	-2.6	-4.1
	20 % errors cortical bone => lung	-1.5	-7.7	-2.0	-8.1	-0.3	0.0	-6.8	-5.3	-5.7
	5 % errors cortical bone => air	-0.5	-1.8	-0.5	-2.0	-0.5	-0.3	-3.0	-1.4	-3.0
	10 % errors cortical bone => air	-0.7	-1.7	-1.0	-2.2	-0.8	-1.5	-5.8	-3.1	-6.2
	20 % errors cortical bone => air	-1.5	-5.1	-1.9	-5.8	-1.8	-1.3	-12.4	-4.7	-10.1

Table A.10: Relative error (in %) in lesions 1 - 9 of the human whole-body study in images reconstructed with all attenuation maps: part 3 (distance-to-interface dependent tissue misclassification). The location of the lesions is listed in table 3.2. The attenuation maps used for comparison are listed in table 3.4.

		Colon				Prostate	Femur
	Lesion	10	11	12	13	14	15
3.2	Distance-to-interface dependent tissue misclassification						
	5 % errors lung => air	0.0	0.0	0.0	0.0	0.0	0.0
	10 % errors lung => air	0.0	0.0	0.0	0.0	0.0	0.0
	20 % errors lung => air	0.0	0.0	0.0	0.0	0.0	0.0
	5 % errors lung => soft tissue	0.0	0.0	0.0	0.0	0.0	0.0
	10 % errors lung => soft tissue	0.0	0.0	0.0	0.0	0.0	0.0
	20 % errors lung => soft tissue	0.0	0.0	0.0	0.0	0.0	0.0
	5 % errors lung => cortical bone	0.0	0.0	0.0	0.0	0.0	0.0
	10 % errors lung => cortical bone	0.0	0.0	0.0	0.0	0.0	0.0
	20 % errors lung => cortical bone	0.0	0.0	0.0	0.0	0.0	0.0
	5 % errors cortical bone => soft tissue	0.0	0.0	-0.1	-0.2	-0.3	-0.3
	10 % errors cortical bone => soft tissue	0.0	-0.1	-0.1	-0.3	-0.4	-0.6
	20 % errors cortical bone => soft tissue	-0.1	-0.2	-0.2	-0.6	-0.8	-1.0
	5 % errors cortical bone => lung	-0.1	-0.2	-0.3	-0.5	-0.8	-1.0
	10 % errors cortical bone => lung	-0.3	-0.3	-0.5	-1.3	-1.5	-2.0
	20 % errors cortical bone => lung	-0.4	-0.4	-0.9	-2.2	-2.6	-3.0
	5 % errors cortical bone => air	-0.1	-0.2	-0.2	-0.5	-0.7	-0.5
	10 % errors cortical bone => air	-0.4	-0.4	-0.6	-1.3	-1.4	-1.3
	20 % errors cortical bone => air	-0.3	-0.6	-0.8	-2.4	-2.4	-2.5

Table A.11: Relative error (in %) in lesions 10 - 15 of the human whole-body study in images reconstructed with all attenuation maps: part 3 (distance-to-interface dependent tissue misclassification). The location of the lesions is listed in table 3.2. The attenuation maps used for comparison are listed in table 3.4.

References

[1] Anger H. *A new instrument for mapping gamma-ray emitters*. Biology and Medicine Quarterly Report. UCRL 3653 1957.

[2] Jaszczak R J, Murphy P H, Huard D, Burdine J A. Radionuclide emission computed tomography of the head with 99mCc and a scintillation camera *J Nucl Med.* 1977;18:373–80.

[3] Keyes J W, Orlandea N, Heetderks W J, Leonard P F, Rogers W L. The Humongotron–a scintillation-camera transaxial tomograph *J Nucl Med.* 1977;18:381–7.

[4] Anger H, Rosenthal D. Scintillation camera and positron camera in *Medical radioisotope scanning*International Atomic Energy Agency, Vienna 1959.

[5] Anger H, Vandyke D. Human bone marrow distribution shown in vivo by iron-52 and the positron scintillation camera *Science.* 1964;144:1587–9.

[6] Robertson JS, Bozzo S. Positron scanner for brain tumors *6th IBM Medical Symposium.* 1964:631–645.

[7] Thompson C, Yamamoto Y, Meyer E. Positome II: A High Efficiency Positron Imaging Device for Dynamic Brain Studies *IEEE T Nucl Sci.* 1979;26:583 – 589.

[8] Muehllehner G, Karp J S. Positron emission tomography imaging–technical considerations *Semin Nucl Med.* 1986;16:35–50.

[9] Bailey D L. 3D acquisition and reconstruction in positron emission tomography *Ann Nucl Med.* 1992;6:123–30.

[10] Defrise M, Townsend D, Geissbuhler A. Implementation of three-dimensional image reconstruction for multi-ring positron tomographs *Phys Med Biol.* 1990;35:1361–72.

[11] Cherry S R, Dahlbom M, Hoffman E J. Evaluation of a 3D reconstruction algorithm for multi-slice PET scanners *Phys Med Biol.* 1992;37:779–90.

[12] Jaszczak R J, Li J, Wang H, Zalutsky M R, Coleman R E. Pinhole collimation for ultra-high-resolution, small-field-of-view SPECT *Phys Med Biol.* 1994;39:425–37.

[13] Beekman Freek J, Have Frans, Vastenhouw Brendan, et al. U-SPECT-I: a novel system for submillimeter-resolution tomography with radiolabeled molecules in mice *J Nucl Med.* 2005;46:1194–200.

[14] Jansen Floris P, Vanderheyden Jean-Luc. The future of SPECT in a time of PET *Nucl Med Biol.* 2007;34:733–5.

[15] Muehllehner G. Effect of resolution improvement on required count density in ECT imaging: a computer simulation *Phys Med Biol.* 1985;30:163–73.

[16] Fahey F H, Harkness B A, Keyes J W, Madsen M T, Battisti C, Zito V. Sensitivity, resolution and image quality with a multi-head SPECT camera *J Nucl Med.* 1992;33:1859–63.

[17] Kinahan P, Defrise M, Clackdoyle R. Analytic image reconstruction methods in *Emission tomography: the fundamentals of PET and SPECT* (Wernick M, Aarsvold J. , eds.)Elsevier Academic Press 2004.

[18] Lalush D, Wernick M. Iterative image reconstruction in *Emission tomography: the fundamentals of PET and SPECT* (Wernick M, Aarsvold J. , eds.)Elsevier Academic Press 2004.

[19] Lange K, Carson R. EM reconstruction algorithms for emission and transmission tomography *J Comput Assist Tomogr.* 1984;8:306–16.

[20] Shepp L A, Vardi Y. Maximum likelihood reconstruction for emission tomography *IEEE T Med Imaging.* 1982;1:113–22.

[21] Fisher R. On the "Probable Error" of a Coefficient of Correlation Deduced from a Small Sample. *Metron.* 1921.

[22] Qi J. Calculation of the Sensitivity Image in List-Mode Reconstruction for PET *IEEE T Nucl Sci.* 2006;53:2746 – 2751.

[23] Badawi R, Marsden P. Developments in component-based normalization for 3D PET *Phys Med Biol.* 1999;44:571–94.

[24] Defrise M, Townsend D W, Bailey D, Geissbuhler A, Michel C, Jones T. A normalization technique for 3D PET data *Phys Med Biol.* 1991;36:939–52.

[25] Hoffman E, Guerrero T, Germano G, Digby W, Dahlbom M. PET system calibrations and corrections for quantitative and spatially accurate images *IEEE T Nucl Sci.* 1989;36:1108 – 1112.

[26] Levin C S, Hoffman E J. Calculation of positron range and its effect on the fundamental limit of positron emission tomography system spatial resolution *Phys Med Biol.* 1999;44:781–99.

[27] Reader AJ, Julyan P, Williams H, Hastings D, Zweit J. EM algorithm system modeling by image-space techniques for PET reconstruction *IEEE T Nucl Sci.* 2003;50:1392–7.

[28] Brasse D, Kinahan PE, Lartizien C, Comtat C, Casey M, Michel C. Correction methods for random coincidences in fully 3D whole-body PET: impact on data and image quality *J Nucl Med.* 2005;46:859–67.

[29] Grootoonk S, Spinks T J, Sashin D, Spyrou N M, Jones T. Correction for scatter in 3D brain PET using a dual energy window method *Phys Med Biol.* 1996;41:2757–74.

[30] Jaszczak RJ, Greer KL, Floyd CE, Harris C, Coleman R. Improved SPECT quantification using compensation for scattered photons *J Nucl Med.* 1984;25:893–900.

[31] Ogawa K, Harata Y, Ichihara T, Kubo A, Hashimoto S. A practical method for position-dependent Compton-scatter correction in single photon emission CT *IEEE T Med Imaging.* 1991;10:408 – 412.

[32] Floyd Carey E, Jaszczak Ronald J, Coleman R. Inverse Monte Carlo: A Unified Reconstruction Algorithm for SPECT *IEEE T Nucl Sci.* 1985;32:779 – 785.

[33] Bowsher J E, Floyd C E. Treatment of Compton scattering in maximum-likelihood, expectation-maximization reconstructions of SPECT images *J Nucl Med.* 1991;32:1285–91.

[34] Beekman F, Jong H, Geloven S. Efficient fully 3-D iterative SPECT reconstruction with Monte Carlo-based scatter compensation *IEEE T Med Imaging.* 2002;21:867 – 877.

[35] Levin C, Dahlbom M, Hoffman E. A Monte Carlo correction for the effect of Compton scattering in 3-D PET brain imaging *IEEE T Nucl Sci.* 1995;42:1181 – 1185.

[36] Ollinger J M. Model-based scatter correction for fully 3D PET *Phys Med Biol.* 1996;41:153–76.

[37] Klein O, Nishina T. Über die Streuung von Strahlung durch freie Elektronen nach der neuen relativistischen Quantendynamik von Dirac *Zeitschrift für Physik A Hadrons and Nuclei.* 1929;52:853–68.

[38] Nehmeh S A, Erdi Y E, Ling C C, et al. Effect of respiratory gating on reducing lung motion artifacts in PET imaging of lung cancer *Med Phys.* 2002;29:366–71.

[39] Boucher Luc, Rodrigue S, Lecomte R, Bénard F. Respiratory gating for 3-dimensional PET of the thorax: feasibility and initial results *J Nucl Med.* 2004;45:214–9.

[40] Livieratos L, Rajappan K, Stegger L, Schafers K, Bailey DL, Camici PG. Respiratory gating of cardiac PET data in list-mode acquisition *Eur J Nucl Med Mol Imaging.* 2006;33:584–8.

[41] Picard Y, Thompson C, Moreno-Cantu J. Motion correction of PET images using multiple acquisition frames *IEEE Nucl Sci Conf R.* 1995;2:963 – 967.

[42] Lopresti B, Russo A, Jones W, Fisher T, Crouch D. Implementation and performance of an optical motion tracking system for high resolution brain PET imaging *IEEE Nucl Sci Conf R.* 1998;2:1127 – 1131.

[43] Fulton R, Tellmann L, Pietrzyk U, Herzog H. Compensation for head movement in 3D PET *IEEE Nucl Sci Conf R.* 2001;4:2013 – 2017.

[44] Meteopolis N, Ulam S. The Monte Carlo method *J Am Stat Assoc.* 1949;44:335–41.

[45] Raeside D E. Monte Carlo principles and applications *Phys Med Biol.* 1976;21:181–97.

[46] Andreo P. Monte Carlo techniques in medical radiation physics *Phys Med Biol.* 1991;36:861–920.

[47] Zaidi H. Relevance of accurate Monte Carlo modeling in nuclear medical imaging *Med Phys.* 1999;26:574–608.

[48] Ljungberg M. Simulation techniques and phantoms in *Emission tomography: the fundamentals of PET and SPECT* (Wernick M, Aarsvold J. , eds.)Elsevier Academic Press 2004.

[49] Jan S, Santin G, Strul D, et al. GATE: a simulation toolkit for PET and SPECT *Phys Med Biol.* 2004;49:4543–61.

[50] Agostinelli S, Allison J, Amako K, et al. Geant4-a simulation toolkit *Nucl Instrum Methods Phys Res B.* 2003;506:250.

[51] Buvat I, Castiglioni I, Feuardent J, Gilardi MC. Unified description and validation of Monte Carlo simulators in PET *Phys Med Biol.* 2005;50:329–46.

[52] Staelens S, Strul D, Santin G, et al. Monte Carlo simulations of a scintillation camera using GATE: validation and application modelling *Phys Med Biol.* 2003;48:3021–42.

[53] Schmidtlein CR, Kirov AS, Nehmeh SA, et al. Validation of GATE Monte Carlo simulations of the GE Advance/Discovery LS PET scanners *Med Phys.* 2006;33:198–208.

[54] Lamare F, Turzo A, Bizais Y, Rest C Cheze Le, Visvikis D. Validation of a Monte Carlo simulation of the Philips Allegro/GEMINI PET systems using GATE *Phys Med Biol.* 2006;51:943–62.

[55] Rechka S, Fontaine R, Rafecas M, Lecomte R. Development and validation of a GATE simulation model for the LabPET scanner *IEEE T Nucl Sci.* 2009;56:3672–9.

[56] Snyder W S, Fisher H L, Ford M R, Warner G G. Estimates of absorbed fractions for monoenergetic photon sources uniformly distributed in various organs of a heterogeneous phantom *J Nucl Med.* 1969:Suppl 3:7–52.

[57] Zubal I G, Harrell C R, Smith E O, Rattner Z, Gindi G, Hoffer P B. Computerized three-dimensional segmented human anatomy *Med Phys.* 1994;21:299–302.

[58] Segars W, Lalush D, Tsui B. Modeling respiratory mechanics in the MCAT and spline-based MCAT phantoms *IEEE Nucl Sci Conf R.* 1999;2:985 – 989 vol.2.

[59] Segars P. *Development of a new dynamic NURBS-based cardiac-torso (NCAT) phantom*. PhD thesisUniversity of North Carolina at Chapel Hill 2001.

[60] Segars WP, Tsui B. MCAT to XCAT: The Evolution of 4-D Computerized Phantoms for Imaging Research *Proc IEEE.* 2009;97:1954–68.

[61] Valk P, Delbeke D, Bailey D, Townsend D, Maisey M. , eds.*Positron emission tomography: clinical practice*. Springer-Verlag London 2006.

[62] Rohren EM, Turkington TG, Coleman RE. Clinical applications of PET in oncology *Radiology.* 2004;231:305–32.

[63] Blake P, Johnson B, VanMeter JW. Positron Emission Tomography (PET) and Single Photon Emission Computed Tomography (SPECT): Clinical Applications *J Neuroophthalmol.* 2003;23:34–41.

[64] Klocke FJ, Baird MG, Lorell BH, et al. ACC/AHA/ASNC guidelines for the clinical use of cardiac radionuclide imaging–executive summary: a report of the American College of Cardiology/American Heart Association Task Force on Practice Guidelines (ACC/AHA/ASNC Committee to Revise the 1995 Guidelines for the Clinical Use of Cardiac Radionuclide Imaging) *Circulation.* 2003;108:1404–18.

[65] Chowdhury FU, Scarsbrook AF. The role of hybrid SPECT-CT in oncology: current and emerging clinical applications *Clin Radiol.* 2008;63:241–51.

[66] Kostakoglu L, Goldsmith SJ. 18F-FDG PET evaluation of the response to therapy for lymphoma and for breast, lung, and colorectal carcinoma *J Nucl Med.* 2003;44:224–39.

[67] Acton PD, Zhuang H, Alavi A. Quantification in PET *Radiol Clin North Am.* 2004;42:1055–62, viii.

[68] Young H, Baum R, Cremerius U, et al. Measurement of clinical and subclinical tumour response using [18F]-fluorodeoxyglucose and positron emission tomography: review and 1999 EORTC recommendations. European Organization for Research and Treatment of Cancer (EORTC) PET Study Group *Eur J Cancer.* 1999;35:1773–82.

[69] Chaiken L, Rege S, Hoh C, et al. Positron emission tomography with fluorodeoxyglucose to evaluate tumor response and control after radiation therapy *Int J Radiat Oncol Biol Phys.* 1993;27:455–64.

[70] Huang S C, Phelps M E, Hoffman E J, Sideris K, Selin C J, Kuhl D E. Noninvasive determination of local cerebral metabolic rate of glucose in man *Am J Physiol.* 1980;238:E69–82.

[71] Reivich M, Alavi A, Greenberg J, et al. Metabolic Mapping of Functional Cerebral Activity in Man Using the 18F-2-Fluoro-2-Deoxyglucose Technique *J Comp Assist Tomogr.* 1978;2.

[72] Tsui B M, Zhao X, Frey E C, McCartney W H. Quantitative single-photon emission computed tomography: basics and clinical considerations *Semin Nucl Med.* 1994;24:38–65.

[73] Ritt P, Vija H, Hornegger J, Kuwert T. Absolute quantification in SPECT *Eur J Nucl Med Mol Imaging.* 2011;38 Suppl 1:S69–77.

[74] Dewaraja Y, Wilderman SJ, Koral K, Kaminski M, Avram A. Use of integrated SPECT/CT imaging for tumor dosimetry in I-131 radioimmunotherapy: a pilot patient study *Cancer Biother Radio.* 2009;24:417–26.

[75] Flux G, Bardies M, Monsieurs M, Savolainen S, Strands SE, Lassmann Michael. The impact of PET and SPECT on dosimetry for targeted radionuclide therapy *Z Med Phys.* 2006;16:47–59.

[76] Sandström M, Garske U, Granberg D, Sundin A, Lundqvist H. Individualized dosimetry in patients undergoing therapy with (177)Lu-DOTA-D-Phe (1)-Tyr (3)-octreotate *Eur J Nucl Med Mol Imaging.* 2010;37:212–25.

[77] Willowson K, Bailey DL, Baldock C. Quantitative SPECT reconstruction using CT-derived corrections *Phys Med Biol.* 2008;53:3099–112.

[78] Willowson K, Bailey DL, Bailey EA, Baldock C, Roach PJ. In vivo validation of quantitative SPECT in the heart *Clin Physiol Funct Imaging.* 2010;30:214–9.

[79] Zeintl J, Vija AH, Yahil A, Hornegger J, Kuwert T. Quantitative accuracy of clinical 99mTc SPECT/CT using ordered-subset expectation maximization with 3-dimensional resolution recovery, attenuation, and scatter correction *J Nucl Med.* 2010;51:921–8.

[80] Mozley P. Weaving single photon imaging into new drug development *Mol Imaging Biol.* 2005;7:30–6.

[81] Weber D A, Ivanovic M. Ultra-high-resolution imaging of small animals: implications for preclinical and research studies *J Nucl Cardiol.* 1999;6:332–44.

[82] Chatziioannou A. Instrumentation for molecular imaging in preclinical research: Micro-PET and Micro-SPECT *Proc Am Thorac Soc.* 2005;2:533-6, 510–11.

[83] Rowland D, Cherry S. Small-animal preclinical nuclear medicine instrumentation and methodology *Semin Nucl Med.* 2008;38:209–22.

[84] Vanderheyden J L. The use of imaging in preclinical drug development *Q J Nucl Med Mol Imaging.* 2009;53:374–81.

[85] Rabi I, Zacharias J, Millman S, Kusch P. A New Method of Measuring Nuclear Magnetic Moment *Phys Rev.* 1938;53:318.

[86] Rabi I, Millman S, Kusch P, Zacharias J. The Molecular Beam Resonance Method for Measuring Nuclear Magnetic Moments. The Magnetic Moments of 3Li6, 3Li7 and 9F19 *Phys Rev.* 1939;58:526–35.

[87] Bloch F, Hansen W, Packard M. The nuclear induction experiment *Phys Rev.* 1946;70:474–85.

[88] Bloch F. Nuclear induction *Phys Rev.* 1946;70:460–74.

[89] Purcell EM, Torrey H, Pound R. Resonance absorption by nuclear magnetic moments in a solid *Phys Rev.* 1946;70:37.

[90] Lauterbur P. Image formation by induced local interactions - examples employing nuclear magnetic-resonance *Nature.* 1973;242:190–191.

[91] Mansfield P. Multi-planar image formation using NMR spin echoes *J Phys C Solid State.* 1977.

[92] Damadian R. Tumor detection by nuclear magnetic resonance *Science.* 1971.

[93] Damadian R, Goldsmith M, Minkoff L. NMR in cancer: XVI. FONAR image of the live human body *Physiol Chem Phys.* 1977;9:97–100, 108.

[94] Mansfield P, Maudsley A A. Medical imaging by NMR *Br J Radiol.* 1977;50:188–94.

[95] Uhlenbeck G, Goudsmit S. Spinning electrons and the structure of spectra *Nature.* 1926;117:264–5.

[96] ZEEMAN P. The effect of magnetisation on the nature of light emitted by a substance *Nature.* 1897;55:347.

[97] Ljunggren S. A simple graphical representation of Fourier-based imaging methods *J. Magn. Reson.* 1983.

[98] Twieg D B. The k-trajectory formulation of the NMR imaging process with applications in analysis and synthesis of imaging methods *Med Phys.* 1983;10:610–21.

[99] Hahn E. Spin echoes *Phys Rev.* 1950;80:580–601.

[100] Vaughan J, Snyder C, DelaBarre L, et al. Whole-body imaging at 7T: preliminary results *Magn Reson Med.* 2009;61:244–8.

[101] Vaughan T, DelaBarre L, Snyder C, et al. 9.4T human MRI: preliminary results *Magn Reson Med.* 2006;56:1274–82.

[102] Symms M, Jäger H R, Schmierer K, Yousry T A. A review of structural magnetic resonance neuroimaging *J Neurol Neurosurg Psychiatr.* 2004;75:1235–44.

[103] Horsfield Mark A, Jones Derek K. Applications of diffusion-weighted and diffusion tensor MRI to white matter diseases - a review *NMR Biomed.* 2002;15:570–7.

[104] Matthews P, Honey G, Bullmore E. Applications of fMRI in translational medicine and clinical practice *Nat Rev Neurosci.* 2006;7:732–44.

[105] Bandettini W P, Arai A E. Advances in clinical applications of cardiovascular magnetic resonance imaging *Heart.* 2008;94:1485–95.

[106] Cha S. Neuroimaging in neuro-oncology *Neurotherapeutics.* 2009;6:465–77.

[107] Johnston C, Brennan S, Ford S, Eustace S. Whole body MR imaging: applications in oncology *Eur J Surg Oncol.* 2006;32:239–46.

[108] Koh DM, Collins DJ. Diffusion-weighted MRI in the body: applications and challenges in oncology *Am J Roentgenol.* 2007;188:1622–35.

[109] Wallis F, Gilbert F J. Magnetic resonance imaging in oncology: an overview *J R Coll Surg Edinb.* 1999;44:117–25.

[110] Marzola P, Osculati F, Sbarbati A. High field MRI in preclinical research *Eur J Radiol.* 2003;48:165–70.

[111] Doty F, Entzminger G, Kulkarni J, Pamarthy K, Staab J. Radio frequency coil technology for small-animal MRI *NMR Biomed.* 2007;20:304–25.

[112] Boone JM, Velazquez O, Cherry SR. Small-animal X-ray dose from micro-CT *Mol Imaging.* 2004;3:149–58.

[113] Carlson SK, Classic KL, Bender C, Russell SJ. Small animal absorbed radiation dose from serial micro-computed tomography imaging *Mol Imaging Biol.* 2007;9:78–82.

[114] Benveniste H, Blackband S. MR microscopy and high resolution small animal MRI: applications in neuroscience research *Prog Neurobiol.* 2002;67:393–420.

[115] Lewis J, Achilefu S, Garbow J, Laforest R, Welch M. Small animal imaging. current technology and perspectives for oncological imaging *Eur J Cancer.* 2002;38:2173–88.

[116] Hill D L, Batchelor P G, Holden M, Hawkes D J. Medical image registration *Phys Med Biol.* 2001;46:R1–45.

[117] Slomka P, Baum R. Multimodality image registration with software: state-of-the-art *Eur J Nucl Med Mol Imaging.* 2009;36 Suppl 1:S44–55.

[118] Beyer T, Townsend D, Brun T. A combined PET/CT scanner for clinical oncology *J Nucl Med.* 2000;41:1369–79.

[119] Weber W, Figlin R. Monitoring cancer treatment with PET/CT: does it make a difference? *J Nucl Med.* 2007;48 Suppl 1:36S–44S.

[120] Hasegawa B, Wong K, Iwata K, et al. Dual-modality imaging of cancer with SPECT/CT *Technol Cancer Res Treat.* 2002;1:449–58.

[121] Flotats A, Knuuti J, Gutberlet M, et al. Hybrid cardiac imaging: SPECT/CT and PET/CT. A joint position statement by the European Association of Nuclear Medicine (EANM), the European Society of Cardiac Radiology (ESCR) and the European Council of Nuclear Cardiology (ECNC) *Eur J Nucl Med Mol Imaging.* 2011;38:201–12.

[122] Keidar Z, Israel O, Krausz Y. SPECT/CT in tumor imaging: technical aspects and clinical applications *Semin Nucl Med.* 2003;23:205–18.

[123] Schlemmer H, Pichler B, Krieg R, Heiss W. An integrated MR/PET system: prospective applications *Abdom Imaging.* 2009;34:668–74.

[124] Pichler B, Kolb A, Nägele T, Schlemmer H. PET/MRI: paving the way for the next generation of clinical multimodality imaging applications *J Nucl Med.* 2010;51:333–6.

[125] Wagenaar D, Kapusta M, Li J, Patt B. Rationale for the combination of nuclear medicine with magnetic resonance for pre-clinical imaging *Technol Cancer Res Treat.* 2006;5:343–50.

[126] von Schulthess G, Schlemmer H. A look ahead: PET/MR versus PET/CT *Eur J Nucl Med Mol Imaging.* 2009;36 Suppl 1:S3–9.

[127] Antoch G, Bockisch A. Combined PET/MRI: a new dimension in whole-body oncology imaging? *Eur J Nucl Med Mol Imaging.* 2009;36 Suppl 1:S113–20.

[128] Heiss W. The potential of PET/MR for brain imaging *Eur J Nucl Med Mol Imaging.* 2009;36 Suppl 1:S105–12.

[129] Nekolla S, Martinez-Moeller A, Saraste A. PET and MRI in cardiac imaging: from validation studies to integrated applications *Eur J Nucl Med Mol Imaging.* 2009;36 Suppl 1:S121–30.

[130] Delso G, Ziegler S. PET/MRI system design *Eur J Nucl Med Mol Imaging.* 2009;36 Suppl 1:S86–92.

[131] Pichler B, Judenhofer M, Wehrl H. PET/MRI hybrid imaging: devices and initial results *Eur Radiol.* 2008;18:1077–86.

[132] Shao Y, Cherry S, Farahani K, et al. Simultaneous PET and MR imaging *Phys Med Biol.* 1997;42:1965–70.

[133] Cherry S, Shao Y, Siegel S, et al. Optical fiber readout of scintillator arrays using a multi-channel PMT: a high resolution PET detector for animal imaging *IEEE T Nucl Sci.* 1996;43:1932 – 1937.

[134] Garlick P B, Marsden P K, Cave A C, et al. PET and NMR dual acquisition (PANDA): applications to isolated, perfused rat hearts *NMR Biomed.* 1997;10:138–42.

[135] MacKewn J, Halsted P, Charles-Edwards G, et al. Performance Evaluation of an MRI-Compatible Pre-Clinical PET System Using Long Optical Fibers *IEEE T Nucl Sci.* 2010;57:1052 – 1062.

[136] Marsden P, Strul D, Keevil S. Simultaneous PET and NMR *Br J Radiol.* 2002;75:S53–9.

[137] Raylman R, Majewski S, Lemieux S, et al. Simultaneous MRI and PET imaging of a rat brain *Phys Med Biol.* 2006;51:6371–9.

[138] Raylman R, Majewski S, Velan S, et al. Simultaneous acquisition of magnetic resonance spectroscopy (MRS) data and positron emission tomography (PET) images with a prototype MR-compatible, small animal PET imager *J Magn Reson.* 2007;186:305–10.

[139] Lucas A J, Hawkes R C, Ansorge R E, et al. Development of a combined microPET-MR system *Technol Cancer Res Treat.* 2006;5:337–41.

[140] Tai Y, Ruangma A, Rowland D, et al. Performance evaluation of the microPET focus: a third-generation microPET scanner dedicated to animal imaging *J Nucl Med.* 2005;46:455–63.

[141] Gilbert K M, Handler W B, Scholl T J, Odegaard J W, Chronik B A. Design of field-cycled magnetic resonance systems for small animal imaging *Phys Med Biol.* 2006;51:2825–41.

[142] Handler W, Gilbert K, Peng H, Chronik B. Simulation of scattering and attenuation of 511 keV photons in a combined PET/field-cycled MRI system *Phys Med Biol.* 2006;51:2479–91.

[143] Bindseil G, Gilbert K, Scholl T, Handler W, Chronik B. First image from a combined positron emission tomography and field-cycled MRI system *Magn Reson Med.* 2011;66:301–5.

[144] Del Guerra A, Belcari N, Bisogni M, et al. Silicon Photomultipliers (SiPM) as novel photodetectors for PET *Nucl Instrum Methods Phys Res A.* 2010;648:S232–5.

[145] Dokhale P A, Silverman R W, Shah K S, et al. Performance measurements of a depth-encoding PET detector module based on position-sensitive avalanche photodiode read-out *Phys Med Biol.* 2004;49:4293–304.

[146] Pichler B J, Swann B K, Rochelle J, Nutt R E, Cherry S R, Siegel S B. Lutetium oxyorthosilicate block detector readout by avalanche photodiode arrays for high resolution animal PET *Phys Med Biol.* 2004;49:4305–19.

[147] Del Guerra A, Belcari N, Bisogni M, et al. Advantages and pitfalls of the silicon photomultiplier (SiPM) as photodetector for the next generation of PET scanners *Nucl Instrum Methods Phys Res A.* 2010;617:223–6.

[148] Piemonte C. A new silicon photomultiplier structure for blue light detection *Nucl Instrum Methods Phys Res A.* 2006;568:224–32.

[149] Saveliev V, Golovin V. Silicon avalanche photodiodes on the base of metal-resistor-semiconductor (MRS) structures *Nucl Instrum Methods Phys Res A.* 2000;442:223–9.

[150] Catana C, Wu Y, Judenhofer M, Qi J, Pichler B, Cherry S. Simultaneous acquisition of multislice PET and MR images: initial results with a MR-compatible PET scanner *J Nucl Med.* 2006;47:1968–76.

[151] Pichler BJ, Judenhofer MS, Catana C. Performance test of an LSO-APD detector in a 7-T MRI scanner for simultaneous PET/MRI *J Nucl Med.* 2006;47:639–47.

[152] Grazioso R, Ladebeck R, Schmand M. APD-based PET for combined MR-PET imaging *Proc Intl Soc Mag Reson Med.* 2005;13:408.

[153] Schlemmer HP, Pichler BJ, Wienhard K. Simultaneous MR/PET for brain imaging: first patient scans *J Nucl Med.* 2007;48 Suppl 2:45P.

[154] Schlemmer H, Pichler B, Schmand M, et al. Simultaneous MR/PET Imaging of the Human Brain: Feasibility Study *Radiology.* 2008;248:1028–35.

[155] Ojha N, Griesmer J, Hu Zhiqiang, et al. PET performance of the GEMINI TF PET — MR: The world's first whole body PET — MRI scanner *IEEE Nucl Sci Conf R.* 2010:2013 – 2015.

[156] Ratib O, Viallon M, Zaidi H, et al. Whole body PET-MRI scanner: first experience in oncology *Proc Intl Soc Mag Reson Med.* 2011;19:761.

[157] Ritzert M, Fischer P, Mlotok V, et al. Compact SiPM based detector module for time-of-flight PET/MR *IEEE Real Time Conf.* 2009:163 – 166.

[158] Schulz V, Solf T, Weissler B, et al. A preclinical PET/MR insert for a human 3T MR scanner *IEEE Nucl Sci Conf R.* 2009:2577 – 2579.

[159] Solf T, Schulz V, Weissler B, et al. Solid-state detector stack for ToF-PET/MR *IEEE Nucl Sci Conf R.* 2009:2798 – 2799.

[160] Breton E, Choquet P, Goetz C, et al. Dual SPECT/MR imaging in small animal *Nucl Instrum Methods Phys Res A.* 2007;571:446–8.

[161] Goetz Christian, Breton Elodie, Choquet Philippe, Israel-Jost Vincent, Constantinesco André. SPECT low-field MRI system for small-animal imaging *J Nucl Med.* 2008;49:88–93.

[162] Meng L, Tan J, Fu G. Design study of an MRI compatible ultra-high resolution SPECT for in vivo mice brain imaging *IEEE Nucl Sci Conf R.* 2007;4:2956 – 2960.

[163] Tan J, Cai Liang, Meng L. A prototype of the MRI-compatible ultra-high resolution SPECT for in vivo mice brain imaging *IEEE Nucl Sci Conf R.* 2009:2800 – 2805.

[164] Wagenaar D, Nalcioglu O, Muftuler L, et al. Development of MRI-Compatible Nuclear Medicine Imaging Detectors *IEEE Nucl Sci Conf R.* 2006;3:1825 – 1828.

[165] Meier D, Wagenaar D, Mahlum G, et al. A SPECT camera for simultaneous SPECT/MRI *IEEE Nucl Sci Conf R.* 2009:2313–2318.

[166] Hamamura M, Ha S, Roeck W, et al. Development of an MR-compatible SPECT system (MRSPECT) for simultaneous data acquisition *Phys Med Biol.* 2010;55:1563–75.

[167] Rosenthal M S, Cullom J, Hawkins W, Moore S C, Tsui B M, Yester M. Quantitative SPECT imaging: a review and recommendations by the Focus Committee of the Society of Nuclear Medicine Computer and Instrumentation Council *J Nucl Med.* 1995;36:1489–513.

[168] Farquhar T H, Llacer J, Hoh C K, et al. ROC and localization ROC analyses of lesion detection in whole-body FDG PET: effects of acquisition mode, attenuation correction and reconstruction algorithm *J Nucl Med.* 1999;40:2043–52.

[169] Hendel RC, Berman DS, Cullom SJ, et al. Multicenter clinical trial to evaluate the efficacy of correction for photon attenuation and scatter in SPECT myocardial perfusion imaging *Circulation.* 1999;99:2742–9.

[170] Hendel R. Attenuation correction: eternal dilemma or real improvement? *Q J Nucl Med Mol Imaging.* 2005;49:30–42.

[171] Garcia E. SPECT attenuation correction: an essential tool to realize nuclear cardiology's manifest destiny *J Nucl Cardiol.* 2007;14:16–24.

[172] Hendel RC, Corbett JR, Cullom SJ, DePuey EG, Garcia EV, Bateman TM. The value and practice of attenuation correction for myocardial perfusion SPECT imaging: a joint position statement from the American Society of Nuclear Cardiology and the Society of Nuclear Medicine *J Nucl Cardiol.* 2002;9:135–43.

[173] Soares E, King M, Byrne C, Gifford H, Lehovich A. The Influence of Photon Attenuation on Tumor-to-Background and Signal-to-Noise Ratios for SPECT Imaging *IEEE Nucl Sci Conf R.* 2007;5:3609–3615.

[174] Steffen I, Mehl S, Heuck F, et al. Attenuation correction of somatostatin receptor SPECT by integrated low-dose CT: is there an impact on sensitivity? *Clin Nucl Med.* 2009;34:869–73.

[175] Wells RG, King MA, Simkin PH, et al. Comparing filtered backprojection and ordered-subsets expectation maximization for small-lesion detection and localization in 67Ga SPECT *J Nucl Med.* 2000;41:1391–9.

[176] Huang S, Hoffman E, Phelps M, Kuhl D. Quantitation in positron emission computed tomography: 2. Effects of inaccurate attenuation correction *J Comp Assist Tomogr.* 1979;3:804–14.

[177] Bai C, Kinahan P, Brasse D, et al. An analytic study of the effects of attenuation on tumor detection in whole-body PET oncology imaging *J Nucl Med.* 2003;44:1855–61.

[178] Chan W L, Freund J, Pocock N A, et al. Coincidence detection FDG PET in the management of oncological patients: attenuation correction versus non-attenuation correction *Nucl Med Commun.* 2001;22:1185–92.

[179] Lonneux M, Borbath I, Bol A, et al. Attenuation correction in whole-body FDG oncological studies: the role of statistical reconstruction *Eur J Nucl Med.* 1999;26:591–8.

[180] Turlakow A, Larson S M, Coakley F, et al. Local detection of prostate cancer by positron emission tomography with 2-fluorodeoxyglucose:

comparison of filtered back projection and iterative reconstruction with segmented attenuation correction *Q J Nucl Med.* 2001;45:235–44.

[181] Hwang AB, Franc B, Gullberg GT, Hasegawa BH. Assessment of the sources of error affecting the quantitative accuracy of SPECT imaging in small animals *Phys Med Biol.* 2008;53:2233–52.

[182] Chow P, Rannou F, Chatziioannou A. Attenuation correction for small animal PET tomographs *Phys Med Biol.* 2005;50:1837–50.

[183] Chang L. A Method for Attenuation Correction in Radionuclide Computed Tomography *IEEE T Nucl Sci.* 1978;25:638 – 643.

[184] Bergström M, Litton J, Eriksson L, Bohm C. Determination of object contour from projections for attenuation correction in cranial positron emission tomography *J Comp Assist Tomogr.* 1982;6:365–72.

[185] Siegel S, Dahlbom M. Implementation and evaluation of a calculated attenuation correction for PET *IEEE T Nucl Sci.* 1992;39:1117–21.

[186] Dahlbom M, Hoffman E. Problems in signal-to-noise ratio for attenuation correction in high resolution PET *IEEE T Nucl Sci.* 1987.

[187] Derenzo S, Budinger T, Huesman R, Cahoon J, Vuletich T. Imaging properties of a positron tomograph with 280 BGO crystals *IEEE T Nucl Sci.* 1981;28:81–9.

[188] Huesman R, Derenzo SE, Cahoon JL, et al. Orbiting transmission source for positron tomography *IEEE T Nucl Sci.* 1988;35:735–9.

[189] Meikle SR, Dahlbom M, Cherry SR. Attenuation correction using count-limited transmission data in positron emission tomography *J Nucl Med.* 1993.

[190] Carson R, Daube-Witherspoon M. A method for postinjection PET transmission measurements with a rotating source *J Nucl Med.* 1988;29:1558–67.

[191] deKemp R A, Nahmias C. Attenuation correction in PET using single photon transmission measurement *Med Phys.* 1994;21:771–8.

[192] Karp J, Muehllehner G, Qu H. Singles transmission in volume-imaging PET with a 137Cs source *Phys Med Biol.* 1995.

[193] Yu S, Nahmias C. Single-photon transmission measurements in positron tomography using 137Cs *Phys Med Biol.* 1995.

[194] King M, Glick S, Pretorius P, et al. Attenuation, scatter and spatial resolution compensation in SPECT in *Emission tomography: the fundamentals of PET and SPECT* (Wernick M, Aarsvold J. , eds.)Elsevier Academic Press 2004.

[195] Osman MM, Cohade C, Nakamoto Y, Wahl R. Respiratory motion artifacts on PET emission images obtained using CT attenuation correction on PET-CT *Eur J Nucl Med Mol Imaging.* 2003;30:603–6.

[196] Kinahan P, Townsend D, Beyer T, Sashin D. Attenuation correction for a combined 3D PET/CT scanner *Med Phys.* 1998.

[197] Bai C, Shao L, Da Silva AJ, Zhao Z. A generalized model for the conversion from CT numbers to linear attenuation coefficients *IEEE T Nucl Sci.* 2003;50:1510–5.

[198] Burger C, Goerres G, Schoenes S, Buck A. PET attenuation coefficients from CT images: experimental evaluation of the transformation of CT into PET 511-keV attenuation coefficients *Eur J Nucl Med.* 2002.

[199] Dizendorf E, Hany TF, Buck A, von Schulthess G, Burger C. Cause and magnitude of the error induced by oral CT contrast agent in CT-based attenuation correction of PET emission studies *J Nucl Med.* 2003;44:732–8.

[200] Yau Y, Chan W, Tam Y, Vernon P. Application of intravenous contrast in PET/CT: does it really introduce significant attenuation correction error? *J Nucl Med.* 2005;46:283–91.

[201] DiFilippo Frank P, Brunken Richard C. Do implanted pacemaker leads and ICD leads cause metal-related artifact in cardiac PET/CT? *J Nucl Med.* 2005;46:436–43.

[202] Kamel EM, Burger C, Buck A, von Schulthess G, Goerres GW. Impact of metallic dental implants on CT-based attenuation correction in a combined PET/CT scanner *Eur Radiol.* 2003;13:724–8.

[203] Hofmann M, Pichler B, Schölkopf B, Beyer T. Towards quantitative PET/MRI: a review of MR-based attenuation correction techniques *Eur J Nucl Med Mol Imaging.* 2009;36 Suppl 1:S93–104.

[204] Rota Kops E, Herzog H. Alternative methods for attenuation correction for PET images in MR-PET scanners *IEEE Nucl Sci Conf R.* 2007:4327–4330.

[205] Le Goff-Rougetet R, Frouin V, Mangin J. Segmented MR images for brain attenuation correction in PET *Proc SPIE.* 1994;2167:725.

[206] Zaidi H, Montandon M, Slosman D. Magnetic resonance imaging-guided attenuation and scatter corrections in three-dimensional brain positron emission tomography *Med Phys.* 2003.

[207] Martinez-Moller A, Souvatzoglou M, Delso G, et al. Tissue classification as a potential approach for attenuation correction in whole-body PET/MRI: evaluation with PET/CT data *J Nucl Med.* 2009;50:520–6.

[208] Schulz V, Torres-Espallardo I, Renisch S, et al. Automatic, three-segment, MR-based attenuation correction for whole-body PET/MR data *Eur J Nucl Med Mol Imaging.* 2010.

[209] Hofmann M, Steinke F, Scheel V. MRI-based attenuation correction for PET/MRI: a novel approach combining pattern recognition and atlas registration *J Nucl Med.* 2008;49:1875–83.

[210] Visvikis D, Costa D C, Croasdale I, et al. CT-based attenuation correction in the calculation of semi-quantitative indices of [18F]FDG uptake in PET *Eur J Nucl Med Mol Imaging.* 2003;30:344–53.

[211] Wang Y, Chiu E, Rosenberg J, Gambhir S. Standardized uptake value atlas: characterization of physiological 2-deoxy-2-[18 F] fluoro-d-glucose uptake in normal tissues *Mol Imaging Biol.* 2007;9:83–90.

[212] Reivich M, Kuhl D, Wolf A, et al. The [18F]fluorodeoxyglucose method for the measurement of local cerebral glucose utilization in man *Circ Res.* 1979;44:127–37.

[213] Vandenberghe S, D'Asseler Y, Koole M. Iterative list mode reconstruction for coincidence data of gamma camera *Proc SPIE.* 2000.

[214] Hubbel J. Photon cross sections, attenuation coefficients, and energy absorption coefficients from 10 keV to 100 GeV *NSRDS-NBS 29.* 1969.

[215] Konik A, Koesters T, Madsen M, Sunderland J. Evaluation of Attenuation and Scatter Correction Requirements as a Function of Object Size in Small Animal PET Imaging *IEEE T Nucl Sci.* 2011;Accepted for publication.

[216] Bergeron M, Cadorette J, Beaudoin J, et al. Performance Evaluation of the LabPET APD-Based Digital PET Scanner *IEEE T Nucl Sci.* 2009;56:10 – 16.

[217] Surti S, Kuhn A, Werner... M. Performance of Philips Gemini TF PET/CT scanner with special consideration for its time-of-flight imaging capabilities *Journal of Nuclear ....* 2007.

[218] Keereman V, Van Holen R, Mollet P, Vandenberghe S. The effect of errors in segmented attenuation maps on PET quantification *Med Phys.* 2011;38:6010–9.

[219] Keereman V, D'Asseler Y, Van Holen R, Vandenberghe S. The effect of inter-patient attenuation coefficient variability on segmented attenuation correction for PET *J Nucl Med.* 2010;51 Suppl 2:1378.

[220] Bottomley P A, Foster T H, Argersinger R E, Pfeifer L M. A review of normal tissue hydrogen NMR relaxation times and relaxation mechanisms from 1-100 MHz: dependence on tissue type, NMR frequency, temperature, species, excision, and age *Med Phys.* 1984;11:425–48.

[221] Stanisz GJ, Odrobina EE, Pun J, et al. T1, T2 relaxation and magnetization transfer in tissue at 3T *Magn Reson Med.* 2005;54:507–12.

[222] Sundaram M, McGuire M H, Schajowicz F. Soft-tissue masses: histologic basis for decreased signal (short T2) on T2-weighted MR images *Am J Roentgenol.* 1987;148:1247–50.

[223] Robson M, Gatehouse P, Bydder M, Bydder G. Magnetic resonance: an introduction to ultrashort TE (UTE) imaging *J Comp Assist Tomogr.* 2003;27:825–46.

[224] Holmes JE, Bydder GM. MR imaging with ultrashort TE (UTE) pulse sequences: Basic principles *Radiography.* 2005;11:163–74.

[225] Schmidt M A, Yang G Z, Gatehouse P D, Firmin D N. FID-based lung MRI at 0.5 T: theoretical considerations and practical implications *Magn Reson Med.* 1998;39:666–72.

[226] Pauly J, Conolly S, Nishimura D, Macovski A. Slice-selective excitation for very short T2 species *Proc Intl Soc Mag Reson Med.* 1989:28.

[227] Glover G H, Pauly J M. Projection reconstruction techniques for reduction of motion effects in MRI *Magn Reson Med.* 1992;28:275–89.

[228] Glover G H, Lee A T. Motion artifacts in fMRI: comparison of 2DFT with PR and spiral scan methods *Magn Reson Med.* 1995;33:624–35.

[229] Rahmer J, Börnert P, Groen J, Bos C. Three-dimensional radial ultrashort echo-time imaging with T2 adapted sampling *Magn Reson Med.* 2006;55:1075–82.

[230] Schenck J F. The role of magnetic susceptibility in magnetic resonance imaging: MRI magnetic compatibility of the first and second kinds *Med Phys.* 1996;23:815–50.

[231] Bergin C J, Glover G H, Pauly J M. Lung parenchyma: magnetic susceptibility in MR imaging *Radiology.* 1991;180:845–8.

[232] Hatabu H, Alsop D C, Listerud J, Bonnet M, Gefter W B. T2* and proton density measurement of normal human lung parenchyma using submillisecond echo time gradient echo magnetic resonance imaging *Eur J Radiol.* 1999;29:245–52.

[233] Knopp MV, Hess T, Schad LR, et al. MR-Tomographie von Lungenmetastasen mit schnellen Gradientenechosequenzen *Der Radiologe.* 1994;34:581–7.

[234] Macovski A. Noise in MRI *Magn Reson Med.* 1996;36:494–7.

[235] Ochs M, Nyengaard J, Jung A, et al. The number of alveoli in the human lung *Am J Respir Crit Care Med.* 2004;169:120–4.

[236] Davis C A, Genant H K, Dunham J S. The effects of bone on proton NMR relaxation times of surrounding liquids *Invest Radiol.* 1986;21:472–7.

[237] Meiboom S, Gill D. Modified spinâĂŘecho method for measuring nuclear relaxation times *Rev Sci Instrum.* 1958;29:688.

[238] Keereman V, Vandenberghe S, De Deene Y, Luypaert R, Broux T, Lemahieu I. MR-based attenuation correction for PET using an Ultrashort Echo Time (UTE) sequence *IEEE Nucl Sci Conf R.* 2008:4656–61.

[239] Keereman V, Fierens Y, Broux T, De Deene Y, Lonneux M, Vandenberghe S. MRI-Based Attenuation Correction for PET/MRI Using Ultrashort Echo Time Sequences *J Nucl Med.* 2010;51:812–8.

[240] Keereman V, De Deene Y, Broux T, Lemahieu I, Vandenberghe S. Estimation of attenuation maps from UTE derived R2 images *Proc Intl Soc Mag Reson Med.* 2009;17:2774.

[241] Keereman V, Vandenberghe S, De Deene Y. *Method and assembly for correcting a relaxation map for medical imaging applications*. WO/2010/094655. European Patent Application. August 25th 2010.

[242] Kato H, Kuroda M, Yoshimura K, Yoshida A. Composition of MRI phantom equivalent to human tissues *Med Phys.* 2005.

[243] Yoo TS, Ackerman MJ, Lorensen WE, et al. Engineering and algorithm design for an image processing Api: a technical report on ITK–the Insight Toolkit *Stud Health Technol Inform.* 2002;85:586–92.

[244] Loening A, Gambhir SS. AMIDE: a free software tool for multimodality medical image analysis *Mol Imaging.* 2003;2:131–7.

[245] Keereman V, Vandenberghe S, De Deene Y, Luypaert R, Broux T, Lemahieu I. MR-based attenuation correction for PET using a UTE sequence *1st Annual Meeting ISMRM Benelux Chapter.* 2008.

[246] Keereman V, Mollet P, Fierens Y, Espana S, Vandenberghe S. Design of a realistic PET-CT-MRI phantom *IEEE Nucl Sci Conf.* 2011.

[247] Bonta D, Wahl RL. Overcorrection of iodinated contrast attenuation in SPECT-CT: phantom studies *Med Phys.* 2010;37:4897–901.

[248] Taschereau R, Chow PL, Chatziioannou AF. Monte Carlo simulations of dose from microCT imaging procedures in a realistic mouse phantom *Med Phys.* 2006;33:216–24.

[249] Willekens I, Buls N, Lahoutte T, et al. Evaluation of the radiation dose in micro-CT with optimization of the scan protocol *Contrast Media Mol Imaging.* 2010;5:201–7.

[250] Vanhove C, Defrise M, Lahoutte T, Bossuyt A. Three-pinhole collimator to improve axial spatial resolution and sensitivity in pinhole SPECT *Eur J Nucl Med Mol Imaging.* 2008;35:407–15.

[251] Rahmer J, Boernert P. Anisotropic 3D Radial Sampling for Ultrashort TE Imaging *Proc Intl Soc Mag Reson Med.* 2006;14:3029.

[252] Vanhove C, Defrise M, Bossuyt A. Improved quantification in single-pinhole and multiple-pinhole SPECT using micro-CT information *Eur J Nucl Med Mol Imaging.* 2009;36:1049–63.

[253] Brown S, Bailey DL, Willowson K, Baldock C. Investigation of the relationship between linear attenuation coefficients and CT Hounsfield units using radionuclides for SPECT *Appl Radiat Isotopes.* 2008;66:1206–1212.

[254] Vanhove C, Defrise M, Franken P R, Everaert H, Deconinck F, Bossuyt A. Interest of the ordered subsets expectation maximization (OS-EM) algorithm in pinhole single-photon emission tomography reconstruction: a phantom study *Eur J Nucl Med.* 2000;27:140–6.

[255] Gullberg G, Huesman R, Malko J, Pelc N, Budinger TF. An attenuated projector-backprojector for iterative SPECT reconstruction *Phys Med Biol.* 1985;30:799–816.

[256] Tetrault M, Viscogliosi N, Riendeau J, et al. System architecture of the LabPET^{TM} small animal PET scanner *IEEE T Nucl Sci.* 2008.

[257] Keereman V, Deleye S, Baete S, Staelens S, De Deene Y, Vandenberghe S. UTE-MR-based attenuation maps for microPET/microSPECT-MR *World Mol Imaging Congr.* 2009.

[258] Keereman V, Fierens Y, Vanhove C, Lahoutte T, De Deene Y, Vandenberghe S. Whole-body MR-based attenuation correction for micro-SPECT-MR *World Mol Imaging Congr.* 2010.

[259] Keereman V, Fierens Y, Vanhove C, Lahoutte T, Vandenberghe S. MR-based attenuation correction for micro-SPECT *Mol Imaging.* 2011;Accepted for publication.

[260] Keereman V, Van Holen R, Vanhove C, Mollet P, Vandenberghe S. Absolute quantification for small-animal PET *IEEE Nucl Sci Conf.* 2011.

[261] Keereman V, Vandenberghe S, De Deene Y, et al. MR-based Attenuation Correction for PET/SPECT using Ultrashort Echo Time (UTE) Sequences *2nd Juelich MR-PET workshop.* 2010.

[262] Keereman V, Fierens Y, De Deene Y, Vandenberghe S. Whole-body MR-based attenuation correction for PET using UTE Sequences *Eur J Nucl Med Mol Imaging*. 2010;47:S220.

List of Publications

Journal papers

[1] Keereman V, Fierens Y, Vanhove C, Lahoutte T, Vandenberghe S. MR-based attenuation correction for micro-SPECT *Mol Imaging.* 2011;Accepted for publication.

[2] Keereman V, Van Holen R, Mollet P, Vandenberghe S. The effect of errors in segmented attenuation maps on PET quantification *Med Phys.* 2011;38:6010–9.

[3] Tsoumpas C, Buerger C, King A, et al. Fast generation of 4D PET-MR data from real dynamic MR acquisitions *Phys Med Biol.* 2011;56:6597–6613.

[4] Keereman V, Fierens Y, Broux T, De Deene Y, Lonneux M, Vandenberghe S. MRI-Based Attenuation Correction for PET/MRI Using Ultrashort Echo Time Sequences *J Nucl Med.* 2010;51:812–8.

Book chapters

[1] Keereman V, Vanhove C, Vandenberghe S. Attenuation correction for emission tomography using ultrashort echo time sequences in *Imaging and spectroscopy of short T2 and T2* components in tissue* (Bydder G, Young I, Fullerton G. , eds.)John Wiley & Sons Ltd. Invited, in press.

Conference proceedings

[1] Keereman V, Mollet P, Fierens Y, Espana S, Vandenberghe S. Design of a realistic PET-CT-MRI phantom *IEEE Nucl Sci Conf.* 2011.

[2] Keereman V, Van Holen R, Vanhove C, Mollet P, Vandenberghe S. Absolute quantification for small-animal PET *IEEE Nucl Sci Conf.* 2011.

[3] Mollet P, Keereman V, Vandenberghe S. Experimental evaluation of simultaneous emission and transmission imaging using TOF information *IEEE Nucl Sci Conf.* 2011.

[4] Keereman V, Vandenberghe S, De Deene Y, et al. MR-based Attenuation Correction for PET/SPECT using Ultrashort Echo Time (UTE) Sequences *2nd Juelich MR-PET workshop.* 2010.

[5] Vandenberghe S, Keereman V, Marsden P, et al. Challenges towards simultaneous PET-MRI *Phys Health Eur Abstr.* 2010.

[6] Keereman V, Fierens Y, Vanhove C, Lahoutte T, De Deene Y, Vandenberghe S. Whole-body MR-based attenuation correction for micro-SPECT-MR *World Mol Imaging Congr.* 2010.

[7] Keereman V, Fierens Y, De Deene Y, Vandenberghe S. Whole-body MR-based attenuation correction for PET using UTE Sequences *Eur J Nucl Med Mol Imaging.* 2010;47:S220.

[8] Mollet P, Keereman V, Vandenberghe S. Simultaneous emission and transmission imaging for PET-MRI using time-of-flight information *J Nucl Med.* 2010;51 Suppl 2:124.

[9] Keereman V, D'Asseler Y, Van Holen R, Vandenberghe S. The effect of inter-patient attenuation coefficient variability on segmented attenuation correction for PET *J Nucl Med.* 2010;51 Suppl 2:1378.

[10] Schulz V, Solf T, Weissler B, et al. Innovative technologies for simutaneous TOF PET/MR *Eur J Nucl Med Mol Imaging.* 2010;37:S219–20.

[11] Vandenberghe S, Keereman V, Staelens S, Schulz V, Marsden P. Effect of geometrical constraints on PET performance in whole body simultaneous PET-MR *IEEE Nucl Sci Conf R.* 2009:3808 – 3811.

[12] Keereman V, Vandenberghe S. PET-MR attenuation correction using an ultrashort echo time sequence *Abstracts 10th UGent-FirW Doctoraatssymposium.* 2009:34–5.

[13] Keereman V, Vandenberghe S, De Beenhouwer J, et al. Scatter effects of MR components in PET-MR inserts *IEEE Nucl Sci Conf R.* 2009:3804 – 3807.

[14] Tsoumpas C, Buerger C, King AP, et al. Simulation of dynamic PET data from real MR acquisitions *IEEE Nucl Sci Conf R.* 2009:3065 – 3068.

[15] Schulz V, Solf T, Weissler B, et al. A preclinical PET/MR insert for a human 3T MR scanner *IEEE Nucl Sci Conf R.* 2009:2577 – 2579.

[16] Keereman V, Deleye S, Baete S, Staelens S, De Deene Y, Vandenberghe S. UTE-MR-based attenuation maps for microPET/microSPECT-MR *World Mol Imaging Congr.* 2009.

[17] Keereman V, De Deene Y, Broux T, Lemahieu I, Vandenberghe S. Estimation of attenuation maps from UTE derived R2 images *Proc Intl Soc Mag Reson Med.* 2009;17:2774.

[18] Keereman V, Vandenberghe S, De Deene Y, Luypaert R, Broux T, Lemahieu I. MR-based attenuation correction for PET using an Ultrashort Echo Time (UTE) sequence *IEEE Nucl Sci Conf R.* 2008:4656–61.

[19] Keereman V, Vandenberghe S, De Deene Y, Luypaert R, Broux T, Lemahieu I. MR-based attenuation correction for PET using a UTE sequence *1st Annual Meeting ISMRM Benelux Chapter.* 2008.

[20] De Deene Y, Baete S, Fieremans E, et al. MR engineering research at the Ghent University *1st Benelux in vivo MR methods symposium.* 2007:78–82.

Patent applications

[1] Keereman V, Vandenberghe S, De Deene Y. *Method and assembly for correcting a relaxation map for medical imaging applications*. WO/2010/094655. European Patent Application. August 25th 2010.